A Computer Vision-Based Structural Health Monitoring Framework: Feature-Mining of Damage for Predictive Numerical Simulations

A Dissertation

by

Mehrdad Shafiei Dizaji

Presented To

The School of Engineering and Applied Science

University of Virginia

In partial fulfillment of the requirements for the degree of

DOCTOR OF PHILOSOPHY

May 2020

A Computer Vision-Based Structural Health Monitoring Framework: Feature-Mining of Damage for Predictive Numerical Simulations

A Dissertation

by

Mehrdad Shafiei Dizaji

Presented To

The School of Engineering and Applied Science

University of Virginia

In partial fulfillment of the requirements for the degree of

DOCTOR OF PHILOSOPHY

Approved by:

Devin K. Harris (Advisor)

Jose P. Gomez

Osman E. Ozbulut

Arsalan Heydarian

Nada Basit

May 2020

ABSTRACT

For the infrastructure in U.S., the structural health monitoring (SHM) community has generalized a strategy with a primary focus of accurately monitoring in-situ behavior to assess performance, detecting damage, and determining structural condition. At the core of this strategy is the need to identify and quantify damage, but also to predict the implications of this damage on the structural system. However, for scenarios where this damage is not visible, this challenge becomes amplified due to the potential for structural failure in the presence of this unknown risk. For these types of structures, a more local strategy is needed, one that is able to provide in-situ information about the current condition state of performance of an individual structure in the absence of previous baseline performance data. This need drives our research question; can internal damage be effectively identified using only limited surface observations obtained from image-based sensing techniques as a non-contact full-field approach?

Recent advancements in camera technology, optical sensors, and image-processing algorithms have made optically-based and non-contact measurement techniques such as photogrammetry and 3D Digital Image Correlation (3D-DIC) appealing methods for non-destructive evaluation (NDE) and SHM. Conventional sensors (e.g. accelerometers, strain gages, string potentiometers, LVDTs) provide results only at a discrete number of points. Moreover, these sensors need wiring, can be time-consuming to install, may require additional instrumentation (e.g., power amplifiers, data acquisition), and are difficult to implement on large-sized structures without interfering with their functionality or may require instrumentation having a large number of data channels. On the contrary, optical techniques can provide accurate quantitative information about full-field displacement, strain and geometry of a structure without contact or interfering with the structure’s functionality.

This dissertation centers around recovering unseen damage within a structural system using limited, but full-field surface deformation measurements. The proposed approach leverages full-field surface deformation measurements of structural elements derived using 3D-DIC coupled within a structural optimization process to search for and identify the presence of invisible damage. The idea initiates from preliminary work that has proven successful in identifying constitutive properties implied for quantifying damage from material distribution in structural specimens. While this preliminary work was promising, the concept needed further research to extend the framework towards a more robust approach that can be used for in-situ assessment of in-service structural systems. The research herein centers on a laboratory scale investigation of structural components, which exhibits variability in its constitutive

properties that are typically uncertain within existing structures and is also vulnerable to internal damage and/or heterogeneous material distributions that are unseen from the surface.

First, full-field sensing measurements from 3D-DIC was applied to update a finite element model (FEM) of a full-size I-shaped steel beam under flexural loading. A hybrid optimization algorithm consisting of a gradient-based and a genetic algorithm (GA) optimizer was introduced to attain and optimize the structural unknowns including constitutive properties and boundary condition assessments. The updated model was illustrated to generate improved estimations of the response through comparisons with ground truth measurements acquired from discrete sensors. Second, based on the previous fact that constitutive properties can be resolved accordingly using St-Id using full-field sensing, the framework was extended to identify regions with internal defects in steel specimens. This work employed a hybrid algorithm combining a GA and a limited-memory Broyden-Fletcher-Goldfarb-Shanno algorithm (LBFGS-B) to execute the optimization problem. While the method showed promise in detecting the existence and vicinity of the defect, recovering the 3D shape of the defect was not possible.

Most recently, the work went one step further and a new approach using full-field surface measurements coupled with topology optimization was proposed to localize and reconstruct the 3D shape of unseen subsurface defects. Thus it aimed to expand on the work and to demonstrate that unlike a limited set of discrete sensing data points or global dynamic properties, the rich data from full-field image-based measurements can enable the identification of a more detailed picture of the internal defects. The main contributions of this dissertation can thus be summarized as: 1) Unlike NDE/T techniques which depend upon specialized sensing equipment (e.g. radars or radiation-based scanners, etc.), the introduced method solely applied digital cameras coupled with structural mechanics to deduce subsurface conditions. 2) The proposed method leverages the rich full-filed response data from DIC to enable the reconstruction of the 3D shape of damage, representing an advancement over current practice which has been limited primarily to identification and basic localization.

Table of Contents

List of Figures

List of Tables

1 CHAPTER 1 – Introduction

1.1 Motivation and Scope

The aging infrastructure network in the United States and much of the developed world is reaching the end of its design service life. Nonetheless, a complete replacement is not feasible due to resource limitations. These aging infrastructure systems are not necessarily going to fail immediately; however, the aging process makes these systems highly vulnerable without assessment. As a result, infrastructure owners are exploring for solutions to mitigate this risk and vulnerability. The premise of SHM is a system performance evaluation strategy with the end goal of characterizing behavior and providing indications of damage and has demonstrated potential as a strategy for temporal condition assessment of the built environment, with a broader vision of exhibiting forewarning of impending failure [1-5].

Thus far, a significant body of SHM research has advanced the body of knowledge, especially in the scope of sensing and analysis techniques. However, a fundamental restriction that remains is the translation of measurable phenomena for full-scale physical systems into information that describes the system's health and condition state. From a research and development perspective, these gaps indicate that SHM is still in its infancy with excellent opportunities for growth and development. As progress is made towards holistic strategies toward building smart and connected communities, the requirement for efficient, low-cost, non-invasive, and data-rich techniques is becoming increasingly essential to the SHM community. Although this dissertation does not propose a complete solution to these challenges, it does describe a novel concept that aims to leverage a data-rich and non-invasive measurement strategy to describe the local and global behavior of a structural system quantitatively and efficiently [6-9].

Figure 1.1 illustrates how the non-contact and non-invasive nature of the proposed approach can help facilitate the assessment of critical infrastructure with minimum disruption of service, while its continuous and full-field sensing provides a unique opportunity for behavior characterization. More broadly, this work aim to quantify structural behavior such as internal and external damage detection from a limited set of measurements on the visible side of a structure. This dissertation specifically describes a refined St-Id and damage detection approach using full-field measurements derived from 3D-DIC to characterize uncertain parameters (i.e. constitutive properties, geometric description and boundary conditions) of a laboratory-scale structural component [6-15].

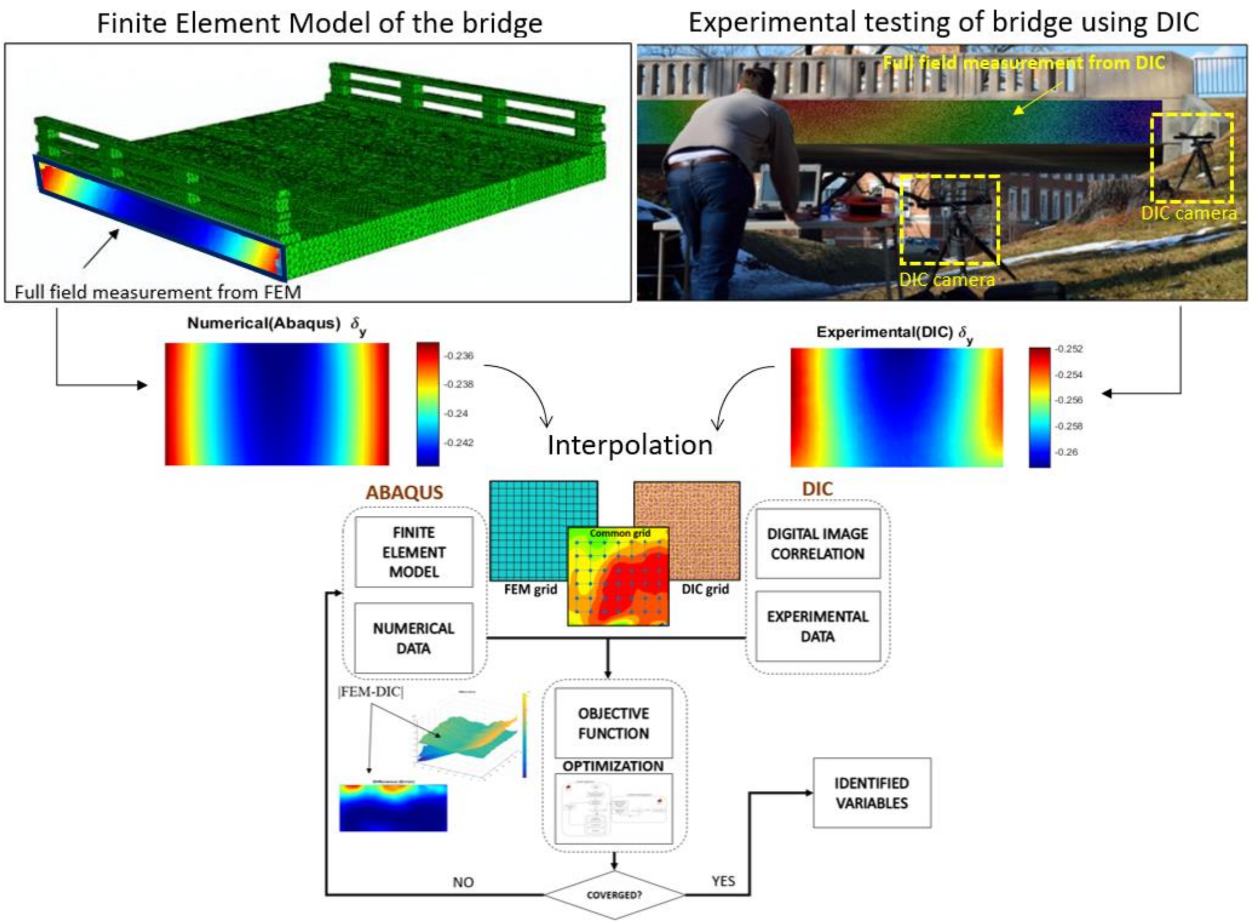

Figure 1.1. Concept of DIC for SHM: full-field data acquisition with minimum disruption of service

3D-DIC, describes a non-contact photogrammetric technique capable of measuring the full-field deformation response of a structural component under loading. DIC relies on tracking the movement and deformation of pixel patterns over a sequence of digital images. The measured component is typically patterned, creating a high-contrast speckled surface, with the correlation or pattern matching algorithm constrained to a subset region to ensure correspondence of unique patterns [16-21]. Across the sequence of images, deformations are measured by tracking pixel movements through space with interpolation used to describe the full-field response across the specimen surface. 2D-DIC leverages planar image sets and can be used to measure in-plane deformation, whereas 3D-DIC extends the principles of photogrammetry using calibrated stereo-paired cameras to measure three-dimensional deformation [22-

27]. The ability to measure deformation have always been vital to the field of experimental mechanics and recent advances in imaging tools and the availability of reliable commercial DIC tools has created opportunities for extending the technique to large scale infrastructure applications [28-32].

The motivation of this dissertation is centered around two essential trends; First, the US infrastructure faces challenges of unprecedented complexity from aging and deterioration, unparalleled demand for service, pressure to urbanize, and natural man-made hazards. Therefore, there is a need for low-cost, non-invasive, and data-rich techniques for the SHM community [5, 33-40]. Second, historically, much of the assessment strategies used to define performance have relied heavily on visual inspection or NDE/T as the standard method to characterize condition state, but research has shown that these strategies yield results that are subjective and somewhat unreliable [33, 38, 40]. Additionally, these condition characterization approaches only provide a description of current damage, but do not link to structural performance to quantify damage rate over time. On the other front of evaluation, there has been a major push in the area of NDE, sensing techniques and sensors, but these advances have also not succeeded in bridging the gap between measurement and performance. Although, both NDE and SHM strategies have demonstrated success for many scenarios, there are still many shortcomings that cannot be readily resolved without highly complicated equipment or costly monitoring systems. Consequently, there is demand for techniques that enable the identification of behavior of in-situ structures such as quantification of deteriorations, in a cost-effective and non-invasive manner. In response to these needs, the central hypothesis of this dissertation research is:

"Structure subsurface conditions (e.g. material properties and internal defects) can be reconstructed within an optimization framework through full-field surface measurements of structural response, obtained from image-based sensing techniques such as 3D-DIC, coupled with a model-based simulation."

In recent years, there have been significant advances in the field of image-based sensing [41]. While these traditional visual assessment techniques have a number of limitations when used in a subjective manner, vision as a quantitative tool has a number benefits for assessment including:

- Image-based assessment is a non-contact technique that requires limited access;
- Image-based assessment is non-invasive, and does not require physical instrumentation;
- Quantitative vision-based techniques align with historical practices of qualitative vision-based inspection;
- Condition and behavioral features can be linked over time scales

This dissertation explores a novel concept that leverages advances in image-based assessment to develop an approach for integration into the domain of SHM. This work aligns with a thrust in the emerging area of image-based SHM (iSHM) and offers the potential for a low-cost high-impact assessment technique for characterizing the operational response of existing structures with minimal service disruption and minimal extensive instrumentation and monitoring equipment. Within the scope of this work, the capabilities of image-based deformation measurement approaches for describing condition state, system behavior, damage identification, and model updating were evaluated. A basic schematic of the image – based St-Id framework is illustrated in Figure 1.2. In summary, the proposed idea lies at the intersection of NDE and SHM and aims to employ full-field sensing to identify the constitutive properties to infer and reconstruct a detailed 3D shape of the internal properties of a structure from constitutive property distribution in the design domain. The measurements derived from DIC provide an unprecedented richness that cannot be acquired using traditional sensing, hence providing the localized detection characteristics of NDE techniques, while derived from mechanical behavior characteristic of SHM approaches.

Therefore, the dissertation leverages 3D-DIC sensing measurements procured from a mechanical loading scheme, for optimizing and updating a FEM to acquire constitutive properties (i.e., internal abnormality of structures is inferred from constitutive property distribution), geometric description, and boundary conditions of the initial numerically presented model. The model updating procedure is formulated as an optimization problem whereby the differences between the measured response and that predicted by the FEM model are iteratively pushed to a minimum. To solve the optimization problem, different optimization techniques are used such as a hybrid GA solver, that combines a metaheuristic evolutionary optimization method (GA) with an iterative gradient descent process and a topology optimization technique. The model parameters corresponding to the optimized model are the identified unknowns of the structural system. It is hypothesized that the full-field response measurements achieved through 3D-DIC provide a robust basis for model updating, optimizing and St-Id. The results of this dissertation illustrate the opportunities offered by 3D-DIC in the SHM domain and demonstrate that tools such as DIC have the potential to provide decision-makers with a comprehensive assessment tool to better describe the performance of the infrastructure network while also being non-contact and non-invasive [6-15]. While these works are limited to laboratory scale experiments under controlled environments, results provide a proof of concept that has the potential for scaling to in-situ evaluation of operational structural systems in the future. This dissertation is a collection of four manuscripts that describe the aforementioned research works. Through the presented results, this dissertation highlights the power of the emerging full-field image-based sensing measurements based on DIC in the field of St-Id and damage detection and while the proposed research effort studied this problem in the context of structural engineering, the findings will potentially benefit a range of communities, including geotechnical, construction, biomedical, and mechanical engineering, all of whom face similar challenges with respect to damage characterization.

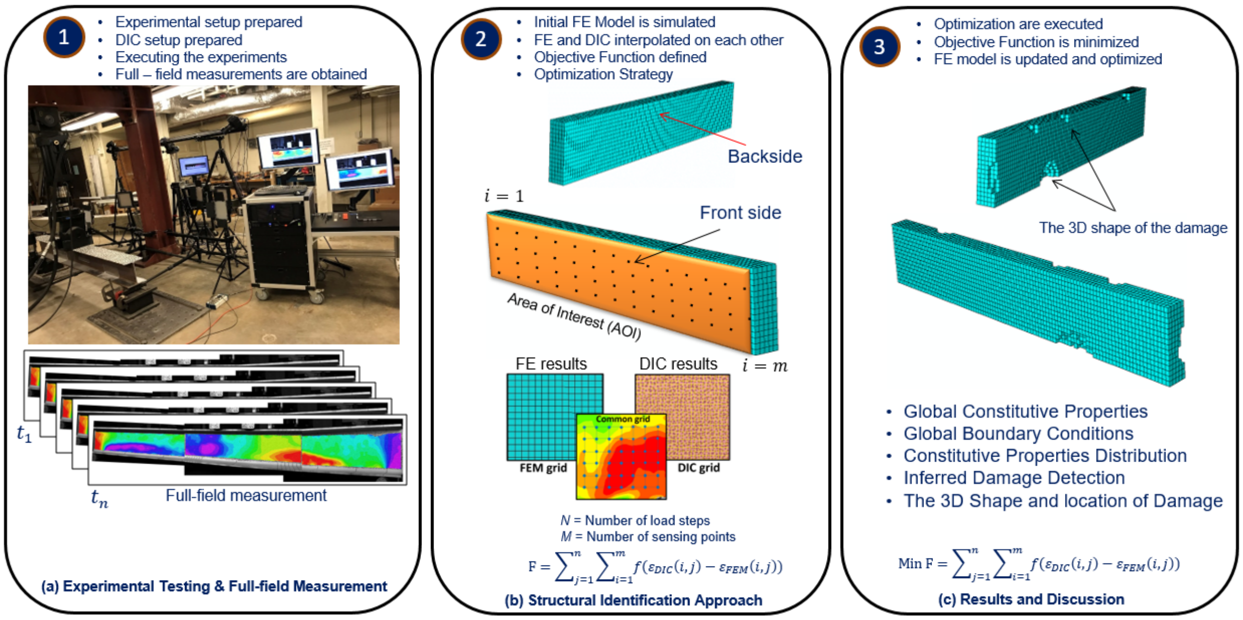

Figure 1.2. Overview of Proposed Image-Based St-Id

1.2 Image-Based Full-Field Sensing Technique

Deformation measurements are vital to the field of structural engineering and engineering mechanics; however, measurement capabilities have historically been limited to localized deformation measurement using classical tools such as strain gauges, linear variable displacement transducers and vibrating wire gauges, most of which require direct contact between the sensor and the specimen. These measurement techniques have been used extensively in SHM and St-Id in the past; however, emerging vision-based approaches have continued to acquire credibility in the field of SHM, as these approaches suggest an efficient approach to collect similar data without being in contact with the structure. DIC, which is one of these vision-based approaches, has roots in the field of experimental mechanics, but is gaining traction as a potential measurement technique suitable for accurately describing the mechanical response of large scale members under loading. DIC builds on the fundamental principles of photogrammetry and provides a mechanism to quantify full-field surface deformation from a series of sequential images of a specimen subjected to loading.

Figure 1.3 conceptualizes the potential advantage of the proposed framework for model updating and St-Id using full-field response measurements (i.e. 3D-DIC) in comparison with those obtained by discrete point sensors (e.g. strain gages, LVDTs, etc.). The dotted line depicts the predictions of an FEM model updated by matching the measurements of only three discrete mechanical sensors. The dashed line reperesents a model updated using a fine grid of points on a full-field response contour (e.g. derived from DIC measurement). In this illustration, it becomes evident that matching a complex function using a limited set of discrete mechanical sensors may closely agree regarding the proximity of the sensors, but may not guarantee a good match in other locations on the specimen. On the other hand, matching an entire full-field response enables a more comprehensive representation of the global and local behaviors throughout the specimen. This advantage is expected to be realized in more complex structural systems, where only a few discrete points may be insufficient to describe the behavior [42]. An example is a structure with geometrical non-uniformities (e.g. a hole or defect) or complicated boundary conditions where the response cannot be uniquely represented by a few discrete sensors. The experimental setup examined in this work is a relatively simple structural system and the work presented in this research represents a series of laboratory examples that provide the foundation for expanding this concept. Future works by the authors aim to illustrate these advantages in more complex structural systems such as full-scale highway bridge structures.

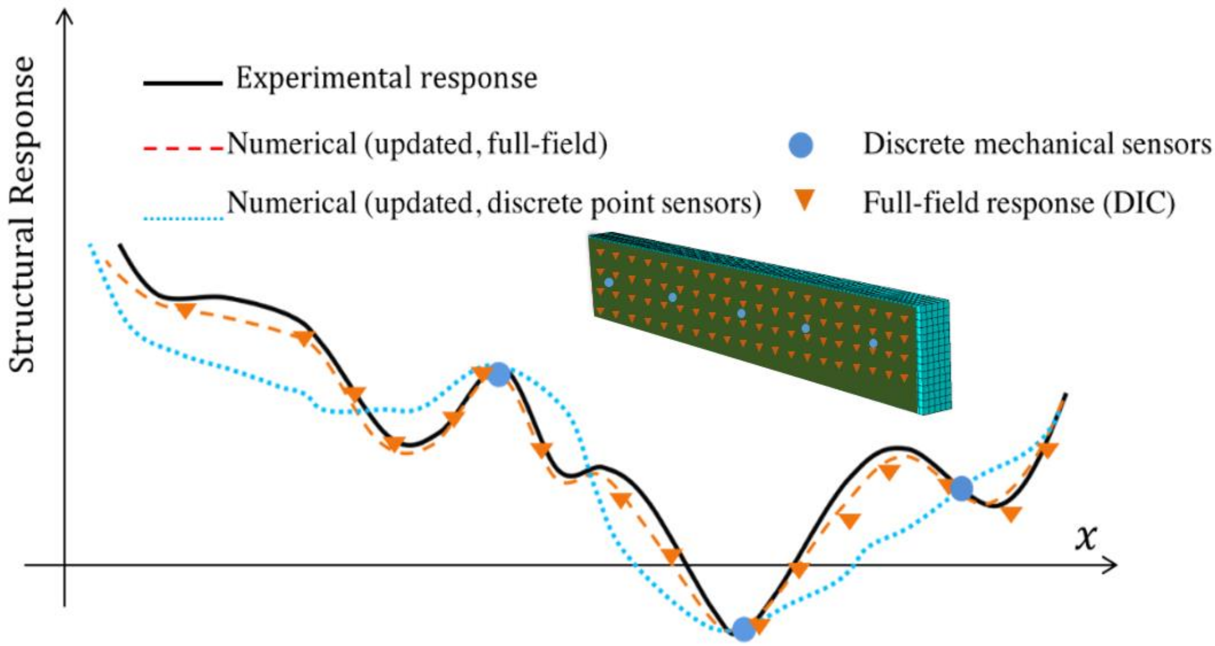

Figure 1.3. Conceptual illustration of impact of full-field sensing on St-Id framework.

1.3 St-Id within SHM Framework

Within the aforementioned SHM framework, numerical models (typically FEM) are commonly used in collaboration with sensing methods to describe the behavior of structural systems. FEM has been used with great success to simulate structural response of idealized systems, but its approximate nature and simplifying assumptions coupled with uncertainties associated with boundary conditions and condition state inherently result in errors when describing existing structural systems [43]. St-Id describes an approach that emphasizes correlation of the response characteristics between a model and experiment or measurement, providing a basis for employing an updated/optimized FE model to characterize critical performance measures of existing structural systems. St-Id is the solution to an inverse problem and aims to minimize differences between analytical and experimental results. The unknown parameters designated as design variables in the FEM are iteratively tuned so as to match the experimentally measured and the numerically computed response as closely as possible. So, this solution is typically formulated as an optimization problem, with an objective of identifying the unknown or uncertain features within the problem space. Satisfactory correlation between the observed experimental behavior and the analytical results is critical, but equally essential in maintaining the physical significance of updated parameters [44]. For this purpose, setting up of an objective or cost function and selecting updating parameters are crucial steps in St-Id. The changes in these parameters are then determined iteratively and pushed to a minimum via an optimization algorithm. St-Id aims to bridge the gap between the model and the real system by developing reliable estimates of the performance and vulnerability through improved simulations. In many St-Id scenarios a cost function is developed and defined in terms of differences between numerical and experimental displacement fields. This function is then minimized on part of the system boundary in an iterative manner, for example by changing the material parameters (constitutive properties) and boundary conditions. Given a unique set of system geometry, material parameters, traction and displacement boundary conditions, the displacement and deformation response of a system is also unique. Hence, assuming the system geometry and boundary conditions are correctly replicated in the FEM, convergence between numerical and experimental displacement fields is achieved only when the constitutive parameters approach their true values. Examples of this optimization concept are available across numerous fields, but representative St-Id examples are available in the literature [45-47]. Within the context of in-service infrastructure systems, St-Id provides a pathway by which the operational response characteristics of a system can be used to characterize performance of the system within its environment.

1.4 Literature review of SHM, NDE and Image-Based techniques

Assessing and quantifying the condition of aging structures is essential to verifying structural integrity, ensuring long-term reliability, and determining when component repair or replacement should be made. A goal in industry is to move away from schedule-based maintenance and toward condition-based monitoring in order to perform assessment of factors that can jeopardize the system's performance [2, 33, 35, 37, 38, 48]. Identifying a strategy to detect damage for engineering systems, structures, and infrastructure is called SHM. SHM involves the observation of the targeted system over time to extract damage-sensitive features, determine the current health state, and predict future condition [2] which is important for damage prognosis and future structure life prediction. SHM plays a key role in the prevention of catastrophic failures, improving the safety of structures and infrastructure, and reducing maintenance downtime and costs. Thus, it is a method for tracking the health of an engineering system by combining damage detection algorithms with structural monitoring devices (e.g., sensors). SHM is often carried out in conjunction with another closely related discipline: NDE often referred to as Non-Destructive Testing (NDT). Those techniques consist of evaluation methods to assess the condition of a targeted system without affecting the system's functionality [40]. Both SHM and NDE techniques aim for early detection and assessment of structural damage to ensure that structures continue to meet life-safety requirements. Human visual inspection techniques are labor-intensive and based on the inspector's opinion and are, thus, subject to variability motivating the need for automated computer-based monitoring systems. Contact-based sensors are commonly used for monitoring a variety of structural systems. One of the most common practices is to record and analyze the data from a network of sensors, either passive or active, embedded or attached onto the monitored structure [49]. These methods include both dynamic and static analyses and have significantly improved over time. Contact-based sensors such as strain-gages, accelerometers, linear voltage displacement transducers (LVDTs), inclinometers, and extensometers are commonly used for SHM and NDE applications [1, 4]. Fiber optic sensors have proven to be valid alternatives to the conventional sensors due to their flexibility, Electro Magnetic Interference (EMI) immunity, and scalability [50, 51]. However, these sensors can be difficult to implement, need wiring, are costly, require power, and once attached are generally not portable for interrogation on multiple engineering systems. For resolving these problems, several researchers proposed using Wireless Sensor Networks [37, 39]. Nevertheless, even these sensors are typically not durable enough to be attached or embedded in the structure and perform measurements throughout a structures lifespan which may be years or decades after its construction (when failures are more likely to occur). Furthermore, most of these sensors can only provide information at a few discrete points [52]. Recent technological developments have provided new NDE techniques for the assessment of different engineering systems. Radiography [53], radioactive computerized tomography [54], radar [48], ultrasonic arrays and acoustic imaging systems [34], acoustic emission [36], and infrared thermography [55] have all been implemented for NDE and SHM and each possesses their advantages and challenges. The readers are referred to the studies of [3, 5, 33, 35, 38, 56, 57] for further information, depending on the specific SHM and NDE applications. New advances in camera technology, optical sensors, and image-processing algorithms allowed the development of a new generation of non-contact measuring methods. Optical-based techniques such as 3D-DIC, have become valuable tools for performing non-contact measurements and extracting structural deformations, full-field displacement and strain and geometry profiles, in civil, and mechanical engineering systems.

1.5 Digital Image Correlation Technique

The ability to measure deformation has been vital to the development of structural engineering theory for decades; however, available methods have typically been limited to localized measurement tools such as strain gauges, linear variable displacement transducers, and vibrating wire gauges [58-60]. Recent advances in the use of laser extensometers and fiber-optic sensors have shown promise [61-65], but these systems require significant instrumentation and are still typically limited to predetermined locations of measurement. While these methods have a proven track record of success, they are not easily implemented on infrastructure applications because of their cost, labor required for setup, and the requirement to place the sensors in contact with the component. Photogrammetric assessment methods [66-68] have shown a great deal of promise for describing the behavior [69-75] and condition state [8, 76, 77] of civil infrastructure systems because of their noncontact nature, relative ease of deployment, and recent improvement of imaging technologies. Photogrammetry and image-based metrology have a long history across a number of engineering disciplines [15]. Stereo-photogrammetric techniques, developed in the early 1970's by Butterfield [78], provide an early example of using image processing to quantify displacement fields. The early work by Peters and Ransom [79] was credited for the concept of using image-based acquisition methods for deformation measurements. However, the numerical correlation algorithms developed by Sutton et al. [80] serve as the foundation for modern methods such as DIC. DIC can generally be described as a full-field noncontact photogrammetric surface measurement technique that utilizes image correlation and tracking techniques on a series of sequential images to describe shape, deformation, and movement of a specimen subjected to loading [15]. Figure 1.4 provides a generic illustration of the DIC workflow for material characterization used in this investigation. DIC extends the principles of photogrammetry, but instead of tracking the displacement of discrete targets, continuous surface displacement data are derived from incrementally tracking unique subsets, which are discretized areas with unique pixel features within the image and interpolation of deformation within the subsets. Surface displacement data, which can be transformed into strain via post-processing, are derived by comparing sequential pairs of digital images taken before and after the deformation. Images can be derived from a variety of sources (e.g., charge coupled device, digital single-lens reflex, etc.), with the choice of camera and lens configuration being influenced by factors such as camera noise, lighting, acquisition speed, and geometric relationships between area of interest (AOI) and field of view.

Within a digital image, pixels are represented as a matrix of color intensities at corresponding locations within the image, thus enabling specific pixels to be tracked during movement or deformation. DIC typically utilizes grayscale images, which are most commonly stored as an 8-bit integer and vary between 0 and 255. To create a unique pattern for image tracking and mapping, a stochastic contrasting speckle pattern [19] is typically applied to the surface of the specimen; however, to improve the efficiency of matching and mitigate correspondence issues associate with pixel uniqueness, images are typically divided into smaller regions or subsets. Within this subset domain, correspondence is achieved by matching the grayscale intensity values of pixels in two successive images and tracking or correlating their movement from image to image. A correlation function is used to minimize the error in locating the unique pixel patterns within the image, which are in turn used to determine deformations from pixel tracking and movement. Eq. 1 shows an example of a least squares approach for optimal correlation estimates [15], but other correlation functions can be found in literature [81, 82]. Sub-pixel resolution is then achieved through interpolation functions describing the continuous field, analogous to the interpolation functions used in the FEM. A more comprehensive treatment of the DIC analysis process for both two dimensions and three dimensions is available in literature [15].

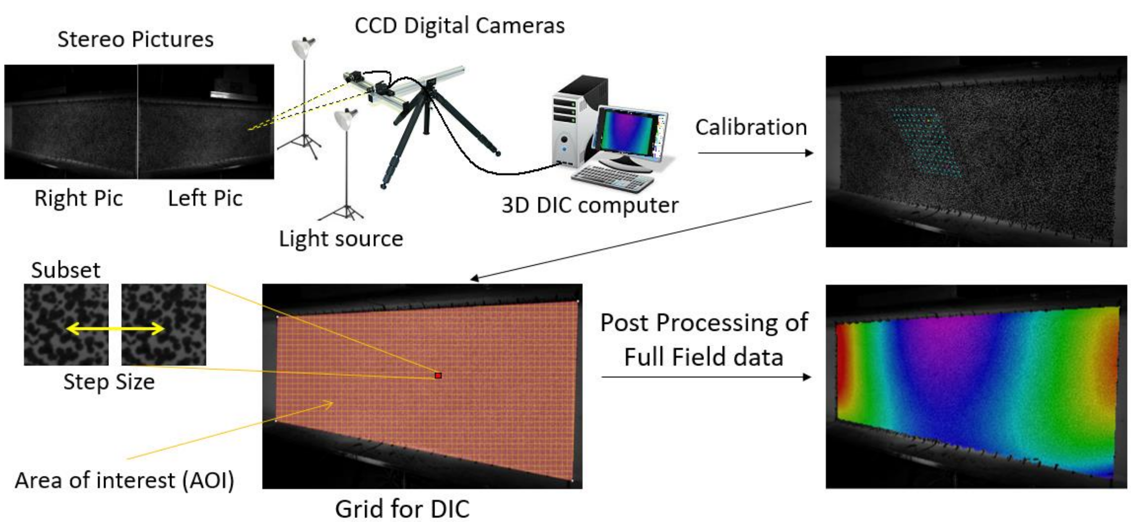

Figure 1.4. Conceptual schematic of DIC

$$C(\overline{x,y},u,v) = \sum_{i,j=-n/2}^{n/2}[I(\overline{x+i,y+j}) - I * (\overline{x+u+i,y+v+j})]^2 \qquad (1\text{-}1)$$

In the Eq. (1), $\boldsymbol{C}$ is the correlation function, $\boldsymbol{n}$ is the subset size, I is image before motion, I^* is the image after motion, $\boldsymbol{u}$, $\boldsymbol{v}$ are displacement in the $\boldsymbol{x}$ *and* $\boldsymbol{y}$ directions, x, y are pixel coordinates in reference image, $\overline{x+i,y+j}$ is pixel value at $(x+i,y+j)$ and $\overline{x+u+i,y+v+j}$ is pixel value at $(x+u+i,y+v+j)$.

Within the family of DIC techniques, two-dimensional (2D-DIC) and three-dimensional (3D-DIC) DIC techniques are typically used to characterize planar and nonplanar (out-of-plane) full-field surface deformation, but volumetric DIC (V-DIC) is an emerging technique for internal deformation characterization. While V-DIC has a great deal of relevance to concrete behavior characterization, it is beyond the scope of this work and will not be discussed further. 2D-DIC requires a single camera to measure the full-field planar deformations on a surface perpendicular to the image plane. The primary limitation of this technique is that any out-of-plane movement or deformation can influence the accuracy of the measurements because of image distortion [83]. As with any photogrammetric measurement technique, the accuracy is highly dependent on the experimental setup. As an example, in a study by Hoult [84] in which out-of-plane movement was minimized, it was demonstrated that 2D-DIC could produce strain values with an error on the order of a few *microstrain* (~less than 5 *microstrain*), which is comparable to the anticipated error in conventional strain gauges. Similarly, 3D-DIC is analogous to the human vision system [85], but instead of human eyes, it uses stereo-paired cameras to capture the three dimensional shape and deformation of the specimen. The stereo imagery allows for the measurement of both in-plane and out-of-plane deformations, albeit out-of-plane deformations are measured at a slightly lower resolution. 3D-DIC is generally needed when the out-of-plane deflections are significant compared to in-plane deformations. It requires a comprehensive calibration that takes into account all of the affecting parameters including lighting, exposure, specking, etc. The accuracy of the calibration process has a direct correlation with the precision and accuracy of the results.

1.6 Research Challenges

The extensive review of St-Id and damage detection literature presented in the previous section highlights a number of challenges and shortcomings that are listed in this section.

- *Challenge 1*: In order to accurately evaluate the system-level behavior, an ideal approach would be the implementation of full scale field tests on a series of representative structures; however, this approach is neither feasible nor cost-effective. Laboratory testing can also be considered as an alternative approach, but challenges with dimensional scaling and simulation of exact boundary conditions are considered as limitations of this method, in addition to associated costs. With today’s computational resources and capabilities, the development of an analytical model to study the performance of intact or damaged structural systems could be best handled numerically, using a tool such as the FEM. While FEM provides an efficient mechanism to simulate the structure system behavior, there are certain challenges that must be properly treated to yield representative results. Of most important challenges to use FE modeling, is how to simulate the constitutive properties, boundary conditions and geometric descriptions as precisely as possible to the actual model; especially if the structures are complicated enough to define those constitutive properties, boundary conditions and geometric description. SHM provides a system performance evaluation strategy with the end goal of characterizing behavior for better modeling of structures (e.g. FEM) and providing indications of damage and even forewarning of impending failure. The majority of existing works, within the domain of SHM measurement techniques, to obtain experimental data for validation purposes, have primarily relied on discrete sensing strategies using sensors physically attached to the structural system of interest. These sensors have proven effective in describing both global and local phenomena, but are limited to providing discrete response measurements of these systems. In fact, modeling of structures demands having enough information about the boundary conditions, geometry description and constitutive properties of the structural elements which cannot be obtained from discrete response measurements. Thus, it is necessary to develop a new SHM techniques.

- *Challenge 2:* Within the current state of practice, a number of NDE techniques have been proposed that primarily leverage principles of wave propagation or radiation imaging in elastic solids. Of such methods include acoustic sounding, impact echo, ultrasonic waves, ground penetrating radar, or infrared thermography. As an alternative strategy, SHM approaches rely on structural sensing to monitor and infer the state of structural health. These approaches typically employ model-based or data-based techniques to identify anomalies in mechanical responses that point to damage. While the use of global dynamic responses or a set of isolated local strain and deformation responses has been relatively successful in providing information about basic constitutive properties and coarse-grained damage indication, the degree to which material or damage properties can be extracted has been limited. While both NDE and SHM strategies have proven to be successful for many scenarios, there are still many shortcomings that cannot be readily addressed without highly sophisticated equipment or costly monitoring systems. As such, there is a need for techniques that enable the detection of such subsurface modes of deterioration in a cost-effective and non-invasive manner.

- *Challenge 3*: There has been substantial work recently on the development of techniques for detecting structural defects and damage. The majority of these works have taken the form of SHM, using sensors and monitoring information to infer the behavior and performance of the underlying structural system. Many of these efforts have centered on how to extract global system characterization from embedded sensors networks (system identification), without focusing on understanding the impacts of localized defects. In parallel with these SHM efforts, the past decade has not seen enough research exploring how to leverage the results of NDE to provide a more global and local representation of system inspection results. To understand internal properties and the condition of structures, innovative methods of reconstructing the 3D geometry of of the defects can be essential.

1.7 Investigation Approach and Dissertation Outline

The overarching goal of this dissertation is to develop efficient and robust methodologies for structural characterization of infrastructure through the application of image-based full-field sensing techniques. In this regard, a series of challenges were identified in the literature. To address these challenges, four areas of study were explained and results of these studies are presented in this dissertation; results are presented in the format of a collection of four manuscripts currently different stages of peer review in international research journals. These manuscripts constitute the next four chapters of this dissertation.

- *Chapter 2* - explores the proposed idea of applying image analysis techniques through a case study on a series of structural test specimens analyzed using 3D-DIC for St-Id. Finite element model updating (FEMU) as an inverse problem was used as the technique for the St-Id. This research aims to address Challenge 1 as described in the previous section. Challenge 1 is addressed through the inclusion of full-field sensing measurements in identifying constitutive properties and boundary conditions. 3D-DIC results provided a rich full-field dataset for the identification process, which was compared against measurements derived from traditional physical in-place sensors typically used in SHM.

- *Chapter 3* – is where the research went one step further and proposed an image-based tomography to detect internal abnormalities of structures using inverse engineering. Image-based techniques have been extensively deployed in the fields of condition assessment and structural mechanics to measure surface effects and deformations such as displacements or strains under loading. Challenge 2 is addressed through this research using 3D-DIC to detect interior anomalies of structural components, inferred from the discrepancy in constitutive properties such as the elasticity modulus distribution of a 3D heterogeneous/homogeneous sample using limited full-field boundary measurements. The proposed technique is an image-based tomography approach for St-Id to recover unseen volumetric defect distributions within the interior of a three-dimensional heterogeneous space of a structural component based on the iterative updating of unknown or uncertain model parameters.
- *Chapter 4* – addresses Challenge 3 by proposing a new approach using full-field surface measurements coupled with topology optimization to localize and reconstruct the 3D shape of unseen subsurface defects. Therefore, this chapter aims to expand on the work in chapter 3 by Dizaji et al. [86] and to demonstrate that unlike a limited set of discrete sensing data points or global dynamic properties, the rich data from full-field image-based measurements can enable the characterization of defects in greater detail. Furthermore, this work demonstrates how perturbations in the observable full-field surface measurements can be used as a proxy to detect unobservable internal abnormalities. In this work, 3D-DIC is used to measure the full-field surface deformation coupled within a topology optimization schema to identify and reconstruct unseen three-dimensional damage.
- *Chapter 5* - illustrates that the proposed method is able to successfully recover fine-grained subsurface damage information from large scale structural components which is otherwise costly and cumbersome to pull out with specialized state-of-the-art NDE/T or SHM methods and can therefore be employed as a promising subsurface damage detection method. To that extent, for very large components, a multi-step procedure can be followed which starts by locating the vicinity of the damage using traditional global-response methods, and then using the proposed technique to obtain a fine-grained and detailed view of the internal damage. Therefore, this chapter intends to address Challenge 3 by proposing a new approach using

full-field sensing integrated with topology optimization to uncover the interior condition of structures followed by finding the location and then reconstructing the 3D geometry of subsurface of the defects.

1.8 Research Significance

The significance of this research centers primarily around a new approach for connecting SHM with NDE to create a structural components condition assessment method based on basic structural response (strains and deformations). This approach differs from traditional NDE, in that it does not rely on specialized NDE equipment (e.g. wave and radiation tomography), but also extends traditional SHM approaches by leveraging the full-field response measurement more typical of NDE methods. This is achieved by interfacing a FEM with full-field and fine-grained measurements from DIC through a topology optimization framework. While model-based damage detection per se is not new, the innovative idea of reconstructing the 3D geometry of subsurface defects via rich full-field surface sensing data can lead to major improvements in our understanding of internal properties and conditions of structures.

2 CHAPTER 2 – Leveraging Full-Field Measurement from 3D Digital Image Correlation for Structural Identification

Mehrdad S. Dizaji Mohamad Alipour, Devin K. Harris

“Dizaji, M. Shafiei, M. Alipour, and D. K. Harris. "Leveraging full-field measurement from 3D-DIC for structural identification." *Experimental Mechanics* 58.7 (2018): 1049-1066.”

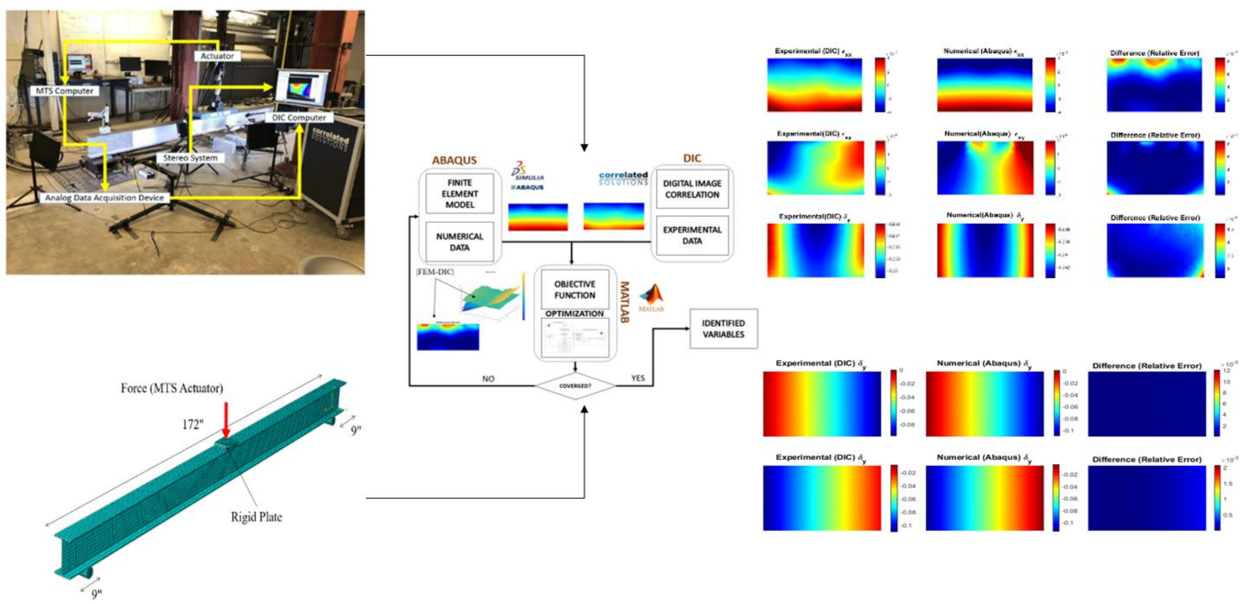

2.1 Abstract

Within the domain of SHM measurement techniques have primarily relied on discrete sensing strategies using sensors physically attached to the structural system of interest. These sensors have proven effective in describing both global and local phenomena, but are limited to providing discrete response measurements of these systems. With the introduction of novel imaging tools and image analysis techniques, such as DIC, the ability to measure the full-field response of these systems provides a novel approach to refining St-Id approaches used in SHM.

This paper explores this proposed concept through a case study on a series of structural test specimens analyzed using 3D-DIC for St-ID. FEMU was used as the technique for the St-Id. For the identification process, ABAQUS was interfaced with MATLAB to converge on the optimal unknown/uncertain system parameters of the experimental setup. 3D-DIC results provided a rich full-field dataset for the identification process, which was compared against measurements derived from traditional physical in-place sensors typically used in SHM. In this work a Hybrid Genetic Algorithm (HGA), which combines the GA as a global optimization and a gradient-based method as a local optimization, was used for the FEMU based on 3D-DIC results of structural specimen subjected to variable loading. To minimize the error between the full field 3D-DIC measurements and FEA model updating results, an objective function was introduced that included the full-field contributions of strains and deformation response. The evolution of this objective function illustrated satisfactory convergence of the identified parameters and the excellent agreement of the experimental and numerical strain and displacement responses after the model updating process confirmed the success of the proposed approach. The results of this study highlight the advantage of this hybrid approach and provide the foundation for effective deployment of the proposed strategy for large-scale structural systems.

Keywords: 3D-DIC, system identification, St-Id, SHM, St-Id, FEMU, SHM, Hybrid Genetic Algorithm (HGA)

2.2 Introduction

Much of the physical infrastructure across the globe was built during eras of growth and with a finite intended service life, but in many cases these systems have continued to operate and have remained in service well beyond this intended period [7]. Infrastructure owners and managing entities have proven capable of keeping these systems functional through routine and preventative maintenance strategies, but often these strategies are reactive in nature and are deployed in response to an observable deterioration mechanism. However, recent structural failures have demonstrated that this approach is not always effective and can have catastrophic and even fatal consequences [87, 88]. The concept of SHM has shown promise as a strategy for temporal condition assessment of the built environment. SHM provides a system performance evaluation strategy with the end goal of characterizing behavior and providing indications of damage and even forewarning of impending failure.

The concept of SHM has existed for several years in various forms across multiple engineering disciplines [89] and has been likened to a human health management system [90], with well-person checkups, preventative intervention, and treatment/surgery being analogized to inspection, maintenance, and repair/retrofit, respectively. The body of knowledge in SHM has grown considerably over the past few decades, but a fundamental challenge that remains is the translation of measurable phenomena derived from full-scale physical systems into information that describes the system's health and condition. To date, significant research has been performed on condition assessment [6, 8] and SHM [91] of infrastructure with advances in novel technologies [92-94] and assessment techniques [95-97]. However, a comprehensive solution also requires integrated strategies for routine inspection, data management, result interpretation and decision support, demonstrating that SHM is still in its infancy with excellent opportunities for growth and development. As society pushes towards a more holistic strategy of smart and connected communities, the need for low cost, non-invasive, and data rich techniques is becoming paramount to the SHM community. This manuscript describes an experimental study that aims to address this challenge by leveraging DIC for St-Id within the SHM framework as a strategy of collecting rich, full-field data without the need for fixed in place sensors. With the challenges associated with an aging infrastructure network [98], non-invasive tools such as DIC have the potential to provide decision-makers with a comprehensive assessment tool to better describe the performance of this network.

This paper presents an experimental study that leverages 3D-DIC as a full-field measurement approach within the broader SHM framework. A synthesis of the findings of this study are presented and organized as follows: first, a strategy for full-field St-Id within the SHM framework is investigated. Next, the experimental setup along with the 3D-DIC configuration is described including the testing objectives and key DIC parameters. A description of the ground truth measurements collected from traditional affixed sensors is also presented. Finally, the preliminary modeling approach using the FEM is described. Leveraging results from the 3D-DIC measurements, a St-Id optimization using the preliminary FEM updated with full-field 3D-DIC results to converge on boundary and constitutive properties of the test specimen. Critical to this updating process was the concept of interpolation between DIC results and FEA results, and optimization process, which is described in detail. Finally, a discussion of the results and conclusions are presented.

2.2.1 Structural Identification within SHM Framework

Within the traditional SHM framework, numerical models, typically FEM, are commonly used to describe the behavior of structural systems. FEM has been used with great success to simulate structural response of idealized systems, but its approximate nature and simplifying assumptions coupled with uncertainties associated with boundary conditions and condition inherently result in errors when describing existing structural systems [14]. St-Id describes an approach that emphasizes correlation of the response characteristics between a model and experiment, providing a basis for using an updated FEM to characterize critical performance measures of existing structural systems. Within St-Id, this inverse problem aims to minimize differences between analytical and experimental results and is usually formulated as an optimization problem. Satisfactory correlation between the observed experimental behavior and the analytical results is critical, but equally essential is maintaining the physical significance of updated parameters [44]. For this purpose, setting up of an objective or cost function and selecting updating parameters are crucial steps in St-Id. The changes in these parameters are then determined iteratively and pushed to a minimum via an optimization algorithm. St-Id aims to bridge the gap between the model and the real system by developing reliable estimates of the performance and vulnerability through improved simulations. This work describes an experimental case study that leverages 3D-DIC for St-Id.

3D-DIC leverages calibrated stereo-paired cameras to enable 3D imaging, allowing for shape and out-of-plane surface deformations to be measured. A comprehensive treatment of DIC is available in the literature [8, 15, 19, 58-85] and not presented here, but additional details on the DIC deployment used in this investigation are provided in a later section. An interesting characteristic of DIC is that the representation of full-field surface deformations is analogous to results derived from FEA, creating the potential for full-field St-Id, a capability that is not possible with discrete sensors. Figure 2.1 provides a generalized illustration of the proposed St-ID strategy used in this investigation, which will be described in more depth in the following sections.

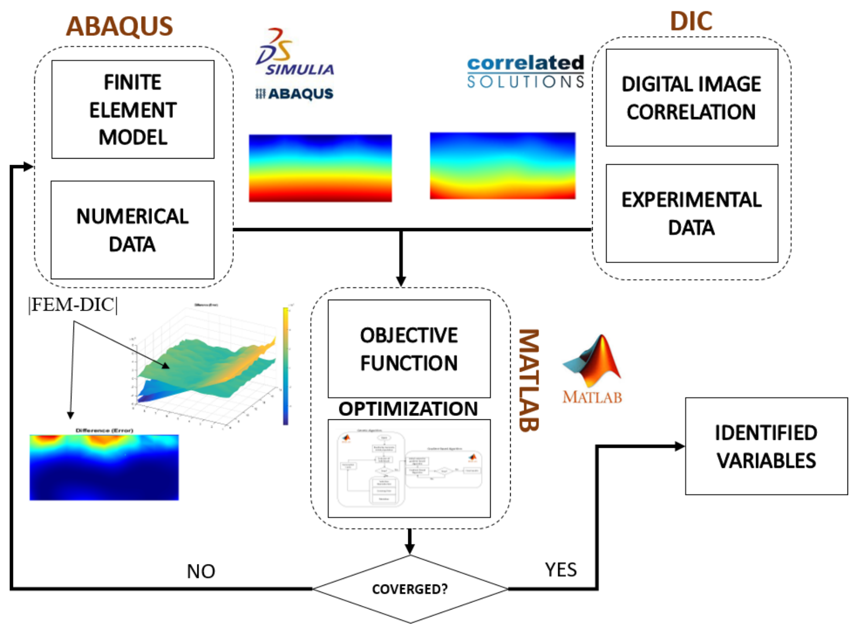

Figure 2.1. Overview of the proposed full-field St-Id process

Generally, for St-Id, a cost function, defined in terms of differences between numerical and experimental displacement fields, is minimized on part of the system boundary in an iterative manner by changing the material parameters and boundary conditions. Given a unique set of system geometry, material parameters, traction and displacement boundary conditions, the displacement and deformation response of a system is also unique. Hence, assuming the system geometry and boundary conditions are correctly replicated in the FEM, convergence between numerical and experimental displacement fields is achieved only when the constitutive parameters approach their true values. Examples of this optimization concept are available across numerous fields, but representative St-Id examples are available in [45-47, 99, 100].

This work explores a new vision-based St-Id framework that allows for full-field structural behavior matching and identification and can result in significant enhancements compared with the use of traditional discrete-point mechanical sensors that are typically used in current SHM and St-Id applications. Figure 2.2 conceptualizes the potential advantage of the proposed framework for model updating and St-Id using full-field response measurements (i.e. 3D-DIC) in comparison with those obtained by discrete point sensors (e.g. strain gages, LVDTs, etc.). The dotted line depicts the predictions of an FEM model updated by matching measurements of only two discrete mechanical sensors. The dashed line is a model updated using a fine grid of points on a full-field response measurement. In this illustration, it becomes evident that matching a complex function using a limited set of discrete mechanical sensors may result in good agreement in the proximity of the sensors, but does not guarantee a good match in other locations on the specimen. On the other hand, matching an entire full-field response enables a more comprehensive representation of the global and local behaviors throughout the specimen. This advantage is expected to be realized in more complex structural systems, where only a few discrete points may be insufficient to describe the behavior. An example is a structure with geometrical non-uniformities (e.g. a hole or defect) or complicated boundary conditions where the response cannot be uniquely represented by a few discrete sensors.

2.3 Experimental Study and Numerical Simulation

For a proof of concept to the proposed full-field St-ID framework, an experimental study was performed. The experimental specimen examined in this work is a relatively simple structural system and the work presented in this paper include a series of laboratory and corresponding numerical model case studies that provide the foundation for expanding this concept. Future works by the authors aim to illustrate these advantages in more complex structural systems such as full-scale highway bridge structures.

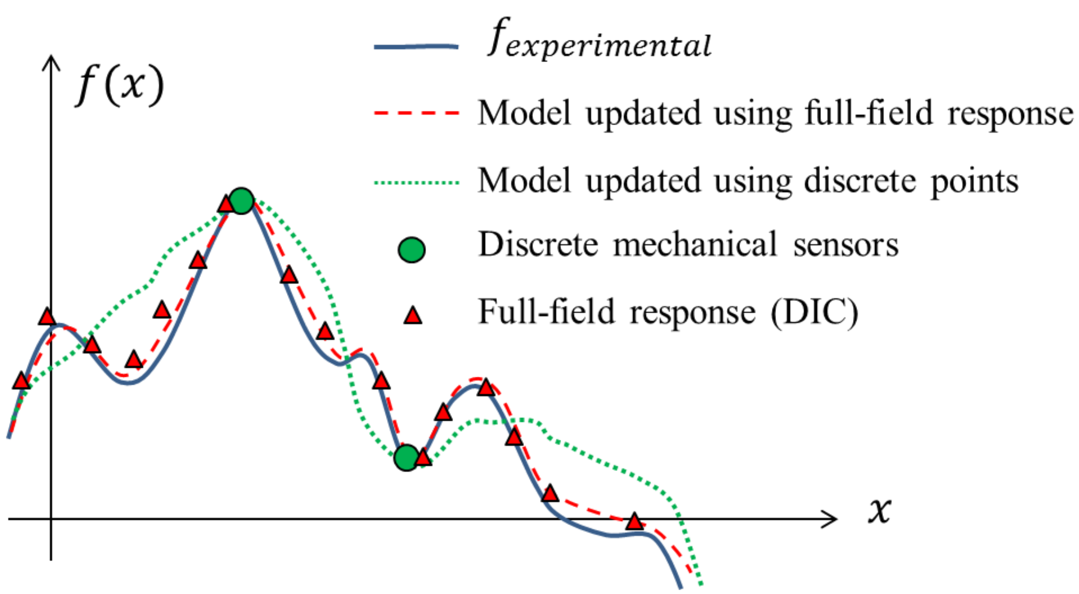

Figure 2.2. FEA model updating using discrete sensors versus full-field response

2.3.1 *Experimental Setup*

In this investigation, an experimental program was developed to evaluate the feasibility of leveraging 3D-DIC in a St-ID/SHM framework. The experimental program included a laboratory scale investigation of a representative steel beam subjected to various loading and boundary conditions. The structural configurations used in this investigation are illustrated schematically in Figure 2.3 and can be described as:

1) Configuration 1 (*CF1*): structural component simply supported (Cylinder) subjected to concentrated load at midspan (Figure 2.3a).
2) Configuration 2 (*CF2*): structural component simply supported (Half Cylinder) subjected to concentrated load at midspan (Figure 2.3b).
3) Configuration 3 (*CF3*): structural component with simple and partial support restraints subjected to a concentrated load at midspan (Figure 2.3c).

The restraint configurations illustrated in Figure 2.4 were intended to mimic idealized boundary and loading conditions and provide a basis for characterizing the differences these idealized conditions and real systems. Figure 2.4 shows the actual boundary and loading fixtures used in experimental set up for different configurations.

The testing program consisted of a series of flexural loading cycles within the elastic range (σ_{yield}= 50 ksi) on a wide-flange hot-rolled structural steel beam (ASTM A992 W10x22). The 172-inch beam was tested in the Structures Laboratory at the University of Virginia and configured for strong-axis bending. The beam was instrumented with Bridge Diagnostic Inc. (BDI) sensors at both midspan and support locations to provide a comparison between traditional SHM sensor results and those derived from the 3D-DIC measurements (Correlated Solutions *VIC-3D*) at the same locations. Three paired DIC camera (Point Grey Grasshopper 2.0 CCD with 5.0MP resolution) systems were used to evaluate the midspan (Schneider 8 mm lens) and two end span (Schneider 12 mm lenses) locations. The midspan camera system utilized a different lens configuration due to the physical constraints of the load frame location relative to the test specimen.

The end and midspan locations were patterned over the full depth of the beam web over 24 in. with the pattern created by applying a flat white paint base coat, followed by random speckle pattern with a permanent marker. Additional details on the pattern and camera setup are provided in a later section. The DIC data acquisition (DAQ) integrated output signals (load and displacement) from MTS actuators and controller to allow for simultaneous acquisition of load, displacement, and images. The BDI DAQ system was not directly linked, but was synchronized manually at the start of each test. Figure 2.5a provides a basic illustration of the experimental setup and instrumentation configuration used during testing.

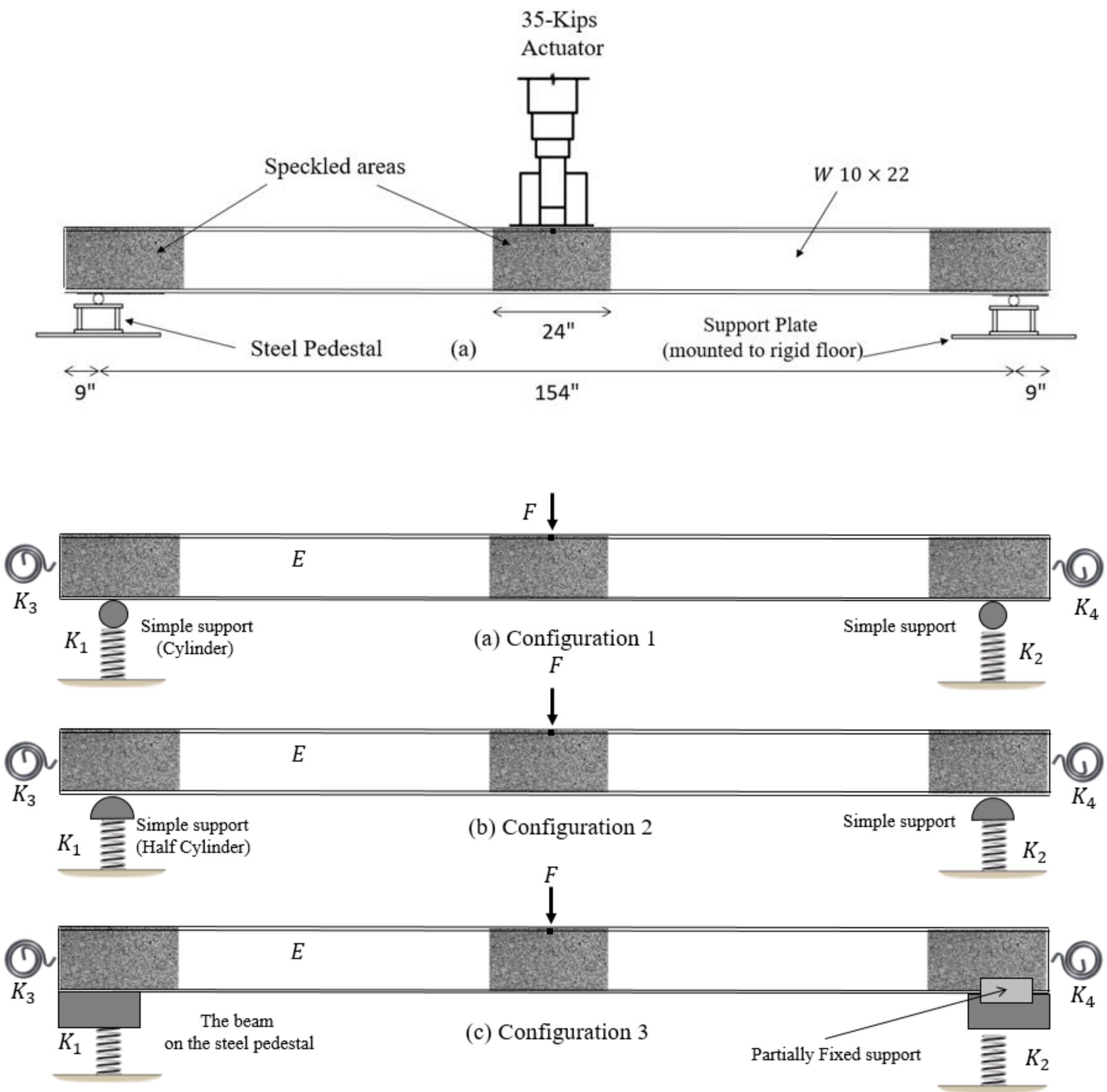

Figure 2.3. Schematic of the steel beam (a) loading and boundary conditions used during experimental testing (b) Configuration 1 (c) Configuration 2 (d) Configuration 3

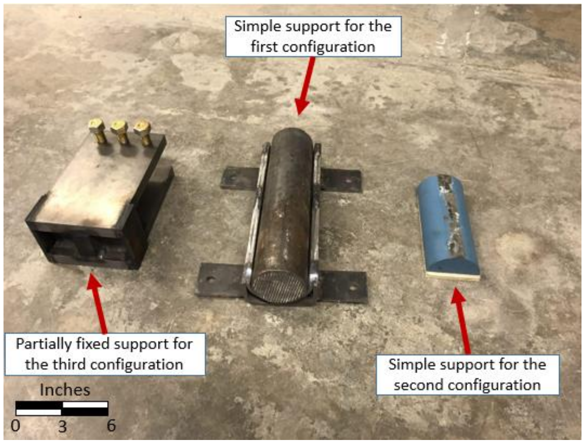

(a)

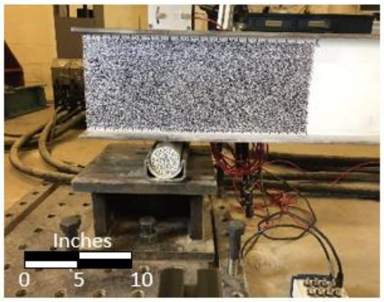

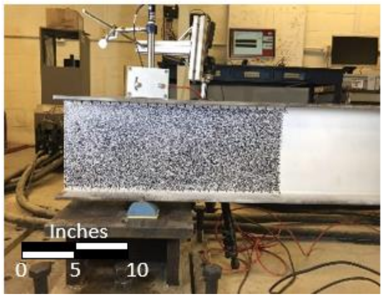

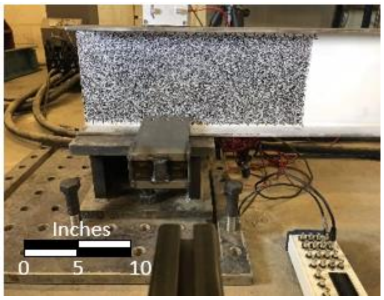

(b) (c) (d)

Figure 2.4. Boundary and loading fixtures (a) different supports used in the tested configurations (b) supports used for the first configuration (c) supports used for the second configuration (d) support used for the third configuration.

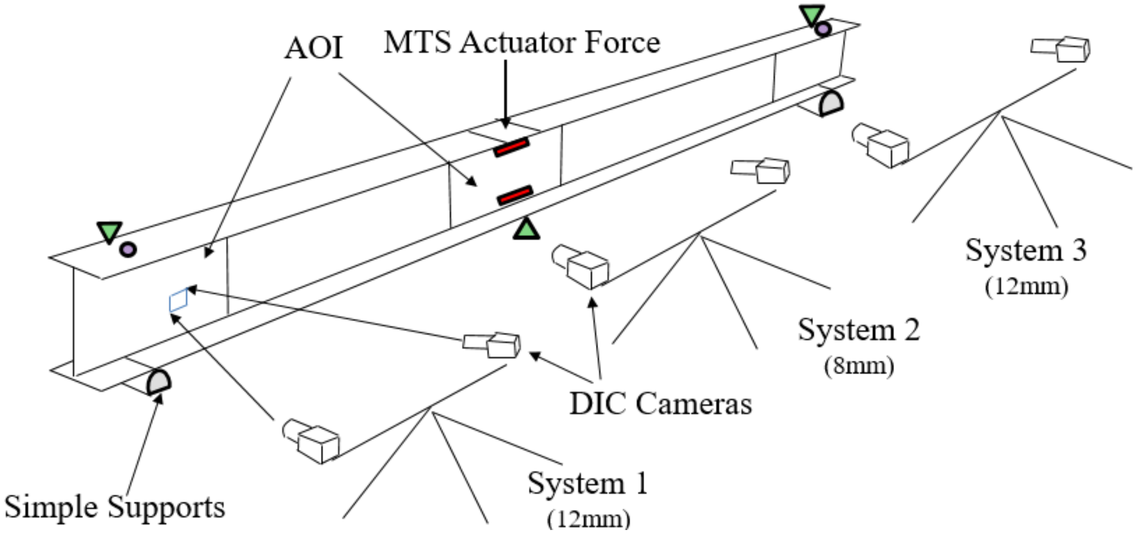

(a)

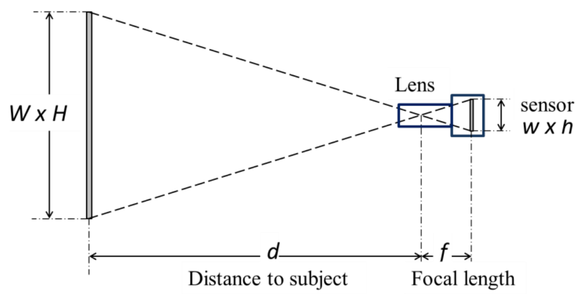

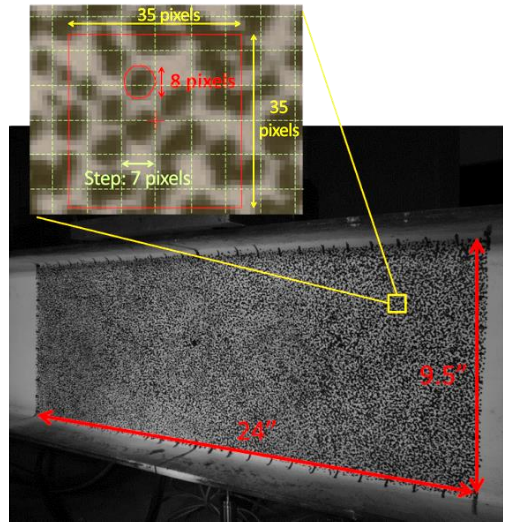

(b)

Figure 2.5. Experimental setup and camera configuration (a) 6 camera setup (3 systems or 3 camera pairs) 1 pair at midspan (8 mm lens) and 1 pair at each support (12 mm lens) (b) Diagram of the optical setup (Left), Field of view, speckle pattern and subsets

2.3.1.1 *Loading regime*

For each of the configurations, the beam was loaded monotonically under displacement-control, with the beam response maintained within the elastic range. The loading sequence consisted of loading the beam to a displacement of 0.05 inch at a rate of 0.002 inch per second, followed by a two-cycle sinusoidal loading from 0.05 inch up to a peak displacement of 0.3 inch, and concluding with an unloading through the reverse of the initial loading sequence. The initial loading and final unloading occurred over a period of 50 seconds (25 seconds each), while the sinusoidal sequence occurred over a period of 500 seconds (250 seconds for each cycle). The BDI DAQ collected data during the loading sequence at 100 Hz while the DIC images were acquired at 2 Hz which resulted in 1143 images.

2.3.1.2 *DIC Setup*

As previously noted, the DIC image acquisition used three sets of stereo-paired digital cameras. Each camera had a 5-megapixel charge coupled device (CCD) image sensor with a resolution of 2448 × 2048. The image sensor for this camera was 2/3” format with dimensions of 0.35” × 0.26”, which accounted for a pixel size of 1.36×10^{-4} inch. The camera was connected to a C-mount optical lens and the acquired data was communicated to the control PC through FireWire cables. To accommodate the specimen within the field of view of cameras with the highest resolution, the design on the imaging setup was achieved by considering the geometrical restraints of the laboratory space (maximum available space from cameras to the beam was about 50 inches) as well as the available optical lenses. Using 12 mm lenses for the end locations and 8 mm lenses for the middle location, the distance of the camera from the beam was calculated using equation 1, where *w/h* is the sensor width/height, *W/H* is the field of view width/height, *d* is the distance to the object, and *f* is the focal length (Figure 2.5b (Left)). Using the dimensions of the speckled region (24” × 9.5”) and leaving a space of at least one inch around each side of the region to accommodate deformations to be captured, the 8mm and 12mm lenses had to be placed at about 23.5” and 35” from the specimen (Figure 2.5b (Right)), respectively, to produce the same field of view.

$$\frac{w}{W} = \frac{h}{H} = \frac{f}{d} \tag{2-1}$$

In preparation for testing, the surface of the test specimen was covered with a fine, dense and random speckle pattern for the correlation process. To achieve a high spatial resolution of calculated results while at the same time being large enough to be resolved in the images, the pattern had an average speckle size of 0.08 inch, which corresponds to approximately 8 pixels in the captured images. For the pixel tracking process in DIC, the area of interest on the speckle pattern is split into rectangular windows or “subsets” and unique patterns of speckles need to be available within each subset to allow for tracking in subsequent frames. The patterns in the subsets is tracked on a grid of a specific “step” size, which dictates the spatial resolution of the calculated points. To achieve a fine grid of unique patterns in subsets, the selection of the subset size was achieved through direct experimentation and a square subset of 35 pixels at a step of 7 pixels was selected (Figure 2.5b (Right)).

2.3.2 *Numerical Simulation*

As previously noted, St-ID requires the development of an initial numerical model that can be updated based on experimentally derived results. In this investigation, FEMs of each loading/boundary condition scenario were developed in ABAQUS, a robust commercially available finite element software package. For each scenario, the steel beam was modeled using a total of 4,300 Continuum 3D hexahedral solid elements (C3D8) with full integration. The geometry was developed from standard section properties available within the AISC Manual of Steel Construction [101].

The boundary supports were modeled as a series of springs (translational and rotational) to represent the deviation from ideal simple and fixed conditions and to allow for updating based on experimental measurements. A global view of the model of the steel beam has been shown in Figure 2.6. With the model representing a relatively non-complex structural component, a dense mesh was not required; however, the mesh density was initially developed and later refined to allow for alignment with the coordinate system of the DIC results. It should be noted that ABAQUS allowed for the development of a direct interface with MATLAB, a multi-paradigm numerical computing environment, which facilitated the iterative parameter optimization algorithm.

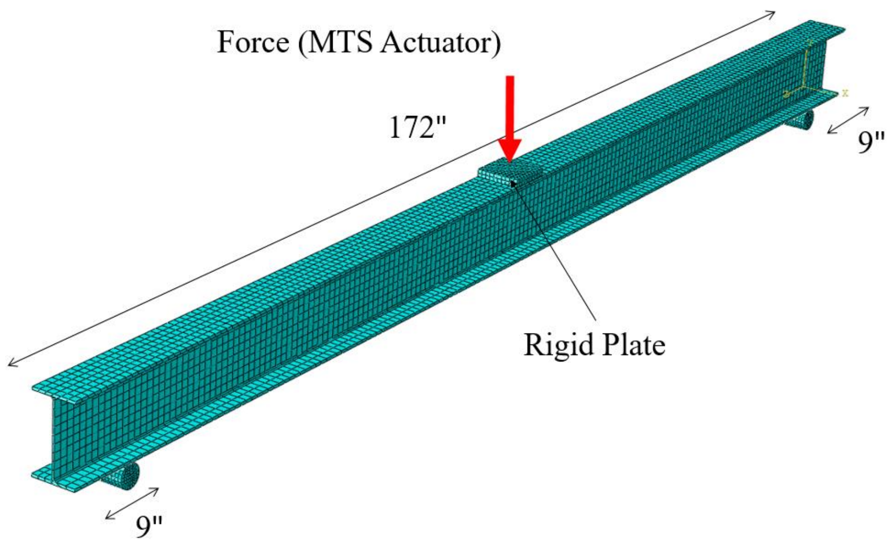

Figure 2.6. Isometric view of representative FEM of the steel beam (Configuration 1 shown)

2.4 Results and Discussion

2.4.1 Measurement noise

Prior to utilizing the DIC results in the St-ID framework, an analysis of the measurement noise was performed. To evaluate the noise in the measurements, a series of images were taken from the zero-load state of the specimen and processed using the same settings used for the rest of the data. While in theory the displacements and strains should be equal to zero in the zero-load state, in practice, noise from different sources affect the measurements. Some of these sources include lighting fluctuations and glare, irregularities and poor quality of speckle pattern, as well as noise resulting from image acquisition (e.g. sensor noise) and quantization [102]. Table 2.1, summarizes the average and standard deviation of the displacement (U, V, W) and strain (ε_{xx}, ε_{yy}, ε_{xy}) measurements in 10 frames with zero load.

The standard deviation of the measurements quantifies the variation of the noise and can be used as an estimate of the resolution of the measurements [103]. To better see the distribution of noise in zero-load frames, Figure 2.7, illustrates histograms of the non-zero displacements and strains in a sample zero-load frame. It is notable that all of the no-load frames have a similar shape with a mean close to zero and a bell-shaped distribution which is in agreement with the expected random Gaussian noise.

Table 2.1. Noise statistics from measurements in 10 frames with zero load at midspan

Variable		**Mean**	**StD**
U	(1/1000 inch)	-0.14	0.83
V		-0.50	0.99
W		-0.18	1.44
ε_{xx}	($\mu\varepsilon$)	1.80	63.02
ε_{yy}		0.96	86.67
ε_{xy}		-0.72	60.12

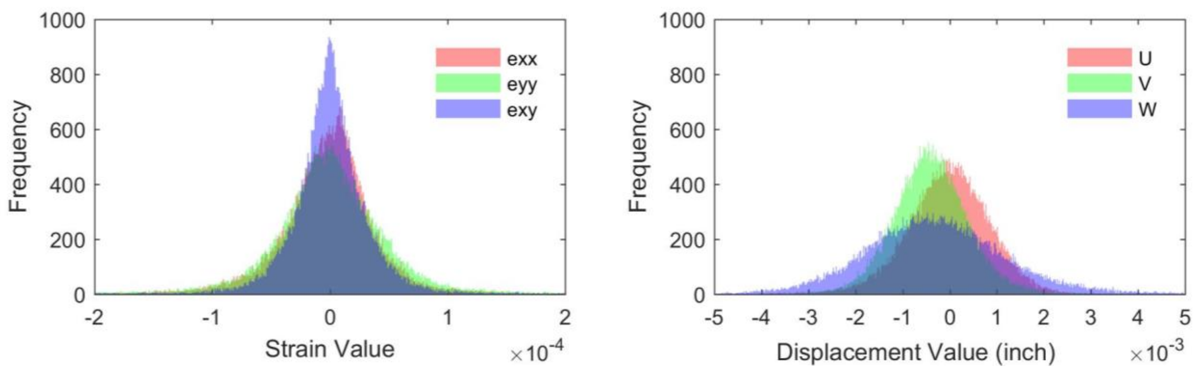

(a) (b)

Figure 2.7. Histogram of non-zero measurements in a sample zero-load frame (a) strain (b) displacement

2.4.2 *DIC results versus reference sensors*

Results from the experimental program provided a basis for comparison of the 3D-DIC measurements with the in-place mechanical sensors that are representative of those used in traditional structural testing and SHM applications. For comparison, a virtual gauge was selected in the DIC system to allow for local strains to be measured within both the tension and compression regions of the cross-section as shown in Figure 8. The evolution of strains (ε_{xx}) at the two locations, A and B (Figure 2.8), along with the corresponding vertical deflection were extracted from the DIC results. Similarly, results from the support locations were extracted from the DIC; however, for this location, only displacements were considered as the strains near the supports are relatively low. Figure 2.9 illustrates a comparison of the results of selected sensors for one of the experiments relative to corresponding BDI sensors. Also, differences between BDI sensors and DIC are quantified in the Table 2.2. The results demonstrate that the measurement derived from both systems are comparable, but the DIC results exhibit a noisier response. This outcome is expected, but it should also be noted that the full-field measurement capability derived from DIC cannot be achieved with local sensing techniques and the full-field measurement provides a unique capability for a more robust St-Id strategy. During the experiments, the DIC measurement also provided a supplemental benefit to the investigation in that vertical deflections were measured at the support locations, which were previously assumed to be fixed in this direction.

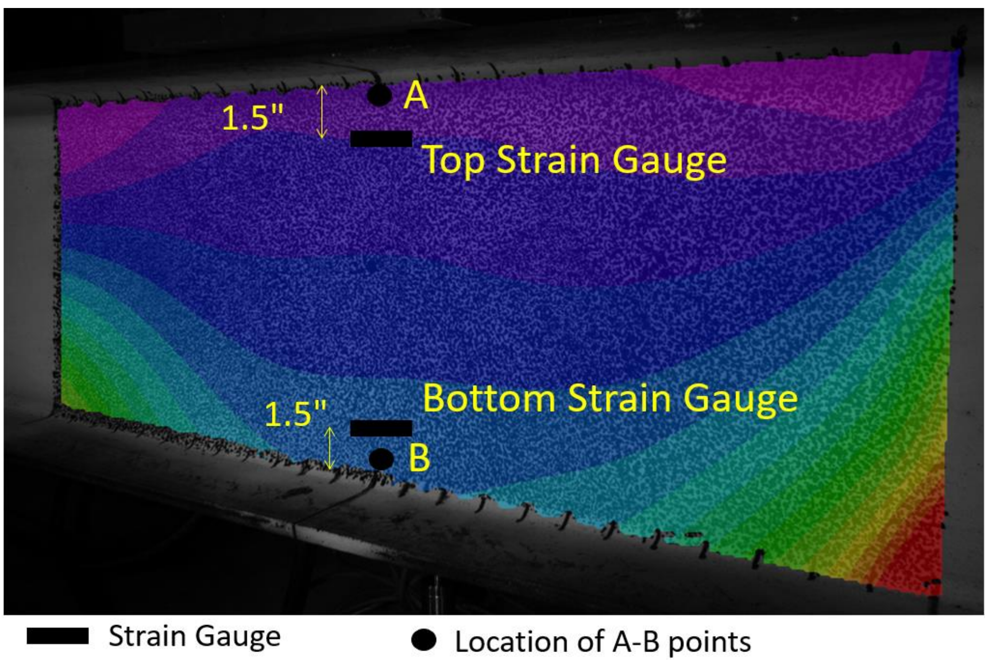

Figure 2.8. Longitudinal ε_{xx} DIC strain fields at the maximum load, t =150 sec, frame#300

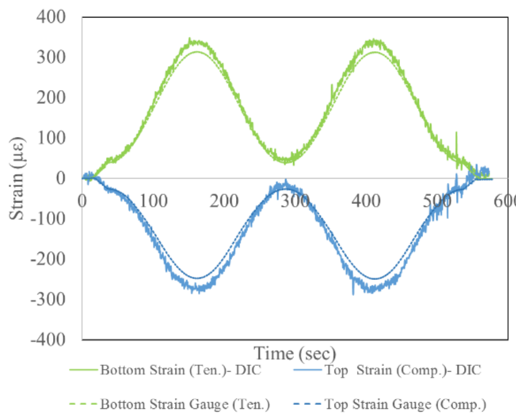

(a)

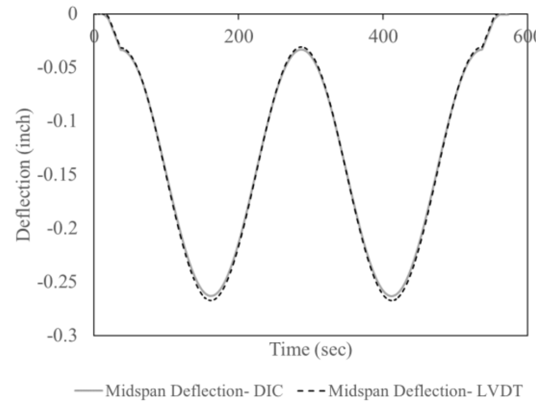

(b)

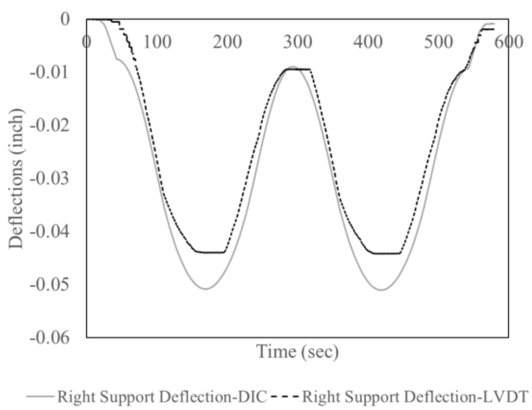

(c)

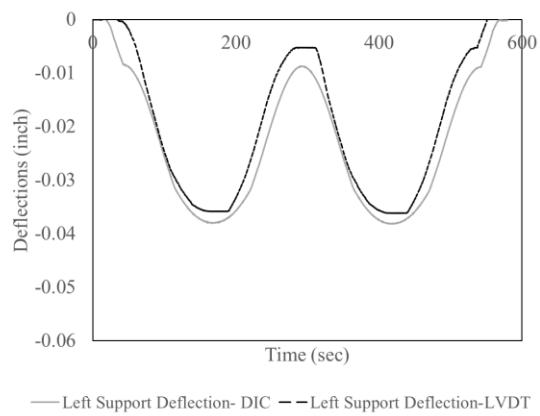

(d)

Figure 2.9. Comparison of results obtained from DIC and mechanical sensors (a) midspan strain; (b) midspan deflection; (c) right support deflection; (d) left support deflection

Table 2.2. Differences between DIC and LVDT

Differences between DIC and LVDT	Top strain	Bottom Strain	Midspan Deflection	Right Support Deflection	Left Support Deflection
Mean absolute percentage difference: $MAPE = \frac{100}{n}\sum_{t=1}^{n}\left\lvert\frac{e_t}{y_{sensor}}\right\rvert(\%)$	6.4	5.4	1.2	12.5	11.5
Maximum difference: $\lvert y_{DIC} - y_{sensor}\rvert$ (μs) & $(in.)$	23	22	0.004	0.007	0.002

Note: $(e_t = y_{DIC} - y_{sensor}, n = number\ of\ measured\ data)$

2.4.3 *Structural identification using FEMU with DIC via HOA*

In a previous study [104], limited non-full-field data derived from DIC measurements were used in an FEMU scheme, but the sparse data used in the refinement was not sufficient for consistent model updating. However, the full-field measurement derived from DIC provided a rational mechanism for performing multi-objective optimization for model updating. In this study, the initial FE models, developed in parallel with the experimental configurations, were updated using a robust optimization algorithm to converge on predictions of the beam's Young's Modulus (E_s) and support stiffness parameters (K_1, K_2, K_3, K_4). As illustrated in Figure 2.3, three scenarios were selected for model updating with variations in the restraint conditions and objective function parameters. The optimization algorithm developed in this investigation incorporated the features of a GA and a gradient-based scheme to iterate on the unknown parameters.

2.4.3.1 *Definition of the objective function*

The identification problem consisted of the determination of structural parameters that minimize the difference between calculated data from a numerical model and a set of experimental data. In this research, the numerical model is a finite element model with the same geometry and boundary conditions as the experimental setup. The identification leverages a generalized cost function (e.g. Equation 2) to evaluate agreement between the numerical and experimental results.

$$F = \frac{1}{N_i}|y_i^{num} - y_i^{exp}| \qquad (2-2)$$

Where F is the cost function, y_i^{num} is the i - th information obtained with the numerical simulation, y_i^{exp} is the i-th information obtained with the set of experiments conducted and N_i is a weight factor. In this study, the experimental data utilized for the definition of the cost function are the strain and displacement fields; however, other measurement data could also be included in the St-Id process.

2.4.3.2 *Interpolation process*

For comparison of the results from these two analyses (e.g. FEM and DIC), a common grid was required to ensure that the measurement/analysis locations are equivalent. To achieve a common reference for comparison between the FEA and DIC results, it was necessary to interpolate the results from the DIC grid over to the FEA grid (or vice versa) or interpolating both results on the new defined mesh grid. In this study, the mapping of both results to a new grid approach was selected. The concept of interpolation process is shown in Figure 2.10 schematically. FEA and DIC results have different mesh grid spacing in the x-y plane. With both results mapped to a common grid, the difference (or error) between FEA and DIC results can be used within the optimization process.

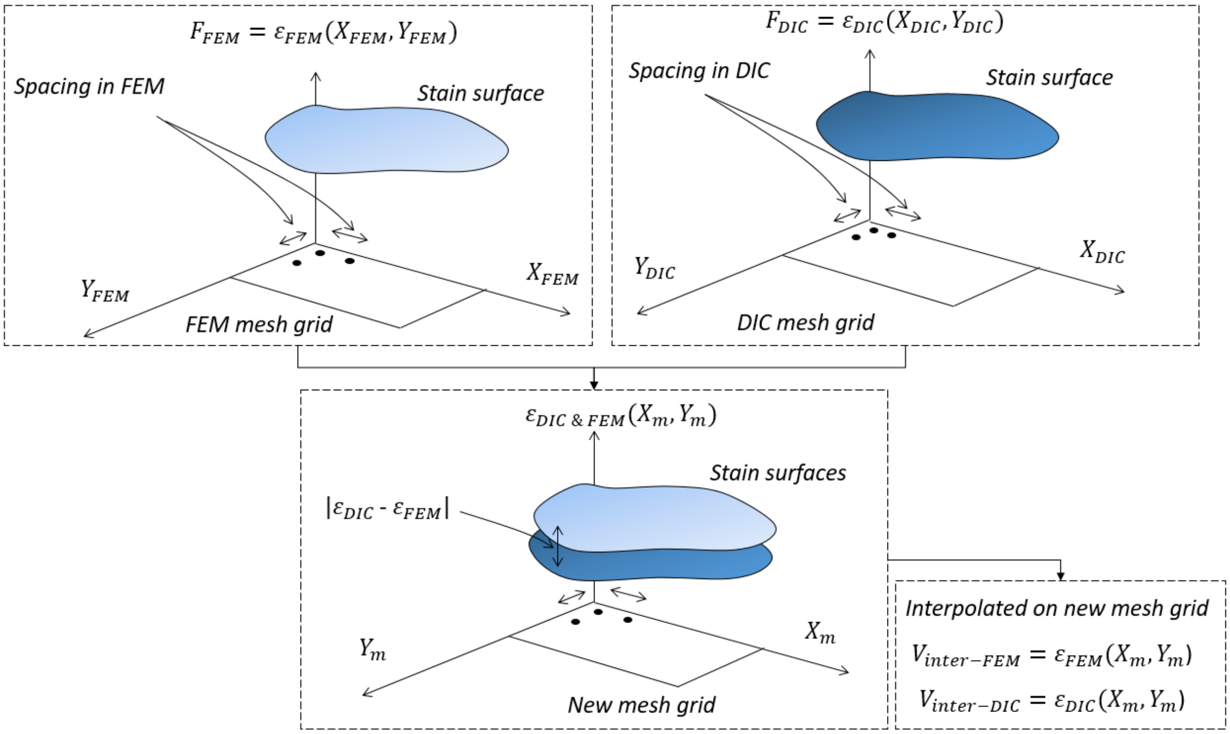

Figure 2.10. Interpolation process

In this work, the interpolation was performed using the MATLAB software. For this process a general mesh grid is first defined and the results from FEM and DIC are interpolated onto the newly defined mesh grid. A bilinear interpolation algorithm was developed for this process, where interpolated values of the new grid are obtained based on the values of the four nearest neighbors forming a quad surrounding the interpolated point. Following the alignment of the experimental and numerical results onto a common grid, the final version of the cost function developed in this study can be written as:

$$\boldsymbol{F} = \sum_{i=1}^{480} \sum_{t=100,150,175s} \left(\frac{|\varepsilon_{xx}^{num}(i,t) - \varepsilon_{xx}^{exp}(i,t)|}{\varepsilon_{xx}^{exp}(i,t)}\right)^2 + \sum_{i=1}^{480} \sum_{t=100,150,175s} \left(\frac{|\varepsilon_{xy}^{num}(i,t) - \varepsilon_{xy}^{exp}(i,t)|}{\varepsilon_{xy}^{exp}(i,t)}\right)^2 + \sum_{i=1}^{480} \sum_{t=100,150,175s} \left(\frac{|\delta_{y}^{num}(i,t) - \delta_{y}^{exp}(i,t)|}{\delta_{y}^{exp}(i,t)}\right)^2 \quad (2\text{-}3)$$

where $\varepsilon_{xx}^{exp}, \varepsilon_{xy}^{exp}$ *and* δ_y^{exp} represent the two components of the strain tensor and displacement, respectively that are extracted at a point i of coordinates x_i at time *t*. The values $\varepsilon_{xx}^{num}, \varepsilon_{xy}^{num}$ *and* δ_y^{num} represent the corresponding values computed from the FEM. In this study, the data for three representative time frames, namely *t=100, 150, 175 sec*., were selected to be included in the cost function to provide a representation of different stages of loading while maintaining a reasonable computational cost.

2.4.3.3 *Optimization Process- Hybrid Genetic Algorithm (HGA)*

In this study a hybridized training algorithm was adopted to minimize the cost function (Equation 3) and derive unknown parameters (E_s, K_1, K_2, K_3, K_4). The algorithm was based on the combination of a GA and a gradient-based algorithm. Both GA and gradient-based techniques are well-established optimization methods and have been used in numerous optimization problems [40]; however, previous literature has shown that in problems involving a large number of parameters, a combination of these two techniques yields superior optimization performance [99].

In the selected HGA, first a genetic optimization step is employed to explore the space of parameters and locate the approximate region of the optimum solution. In the second step, a gradient-based method is utilized to continue the search within the approximate region to quickly converge on the precise location of the optimum solution. As a result, the favorable characteristics of both methods namely the efficient exploration of the space by the GA and the superior convergence of the gradient-based methods are leveraged to achieve an efficient optimization. Figure 2.11 illustrates a basic flowchart of the HGA procedure adopted in this work. As shown, a feasible initial guess for the parameters is used to start the process. The initial guess is used to generate an FEA model which upon analysis will be evaluated in the cost function. If the stopping criteria are not met, a new solution is generated through different operations in GA (e.g. selective reproduction, crossover and mutation). The new solution gives rise to a new FEA model and the process will be repeated as necessary. Once the stopping criteria are satisfied, the final solution of GA will be used to initiate the gradient-based scheme. This step will continue until convergence criteria are satisfied when the final optimal solution is identified.

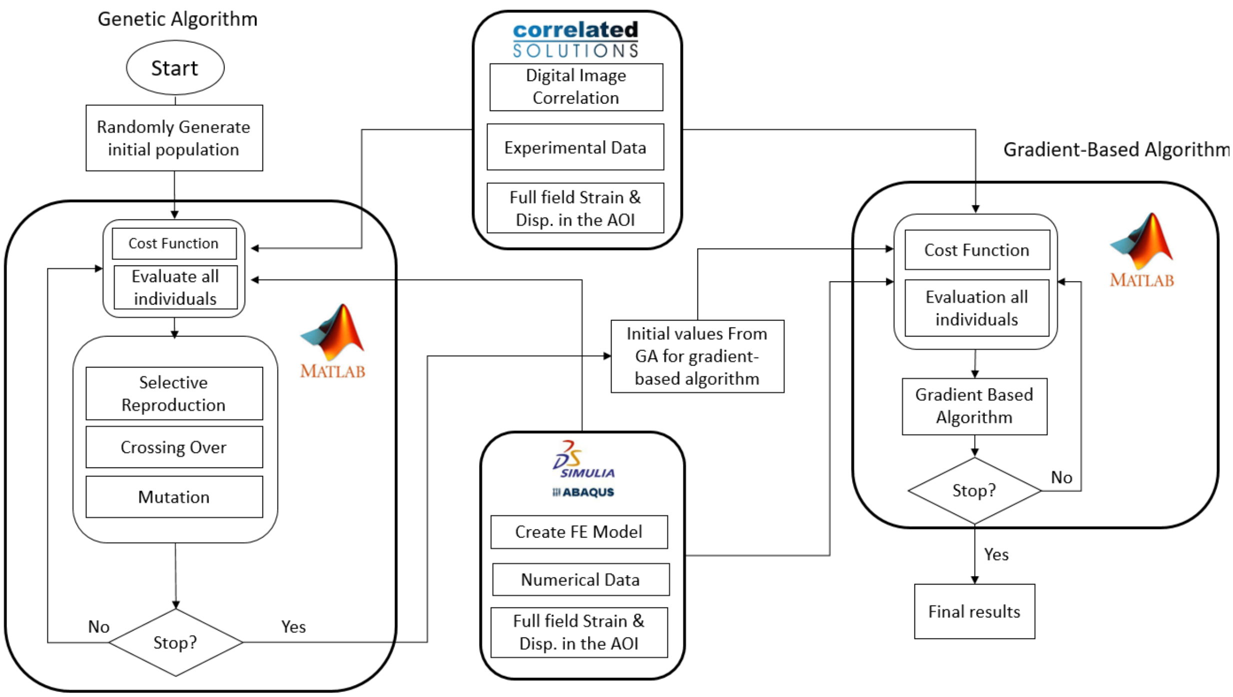

Figure 2.11. Overview of the proposed HGA

Table 2.3 shows the initial values selected within the feasible range (maximum and minimum values) used as the initial guess for the parameters in the HGA procedure. Before the updating process, an initial model was created based on the initial values shown in Table 2.3. Table 2.4 presents three representative sets of training parameters to be used within the GA based on literature [105]. For the parameters used in the algorithm, N_{pop} represents the initial population, N_{elites} represents population of elites which go directly to the next generation, N_{mut} represents the population which are randomly selected for mutation, μ represents the probability rate of mutation, N_{pairs} represents the selecting parents for mating, and *iterations* describe stopping criteria for termination. It should be noted that optimization process represents a trade-off between computational time and solution accuracy and that the parameters selected in this study only represent three optimization scenarios aimed toward validity of the approach rather than convergence to the exact solution.

Table 2.3. Initial, minimum and maximum values of the updating parameters

Material parameter	E_s (ksi)	K_1 (lb/in.)	K_2 (lb/in.)	K_3 (Kip in./rad)	K_4 (Kip in./rad)
Initial	25,000	70,000	70,000	2,000	2,000
min	20,000	50,000	50,000	50	50
max	40,000	1,500,000	1,500,000	500,000	500,000

Table 2.4. Parameters of the GA for the three identification tests for the first configuration

GA Parameter Group (PG)	N_{pop}	N_{elites}	N_{mut}	μ	N_{pairs}	*Iterations*
A	10	1	2	0.04	7	40
B	20	2	4	0.04	14	20
C	50	4	8	0.04	28	20

2.4.3.4 *Solution Convergence*

Configuration 1 (*CF1*) was used to evaluate the performance and efficiency of the parameter groups presented in Table 4. In this context, performance was described as the capability to converge to a rational solution of E_s (assumed to be 29,000 ksi) at the global minima, with efficiency described by the time of solution. An illustration of the solution efficiency is shown in Figure 2.12, which highlights the evolution of the cost function as the parameters converge towards their optimal solution. As seen in this figure, the GA training was stopped in each case at 20 epochs where an obvious plateau would be reached in the cost function and the parameters. At this point, the gradient-based algorithm was initiated which further minimized the cost function and resulted in the final convergence. Table 2.5 includes the parameter results of the optimization solutions for this configuration. The results demonstrate that *CF1B* and *CF1C* both exhibit satisfactory performance when compared to *CF1A*, but the computational cost for *CF1C* is much higher without a significant improvement in performance. *CF1A* does not approach a rational solution for E_s and appears to be stuck at some local minima, highlighting the importance of the number of individuals (N_{pop}) used in the first generation of the hybrid-optimization algorithm. Our rationale for selecting the parameter group B was based primarily on solution time (or computational cost) along with the convergence outcome for the one parameter with a generally well-known value, modulus of elasticity E_s. Future studies on this topic will explore the selection of optional parameters.

Table 2.5. Identified optimal parameters based on HGA for different parameters of the GA for the first configuration

Configuration/ Parameter Group	E_s (ksi)	K_1 (lb/in.)	K_2 (lb/in.)	K_3 (Kip in./rad)	K_4 (Kip in./rad)	Solution time (Hour)
CF1A	27,488	92,551	90,165	125	188	20
CF1B	29,100	97,416	90,020	80	54	20
CF1C	29,244	98,018	88,000	55	66	50

As noted convergence for each of the final parameter selections manifested as a plateau in each parameter. For the modulus of elasticity parameter, the rational solution for steel provided a reference for comparison; however, for the restraint conditions no such comparison was available. To evaluate the final parameters for the boundary restraints a convergence study was performed to correlate the degree of model restraint relative to the idealized solution. For the pin-roller condition, the expectation was zero rotational restraint and infinite vertical restraint, whereas the expectation for the fixed condition maintained that same vertical restraint, but included infinite rotational restraint.

The parametric study used for both types of boundary conditions were based on the assumption that for full restraint (either vertical or rotational), the displacement or rotations would converge to a value of zero (or near zero). For the displacement, this hypothesis was tested in the FEA model by selecting a target value in a displacement-controlled analysis (i.e. 0.3 in) and evaluating the model response with varying restraint stiffness values. For the vertical support springs, this initially resulted in the springs deforming and the midspan displacement not reaching the 0.3 threshold. This process was iterated until a plateau was reached in the midspan displacement (which was the threshold value selected). This plateau was assumed to represent full vertical restraint. This value was considered 100% fixity and all other values (%) were determined relative to this maximum. A similar approach was used for the rotational restraint, but the threshold used was the end rotation value, which was assumed to converge to zero for full fixity.

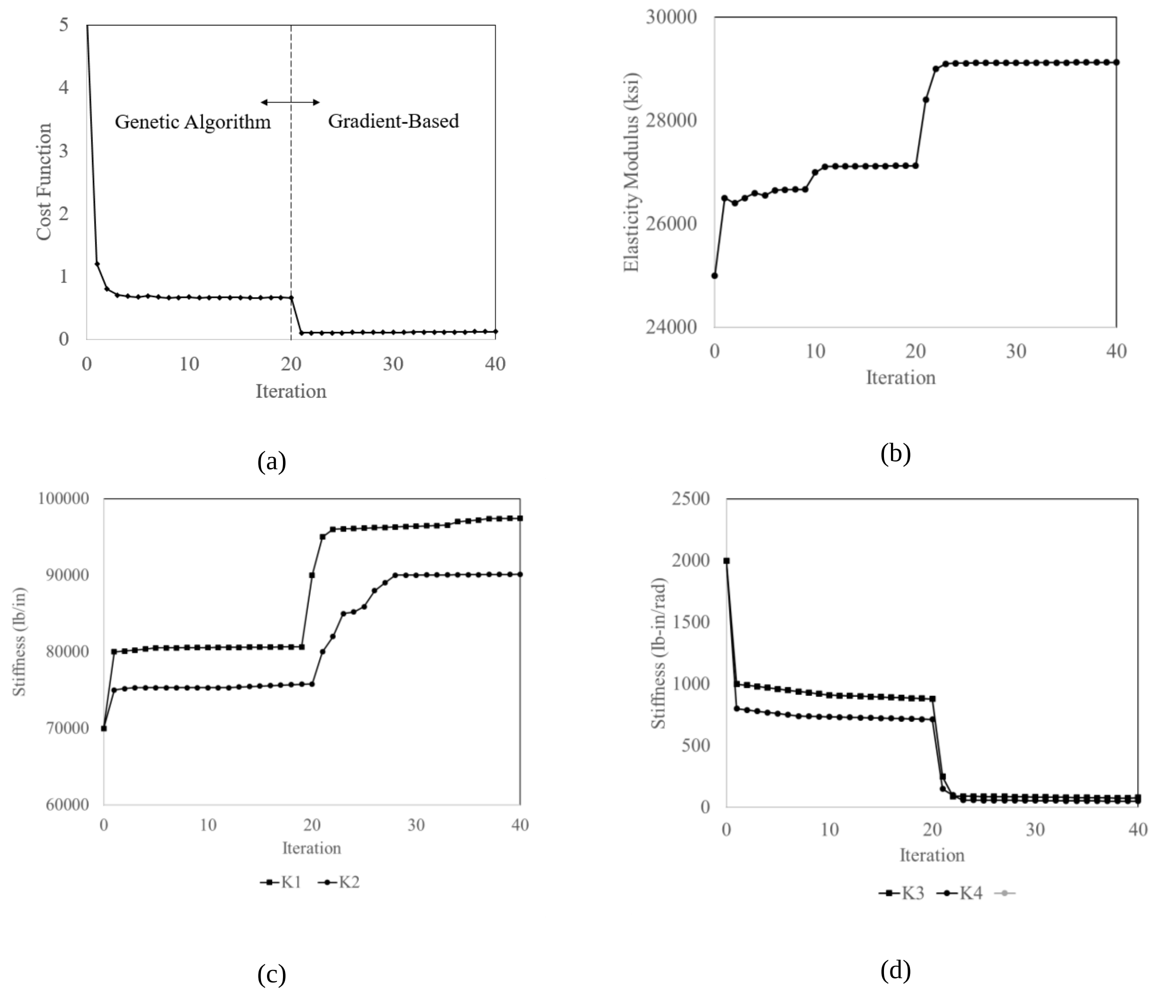

Figure 2.12. Evolution of unknown parameter convergence versus iterations for CF1B (a) Cost Function (b) Modulus of Elasticity (c) K_1, K_2 (d) K_3, K_4

The convergence study used the FEM of the test beam with the boundary restraint stiffnesses parameterized. Using the model, the values of the boundary restraints (e.g. K_1 /K_2 and K_3/ K_4) were varied iteratively to establish the upper and lower bounds of the restraint stiffness required to mimic the idealized solutions (i.e. simple and fixed conditions). This idealized solution is realized when the selected degree of freedom converges to a plateau, indicating additional restraint stiffness does not yield additional restraint resistance. The resulting convergence study demonstrated that a fixed vertical restraint stiffness equates to 250,000 lb/in, whereas full rotational restraint equates to 500,000 Kip in./rad. For the configurations evaluated in this study, Figure 2.13 illustrates the evolution of restraint as the vertical and rotational restraints approach the idealized solutions. Also Figure 2.14 illustrate the evolution of rotational restraint values which is acquired by selecting different values for rotational spring stiffness of one of the supports and then analyzing the beam using ABAQUS to obtain the evolution of support rotation values.

When comparing the updated restraint stiffness values, it is evident that the boundary conditions of the three configurations represent some fraction of the idealized boundary conditions (0.016% for configurations 1 and 2, and 0.04% for configuration 3). This level of rotational fixity was expected for the first two configurations which were designed to be rotationally unrestrained. However, for configuration 3, this percentage, while larger than the two unrestrained configurations, is much lower than expected (Figure 2.13a). This demonstrates the inefficiency of the designed clamping system in creating rotational fixity. Upon further examination, it was noted that the clamping device used in this configuration acted on a limited length (4 in.) of only the lower flange and was thus not able to effectively restrain the rotation of the beam end. A more robust mechanism for fixing the ends of both top and bottom flange over a sufficient length will be required for creating an actual rotationally fixed support conditions.

Similarly, for the vertical spring stiffness (K_1 and K_2), the updated stiffness values are approximately 40% of the expected vertical restraint (Figure 2.13b). The reduction for the vertical restraint was attributed to the support deformation that occurred during the early stages of loading due minor gaps or spacing in the pedestals and associated fixtures. The support movement dissipated at approximately 86% of the peak load, which is illustrated in the load deflection response of the supports (Figure 2.13c – d), the slope of which correlates to the average support vertical restraint stiffness (K_1 and K_2).

In Figure 2.13c – d: Left and Right support force-deflections are quite nonlinear (but elastic). As these values of reported stiffness are a representative average. This turned out to be a by-product of the experimental setup and could not be easily controlled. Consideration was given to starting the analysis after the point of support stiffening, but it was decided to include this effect in the model updating process for illustrative purposes.

In Figure 2.14, the evolution of rotational stiffness spring versus support rotation values, obtained from ABAQUS, is plotted for the purpose of knowing how we have selected maximum rotational spring stiffness domain for the optimization process appropriately. As it can be seen in Figure 2.14, beyond a support restraint stiffness of 500,000 Kip-in/rad, little difference are observed within the support rotation values. Importantly, it has to be noted that in the optimization process if a large domain for the unknown parameters is selected, such as the rotational spring stiffness, poor parameter estimates are likely unless a large population for the GA is selected, which in turn would increase computational cost. Owing to that, selection of the domain of the parameters must be done with consideration of these tradeoffs. This concept is shown in Figure 2.14, in which an initial and maximum range for the rotational spring stiffness were chosen accordingly. In future works, the sensitivity of optimization parameters such as population size will be studied in more depth.

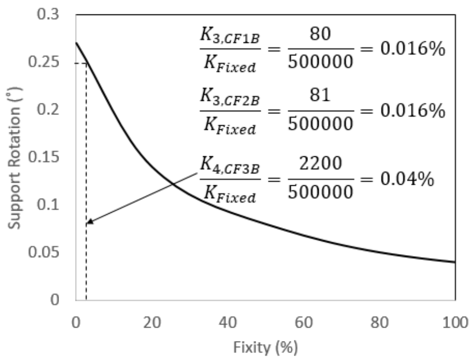

(a)

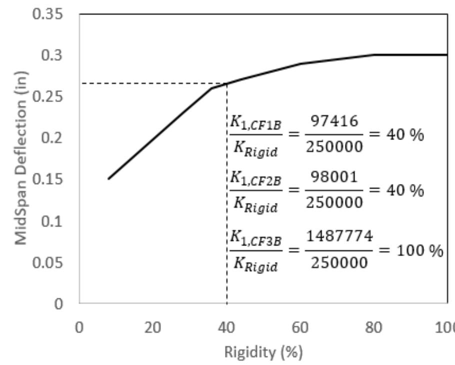

(b)

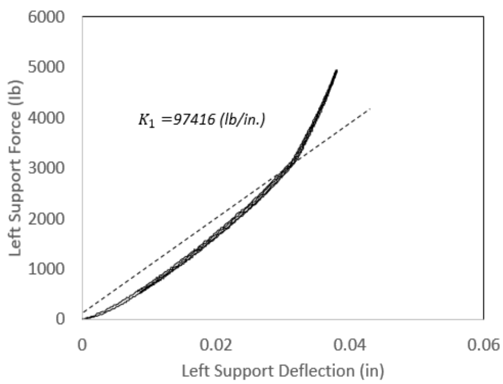

(c)

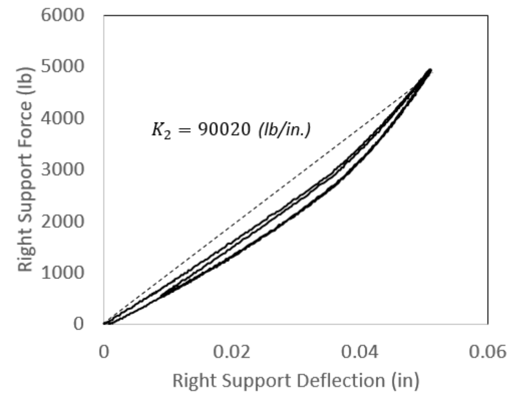

(d)

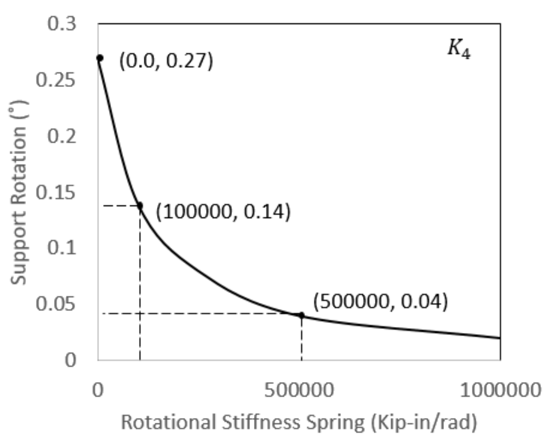

(e)

Figure 2.13. Convergence study on restraint stiffness (a) evolution of rotational restraint fixity of the supports (b) evolution of vertical restraint rigidity of supports (c) force versus left support deflection (d) force versus right support deflection (e) Rotational

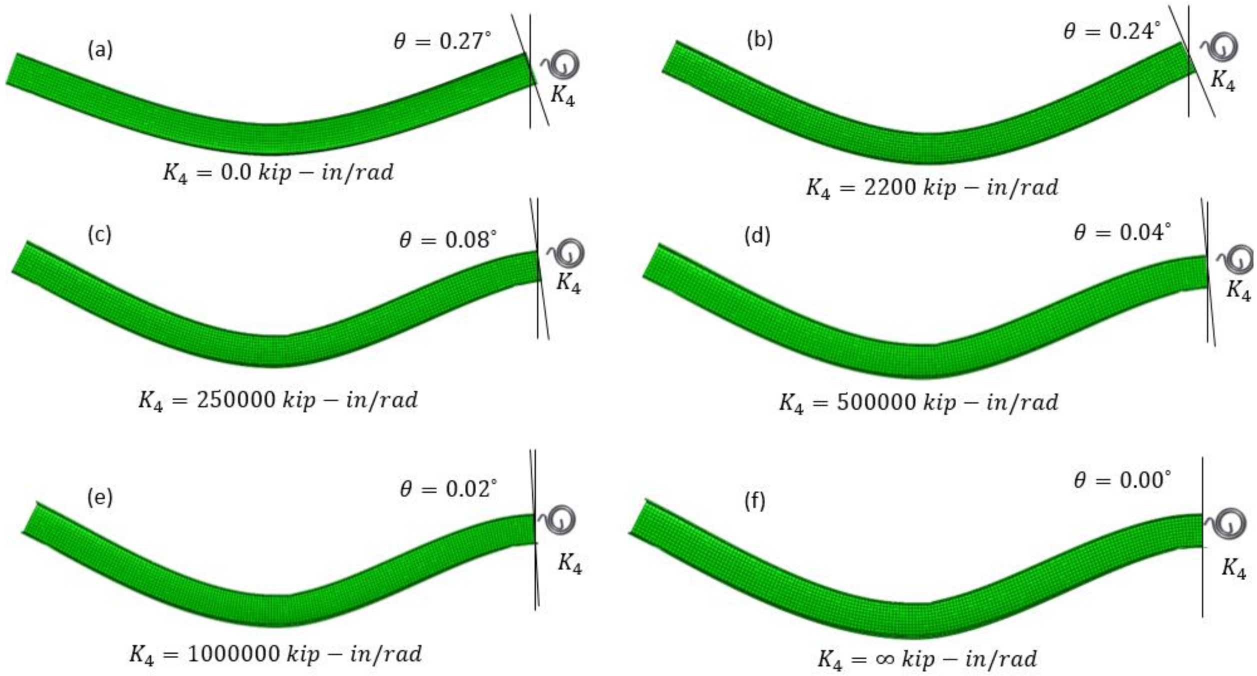

Figure 2.14. Rotational Spring Stiffness variance versus degree of rotations

With the rationality of the optimized parameters established, it was determined that the parameter group B yielded the most efficient optimization solution and was selected for evaluation of the other two configurations (*CF2* and *CF3*). Using this parameter group, the final identified parameters are presented in Table 2.6 for all three test configurations.

Table 2.6. Identified optimal parameters for different configurations for group B set of parameters of the GA

Configuration/ Parameter Group	E_s (ksi)	K_1 (lb/in.)	K_2 (lb/in.)	K_3 (Kip in./rad)	K_4 (Kip in./rad)
CF1B	29,100	97,416	90,020	80	54
CF2B	29,511	97,501	91,888	48	101
CF3B	29,984	1,568,698	1,384,224	249	2,200

A comparison between the full-field contours of the DIC and the updated FE model are presented in Figure 2.15 and Figure 2.16 for the midspan and support locations, respectively for *CF1B*. Figure 2.15 illustrates a comparison of the longitudinal strain (ε_{xx}), shear strain (ε_{xy}), and vertical deflection (δ_y). From this comparison, it is evident that the updated model is able to reproduce the responses derived from the experiment as illustrated by the minimal error exhibited within the area of interest. It should be noted that the localized errors in the longitudinal strain contours are likely associated with local stress concentrations that occur on the top of the beam at the location of the load application. Figure 2.16 illustrates a comparison of the deflections at the end locations showing excellent agreement. It is also notable that while the vertical deflection right above the supports were initially expected to be zero, some support settlement can be seen in the results. Similar to the midspan location, the error between the DIC measurement and updated model is minimal across the area of interest. Similar results were derived for *CF2B* and *CF3B*, but are not included in this manuscript.

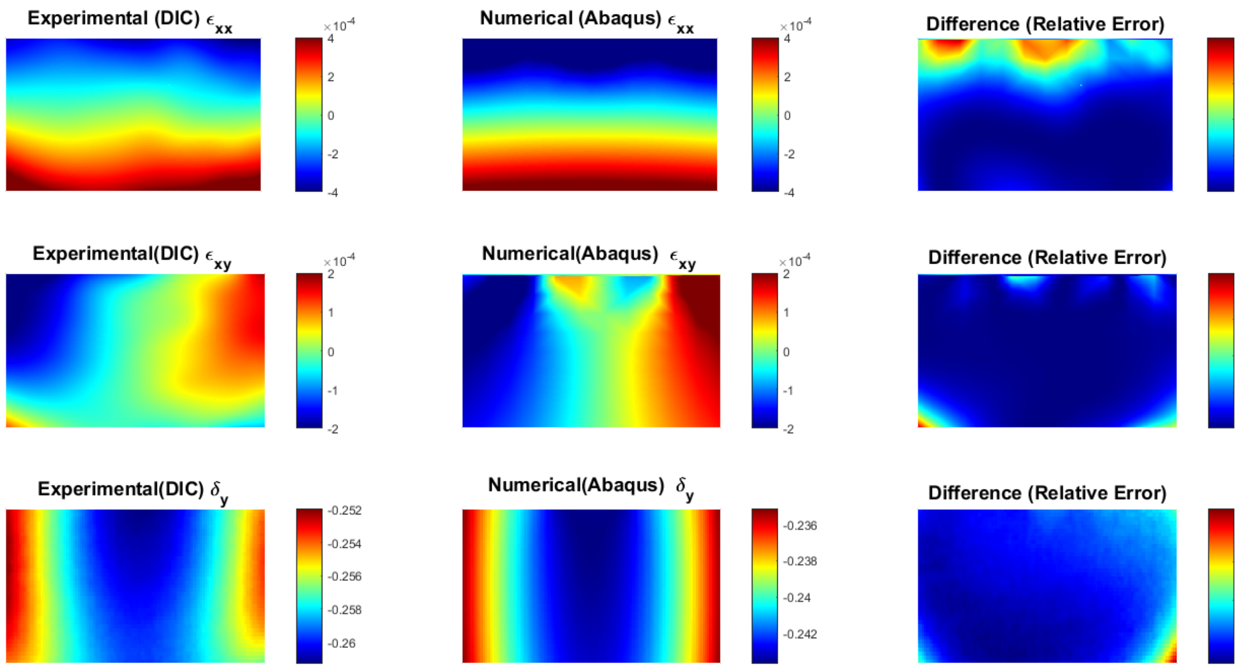

Figure 2.15. Contour plots of the experimental strain fields, the numerical strain fields and their absolute difference for the middle span for the components $\varepsilon_{xx}, \varepsilon_{xy}, \delta_y$ at t=150 sec for CF1B.

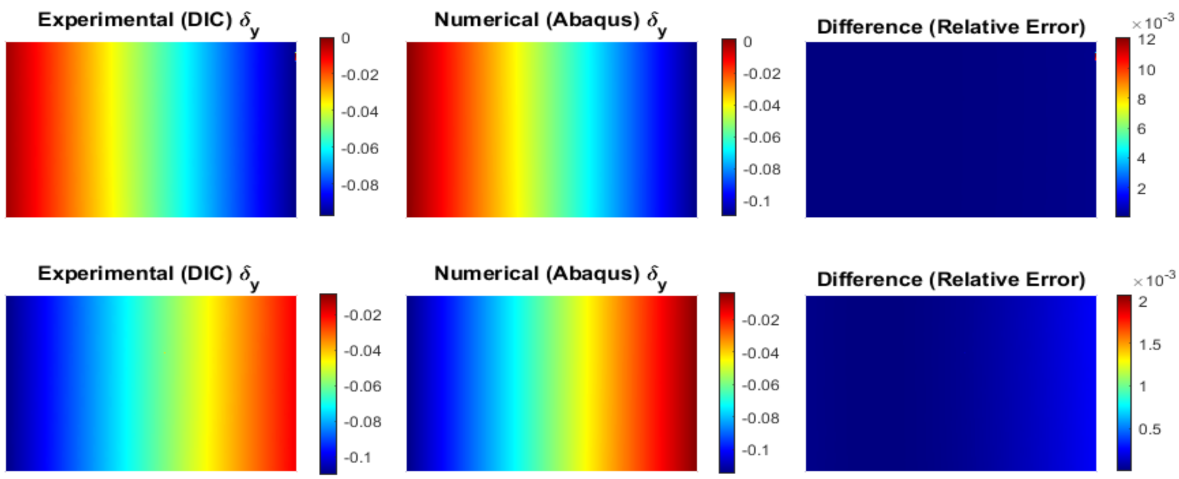

Figure 2.16. Contour plots of the experimental strain fields, the numerical strain fields and their absolute difference for the component δ_y (first row for left span and second row for right span) at t=150 sec for CF1B

2.4.4 *Performance of Updated FE Model*

To investigate the effectiveness of the identification procedure, the performance of the model before and after updating can be evaluated versus the results derived from the experiments. For this evaluation, two points of interest for *CF1B* were selected for comparison, namely points A and B which were previously described in Figure 2.8. The temporal evolution of the longitudinal strain both before and after the updating process are shown in Figure 2.17a – b , respectively. Also, a summary of the percent difference, described as the mean absolute percentage error (MAPE) between DIC and FEM, for the three configurations before and after model updating, are presented in Table 2.7. Comparing the results from the updated model with those derived from the DIC measurements demonstrate the success of the identification procedure, in that the revised strain response now tracks along with those derived from the experiment. It is seen that the evolution of local strain is correctly described over the entire loading sequence, with comparable magnitudes and falls within about an 8% error window of the measured response. Similar results were derived for *CF2B* and *CF3B*, but are not included in this manuscript. This outcome demonstrates that full-field measurement techniques are sufficiently robust for use in the St-Id framework for SHM.

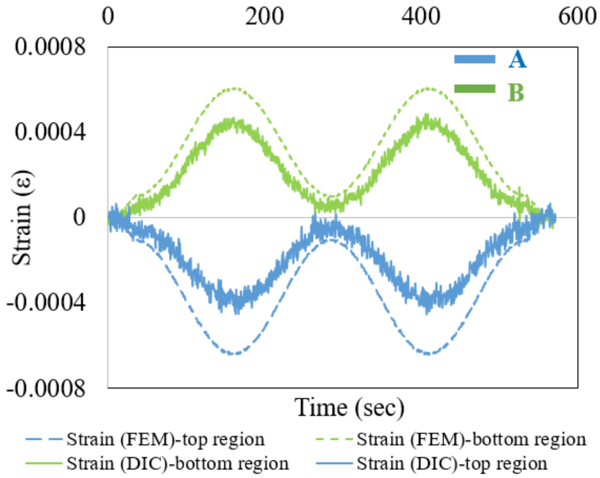

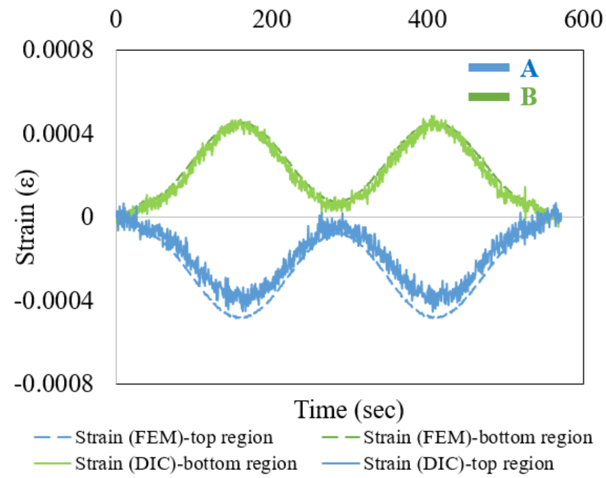

(a) (b)

Figure 2.17. Comparison of the evolution of the longitudinal strains εxx for CFB1 between the numerically computed values and the values obtained using DIC at points A-B shown in Fig. 8, for (a) before model updating, (b) after updating

Table 2.7. Summary of differences between DIC and FEM before and after model updating for the mentioned points.

		Before model updating (BMU)		After model updating (AMU)	
		Top Strain (A)	Bottom Strain (B)	Top Strain (A)	Bottom Strain (B)
Mean absolute percentage error: $MAPE = \frac{100\%}{n}\sum_{t=1}^{n}\lvert\frac{e_t}{y_{sensor}}\rvert\ (\%)$	Configuration 1	35	24	8	3
	Configuration 2	38	22	12	5
	Configuration 3	32	17	7	6

Note: $(e_t = y_{\text{BMU}} - y_{AMU}, n = number\ of\ measured\ data)$

2.5 Conclusion

In this study, a structural identification procedure was developed to identify the material properties and boundary conditions of the experimental setup of a steel beam under flexural loads using full field measurements derived from 3D-DIC. This paper describes the core components of the St-Id process including the experimental setup, numerical model development, creation of common reference plane, and model updating. Conventional mechanical sensors typically used in St-Id applications were also installed on the experimental specimen to provide context for comparison with the current practice. In this work, both deflections and local strain fields were successfully used in the updating procedure through the deployment of a cost function that included the relevant components of full-field structural response in a number of different stages of loading. This cost function was then pushed to zero by leveraging an efficient optimization algorithm consisting of a hybrid of GA and a gradient-based optimizer.

A number of different optimization parameters were tested and compared in terms of convergence performance as well as computational efficiency. The examination of the evolution of the cost function as well as the identified parameters versus time demonstrated satisfactory convergence. The excellent agreement of the strain and displacement responses achieved after the completion of the updating process confirmed the efficacy of the proposed identification method. It was also observed that while the responses obtained through DIC were relatively noisier than the physical sensors, the full-field measurement provided a rich dataset for a stable and robust St-Id. Overall, the St-Id results obtained in this work suggest that image-based measurements sensing using 3D-DIC can be successfully used as an alternative to physical in-place sensors for characterizing the response of large scale structural systems.

Future work is expected to further explore the potential for reducing the noise within the experiments, optimal parameter selection for the parameter identification, evaluation of the range of applicability with respect to uncertainty in the updated parameters and applying different boundary condition configurations to demonstrate the capability of the proposed approach. These areas of focus are critical to the applicability of the proposed approach to more complex structural systems.

3 CHAPTER 3 – Image-based Tomography of Structures to Detect Internal Abnormalities using Inverse Approach

Mehrdad S. Dizaji Mohamad Alipour, Devin K. Harris

“Dizaji, M. Shafiei, M. Alipour, and D. K. Harris. " Image-based Tomography of Structures to Detect Internal Abnormalities using Inverse Approach." *Experimental Techniques*, Submitted.”

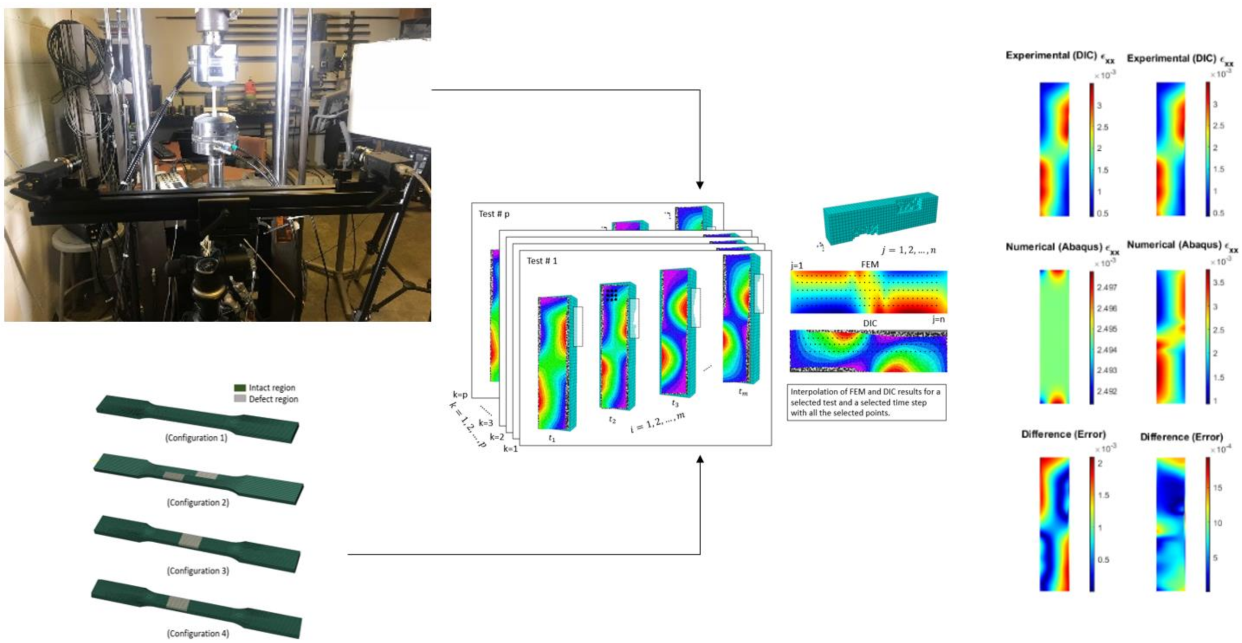

3.1 Abstract

Image-based techniques have been extensively deployed in the fields of condition assessment and structural mechanics to measure surface effects and deformations such as displacements or strains under loading. 3D-DIC is one technique frequently used to quantify full-field strain measurements. This research uses 3D-DIC to detect interior anomalies of structural components, inferred from the discrepancy in constitutive properties such as elasticity modulus distribution of a three-dimensional heterogeneous/homogeneous sample using limited full-field boundary measurements. The proposed technique is an image-based tomography approach for St-Id to recover unseen volumetric defect distributions within the interior of a three-dimensional heterogeneous space of a structural component based on the iterative updating of unknown or uncertain model parameters. The approach leverages full-field surface deformation measurements of structural elements as ground truth measurements coupled with a FEMU process that leverages a novel hybridized optimization algorithm for convergence. This paper presents a case study on a series of structural test specimens with artificial damage. An ABAQUS script tool was used to provide an iterative interface between the FEM script and an optimization package. Within the St-Id framework, the evolution of the selected objective function illustrated precise convergence of the identified elasticity modulus distribution and the resulting updated model at later stages of loading correlated with the ground truth experimental response. The results illustrate the potential to detect invisible internal defects from surface observations and to characterize internal properties of materials from their observed mechanical surface response.

Keywords*:* Inverse Problem, 3D-DIC, Full-field measurement, Image based Tomography, Hybrid Algorithm, Optimization, Interior defects, damage identification

3.2 Introduction

Material properties such as elastic modulus, shear modulus or Poisson's ratio are critical to both the design and evaluation processes of engineered systems ranging from buildings to aerospace structures, as these properties serve as the link (constitutive law) between stress and strain [106], which describe the response of these engineered systems. In many cases, these material properties can be derived using standard testing approaches, but these tests are typically suitable to virgin materials that are not part of an existing system [107]. Typically, the measurement of these constitutive properties for existing structural systems requires an indirect in-situ measurement that can be correlated with a specific material property or the destructive extraction of a representative sample for traditional testing. However, in many cases, these types of measurements are insufficient or representative samples cannot be extracted and alternative approaches are necessary. In these cases, an inverse engineering solution for St-Id aims to resolve the non-homogeneous material properties, demanding the knowledge of interior and exterior deformation fields such as displacement/strain fields and boundary conditions. One extension of this inverse engineering solution is in discovering the presence of internal abnormalities (e.g., internal geometric features such as voids or other types of defects), presumed as a locally heterogeneous status inferred from non-uniform stochastic elastic modulus distribution in the interior of a three-dimensional region of a sample.

Ideal solutions to this type of inverse problem require measurements of deformation fields such as displacement/strain fields internal to the body of the solid. In medical applications, internal properties of a sample can be observed by non-destructive imaging tools, such as ultrasound devices, which depend on utilizing high-frequency sound waves to produce dynamic visual images of a sample/organs. The sound waves are transmitted to the area to be examined and the returning echoes are captured to provide a "Live" image of the area. Magnetic resonance imaging (MRI) and optical coherence tomography (OCT), which are alternative non-invasive imaging technologies suitable for internal three-dimensional imaging, rely on magnets to produce a strong magnetic field that forces protons in a sample to align with that field. These technologies rely on the excitation and detection of changes in the direction of the rotational axis of protons found in the water that makes up living tissues [108], which can be used to identify displacement fields from the image sequences [108-116]. A more recent medical imaging modality, termed "*elastography"*, is based on mapping a sample's stiffness via mechanical properties (i.e. elastic modulus, Poisson's ratio, etc.) to known displacement fields [114-116]. These maps provide additional and complementary information to categorize material types or detect abnormal heterogeneous state of a sample based on changes in their material property distribution such as an elasticity property. These methods can serve to assess the volumetric displacement of a sample; however, their use is usually limited to biological tissues. For most materials of engineering interest, such as metals, concrete, reinforced concrete, etc., the previously denoted techniques cannot be practically applied. For instance, magnetic resonance imaging (MRI) technology cannot be employed on metals and reinforced concrete because the powerful magnetic field of the MRI system can attract objects made from certain metals and cause them to move suddenly with great force. Internal properties of a component can be observed using advanced non-destructive methods such as full-field optical techniques. Recently, the X-ray computed tomography (XCT), a 3D imaging technique commonly used in medicine, has been broadly employed to identify the internal properties of the structural components due to its high resolution, non-destructive nature and ability to clearly visualize details including internal anomalies such as different streams of defects. Moreover, XCT can be combined with Digital Volume Correlation algorithms (DVC) to map the relative deformations between consecutive XCT images with high resolution [117]. Although this technique is very promising, it presents a series of limitations: it requires expensive and complex equipment (e.g. X-ray computed tomography (XCT) [118, 119]), the investigated material needs to have a random internal pattern (e.g. foams, bones tissue, composites etc. [120, 121]), and the correlation algorithms are computationally expensive. Moreover, the procedure to implement the XCT technology requires loading of the sample while scanning which is difficult, especially for complicated structures (i.e. in-situ full-scale and complicated structures) [122].

A proposed alternative approach to address the inverse problem in elasticity is to solely use the exterior surface measurements of a sample. From an equipment perspective, measuring surface deformations requires only a set of cameras to capture the image of the surface of the sample during external loading. Thus, the experimental setup is significantly cheaper and less complex when compared to XCT. This approach has been successfully demonstrated to recover target material property distributions using limited surface observations with simulated and experimental data. More recently, Mei et al. [114, 123-125] proposed a strategy to solve the inverse problem in elasticity for a simulated experiment for the shear modulus distribution using only surface deformations. Their methodology does not require a priori information about the problem domain and is based on finite element techniques, where the shear modulus distribution is represented as unknowns on the mesh nodes and interpolated with finite element shape functions. Mei et al. [124] tested their method on a problem domain consisting of an inclusion embedded in a homogeneous background and recovered the shear modulus distribution using simulated surface displacement fields. While their approach proved successful for the tested scenario, the type of optimization algorithm used in their work has the potential for getting trapped in a local minimum for more complex problems.

While state-of-the-art methods all need specialized scanners (e.g. XCT, ultrasound, OCT, MRI, etc.) or physics rules, the image-based tomography approach proposed in this paper utilizes digital cameras to gather exterior (i.e. surface in 3D sample) full-field measurements of a sample to adjust an initial FEM via an optimization algorithm and recover the elastic modulus distribution, from which the internal abnormalities can be inferred. Image-based techniques using digital cameras are frequently employed to measure surface displacements/strains on a sample under external loading. One of these image-based techniques, DIC, is a non-contact photogrammetric technique used to measure full-field deformation (2D and 3D) from a sequence of images. From the sequence of images, deformations are measured by tracking pixel movements through correlated speckle pattern subsets from image to image. Deformations within subsets are interpolated, similar to the FEM, providing the ability to describe the full-field deformation over the specimen surface. Some applications of the DIC technique can be found in the literature [8, 15, 19, 58-85], with examples of displacement or strain measurements based on DIC typically used to adjust and improve the mechanical characterization of solids [126-130]. A comprehensive treatment of DIC is available in the literature [16-21] and not presented herein, but additional details on the DIC deployment used in this investigation are provided in a later section.

Recently, the authors took advantage of the DIC technique as a full-field measurement approach for constitutive property identification of a full-scale steel component using a St-Id approach [42, 104, 131, 132]. The results of these previous studies demonstrated the robustness of the proposed hybrid approach for identifying uncertain/unknown system parameters. In this paper, an experimental program was developed to evaluate the feasibility of extending this hybrid approach in an inverse problem to detect internal features of a structural components or systems merely by surface measurements, without a priori postulation about the internal features of a structure. As a preliminary investigation, an inverse problem methodology was established for FEMU with 3D-DIC measurements of four steel coupons with artificially simulated defects subjected to variable loadings. The defined inverse problem was then used for the St-Id including surface and internal defect geometries, constitutive properties and boundary conditions. To detect damage, sections of the FEM along with surface 3D-DIC measurements were considered as inputs into an objective function aimed at simultaneous local and global system parameter identification.

3.3 Methodology

The hypothesis of this work centers on the premise that internal defects can be delineated and/or inferred by their material constitutive properties distribution such as elastic modulus, shear modulus, density, or other material properties, and further described physical properties such as the shape, size, and position. The mechanisms employed herein to identify material properties of an internal area of a sample are informed by an image-based measurement approach which takes advantage of the heterogeneous characteristics of surface strains during loading to deduce internal properties (e.g. geometric features or defects) of the structure. Full-field surface deformation measurements derived from 3D-DIC have the potential to illustrate unseen anomalies within a solid body while also being non-invasive and data-rich.

Traditionally, to simulate a structural component, a FEM can be created, assuming the element is globally homogeneous. However, non-uniform distribution of materials, (e.g. porosity, etc.), interlayer fractures, and defects are inherent to manufactured structural materials and can occur during the manufacture, resulting in a non-homogeneous internal property. For structural components with defects, the distribution of these internal non-homogeneous properties under loading (i.e. mechanical/thermal loadings) manifest in the form of perturbed strains/deformation patterns on the surface of the component. An example of the effects of non-uniform properties on strain/displacement patterns is demonstrated in Figure 3.1, using a tensile test of four similar coupons with different artificially manufactured defect features on the back side to mimic damaged regions, which are described as follows: (a) coupon specimen without any defect on the surface, subjected to tensile load, (b) coupon specimen with two artificially manufactured defects on the back side of the sample, which are invisible from the front side of the specimen subjected to tensile load, (c) coupon specimen with one artificially manufactured defect on the back side on the top region of the sample subjected to tensile load, and (d) coupon specimen with one artificially manufactured defect on the back side on the middle region of the sample subjected to tensile load.

During measurement, all of the coupons were tested in the same way; nonetheless, due to the damaged features on the back side of the coupons in configurations 2-4, the surface full-field strain and displacement patterns in different directions were clearly differentiable between the four represented specimens at the same load level. The non-homogeneous full-field strain/displacement patterns on the surface of the coupons can be inferred as a hologram of interior information such as existence of internal anomalies (e.g. defects). Therefore, in the proposed approach, an inverse problem is utilized to interpolate and tune those non-homogeneous surface patterns on the corresponding full-field strain/displacement surface pattern from numerical model by adjusting the variables (e.g. constitutive properties, boundary conditions or geometric properties) to infer internal properties (e.g. internal defects). Extracting more information from the surface of a sample can help to better imply and interpret the interior properties.

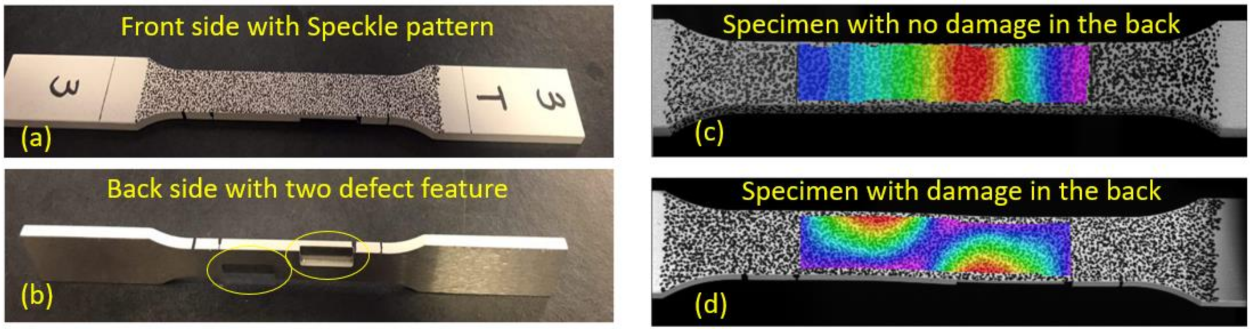

Figure 3.1. Illustration of different specimens with DIC patterns (a) front side of coupon specimen with damage in the back, (b) back side of the coupon specimen with two rectangular damage, (c) longitudinal full-field strain pattern for the specimen without any dama

By leveraging 3D-DIC as a full-field measurement technique, and the observed strain/displacement patterns, the non-homogeneous internal status of the samples can be extracted locally and globally, by interfacing the initial FEM with the measurements and updating the structural model until convergence. The proposed method is described as an image-based tomography of a structural components using an inverse approach.

3.4 Experimental setup

In this investigation, an experimental program was developed to evaluate the feasibility of leveraging 3D-DIC in a FEMU process to detect internal features of structural components. The experimental program included a laboratory-scale investigation of four representative coupon samples subjected to the same displacement-controlled loading and boundary conditions. The structural configurations used in this work are illustrated schematically in Figure 3.2a and can be described as:

1) Configuration 1: coupon specimen without any defect on the surface, subjected to tensile load.
2) Configuration 2: coupon specimen with two artificially manufactured defects on the back side of the sample, subjected to tensile load.

3) Configuration 3: coupon specimen with one artificially manufactured defect on the back side on the top region of the sample, subjected to tensile load.

4) Configuration 4: coupon specimen with one artificially manufactured defect on the back side on the middle region of the sample, subjected to tensile load.

These test configurations give rise to heterogeneous and non-uniform in-plane strain fields, (i.e. longitudinal, transverse, and shear strain components), as well as in-plane/out-of-plane displacement fields (i.e. longitudinal, transverse, and out-of-plane components). The geometric dimensions of the coupon specimens are shown in Figure 2(b). Also, the experimental and DIC setup are illustrated in Figure 3.3 where the Area of Interest (AOI) has been defined as the region on the specimen where the DIC measurements are compared with numerical simulations. For this experimental validation, four simple tension tests were performed using A36 steel coupon specimens according to the test method defined in ASTM E8 [107]. The mechanical response of the specimens was measured by 3D-DIC to describe full-field surface measurements of displacement and strain of the coupons, analogous to the types of results derived from a FEM. A commercially available DIC system from Correlated Solutions Inc. was used in this investigation [102].

The DIC system components consisted of a camera system, an image acquisition package (VicSnap), and 3D-DIC post-processing software (Vic-3D). The DIC image acquisition used one set of two stereo-paired digital cameras, 5-megapixel charge coupled device (CCD) image sensor with a resolution of 2448×2048. The camera was connected to a C-mount optical lens (12 mm) and the acquired data was communicated to the control PC through FireWire cables. The camera pair was positioned 0.6 m from the coupon which yielded a field of view (FOV) of 0.7 x 0.7 m. For the experiment, the basic process consisted of specimen preparation, camera setup (focusing, calibration, and image acquisition), and post-processing of results. Prior to testing, the surface of each specimen was covered with a fine, dense and random speckle pattern (flat white paint for base and fine tip permanent marker for pattern) for the correlation process. For the pixel tracking process in DIC, the area of interest on the speckle pattern was split into rectangular windows or “subsets” and unique patterns of speckles remained available within each subset to allow for tracking across subsequent frames. The patterns in the subsets were tracked on a grid of a specific “step” size, which dictated the spatial resolution of the calculated points. To achieve a fine grid of unique patterns in subsets, the selection of the subset size was determined through direct experimentation during post-processing and a square subset of 23 pixels at a step of 7 pixels was selected. For more details regarding DIC setup, the reader is referred to the authors' previous works [42, 104, 131, 132].

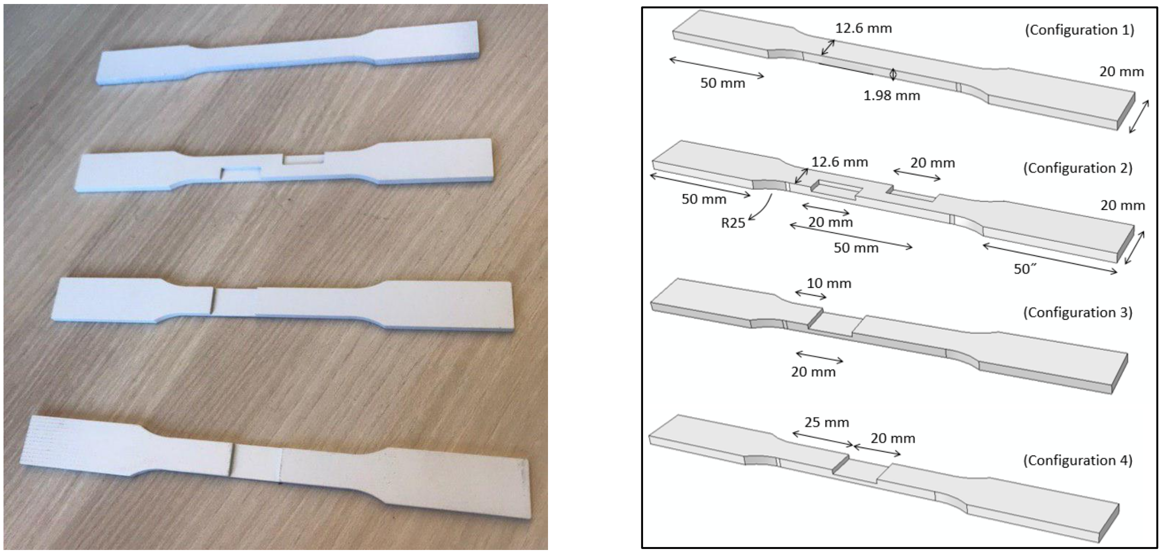

(a) (b)

Figure 3.2. Intact and simulated damage coupons (a) painted steel coupon specimens used in the experimental setups, and (b) geometric dimension of the coupon specimens

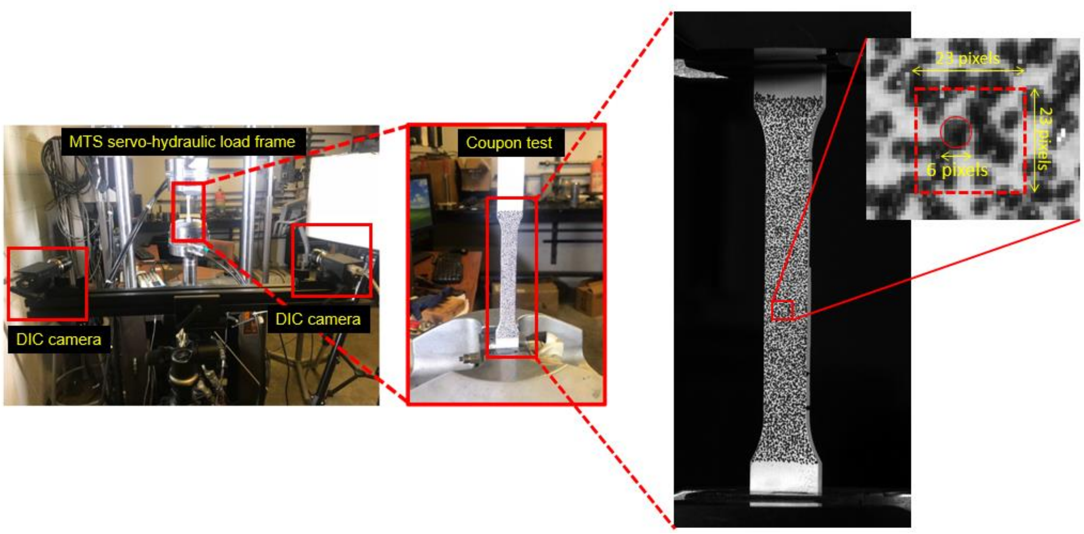

Figure 3.3. Experimental and DIC setup configuration (one system including two CCD cameras)

3.5 Numerical implementation

As previously noted, the FEM updating process requires the development of an initial numerical model that can be updated based on experimentally derived behavior results. In this investigation, the FEM model of the sample was developed in ABAQUS [10], a robust commercially available finite element software package. The specimen was modeled using a total of 4,300 continuum 3D hexahedral solid elements (C3D8) with full integration. The FEM and mesh configuration of the coupon specimens are shown in Figure 3.4a. In Figure 3.4b, the partitioned region for configuration 2, considered an optimization process, is described as an example and for the other configurations the same region is partitioned differently. It should be noted that ABAQUS allowed for the development of a direct interface with the optimization package, which facilitated the iterative parameter optimization algorithm via the Python tool. In this work, the initial FEM of the specimen was created using the Graphical User Interface (GUI) of ABAQUS allowing for the model developed script to be extracted. The extracted script was iteratively interfaced with the Python package, which are described in a later section. The basic procedures are described by the following steps: (1) create initial model and save the model, (2) use the saved ABAQUS model to create the script files of the model development, (3) create output (i.e. load/deformation response), (4) repeat the calculation by running the generated script files, and (5) adjust the script to create a different model or output.

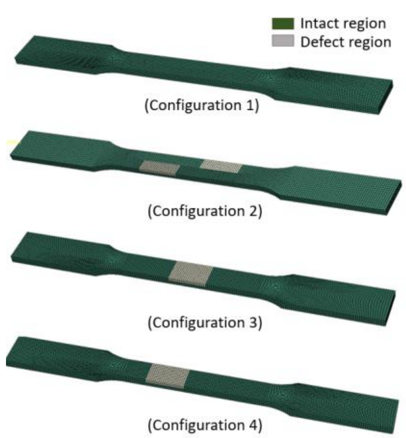

(a)

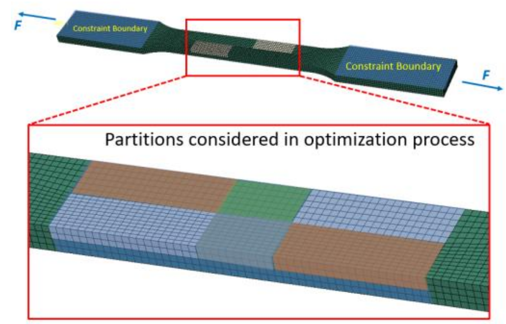

(b)

Figure 3.4. FEM of the coupons, and (b) constraint boundary conditions, the direction of external loading and the partitioned regions considered in optimization process for configuration 2

3.6 Definition of the objective function

The proposed method is based on inverse problem and finite element techniques as well as special distribution of modulus of elasticity, represented as an unknown design variable, within the finite element mesh. The number of unknown design variables (i.e. elasticity modulus values) are equal to the total of finite elements plus unknown parameters belonging to boundary conditions of the structure. The basic principle of inverse problem is to minimize the discrepancy between the experimentally measured and numerically computed response by revising the unknown variables of the FEM. In this investigation a hybridized minimization algorithm was used to minimize the following cost function (Equation 1):

$$F(\boldsymbol{E}) = \sum_{k=1}^{p}\sum_{i=1}^{m}\sum_{j=1}^{n_i}\left[\left(\frac{\varepsilon_{xx,ij}^{exp}-\varepsilon_{xx,ij}^{num}(E)}{\varepsilon_{xx,ij}^{exp}}\right)^2+\left(\frac{\varepsilon_{yy,ij}^{exp}-\varepsilon_{yy,ij}^{num}(E)}{\varepsilon_{yy,ij}^{exp}}\right)^2+\left(\frac{\varepsilon_{xy,ij}^{exp}-\varepsilon_{xy,ij}^{num}(E)}{\varepsilon_{xy,ij}^{exp}}\right)^2+\left(\frac{\delta_{yy,ij}^{exp}-\delta_{yy,ij}^{num}(E)}{\delta_{yy,ij}^{exp}}\right)^2\right] \qquad (3\text{-}1)$$

With $\boldsymbol{E}$ is the vector of unknown design variables which are the constitutive properties of the finite elements, $\boldsymbol{p}$ the number of experimental tests ($\boldsymbol{p}$ = 1 in this work), $\boldsymbol{m}$ the number of load steps ($\boldsymbol{m}$ = 20 in this work) and $\boldsymbol{n_i}$ the number of data points in the DIC measurement at load step $\boldsymbol{i}$. The subscripts $\boldsymbol{exp}$ and $\boldsymbol{num}$ indicate the experimental and numerical responses, respectively. The three components of the strain tensor and the longitudinal component of displacement are represented by $\boldsymbol{\varepsilon_{xx}^{exp}}, \boldsymbol{\varepsilon_{yy}^{exp}}, \boldsymbol{\varepsilon_{xy}^{exp}}$ and $\boldsymbol{\delta_{yy}^{exp}}$ respectively that are extracted at a point i of coordinates x_i at time *t*. Similarly, $\boldsymbol{\varepsilon_{xx}^{num}}, \boldsymbol{\varepsilon_{yy}^{num}}, \boldsymbol{\varepsilon_{xy}^{num}}$ rand $\boldsymbol{\delta_{yy}^{num}}$ represent the corresponding values computed from the FEM. The proposed objective function and its components are shown in Figure 3.5 schematically.

Defining a proper model for the objective function can prevent the problem from having a non-unique solution. While from a purely mechanical point of view, it would be expected that such an approach would yield non-unique solutions, a successful solution is possible by using multiple load steps and boundary strains/displacement data sets from multiple load configurations, sequentially applied at discrete locations around the specimen [42, 104, 131, 132]. Therefore, to ensure uniqueness of the final solution of the inverse problem, a large value (note that the maximum value for $\boldsymbol{m}$ is equal to the number of time steps. The larger the value of $\boldsymbol{m}$ applied in objective function, the higher the chance of ensuring uniqueness of the final solution, in an expense of more computational cost) of $\boldsymbol{m}$ was used in Equation 1.

Another reason for using a large value for $\boldsymbol{m}$ is that the full-field DIC measurements can have noise and uncertainties in each load step. Some of the noise sources include lightning fluctuations, glare, irregularities, and poor quality of speckle pattern, as well as noise resulting from image acquisition (e.g. sensor noise) and quantization [102]. Moreover, the interpolation of DIC and FEM can also be a possible source of uncertainties. Therefore, to decrease such uncertainties, utilizing large numbers for $\boldsymbol{m}$ was chosen, in this work $m = 20$ and $p = 1$. However, utilizing a large number for $\boldsymbol{m}$ can increase computational cost dramatically. As such, parallel optimization methods are used to decrease the high computational costs.

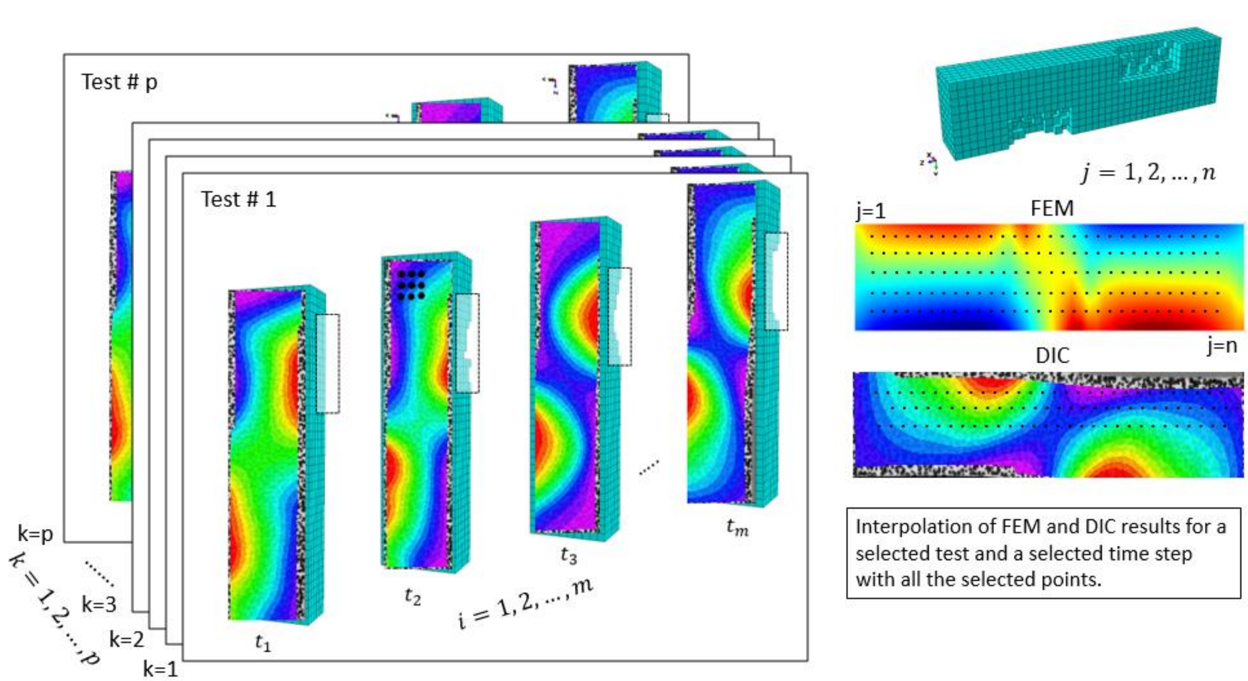

Figure 3.5. Components of the objective function

3.7 Description of optimization techniques

Many optimization algorithms are available for minimizing an objective function. In this work, a hybrid algorithm combining a GA [105] and a limited-memory Broyden-Fletcher-Goldfarb-Shanno algorithm (L-BFGS-B), is introduced and used to solve the optimization problem. In this work, a GA was used to perform a preliminary search in the solution space for locating the neighborhood of the solution with the L-BFGS-B algorithm used to refine the best solution provided by the GA. Both GA and L-BFGS-B techniques are well-established optimization methods and have been used in numerous optimization problems [99]; however, previous literature has shown that in problems involving a large number of parameters, a combination of these two techniques yields superior optimization performance. The optimization scheme employed in this paper is a hybrid optimization algorithm (HOA) consisting of two steps. First, a genetic optimization step is employed to explore the space of parameters and locate the approximate region of the optimum solution. The stopping criteria is the number of iterations. After a certain number of iterations, which is selected according to population size and computational cost, the GA halts. After running the global optimization, it is often worthwhile to then use the global optimum as a starting point for a local optimization to "polish" the optimum to a greater accuracy. Many of the global optimization algorithms devote more effort to searching the global parameter space than in finding the precise position of the local optimum accuracy. In the second step, a gradient-based method is utilized to continue the search within the approximate region to quickly converge on the precise location of the optimum solution. As a result, the favorable characteristics of both methods, namely the efficient exploration of the space by the GA and the superior convergence of the gradient-based methods, are leveraged to achieve an efficient optimization. The stopping criteria for L-BFGS-B algorithm is realized when there is no more significant decrease in objective function.

A feasible initial guess for the parameters is used to start the process. The initial guess is used to generate a FEM which, upon analysis, is evaluated within the objective function. If the stopping criteria are not met, a new solution is generated through different operations in the GA (e.g. selective reproduction, crossover, and mutation). The basic operations involved in the design of the GA developed in this study have been documented in various studies by Dizaji et. al [42, 104, 131, 132]. The new solution gives rise to a new FEA model and the process is repeated as necessary. Once the stopping criteria are satisfied, the final solution of GA is used to initiate the gradient-based scheme. A GA is utilized to perform a preliminary search in the solution space and to locate the neighborhood of the solution. Then, using the best solution found with the GA as initial guess, a gradient-based optimization method is implemented to quickly converge towards the optimum solution. The optimization tool (L-BFGS-B) is then used to refine the GA solution. This step will continue until convergence criteria are satisfied and the final optimal solution is identified. Those unknown design variables are determined iteratively by minimizing the objective function *(*Equation 1*)*.

Table 3.1 presents an actual set of optimization parameters used with GA based on literature [133, 134]. The parameters used in the algorithm are described as follows: N_{pop} represents initial population, N_{elites} represents population of elites which go directly to the next generation, N_{mut} represents the population which are randomly selected for mutation, μ represents the probability rate of mutation, N_{pairs} represents the selecting parents for mating, and *iterations* describe the stopping criteria for termination.

The L-BFGS-B algorithm requires the evaluation of the objective function and its gradient with respect to the modulus of elasticity. Since the real objective function is unknown, it is approximated by a second order Taylor series around the current design variables. The input arguments for the L-BFGS-B subroutine are the gradient of the objective function with respect to the unknown element elasticity modulus distribution and the functional value at each minimization call. The subroutine then returns with an updated estimate of the parameters and this process is repeated until the change in the objective function is smaller than a specified tolerance. To implement the L-BFGS-B algorithm, an open source Python optimization package was used [78]. The primary objective of the L-BFGS-B algorithm is to calculate gradient of the objective function, which is calculated using finite differentiation [135, 136].

Table 3.1. Parameters of the GA for the three identification tests for the first configuration

PG	N_{pop}	N_{elites}	N_{mut}	μ	N_{pairs}	*Iterations*	*Solution time (Hour)*
1	50	3	8	0.04	28	500	80
2	20	2	4	0.04	14	500	30
3	10	1	2	0.04	7	500	14

3.8 Results and discussion

The proposed technique performs modifications to the corresponding constitutive parameters in the affected regions while maintaining the original geometry. Refinements are comprised of adjustments to stiffness or overall scaling of material constitutive parameters. This approach aligns with constitutive law modifications based on traditional damage-mechanics theory, in which the effective stiffness is diminished based on the history of applied loads [10]. The ultimate goal of this work is not only to diagnose the current geometric description of a structure, but also to predict/project damage evolution of the structure, allowing for accurate evaluation of the capacity of the structural component.

During the optimization process, the properties of each partition are selected as design variables which can be modified iteratively, based on the optimization algorithm. For this study, parameter group 2 (PG2) was selected for the evaluation. For each load step, the results from 3D-DIC and FEA are interpolated onto a common grid, and the error, which is defined as the discrepancy between 3D-DIC and FEA results, is calculated. Then, the design variables are modified according to the optimization algorithm until the results of DIC and FEA are correlated with each other to within a tolerance of 5 percent error. The geometric features (e.g. the features which belong to internal and external defects) of the numerical simulation are iteratively recognized at the end of the optimization process via changes in the constitutive properties of the elements at the corresponding location. The initial FEM is then updated based on the heterogeneous DIC patterns which have evolved over the elastic region of the material to project initial geometric description. The initial geometry of a structure can consist of different features such as holes inside or existing defects. Those features would be expected to yield heterogeneous DIC patterns on the surface, which help to identify those features requiring tuning in the numerical results through the inverse method. During the inverse problem process, the finite elements are modified from the selected initial values to their expected values. If the finite element belongs to a defect (e.g. holes, damaged region etc.), its expected value will be adjusted through the optimization process from an initial value to near zero. All the regions were iteratively modified and updated to mimic the initial projected geometric description implied as the current damage.

3.8.1 Defect detection using simulated experiment

To evaluate the feasibility of the proposed approach using the simulated measurements, a FEM of a coupon specimen with simulated defects was created and analyzed within the elastic range. The objective was to evaluate the feasibility using idealized surface measurements (i.e. full-field strain and displacement measurements) analogous to those derived from a DIC measurements. A corresponding intact coupon model, without any simulated damage, was developed for initialization of the optimization process. Configuration 2 (Figure 2b) was used for this numerical study and the identification process included surface strain and displacement fields (i.e. $\boldsymbol{\varepsilon}_{xx}$, $\boldsymbol{\varepsilon}_{xy}$, $\boldsymbol{\varepsilon}_{yy}$, and $\boldsymbol{\delta}_{yy}$) were used to reconstruct the elastic modulus distribution. Table 2 shows the initial values selected within the feasible range (maximum and minimum values) used as the initial guess for the parameters in the optimization procedure. As shown in Table 2, there are 10 unknown design variables which can be adjusted during the optimization process.

Results from that identification process are also presented in Table 3.2, which demonstrate that the updated elastic modulus is well adjusted using only 20 surface strain and displacement fields for the simulated surface measurements. In Table 2, E_{ADS} stands for Artificially Damages Section (ADS) and E_{IS} stands for Intact Section (IS). To demonstrate performance of the proposed approach, Equation 2 is defined as follows:

$$E_T = \frac{E_{updated} - E_m}{E_m} \times 100 \tag{3-2}$$

where E_m was assumed as 200GPa for the idealized modulus of elasticity of the coupon for A36 steel [4].

The partitions corresponding to the simulated defects, E_1^{ADS} and E_2^{ADS}, exhibit dramatic reductions, 99 and 98.9%, respectively, demonstrating that the defects were recovered properly. Simultaneously, the intact regions all converge to within 1% of the idealized modulus of elasticity. These initial results demonstrated the feasibility of the proposed St-Id approach, prompting further evaluation using the proposed full-field experimental approach.

Table 3.2. Initial, minimum and maximum, updated and target values of the updating parameters for configuration 2

E (MPa)	E_1^{ADS}	E_2^{ADS}	E_1^{IS}	E_2^{IS}	E_3^{IS}	E_4^{IS}	E_5^{IS}	E_6^{IS}	E_7^{IS}	E_8^{IS}
Initial	150,000	180,000	110,000	300,000	220,000	90,000	120,000	50,000	280,000	320,000
min	50,000	50,000	50,000	50,000	50,000	50,000	50,000	50,000	50,000	50,000
max	450,000	450,000	450,000	450,000	450,000	450,000	450,000	450,000	450,000	450,000
Updated	1,122	2,050	199,223	200,776	197,990	201,999	199,001	200,333	200,888	201,992
Expected Value	0.0	0.0	200,000	200,000	200,000	200,000	200,000	200,000	200,000	200,000
E_T (%)	**-99**	**-98.9**	-0.38	+0.38	-0.1	+0.99	-0.49	+0.16	+0.44	+0.99

3.8.2 *Defect detection using experimental 3D-DIC measurements*

To evaluate the performance of the proposed approach, an experimental study was initiated where controlled rectangular zones of artificial damage were machined into the back side of the coupons (i.e. configurations 2-4) to simulate damage on a component (Figure 3.2) that would be unseen from the measurement surface. For the defined configurations, the initial FEMs of the coupons were partitioned into 10 sections and material properties of each partition were considered within the updating process, as inputs into an objective function aimed at the simultaneous local and global system parameter identification. The selection of 10 sections provided a rational selection for this evaluation; however, additional partitioning is feasible, but at an increased computational cost due to an expanded search region within the optimization process. In this work, defects on the unseen side of the model were constrained to locations that aligned with separate partitions, which limits the search space, but ensures that the entire structural component response is considered. The partitions which were considered within optimization process for all the configurations are illustrated in Figure 3.6. It should be noted that E_{ADS} is the acronym for the elastic modulus of artificially damaged section (ADS) and E_{IS} is the acronym for the elastic modulus of intact section (IS). According to the proposed method, after the optimization process, the value of the elastic modulus for the partitions which belong to defects are expected to decrease dramatically to infer the existence of defects in that partition, similar to the observations within the simulated experiments.

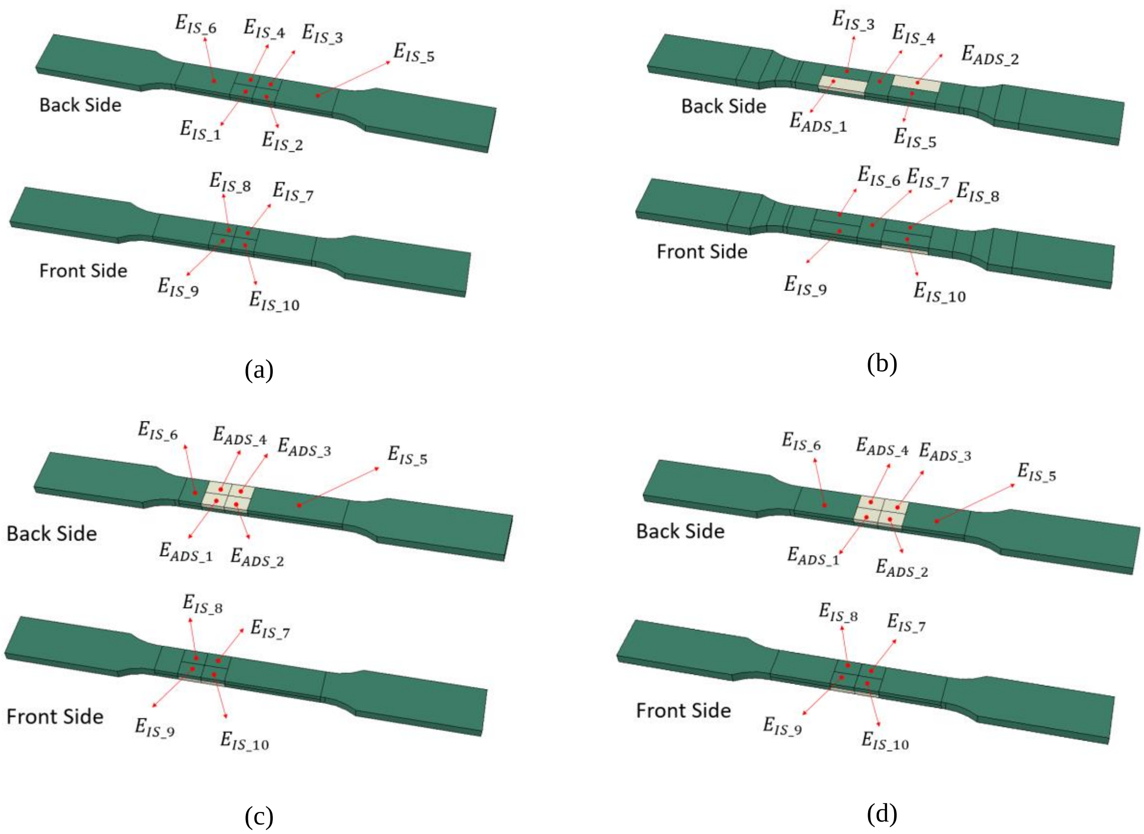

Figure 3.6. Divided partitions of the configurations to import into optimization process, (a) configuration 1, (b) configuration 2, (c) configuration 3, and (d) configuration 4

For comparison of the results, it is necessary to interpolate the results from DIC and FEM on a new defined mesh grid. With both results mapped on a common grid, the discrepancy between FEA and DIC results can be used within the optimization process [42, 104, 131, 132]. Using the proposed hybridized algorithm, the minimization of the objective function was performed for 500 epochs where the first 50 epochs utilized the GA and the optimization process for the remaining epochs were performed using the L-BFGS-B method. It should be noted that the starting point of the L-BFGS-B algorithm is the last optimal point obtained from the GA. The summary of results for the elastic modulus of the selected partitions before and after optimization process for all configurations are illustrated in Table 3.3. As expected, it was observed that the elastic modulus belonging to the defect regions converged to significantly smaller values when compared to the region without any defect features. These results confirmed that the proposed approach was capable of inferring the existence of the defect regions from constitutive property of material properly. The convergence of the objective functions for all the configurations are plotted in the Figure 7. According to the results shown in Table 3 and Figure 3.7, it can be concluded that the proposed approach has the capability of converging to the desired global minimum.

3.8.3 *Optimization efficiency*

As previously noted, the selection of parameters for the hybrid optimization approach were selected based on available literature; however, these parameters have the potential to impact the convergence potential and efficiency. In this section, the performance and efficiency of the optimization parameters presented in Table 3.1 are evaluated using configuration 2 as a case study. In this study, the performance of the sets of the parameters of the GA can be defined as the capability to converge to a rational solution of E at the global minima with efficiency described by the computational cost. An illustration of the solution efficiency is shown in Figure 3.8, which highlights the evolution of the objective function as the design variables converge towards their optimal solutions. As it can be seen, the GA was halted in each case at 50 epochs where an obvious plateau was reached in the objective function and the parameters. After this point, the L-BFGS-B algorithm was initiated which further minimized the objective function and resulted in the final convergence. The results demonstrate that Parameter Group 1 (PG 1) and Parameter Group 2 (PG 2) both exhibit satisfactory performance when compared to Parameter Group 3 (PG 3), but the computational cost for PG 1 is much higher without an efficient improvement in performance such as applying multi-processing procedure in the algorithm and parallelizing the iterations, suggesting that PG 2 is more efficient. It is also worth noting that PG 3 does not converge to the optimal solution, which implies that the solution may be stuck at a local minimum. This outcome highlights the importance of the number of population size, $N_{pop,}$ used in the GA. Parameter Group 2 was deemed the most effective amongst the available parameter options and was selected for further evaluation of the approach based primarily on computational cost; however, a more comprehensive study on optimal parameters may be warranted, but beyond the scope of this investigation.

Table 3.3. Summary of differences between elasticity modulus of the selected partitions before and after optimization process for all the configurations

Configuration 1										
E (MPa)	E_1^{IS}	E_2^{IS}	E_3^{IS}	E_4^{IS}	E_5^{IS}	E_6^{IS}	E_7^{IS}	E_8^{IS}	E_9^{IS}	E_{10}^{IS}
Initial	420,000	160,000	180,000	220,000	120,000	70,000	80,000	110,000	220,000	400,000
Updated	208,998	191114	203,224	195,444	198,001	188001	189,001	196,555	202114	210,012
Expected Value	200,000	200,000	200,000	200,000	200,000	200,000	200,000	200,000	200,000	200,000
E_T (%)	+4.5	-4.4	+1.6	-2.5	-1.0	-6.0	-5.5	-2.0	+1.3	+5.0
Configuration 2										
E (MPa)	E_1^{ADS}	E_2^{ADS}	E_3^{IS}	E_4^{IS}	E_5^{IS}	E_6^{IS}	E_7^{IS}	E_8^{IS}	E_9^{IS}	E_{10}^{IS}
Initial	150,000	180,000	110,000	300,000	220,000	90,000	120,000	50,000	280,000	320,000
Updated Value	6,557	9,122	189,223	208,776	191,990	209,999	189,001	206,333	204,888	209,992
Expected Value	0.0	0.0	200,000	200,000	200,000	200,000	200,000	200,000	200,000	200,000
E_T (%)	**-96.0**	**-95.0**	-5.5	+4.4	-4.0	+5.0	-5.5	+3.3	+2.5	+4.5
Configuration 3										
E (MPa)	E_1^{ADS}	E_2^{ADS}	E_3^{ADS}	E_4^{ADS}	E_5^{IS}	E_6^{IS}	E_7^{IS}	E_8^{IS}	E_9^{IS}	E_{10}^{IS}
Initial	110,000	250,000	130,000	290,000	180,000	60,000	220,000	180,000	250,000	420,000
After	7,445	8,445	9,984	8,554	189,222	179,000	208,000	191,224	206,002	210,111
Ideal	0.0	0.0	200,000	200,000	200,000	200,000	200,000	200,000	200,000	200,000
E_T (%)	**-96.0**	**-95.7**	**-95.0**	**-95.7**	-5.5	-10.5	+4.0	-4.4	+3.0	+5.0
Configuration 4										
E (MPa)	E_1^{ADS}	E_2^{ADS}	E_3^{ADS}	E_4^{ADS}	E_5^{IS}	E_6^{IS}	E_7^{IS}	E_8^{IS}	E_9^{IS}	E_{10}^{IS}
Initial	170,000	220,000	280000	130,000	100,000	140,000	220,000	170,000	70,000	150,000
Updated Value	11,224	8,225	9,879	5,469	181,003	195,224	211,225	194,225	179,887	190,336
Expected Value	0.0	0.0	200,000	200,000	200,000	200,000	200,000	200,000	200,000	200,000
E_T (%)	**-94.0**	**-95.9**	**-95.0**	**-97.0**	-9.5	-2.4	+5.5	-3.0	-10.5	-5.0

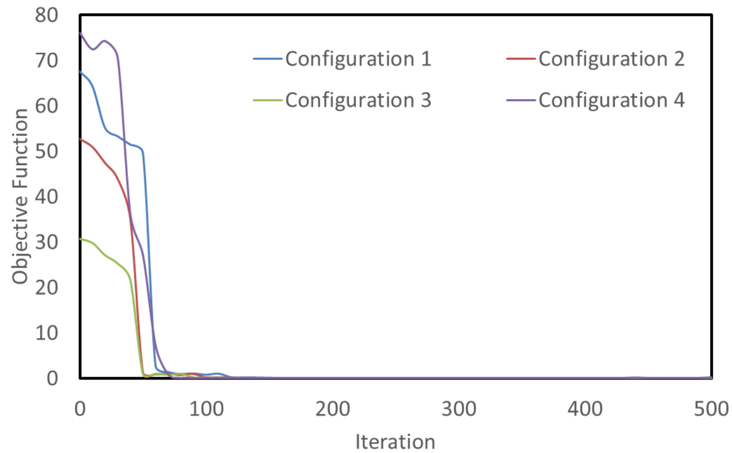

Figure 3.7. The convergence of the objective function for the defined configurations

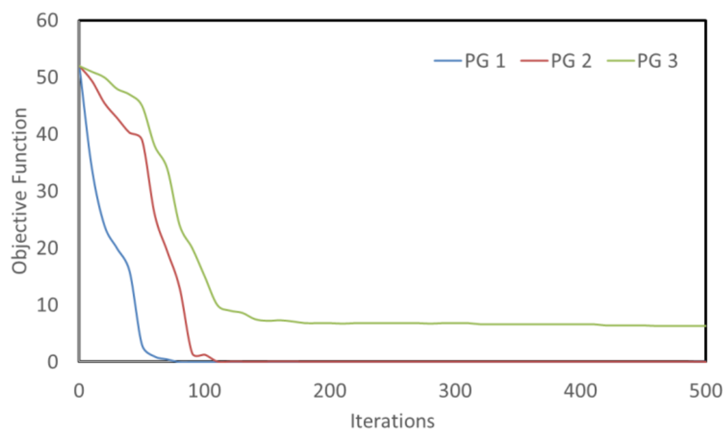

Figure 3.8. Convergence of the objective function with different sets of parameters for the GA

For configuration 2, the optimization convergence of the objective function and elastic modulus of the partitioned sections are shown in Figure 3.9a – b. In the first step of the optimization process, the objective function was reduced from 52 to 43 during the optimization process. In the second step of the optimization process, the objective function was reduced from 43 to 0.2 during the optimization process. Moreover, in order to show the superiority of the new proposed algorithm, the optimization process was conducted for three separate cases for 500 epochs: 1) only GA was used for optimization, 2) only the gradient-based algorithm was used for optimization and 3) Hybridized Genetic Algorithm (HGA) was used for optimization. As seen in Figure 3.9a, using the proposed hybrid algorithm, the objective function has decreased more than the two base algorithms when applied alone. This demonstrates the efficiency of the hybridized optimization scheme in reducing the objective function. Moreover, the initial values and corresponding optimized solutions illustrated in Figure 3.9c show proper convergence of the initial values toward their expected solutions. It should be noted that for each partitioned section, a different initial value was selected to show the capability of the proposed method in converging to the expected target value accordingly regardless of the starting point. As can be seen from Figure 3.9b – c, even though initial design variables are different, their final updated values converged to the correct expected target value properly.

The full-field strain measurements from DIC and FEA, along with the absolute error, before and after model updating, are shown in Figure 3.10 where the initial FEM yields distinctly different contour patterns for the longitudinal strain than the experimental response, but following convergence to the final solution, the patterns nearly mirror each other. Through this convergence, the error, which describes the differences between the model prediction and experimental results, drops an order of magnitude from the initial prediction.

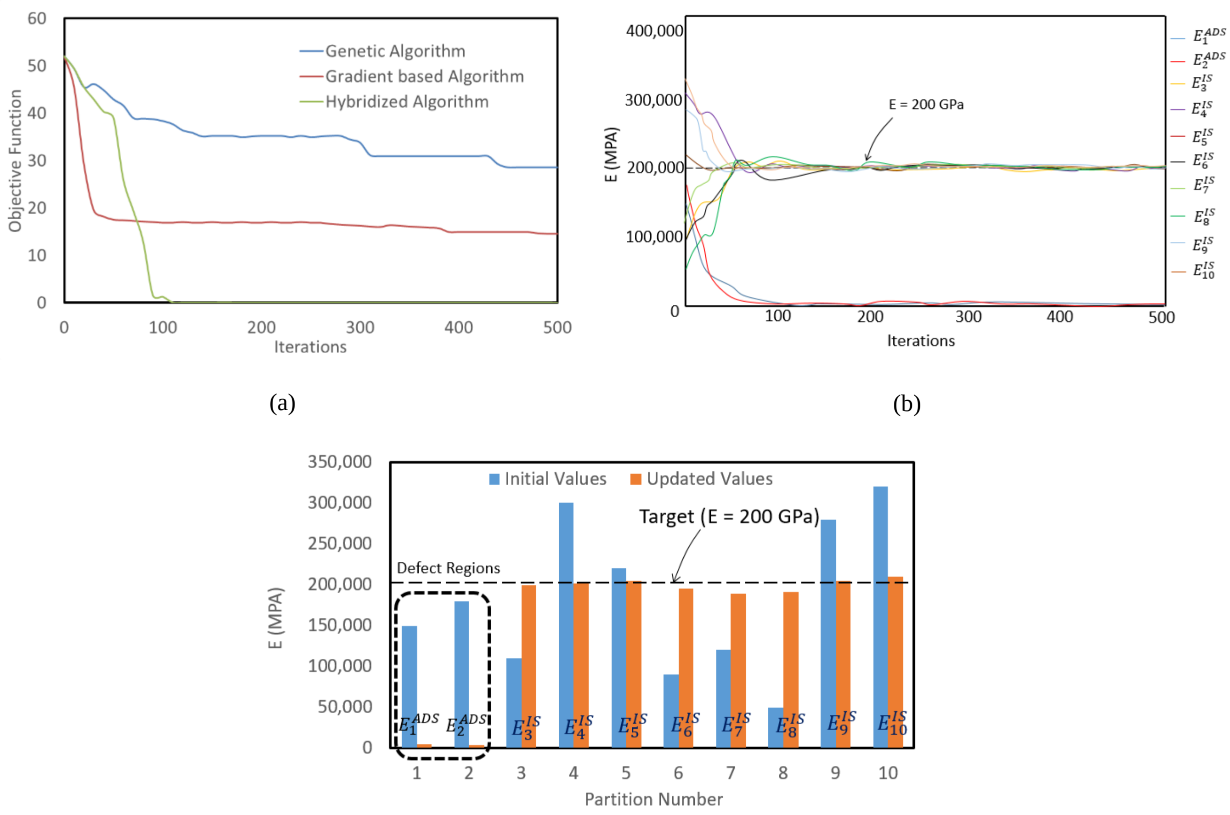

(a) (b)

(c)

Figure 3.9. Objective function convergence for different optimization algorithms, (b) elasticity modulus convergence, and (c) initial and final values of design variables

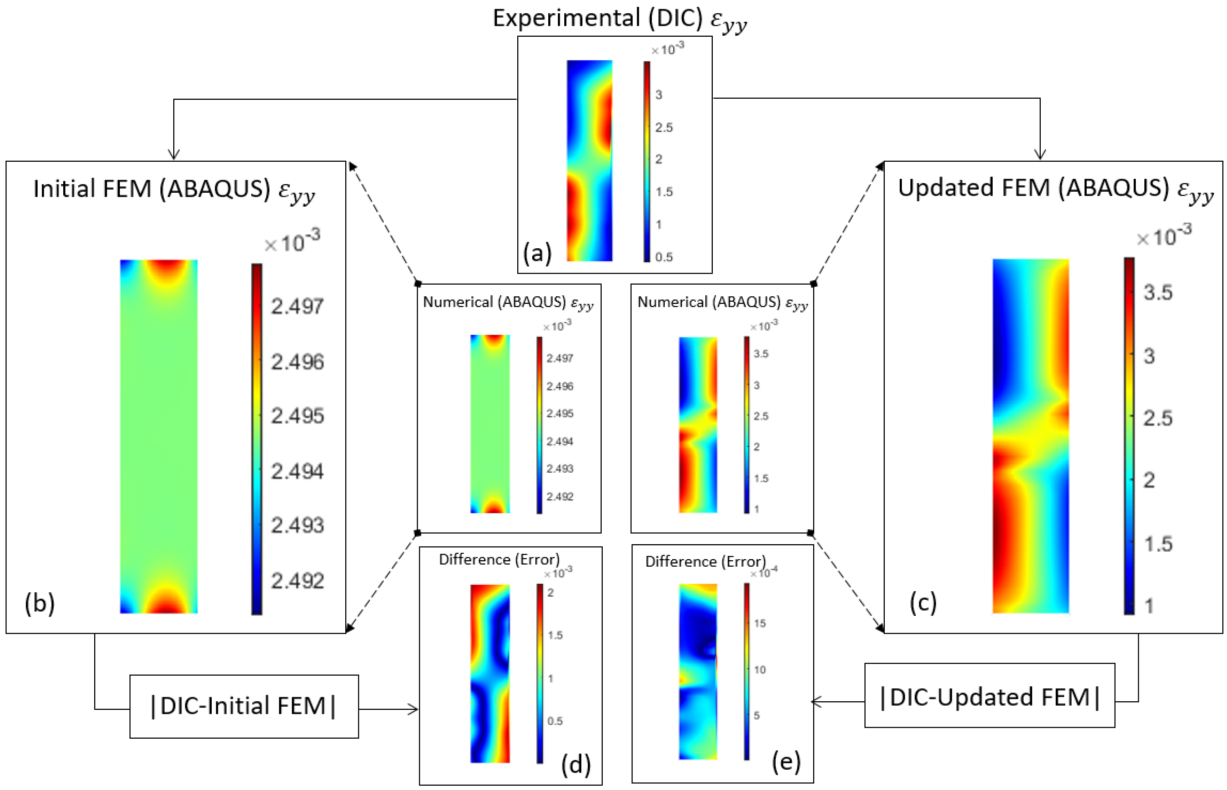

Figure 3.10. Full-field measurements obtained from DIC and FE, along with the absolute error, before and after model updating (a) 3D-DIC results, (b) initial finite element results, (c) updated FEM, (d) the error between DIC and initial model, and (e)

3.8.4 Optimization robustness

Many optimization problems have multiple optima, i.e. non-unique solutions. The non-convexity typically means that several different local minima (which is what the gradient-based algorithms locates) and different solutions to the same discretized problem can be found when choosing different starting solutions and different parameters of the algorithms. Global optimization methods seem to be unable to handle problems of the size of a typical inverse problem with a large number of design variables; however, it is important to observe that most problems in inverse techniques are not convex. In this work, additional results derived from the use of multiple load steps increments (i.e. 20 load step) were used to strengthen the convergence and ensure the uniqueness of the solution. To investigate the robustness of the method and ensure the results were not sensitive to and dependent on the initial values, a series of iterations with different initial values were performed (Table 3.4). The values of the E_1^{ADS}, E_2^{ADS} and E_3^{IS} were used to evaluate the optimization performance with their convergence trends plotted in Figure 3.11. As can be noted from Figure 3.11a – c, even though the initial points are selected randomly for the 4 different initial sets, the proposed algorithm consistently converges to the optimal values. Also, the initial values and corresponding optimized solutions for different sets of initial scenarios are illustrated in the Figure 3.12. As shown in Figure 3.12, even though the initial values are selected randomly, the proposed approach is able to converge towards unique and consistent solutions accordingly. A summary of the initial design variables and their corresponding optimized solutions for the different initial configurations are presented in Table 3.4 for reference.

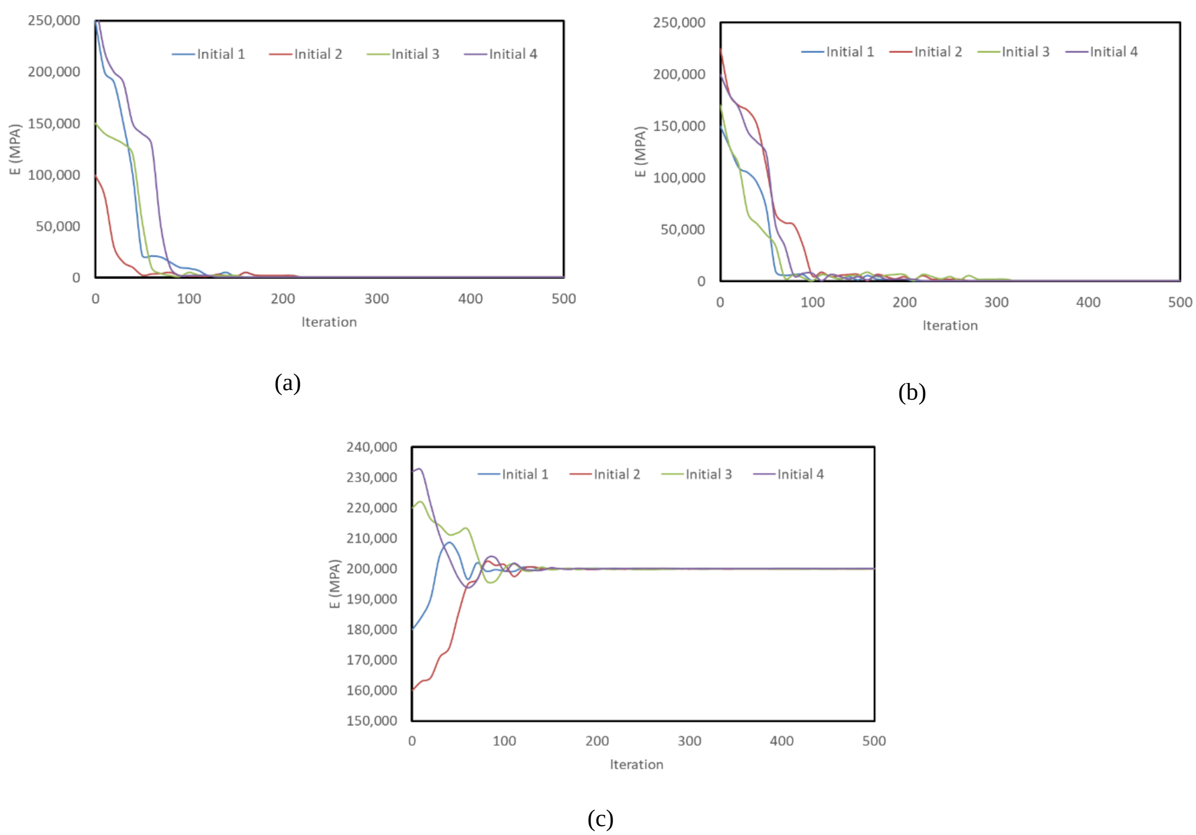

Figure 3.11. Initializing the optimization procedure with different start point (a) the convergence of E_1^{ADS}, (b) the convergence of E_2^{ADS}, and (c) the convergence of E_3^{IS}

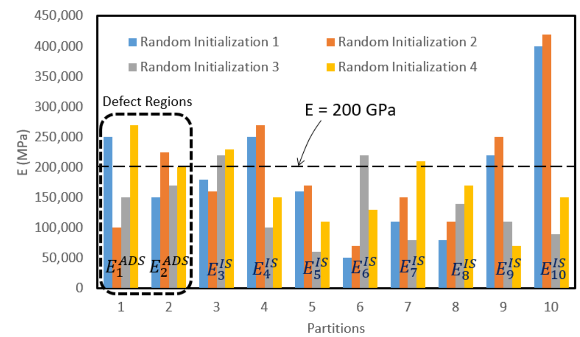

(a)

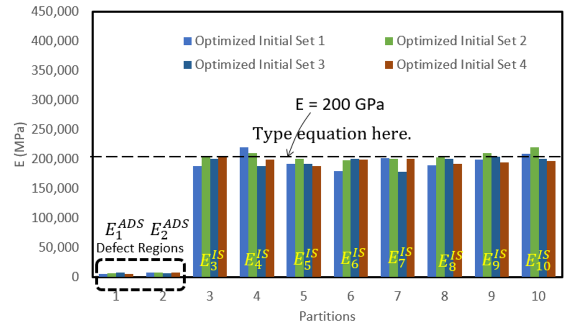

(b)

Figure 3.12. Comparison of initial and final properties for partitions within CF2 (a) initial properties, (b) final properties

Table 3.4. Summary of elastic modulus convergence for selected partitions for different parameter initializations (Config. 2)

Initial set 1										
E (MPa)	E_1^{ADS}	E_2^{ADS}	E_3^{IS}	E_4^{IS}	E_5^{IS}	E_6^{IS}	E_7^{IS}	E_8^{IS}	E_9^{IS}	E_{10}^{IS}
Before	250,000	150,000	180,000	250,000	160,000	50,000	110,000	80,000	220,000	400,000
Updated	5,445	7,889	188,811	220,110	192,001	180,330	202,001	190,111	200,002	209,002
Expected	0.0	0.0	200,000	200,000	200,000	200,000	200,000	200,000	200,000	200,000
E_T (%)	**-97.0**	**-96.0**	-5.6	+10.0	-4.0	-9.8	+1.0	-5.0	+0.0	+4.5
Initial set 2										
E (MPa)	E_1^{ADS}	E_2^{ADS}	E_3^{IS}	E_4^{IS}	E_5^{IS}	E_6^{IS}	E_7^{IS}	E_8^{IS}	E_9^{IS}	E_{10}^{IS}
Before	100,000	225,000	160,000	270,000	170,000	70,000	150,000	110,000	250,000	420,000
Updated	7,700	8,098	203,033	210,222	200,332	199,003	201,000	203,003	210,993	220,223
Expected	0.0	0.0	200,000	200,000	200,000	200,000	200,000	200,000	200,000	200,000
E_T (%)	**-96.0**	**-95.9**	+1.5	+5.1	+0.2	-0.5	+0.5	+1.5	+5.5	+10.0
Initial set 3										
E (MPa)	E_1^{ADS}	E_2^{ADS}	E_3^{IS}	E_4^{IS}	E_5^{IS}	E_6^{IS}	E_7^{IS}	E_8^{IS}	E_9^{IS}	E_{10}^{IS}
Before	150,000	170,000	220,000	100,000	60,000	220,000	80,000	140,000	110,000	90,000
Updated	8,955	6,773	200,322	188,555	192,222	200,433	179,007	201,222	205,055	200,443
Expected	0.0	0.0	200,000	200,000	200,000	200,000	200,000	200,000	200,000	200,000
E_T (%)	**-95.0**	**-96.6**	+0.2	-5.7	-3.9	+0.2	-10.5	+0.6	+2.5	+0.2
Initial set 4										
E (MPa)	E_1^{ADS}	E_2^{ADS}	E_3^{IS}	E_4^{IS}	E_5^{IS}	E_6^{IS}	E_7^{IS}	E_8^{IS}	E_9^{IS}	E_{10}^{IS}
Before	270,000	200,000	230,000	150,000	110,000	130,000	210,000	170,000	70,000	150,000
Updated	5,445	7,889	204,444	199,994	188,444	199433	200,345	192,022	195045	197,331
Expected	0.0	0.0	200,000	200,000	200,000	200,000	200,000	200,000	200,000	200,000
E_T (%)	**-97.3**	**-96.0**	+2.2	-0.0	-5.8	-0.3	+0.2	-3.9	-2.5	-1.3

3.8.5 *Experimental validation*

Once internal defects inside a component are detected using the proposed image-based tomography method, the updated model, which includes the detected defects, should be able to describe future behavior of the component under future loads. To evaluate the updated model under new loads, the numerical model of the coupon was used to predict strain measurements for comparison with DIC results (Figure 3.13). The new loading included a displacement-controlled tensile load applied using the testing machine as a separate test from those used in the updating process. Again, configuration 2 was used as the defective test specimen for this validation. Table 3.5 shows the comparison of strains at six selected regions of the specimen with those predicted using both the initial and updated models at the load level of 40 percent of the yielding load. This table shows a very good agreement (<10% maximum difference) between strains from the updated model and the experimental results. As expected, the error between the experimental and numerical values decreases significantly when using the updated model compared with the initial model. This verifies the effectiveness of the proposed approach in extracting the true properties of a component, which can be used for more realistic prediction of its response under future loads.

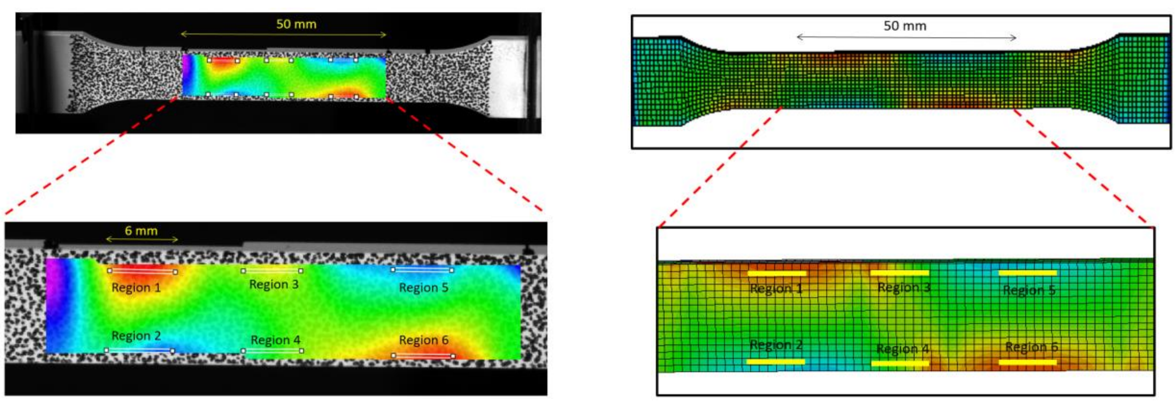

(a) (b)

Figure 3.13. Prediction correspondence between experimental and undated numerical results (a) 3D-DIC results at load level of 40% of yield, (b) FEMing results at load level of 40% of yield

Table 3.5. Longitudinal strain comparison of the experimental results with initial and updated model predications at 40% of yield stress (CF 2)

Selected Regions	Initial Model (με)	|DIC-Initial|/DIC (%)	Updated Model (με)	|DIC-Updated|/DIC (%)	DIC results (με)
1	655	41.9	987	**12.5**	1,128
2	744	66.0	412	**8.0**	448
3	698	25.0	887	**5.4**	938
4	877	15.0	702	**7.8**	762
5	698	60.0	392	**10.0**	436
6	790	33.0	1,102	**7.0**	1,185

3.9 Conclusion

The purpose of this preliminary investigation was to evaluate the feasibility of leveraging full-field measurements for St-Id, with a goal of recovering the volumetric interior defect distribution in structural components. Within this image-based tomography framework, steel coupon specimens with simulated defects were used to evaluate the performance of the St-Id approach that utilized an inverse approach to identify unknown and uncertain constitutive properties of the material based on full-field deformation measurements correlated with finite element predictions.

DIC was utilized to extract full-field deformation measurements of the test specimen, subjected to standard ASTM E8 tension testing, with the measurements collected of only the intact surface (i.e. simulated defect unseen by the cameras). The corresponding FEMs of the specimens were divided into a set of regions with uniform modulus of elasticity, each of which had random initial stiffness values. To establish the FEMU scheme, the ABAQUS solver was interfaced with an optimization package and the unknown parameters were adjusted iteratively until finding the optimal values. The optimization strategy leverages a GA to perform the global search and a limited-memory Broyden-Fletcher-Goldfarb-Shanno scheme for the local search for the optimal solution parameters. As a result of the optimization process, all of the intact regions converged to elastic modulus close to expected value of 200 GPA for A36 steel, with the exception of the notch regions that showed a dramatic reduction in elastic modulus, which approached the expected value of zero for a void. These outcomes demonstrated the ability of the proposed image-based tomography framework to identify internal defects in the form of anomalies in material constitutive properties. Moreover, to evaluate the uniqueness of the solution of the proposed approach, different sets of initial values were selected to show the insensitivity of the results to the selected initial values. The results showed that, even though the initial points were selected randomly for the 4 different sets, the proposed algorithm had the capability to converge to the optimal values.

The results of this preliminary investigation and the ability of the proposed method to detect internal abnormalities hint at the possibility of determining not only the material distribution of a specimen, but also determining the location, dimensions, and shape of the defect. The results of this paper are encouraging and may open up new opportunities to characterize heterogeneous materials for their mechanical property distribution.

4 CHAPTER 4 – Subsurface Condition Assessment and Structural Health Monitoring of Structures Using Digital Image Correlation and Topology Optimization

Mehrdad S. Dizaji, Mohamad Alipour, Devin K. Harris

"Dizaji, M. Shafiei, M. Alipour, and D. K. Harris. " Subsurface Condition Assessment and Structural Health Monitoring of Structures Using Digital Image Correlation and Topology Optimization ", to be submitted."

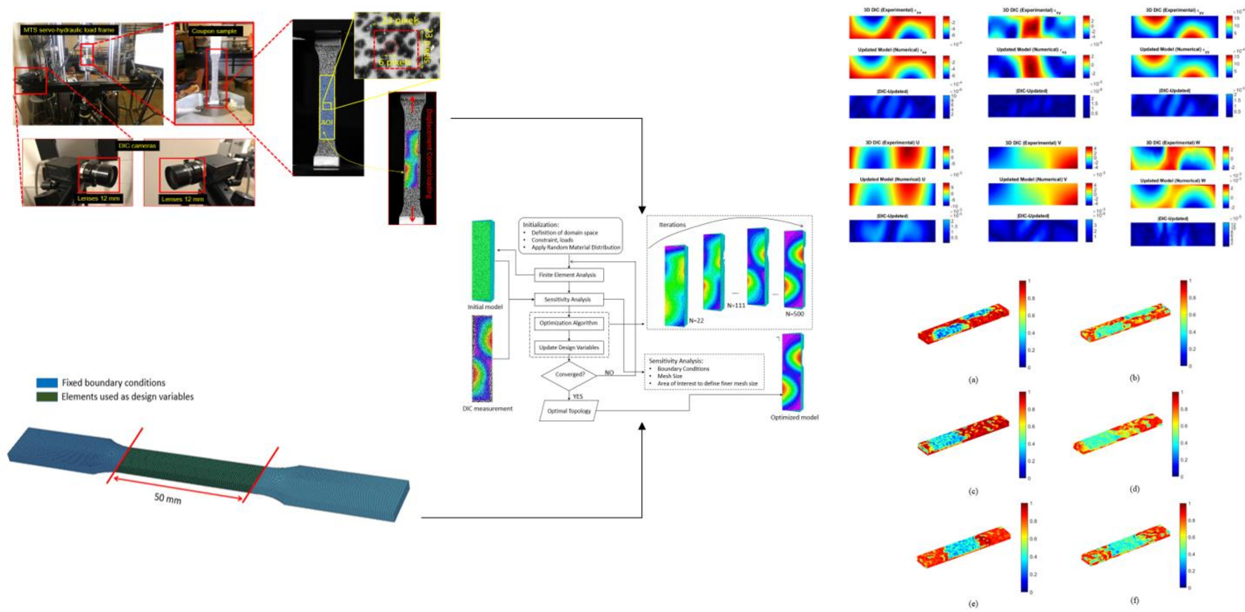

4.1 Abstract

Detecting subsurface defects in structural members is a challenging yet important part of condition assessment of structures. Existing methods in this regard are either based on NDE/T, or SHM concepts. NDE/T methods suffer from the need for expensive equipment usually based on wave propagation or radiation imaging. Damage detection based on SHM usually relies on global vibration response which has proven successful in informing the existence and sometimes coarse-grained location information about damage, but is fairly limited in reconstructing the 3D shape of internal damage. This paper proposes to leverage full-field response data obtained by DIC in a topology optimization

framework to reconstruct the internal damage in members. In other words, this paper shows how perturbations in the observable full-field surface measurements can be used as a proxy to detect the unobservable internal abnormalities.

An initial FEM of the structure is first created to discretize the member into elements whose constitutive properties (e.g. modulus of elasticity) are treated as unknowns in the optimization problem. The goal of the optimization is to minimize the differences between the observed full-field response measured experimentally using DIC, and that computed numerically using the model. To that end, an objective function is computed by interpolating both responses onto a common grid and summing up the residuals on relevant response terms, which was then pushed to a minimum via the method of moving asymptotes (MMA) as the optimization algorithm.

The framework was evaluated on a series of simulated and real-world experiments using steel coupon specimens with artificially manufactured defects. Results show that the proposed method is capable of detecting and reconstructing location extent, and shape of the damage with average F1-scores of 82.8% and 69.6% on simulated and real experiments, respectively. Furthermore, a detailed sensitivity analysis demonstrated the effect of various factors on the performance of the proposed approach, including different optimization starting points, defect severity, sensing density, and discretization density. Results from this have demonstrated that the proposed method is successfully able to extract detailed internal damage information that is otherwise expensive and difficult to achieve with state-of-the-art methods and can therefore be used as a promising subsurface damage detection method.

Keywords*:* Topology Optimization, 3D-DIC, Full-field measurement, Image based Tomography, Method of Moving Asymptotes (MMA), Optimization, Interior defects, SHM, St-Id.

4.2 Introduction

Growing concerns over the state of health of the increasingly aging infrastructure have prompted the development of condition assessment methods for existing structures. While a myriad of innovative methods has been proposed to automate and facilitate the detection of externally *visible* defects in structural inspections [137-141], accurate identification of *internal* factors such as material constitutive properties, structural conditions (e.g. boundary conditions), and internal damage and deterioration mechanisms is equally important, if not more so, in ensuring the safety and integrity of infrastructure. In this regard, identifying unknown material and structural properties and detecting damage in existing structures and constructed facilities has been a focus of significant attention in the research community [142]. Numerous innovations in the fields of nondestructive evaluation and testing (NDE/T) and SHM have been developed over the last decades. NDE/T techniques have been proposed that primarily leverage principles of wave propagation or radiation imaging in elastic solids [143]. Some of such methods include impact echo (IE), electrical resistivity (ER), ground-penetrating radar (GPR), half-cell potential (HCP), ultrasonic surface waves (USW), ultrasonic testing (UT), impulse response (IR), and infrared thermography (IRT). As the names of the methods imply, this approach relies upon specialized equipment and sensors, and the literature indicates a number of reliability and interpretability challenges for them [122, 125]. As an alternative strategy, SHM approaches rely on structural sensing to monitor and infer the state of structural health. These approaches typically employ model-based [144-146] or data-based [147-150] techniques to identify anomalies in mechanical response that point to underlying damage. While the use of global dynamic response [147] or a set of isolated strain and deformation response points [148] has been relatively successful in providing information about coarse-grained damage indication, the degree to which material or damage properties can be extracted has been limited. For example, using modal response for damage detection requires a minimum severity of damage to noticeably affect the measured response. On the other hand, using a discrete set of sensing points (e.g. strain gages) requires prior knowledge of the behavior to decide and optimize the sensor installation locations, and a series of works have been dedicated to studying the optimum sensor locations for damage detection [151-154]. Furthermore, even when the discrete sensor network is optimized, it may not provide sufficient sensing resolution to reconstruct damage [155]. While both NDE/T and SHM strategies have proven relatively successful for many scenarios, there are still many shortcomings that cannot be readily addressed without highly sophisticated equipment or costly monitoring systems. As such, there is an opportunity space for new approaches that enable the detection of such subsurface properties and modes of deterioration in a cost-effective and non-invasive manner.

One of the highly promising approaches to extracting such internal information is through solving an inverse problem, where observed experimental response and the rules of physics governing the problem are used to infer the underlying causal properties and damage responsible for the observed response. An inverse engineering solution for St-Id aims to reconstruct and recover structural unknowns (e.g. material properties, boundary conditions, and damage), given knowledge of interior and exterior deformation fields such as displacement/strain fields and boundary conditions. This information can be obtained by means of a variety of sensing equipment that measure the mechanical response of the structure under external loading. One of the primary ways to solve the inverse problem is through FEMU, where a FEM model is iteratively fine-tuned until it can closely replicate the observed experimental response [156]. This is usually achieved by formulating the model tuning as an optimization problem that minimizes the residual between the ground truth observations and the predicted numerical counterparts. A successful inverse solution, therefore, depends on the adequacy of the response used for tuning the model, and the optimization scheme employed. Traditional St-Id and damage detection literature usually leverages experimental or operational observations in the form of global dynamic response (e.g. natural frequencies, mode shapes, damping ratios) usually captured via accelerometers [46], or local quasi-static strain and deformation response obtained from point sensors (e.g. strain gages) [45]. However, it has been shown that the limited sensing resolution provided by discrete point sensors, while useful to detect the existence of damage, may not be not sufficient for fine-grained damage localization and quantification [9, 22, 157, 158].

In response, the use of a substantially finer and richer representation of local strain and deformation response in the form of full-field surface measurements captured via DIC has been recently studied as a damage detection method. Tools such as DIC have the potential to provide decision-makers with a comprehensive assessment tool to better describe the performance of SHM network while also being non-invasive and data-rich.

LeBlanc et al. used 3D-DIC measurements of the surface of a large-scale composite wind turbine blade and observed good agreement between observed strain amplification and curvature discontinuity in DIC results with the location of cracks previously detected in visual inspections [28]. However, this work did not use the full-field information for updating a model or estimating unknown parameters.

This paper proposes a new approach using full-field surface measurements coupled with topology optimization to localize and reconstruct the 3D shape of unseen subsurface defects. Therefore, this paper aims to demonstrate that unlike a limited set of discrete sensing data points or global dynamic properties, the rich data from full-field image-based measurements can enable the identification of a more detailed picture of the internal defects. Furthermore, this work demonstrates how perturbations in the observable full-field surface measurements can be used as a proxy to detect the unobservable internal abnormalities. In this work, 3D-DIC is used to measure the full-field surface deformation and coupled within a topology optimization schema to identify and reconstruct unseen three-dimensional damage. The following subsections briefly describe 3D-DIC and topology optimization, but more comprehensive reviews of these topics are available in the literature. The following section describes topology optimization as the process used to reconstruct such internal features from full-field sensing data.

4.3 3D Digital Image Correlation Technique (3D-DIC)

3D-DIC is a well-established technique in the field of experimental mechanics and works by comparing digital photographs of a component or test piece at different stages of deformation and or tracking (via pattern correlating algorithms) pattern deformations between images. Through this pattern matching and process, the technique is able to describe full-field surface measurements of displacement and strain, analogous to the types of results derived from a FEM [16-21]. DIC builds on the fundamental principles of photogrammetry and provides a mechanism to quantify full-field surface deformation from a series of sequential images of a specimen subjected to loading. Surface displacement data, which can be transformed into strain via post-processing, is derived by correlating patterns within an image and comparing sequential pairs of digital images taken before and after the deformation [22-27]. This process involves a template matching and tracking scheme in which images taken from the surface of a loaded specimen are split to fine grids which act as reference templates. A search process attempts to find a match for each template in the subsequent image by maximizing the correlation of patterns of pixels, thereby determining the movement of points on the surface of the specimen. The tracking of these movements in the images throughout the loading provides the full-field surface deformation, from which other structural responses can be calculated. The DIC technique can be deployed using a single camera to quantify planar surface deformations (2D-DIC), or configured for three-dimensional surface deformation (3D-DIC) by using stereo-paired cameras (Figure 4.1).

Stereo-vision is a well-established problem in computer vision that involves triangulation and correspondence between images from different vantage points from which depth information can be recovered. Stereo calibration is a major part of the 3D-DIC process and determines the intrinsic (e.g. focal length) and extrinsic properties (relative location and orientation) of the system of cameras. Images can be derived from a variety of sources (e.g. CCD, DSLR, etc.) with the choice of camera and lens configuration influenced by factors such as camera noise, lighting, acquisition speed, and geometric relationships between area of interest and field of view. A comprehensive treatment of DIC is not presented in this paper, but is available in the literature [16, 20, 22, 70, 72, 77, 102, 159, 160].

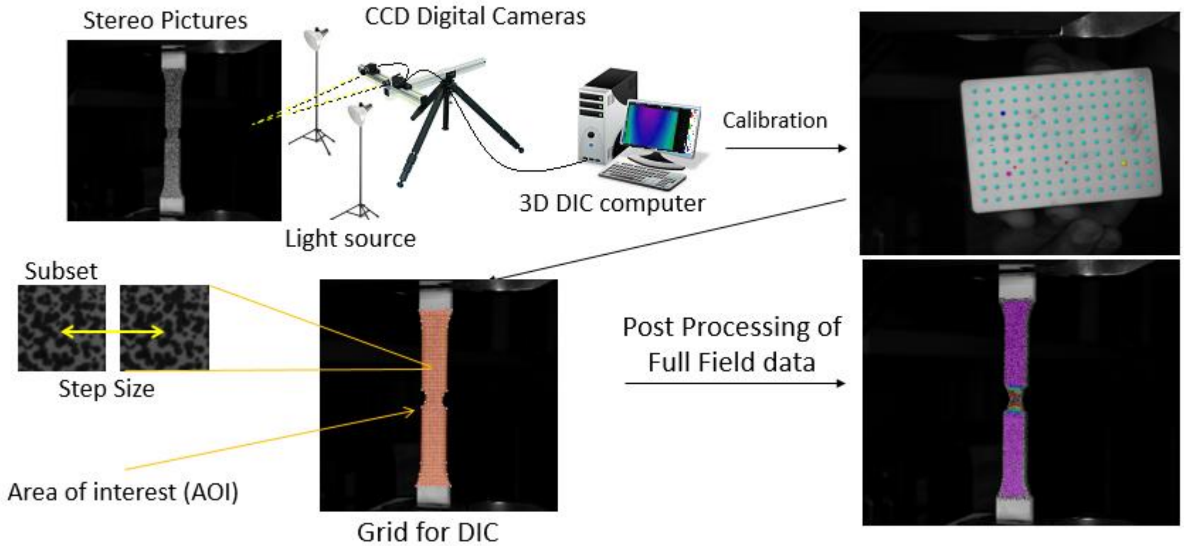

Figure 4.1. Schematic of the process of using 3D-DIC for structural response sensing including data acquisition and processing

4.4 Topology Optimization

Topology optimization (TO) is a mathematical framework that seeks to find the optimum structural layout and material distribution under a set of loading scenarios, boundary conditions and constraints. This approach is effective for finding the optimum design of a structure, which can be defined as one with the minimum weight or alternatively minimum compliance with a fixed material weight. A topology optimization problem usually starts with a preliminary FE model whose performance is evaluated and is iteratively fine-tuned to optimize the desired performance. In the case of structural design, once the component is discretized into a mesh of finite elements, the material constitutive properties of each element can be treated as the unknown variables of the problem. The optimization can be solved using a number of different techniques including gradient-based methods such as the optimality criteria algorithm and the Method of Moving Asymptotes [161], or non-gradient-based algorithms such as Particle Swarm Algorithms or GAs.

While the two problems of structural design and condition assessment and damage detection are usually regarded as different problems with contracting objectives (creating a new structure versus evaluating an existing one), they are fundamentally similar in their use of structural mechanics to correlate structural properties to the observed response. This paper argues that the condition assessment and damage detection problem can be reformulated as a topology optimization problem by considering the sensing data as an additional constraint. It follows that damage and defects in the existing structure being evaluated will be reproduced as cavities or soft regions within the optimized structure. A close look at the literature shows that there are a few examples of the use of topology optimization in damage detection problems, most of which use global frequency response. A closer look at the relevant literature shows that a few papers have used the topology optimization framework for structural damage detection. Using element-based topology optimization methods, Lee et al. utilized the Methods of Moving Asymptotes (MMA) to minimize discrepancy between some points of frequency response functions of the model and the real structure [162]. Nishizu et al. also exploited topology optimization to identify defects based on natural frequencies and by using MMA [163]. Recently, a level set based approach was proposed by Zhang et al. to find the location of damages again by considering natural frequencies [164].

Niemann et al. work focused on the development of a damage detection and localization tool using topology optimization approach [39]. The approach was based on the correlation of a local stiffness loss and the change in modal parameters due to damages in structures. The loss in stiffness is accounted by the topology optimization approach for updating undamaged numerical models towards similar models with embedded damages. In the process of experimental validation, their method could localize separate damage zones, but the results become less clear and the optimization might get stuck in wrong local optima regarding the results of CT-Scans of the specimens. But it can be assumed, that the poor results for some of their cases follow from the lack of constraint data and not taking into account stain and displacement data into their optimization process [165].

4.5 Research Significance

This paper investigates the use of full-field structural response (e.g. strains and deformations) in a structural component obtained by the DIC technique within a topology optimization framework to detect, locate, and reconstruct internal defects. In this framework, strain and deformation patterns perturbed by the existence of subsurface defects guide the reconstruction of the underlying material distribution that is responsible for the observed response patterns. To the best of the authors' knowledge, this paper is the first to use full-field strain and deformation response using DIC within a topology optimization framework to detect and reconstruct the 3D shape of the defect. The main contributions of this paper can thus be summarized as:

- Unlike NDE/T techniques which rely on specialized sensing equipment (e.g. radars or radiation-based scanners, etc.), the proposed method used cameras coupled with structural mechanics to infer subsurface conditions.
- The proposed method leverages the rich full-filed response data from DIC to enable the reconstruction of the 3D shape of damage, representing an advancement over current practice which has been limited primarily to identification and basic localization.
- The sensitivity analysis performed in this paper studied the effect of different parameters such as sensing density and optimization starting points on the damage detection performance of the proposed method. It was shown that enhancing the sensing density increased the detection ability of the approach. This proves the value of using full-field DIC sensing data compared with a limited set of discrete point mechanical sensor in reconstructing the detailed shape of internal damage. Also, the proposed approach was exhibited to converge to indistinguishable detection results with a series of several different random starting points.

While the capability and promise of the proposed technique is shown in this paper, it should be noted that in order to detect damage in a large structural component, large areas may need to be subject to the surface preparation required for DIC, and multiple sets of cameras may be required to cover the area of interest. However, the DIC technique has been shown to continue to be effective in relatively large components, such as a wind turbine blade designed and tested by a team led by Sandia National Laboratories and manufactured by TPI Composites Inc. [166]. Furthermore, for very large components, a multi-step procedure can be followed which starts by locating the vicinity of the damage using traditional global-response methods, and then using the proposed technique to obtain a fine-grained and detailed view of the internal damage.

4.6 Proposed Approach

The hypothesis of this work centers on the premise that internal defects can be delineated and inferred in terms of the distribution of material constitutive properties such as elastic modulus throughout the component. In other words, an internal void, crack, or delamination in a structure can be represented by a region with reduced elastic modulus, which will reflect in the form of disruptions to the strain and deformation fields once the model is analyzed under loads. The mechanism employed herein to identify such internal defects are therefore informed by an image-based measurement approach which takes advantage of the heterogeneous characteristics of surface strains during loading to deduce internal properties (e.g. geometric features or defects) of the structure. Full-field surface deformation measurements derived from 3D-DIC have the potential to reveal unseen anomalies within a solid body while also being non-invasive and data-rich. The full-field data derived from 3D-DIC provides an advantage over discrete sensing as the measurement approach aligns with the continuum features of a numerical model.

Figure 4.2 shows this concept, using a tensile test of four similar steel coupon specimens with different artificially manufactured defects on the backside to mimic damaged regions. The selected deformation responses clearly illustrate that subsurface defects (or unseen defects) perturb the surface strain and deformation fields on the observed surface, and that the quantitative comparison of the uniform responses of the intact specimen with the perturbed fields of a defective sample can signify the potential for an underlying abnormality.

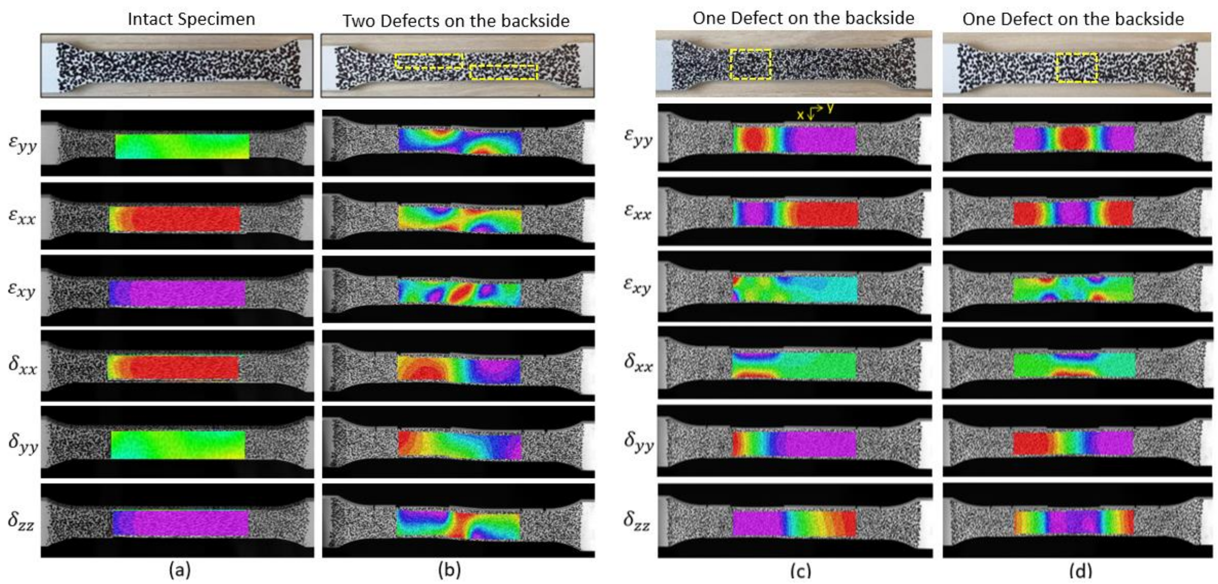

Figure 4.2. Qualitative strain and deformation patterns generated using DIC for coupon specimens with different defects under uniaxial tensile loads: (a) without any defect, (b) with two defects on the back side, (c) with one defect on the back side on the

This paper proposes to leverage these full-field response patterns measured using DIC to reconstruct potential internal damage. In this framework, DIC provides a rich data set for evaluation when compared to physical sensors, and the full-field measurement derived from DIC provides a mechanism for performing multi-objective optimization to identify unknown internal stiffness distribution. Figure 4.3 illustrates the proposed optimization process. This process starts with an initial FEM model that is constructed based on nominal observable properties of the component and without any prior knowledge of potential internal abnormalities. The residual between the full-field DIC response and that predicted by the initial model will then be pushed to a minimum in an optimization process by fine-tuning the initial model. During the optimization process, the properties of each element (e.g. modulus of elasticity) are selected as unknown parameters, and will be iteratively fine-tuned until a convergence criterion is satisfied. Once the optimization converges, the final modulus of elasticity distribution of the model will be used to decide the locations of internal damage by interpreting areas of low stiffness as internal damage.

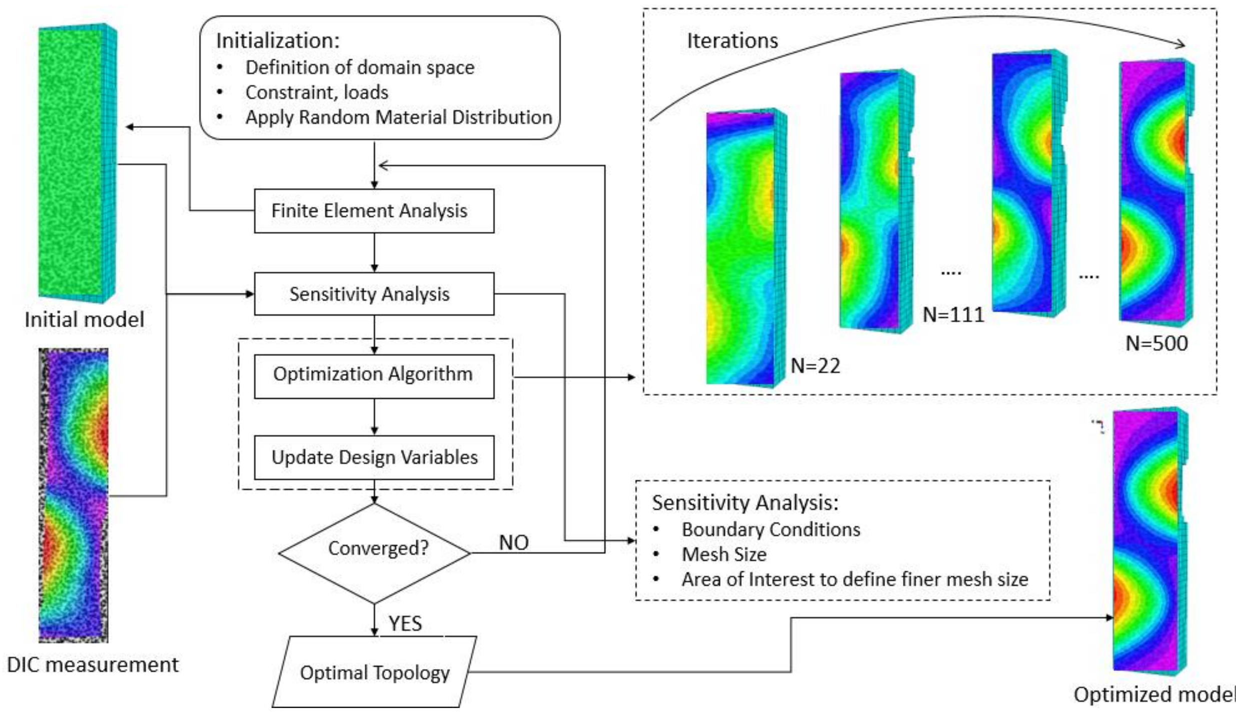

Figure 4.3. Flowchart represents a conceptual scheme for the topology optimization

In earlier investigations using FEMU, the structure would be subdivided to a few candidate regions likely to include damage and the model updating process would identify the region of interest [86]. The region-based damage detection is valid only when prior information on candidate damaged areas is available beforehand. This limitation may be overcome by applying topology optimization, which was originally developed to find an optimal material distribution for a structure having minimum compliance and subject to a given volume usage [161]. To the authors' best knowledge, the present paper is the first study to formulate a damage detection problem as a topology optimization design problem. In this investigation, a topology design formulation suitable for full field measurement data-based damage detection is developed. The essential steps of the developed formulation are as follows:

1. The design domain is first discretized by the FEM representing an undamaged structure at the start of the topology optimization process. The damaged elements will later be identified as voids in the proposed method.
2. After mapping to a common reference plane, full-field strains and displacement measurements using the DIC technique are compared with the corresponding response from the FE model and their residual is used in the objective function.
3. In each optimization iteration, element properties are treated as damage variables and are varied such that the objective function is minimized. If the damage variables are not fully converged to either the value of a void (completely damaged) or the value of a solid (completely intact) after an optimization iteration, all elements having damage variables below a prescribed threshold are reused as damaged elements at the next optimization iteration and the remaining elements are considered intact. This process is repeated until convergence.

4.7 Optimization Problem for Damage Detection

The damage detection problem can be defined in terms of an optimization problem where a numerical model is fine-tuned such that the residual difference between the numerical response and the experimental measurements is minimized. Fine-tuning of the model is carried out by varying the stiffness distribution throughout the structure through the damage variable (x). To perform the minimization, the residuals are summarized in the form of an objective (or penalty) function, ($C(\mathbf{x})$), that usually has the general form of a summation of different components of the residuals between the two responses over the region of interest. In this investigation, quasi-static response data including strains and deformations were used in the following objective function:

$$C(\mathbf{x}) = \sum_{k=1}^{p} \sum_{i=1}^{m} \sum_{j=1}^{q} \left[\left(\frac{\varepsilon_{xx,ij}^{exp} - \varepsilon_{xx,ij}^{num}(\mathbf{x})}{\varepsilon_{xx,ij}^{exp}} \right)^2 + \left(\frac{\varepsilon_{yy,ij}^{exp} - \varepsilon_{yy,ij}^{num}(\mathbf{x})}{\varepsilon_{yy,ij}^{exp}} \right)^2 + \left(\frac{\varepsilon_{xy,ij}^{exp} - \varepsilon_{xy,ij}^{num}(\mathbf{x})}{\varepsilon_{xy,ij}^{exp}} \right)^2 + \left(\frac{\delta_{xx,ij}^{exp} - \delta_{xx,ij}^{num}(\mathbf{x})}{\delta_{xx,ij}^{exp}} \right)^2 + \left(\frac{\delta_{yy,ij}^{exp} - \delta_{yy,ij}^{num}(\mathbf{x})}{\delta_{yy,ij}^{exp}} \right)^2 + \left(\frac{\delta_{zz,ij}^{exp} - \delta_{zz,ij}^{num}(\mathbf{x})}{\delta_{zz,ij}^{exp}} \right)^2 \right] \qquad (4\text{-}1)$$

Where $\mathbf{x}$ is the vector of unknown design variables which are the constitutive properties of the finite elements, $\boldsymbol{p}$ is the number of experimental tests ($\boldsymbol{p}$ = 1 in this work), $\boldsymbol{m}$ is the number of load steps ($\boldsymbol{m}$ = 1 in this work) and $\boldsymbol{q}$ the number of data points in the DIC measurement at load step $\boldsymbol{i}$. The subscripts ***exp*** and ***num*** indicate the experimental and numerical responses, respectively. Three components of the strain tensor and the corresponding component of displacement are represented by $\boldsymbol{\varepsilon}_{xx}^{exp}, \boldsymbol{\varepsilon}_{yy}^{exp}, \boldsymbol{\varepsilon}_{xy}^{exp}$ and , $\boldsymbol{\delta}_{xx}^{exp}, \boldsymbol{\delta}_{yy}^{exp}, \boldsymbol{\delta}_{zz}^{exp}$ respectively that are extracted at point j at the time *i*. Similarly, $\boldsymbol{\varepsilon}_{xx}^{num}, \boldsymbol{\varepsilon}_{yy}^{num}, \boldsymbol{\varepsilon}_{xy}^{num}$ rand $\boldsymbol{\delta}_{xx}^{num}, \boldsymbol{\delta}_{yy}^{num}, \boldsymbol{\delta}_{zz}^{num}$ represent the corresponding values computed from the FEM considering an assumed stiffness distribution denoted by damage variables *x*. The proposed objective function and its components are shown in Figure 4.4 schematically.

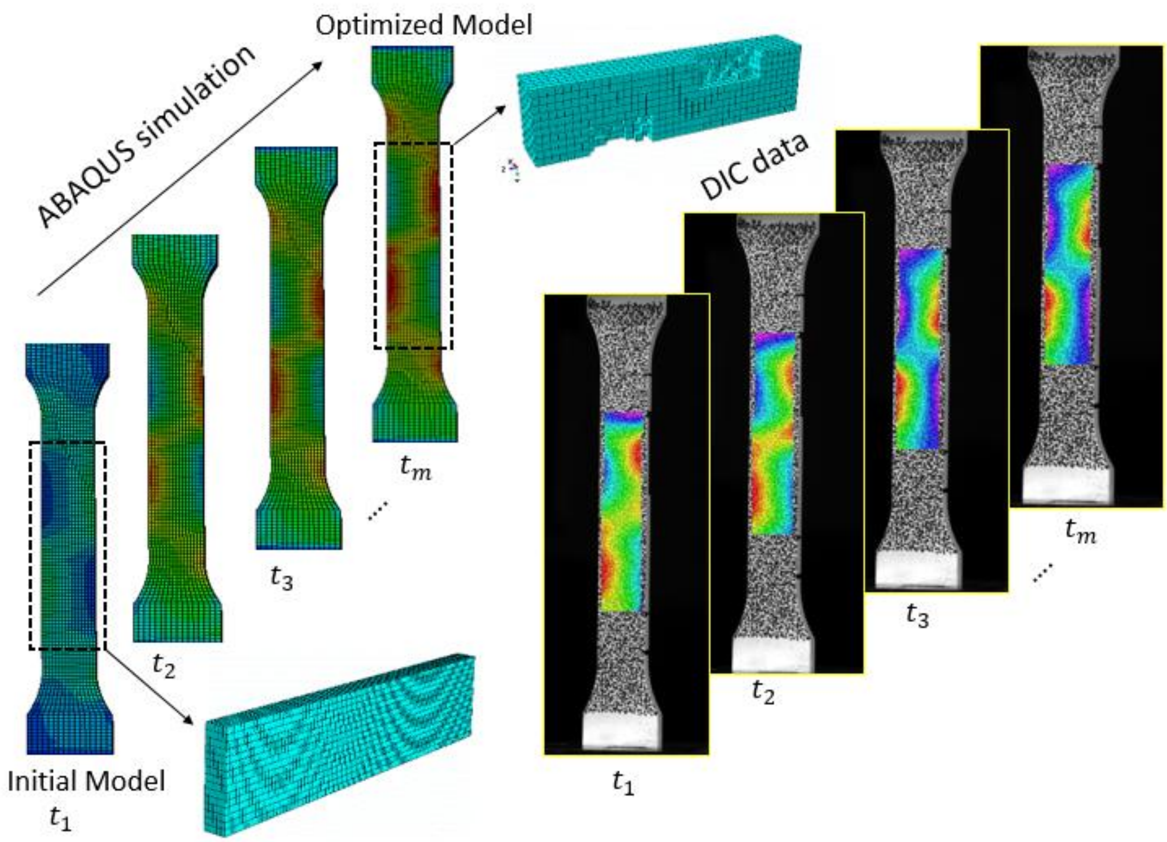

Figure 4.4. Components of the objective function

4.7.1 *Interpolation procedure*

Numerical results from an FEM model and experimental measurements from DIC are computed on two different grids determined independently through the FEM discretization and the DIC processing. As a result, to accurately compare the two sets of responses and compute the objective function, a common reference grid is required to ensure that the measurement/analysis locations are equivalent. To that end, it is necessary to interpolate the results from the DIC grid over to the FEA grid (or vice versa) or to interpolate both results on a newly-defined mesh grid. The concept of interpolation process is schematically shown in Figure 4.5. FEA and DIC results have different mesh grid spacing in the x-y plane. With both results mapped onto a common grid, the residuals between FEA and DIC results can be calculated within the optimization process. A bilinear interpolation algorithm has been developed for such interpolation, where interpolated values of the new grid are obtained based on the values of the four nearest neighbors forming a quad surrounding the interpolated point. The mapping scheme has proven effective in prior works related to global system identification [42, 104].

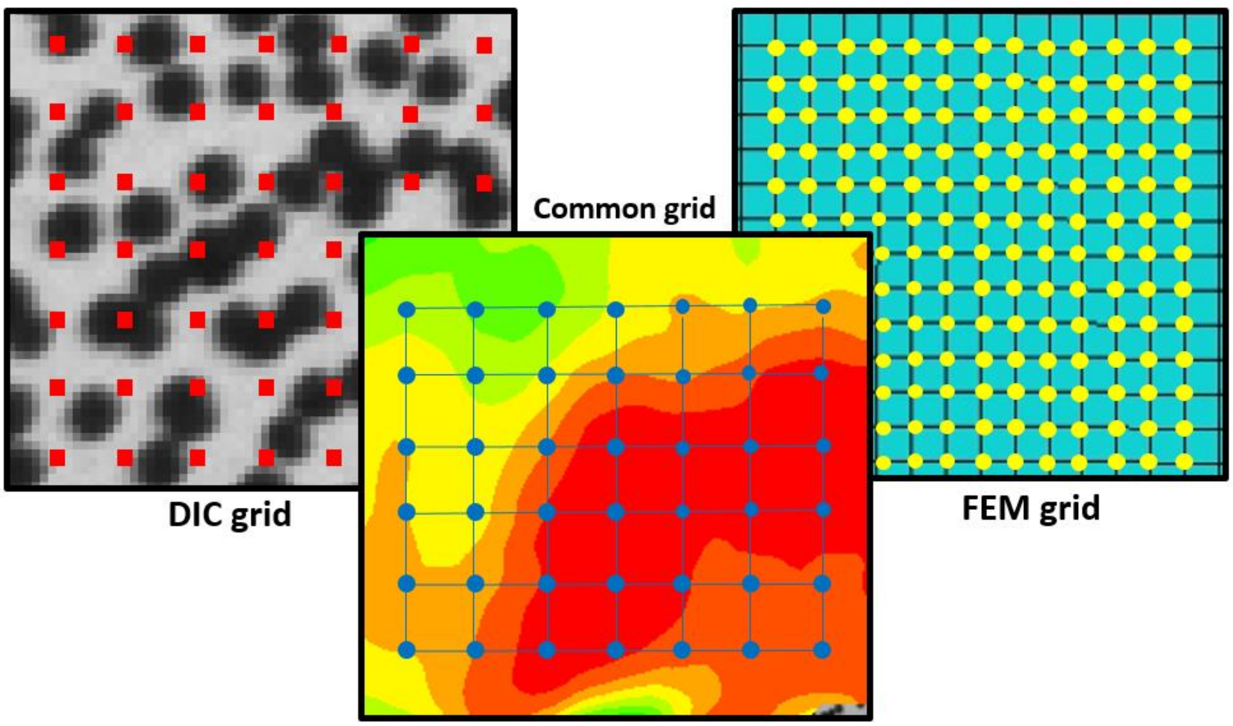

Figure 4.5. Interpolation of the experimental and numerical measurements into a common grid

4.7.2 *Damage Detection Using Topology Optimization*

In this research, topology optimization is used as a tool to find damaged regions in the structure. To achieve this, damage is assumed to manifest as a stiffness reduction and therefore the stiffness material is decreased in damaged areas throughout the structure. A topology optimization routine is used to find the material distribution that most closely replicates the observed surface response (strains and deformations). For this purpose, the Solid Isotropic Material with Penalization (SIMP) model is used and is described within this section.

SIMP, which was originally proposed by Bendsoe and Kikuchi (1988) and Rozvany and Zhou (1992) [167, 168], is one of the most effective mathematical methods for topology optimization. This method predicts an optimal material distribution within a given design space, under prescribed loading scenarios, boundary conditions, manufacturing constraints, and performance requirements. The SIMP method is based on a heuristic relation between (relative) element stiffness density x_i and element Young's modulus (Elastic Modulus) E_i given by

$$E_i = E_i(x_i) = x_i^p E_0,\ \ x_i \epsilon (0,1] \qquad (4\text{-}2)$$

Where E_0 is the elastic modulus of the base solid material and p is the penalization power (p>1). To account for lower-stiffness material that can be considered voids in the structure, the modified SIMP approach is given by

$$E_i = E_i(x_i) = E_{min} + x_i^p(E_0 - E_{min}),\ \ x_i \epsilon (0,1] \qquad (4\text{-}3)$$

Where E_{min} is the elastic modulus of the low-stiffness material (void), which is small but non-zero to avoid singularity of the finite element stiffness matrix. Topology optimization methods are known to encounter numerical difficulties such as mesh-dependency, checkerboard patterns and local minima [161], Therefore to mitigate such issues, researchers have proposed the use of regularization techniques [169, 170] that aim to prevent encountering aforementioned numerical difficulties. One of the most common approaches is the use of density filters that is shown in Eq. (4). A basic filter density function can be defined as

$$\tilde{x}_i = \frac{\sum_{j\in N_i} H_{ij} v_j x_j}{\sum_{j\in N_i} H_{ij} v_j} \qquad (4\text{-}4)$$

Where N_i is the neighborhood of an element x_i with volume v_i and H_{ij} is a weight factor. The neighborhood is defined as

$$N_i = \{j : dist(i,j) \leq R\} \qquad (4-5)$$

Where the operator $dist(i,j)$ computes the distance between the centers of the elements i and j, and R is the size of the neighborhood or filter size. The weight factor H_{ij} may be defined as a function of the distance between neighboring elements, for example

$$H_{ij} = R - dist(i,j), \tag{4-6}$$

Where $j \in N_i$. The filtered density $\tilde{x}_i$ defines a modified (physical) stiffness density field that is now incorporated in the topology optimization formulation and the SIMP model as

$$E_i = E_i(x_i) = E_{min} + \tilde{x}_i^p(E_0 - E_{min}),\ \ \tilde{x}_i \,\epsilon(0,1] \tag{4-7}$$

The regularized SIMP interpolation formula by Eq. (7) was used in this work.

Finite Element Analysis: Following the regularized SIMP method given by Eq. (7) and generalized Hooke's law, the three-dimensional constitutive matrix for an isotropic element i can be interpolated from void to solid as

$$C_i(\tilde{x}_i) = E_i(\tilde{x}_i)C_i^0, \qquad x_i \,\epsilon(0,1] \tag{4-8}$$

Where C_i^0 is the constitutive matrix with unit Young's modulus, which is given by

$$C_i^0 = \frac{1}{(1+\nu)(1-2\nu)} \times \begin{bmatrix} 1-\nu & \cdots & 0 \\ \vdots & \ddots & \vdots \\ 0 & \cdots & (1-2\nu)/2 \end{bmatrix} \tag{4-9}$$

Where ν is the Poisson's ratio of the isotropic material. Using the FEM, the elastic solid element stiffness matrix is the volume integral of the elements constitutive matrix $C_i(\tilde{x}_i)$ and the strain-displacement matrix B in the form of

$$k_i(\tilde{x}_i) = \iiint_1^{+1} B^T C_i(\tilde{x}_i) B d\xi_1 d\xi_2 d\xi_3 \tag{4-10}$$

Where ξ_e are the natural coordinates used in FEM. The strain-displacement can be obtained from $\varepsilon = \boldsymbol{B}u$ in which $\boldsymbol{B}$ is the strain-displacement matrix.

Using the SIMP method, the element stiffness matrix is interpolated as

$$k_i(\tilde{x}_i) = E_i(\tilde{x}_i)k_i^0 \tag{4-11}$$

Where $k_i^0(\tilde{x}_i)$ is defined as follows

$$k_i^0(\tilde{x}_i) = \iiint_1^{+1} B^T C^0 B d\xi_1 d\xi_2 d\xi_3 \tag{4-12}$$

The global stiffness matrix K is obtained by the assembly of element-level counterparts k_i as

$$K(\tilde{x}) = \mathcal{A}_{i=1}^{n} k_i(\tilde{x}_i) = \mathcal{A}_{i=1}^{n} E_i(\tilde{x}_i) k_i^0 \tag{4-13}$$

Where n is the total number of elements. Using the global versions of the element stiffness matrices K_i and K_i^0, the previous equation is expressed as

$$K(\tilde{x}) = \sum_{i=1}^{n} K_i(\tilde{x}_i) = \sum_{i=1}^{n} E_i(\tilde{x}_i) K_i^0 \tag{4-14}$$

Where K_i^0 is a constant matrix. Using the interpolation function defined in (4-7), it can be rewritten as

$$K(\tilde{x}) = \sum_{i=1}^{n} [\, E_{min} + \tilde{x}_i^p (E_0 - E_{min})] K_i^0 \tag{4-15}$$

Finally, the nodal displacement vector $U(\tilde{x})$ is the solution of the equilibrium equation

$$\mathbf{K}(\tilde{\mathrm{x}})\mathbf{U}(\tilde{\mathrm{x}}) = \mathbf{F} \tag{4-16}$$

Where **F** is the vector of nodal forces which is independent of the physical stiffness densities x.

To summarize, the following formulation presents the proposed topology optimization setup for interior defect detection:

$\boldsymbol{Find}$ $\quad x = [x_1, x_2, \ldots, x_e, \ldots, x_n]^T$

$\boldsymbol{minimize}$ $\quad \boldsymbol{C}(\tilde{x})$

$\mathrm{F} = \mathbf{K}\mathrm{U}$

$\mathrm{x} \in \chi, \qquad \chi = \{\mathrm{x} \in \mathbb{R}^n \;:\; 0 \leq \mathrm{x} \leq 1\}$

where the physical densities $\tilde{x} = \tilde{x}(x)$ are defined by (4-4), n is the number of elements used to discretize the design domain

4.8 Optimization Algorithm

A fundamental component of the proposed approach is to use optimization to push the objective function to a minimum. For this objective function, the goal centers on minimizing the difference in responses between the finite element results and experimental DIC results, along with the elimination of elements describing unseen damaged regions. In this paper, the Method of Moving Asymptotes (MMA) is used to minimize the objective function. This algorithm has proven to be versatile and well-suited for large-scale topology optimization problems [161, 167-169]. MMA is a mathematical algorithm for solving smooth nonlinear optimization problems through an iterative process where a new strictly convex sub-problem is generated and solved for each iteration. Each generated convex sub-problem is an approximation of the original problem with a set of parameters that set the curvature of the approximation and act as asymptotes for the associated sub-problem. The convergence of the overall process is stabilized by moving these asymptotes between each iteration. The details of the method are explained as follows:

4.8.1 Method of Moving Asymptotes (MMA)

Given the current design x_k, the MMA approximation of the objective function leads to the following linear programming problem:

$$find \qquad \boldsymbol{x}$$

$$minimizae \qquad \sum_{\boldsymbol{i=1}}^{\boldsymbol{n}}\left[\frac{\left(\boldsymbol{x_i^{(k)}-L_i^{(k)}}\right)^{\boldsymbol{2}}}{\boldsymbol{x_i-L_i^{(k)}}}\ \frac{\boldsymbol{\partial c}}{\boldsymbol{\partial x_i}}\ (\widetilde{\boldsymbol{x}}^{(\boldsymbol{k})})\right]\ ,\quad x \in \chi^{(k)}$$

Where

$$\chi^{(k)} = \{x \in \chi | 0.9L_i^{(k)} + 0.1x_i^{(k)} \leq x_i \leq 0.9U_i^{(k)} + 0.1x_i^{(k)}, i = 1, \dots, n.\}$$

The lower and upper asymptotes $L_i^{(k)}$ and $U_i^{(k)}$ are iteratively updated to mitigate oscillation or improve convergence rate. The heuristic rule proposed by Svanberg (1987) [171] is as follows: for k=1 and k=2,

$$U_i^{(k)} + L_i^{(k)} = 2x_i^{(k)} \qquad (4\text{-}17)$$

$$U_i^{(k)} - L_i^{(k)} = 1 \qquad (4\text{-}18)$$

For $k \geq 3$,

$$U_i^{(k)} + L_i^{(k)} = 2x_i^{(k)} \qquad (4\text{-}19)$$

$$U_i^{(k)} - L_i^{(k)} = \gamma_i^{(k)} \qquad (4\text{-}20)$$

Where

$$\gamma_i^{(k)} = \begin{cases} 0.7 \ (x_i^{(k)} - x_i^{(k-1)})(x_i^{k-1} - x_i^{k-2}) < 0 \\ 1.2 \ (x_i^{(k)} - x_i^{(k-1)})(x_i^{k-1} - x_i^{k-2}) > 0 \\ 1 \ \left(x_i^{(k)} - x_i^{(k-1)}\right)\left(x_i^{k-1} - x_i^{k-2}\right) = 0 \end{cases} \qquad (4\text{-}21)$$

Note from (17) that the signs of three successive iterations are stored. If the signs are opposite, meaning x_i oscillate, the two asymptotes are brought closer to $x_i^{(k)}$ to have a more conservative MMA approximation. On the other hand, if the signs are same, the two asymptotes are extended away from $x_i^{(k)}$ in order to speed up the convergence. The MMA algorithm is described in Algorithm 1:

Algorithm 1 MMA Algorithm

Choose an initial feasible design $x^{(0)}$; set $k \leftarrow 0$;

while (convergence criteria are not met) **do**

  if k=1 or k=2 **then**

    Update L_i^k and U_i^k using (4-17, 4-18)

  else

    Update L_i^k and U_i^k using (4-19, 4-20) and (4-21)

  end if

  Calculate derivative of objective function

  Solve the MMA sub-problem (41) to obtain $\tilde{x}^{k+1}$;

  Set $x^{k-2} \leftarrow x^{k-1}$, $x^{k-1} \leftarrow, x^k \leftarrow x^{k+1}$;

  Set $k \leftarrow k + 1$;

end while

In this paper, an implementation of the MMA provided in the NLOPT package [47] was used. The optimization was run for a maximum of 500 iterations as convergence is known to happen within 250-350 iterations, based on our trial and error and recommendations from the literature [161].

4.9 Experimental Design

An experimental program was executed to demonstrate the potential of the proposed framework. The experimental program was designed to evaluate the feasibility of leveraging 3D-DIC in a topology optimization framework to detect internal features of structural components. This program included a formulation evaluation, sensitivity study, and a laboratory-scale investigation of three representative steel coupon specimens subjected to the same displacement-controlled tensile loading and boundary conditions. The structural configurations used in this work are illustrated schematically in Figure 5 and can be described as follows:

1. Configuration 1: intact coupon specimen with no defects.
2. Configuration 2: coupon specimen with two artificially-manufactured defects on the back side, which are shown in Figure 5 with corresponding dimensions.
3. Configuration 3: coupon specimen with one artificially-manufactured defect on the back side at the middle region of the specimen; the exact location and shape of the defects are depicted in Figure 5.
4. Configuration 4: coupon specimen with one artificially manufactured defect on the back side on the top region of the specimen; corresponding dimensions for the defect is described in Figure 5.

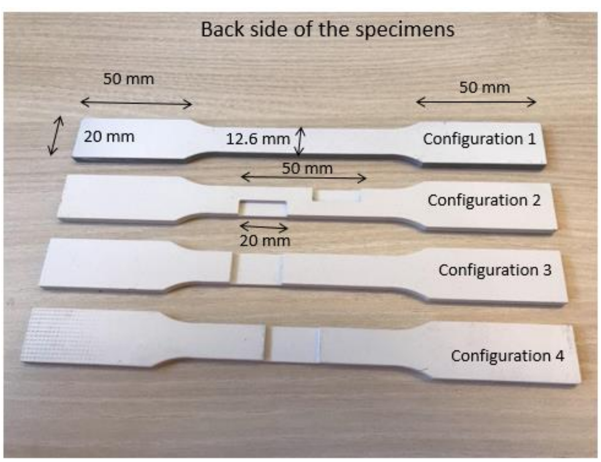

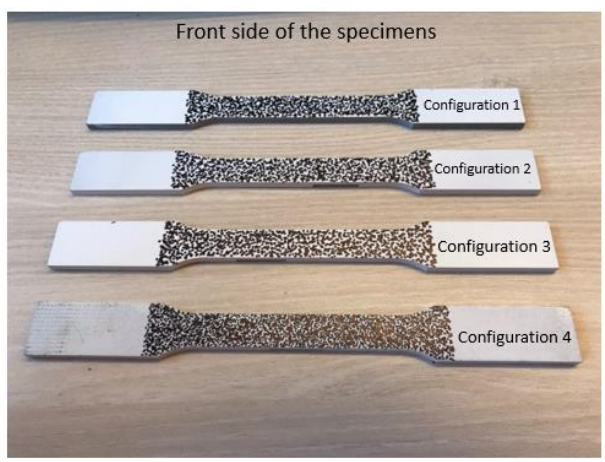

(a) (b)

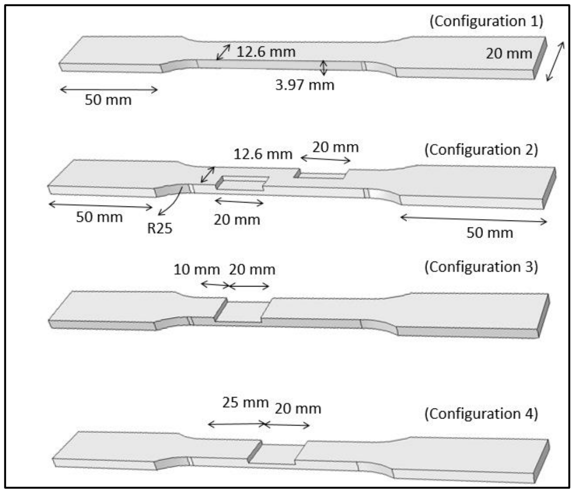

(c)

Figure 4.6. (a) Geometric dimensions of the specimens (Back side of the specimen), (b) Coupon specimens and their speckled front side, (c) the dimensions of the defects.

4.9.1 *Quasi-Static Mechanical Testing*

The experimental program consisted of a series of quasi-static tests under uniaxial tensile loading within the elastic range of the structural steel coupon specimens. These test configurations give rise to heterogeneous and non-uniform in-plane strain fields, (i.e. longitudinal, transverse and shear strain components), as well as in-plane/out-of-plane displacement fields (i.e. longitudinal, transverse and out-of-plane components). The experimental setup including the DIC system employed is illustrated in Figure 4.6. In this figure, the Area of Interest (AOI) has been defined, which is the zone where the DIC measurements are compared with numerical simulations. For this experimental validation, a simple tension test was performed using three A36 structural steel coupon specimens according to the test method defined in ASTM E8 [107]. The mechanical response of the specimens was measured by 3D-DIC to describe full-field surface measurements of displacement and strain, analogous to the types of results derived from a FEM.

A commercially available DIC system from Correlated Solutions Inc. was used in this investigation [102]. This system consists of a camera system, an image acquisition package (VicSnap), and 3D-DIC post-processing software (Vic-3D). The DIC image acquisition used one set of stereo-paired digital cameras with a 5-megapixel charge coupled device (CCD) image sensor. The cameras were outfitted with a C-mount optical lens (12 mm focal length) and the acquired data was communicated to the control PC through FireWire cables. The camera pair was positioned 2 feet from the coupon which yielded a field of view (FOV) of 2.4 x 2.4 feet. For the experiment, the basic process consisted of specimen preparation, camera setup (focusing, calibration, and image acquisition), and post-processing of results. To perform the testing, the surface of the specimen was covered with a fine, dense and random speckle pattern (flat white paint for base and fine tip permanent marker for pattern) to help with the correlation process. For the correlation process in DIC, the area of interest on the speckle pattern was split into rectangular windows or "subsets" such that unique patterns of speckles remained available within each subset to allow for tracking in subsequent frames. The patterns in the subsets were tracked on a grid of a specific "step" size, which dictated the spatial resolution of the calculated points. To achieve a fine grid of unique patterns in subsets, the selection of the subset size was determined through direct experimentation during post-processing and a square subset of 23 pixels at a step of 7 pixels was selected (Figure 4.7). For more details regarding DIC setup, the reader is referred to the authors' previous works [42, 104, 131, 132]. The DIC data acquisition (DAQ) integrated output signals (load and displacement) from MTS actuators to allow for simultaneous acquisition of load, displacement, and images.

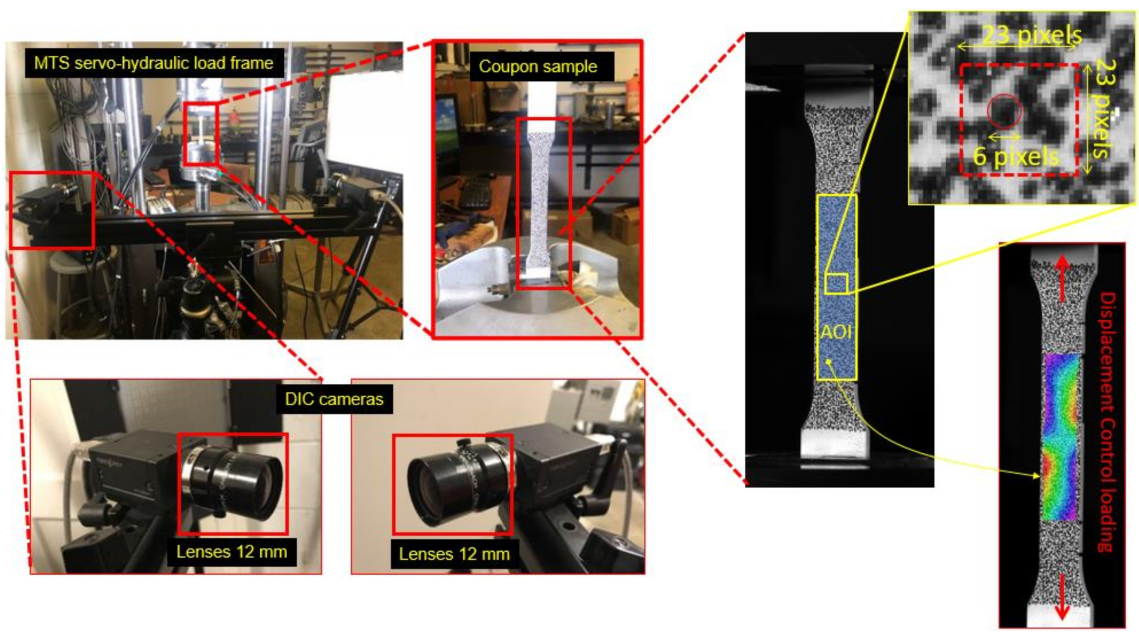

Figure 4.7. Experimental DIC setup configuration (one system including two cameras)

4.9.2 *Measurement noise*

This section presents an analysis of the measurement noise performed on DIC measurements. Before the actual tensile tests, a series of images were taken where no load was applied to the specimen which were then processed using the same settings used for the rest of the data. It is widely known that noise from different sources affect the measurements resulting in displacements and strains that are not equal to zero under no loads (as theoretically expected). Examples of sources of measurement noise in DIC include non-uniform lighting and glare, poor quality of speckle pattern, as well as image acquisition (e.g. sensor noise) and quantization noise [42, 104, 132]. The average and standard deviation of the three components of displacement (U, V, W) and strain ($\varepsilon_{xx}, \varepsilon_{yy}, \varepsilon_{xy}$) measurements in 10 unloaded frames are summarized in Table 4.1. Ideally, the mean value of the zero-load measurements should be close to zero and the standard deviation quantifies the variation of the noise and can be used as a metric for the noise level in the measurements [103]. Based on this table, the measurements have an estimated deformation and strain noise level of about 0.00077 in and 28, respectively. Finally, Figure 4.8 illustrates histograms of the non-zero displacements and strains in a sample zero-load frame to illustrate the distribution of noise in each configuration. It can be observed in Figure 4.8 that the measurements of all configurations show a bell-shaped distribution with a mean close to zero, which is in agreement with the expected random Gaussian noise.

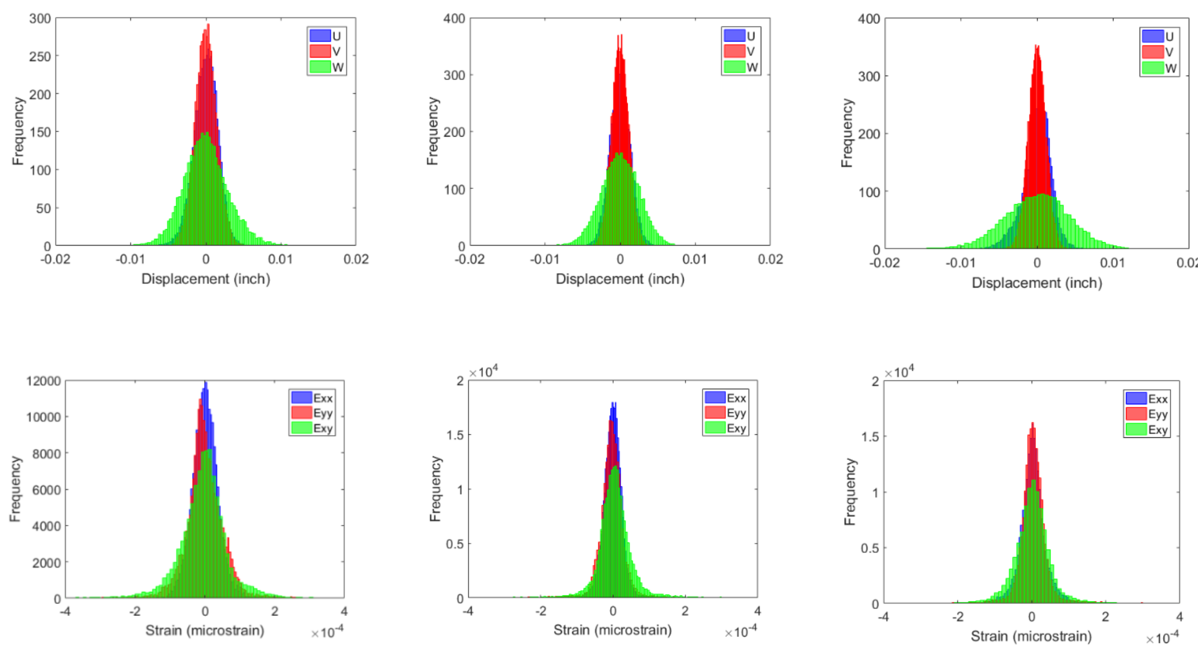

(a) (b) (c)

Figure 4.8. Histogram of non-zero measurements in a sample zero-load frame for the coupons with various associated defects in the back side, (a) Configuration 2, (b) Configuration 3, (c) Configuration 4

Table 4.1. Noise statistics from measurements in 10 frames with zero load for the defined configurations.

Variable		Configuration 2		Configuration 3		Configuration 4	
		Mean	StD	Mean	StD	Mean	StD
U	($\frac{1}{1000}$ $in.$)	0.55	0.65	0.65	0.55	0.51	0.45
V		-0.39	0.77	0.35	0.66	-0.55	0.48
W		0.61	0.58	-0.51	0.44	0.64	0.68
ε_{xx}	(με)	0.45	54.02	0.45	15.02	0.33	38.02
ε_{yy}		-0.64	56.67	0.55	45.67	-0.39	45.55
ε_{xy}		0.55	49.12	-0.48	18.12	0.61	18.12

4.9.3 Numerical implementation

The proposed damage detection method relies on the fine-tuning of a representative FEM model of the component to match the experimentally-measured response. To develop the FEM models in this paper, ABAQUS, a robust commercially available finite element software package was used [10]. The specimen was modeled using a total of 3,360 continuum 3D hexahedral solid elements (C3D8) with full integration. The FEM and mesh configuration of the coupon specimens are illustrated in Figure 4.9. As shown in this figure, the middle region of the specimen for which DIC measurements exist, was used for extracting strains and deformations, and the stiffness of the corresponding elements were used as design variables in the topology optimization process. In this work, the initial FEM of the specimen was created using the Graphical User Interface (GUI) of ABAQUS, which then allows the model to be described by a script that contains all modeling decisions and parameters. The extracted script was iteratively interfaced with Python optimization packages to carry out the topology optimization procedure outlined in the previous sections. The basic steps involved in this process can be described as: (1) Creating the initial model and saving it, (2) Using the saved ABAQUS model to create a script that contains all modeling parameters, (3) Creating output (i.e. load/deformation response), (4) Redoing the calculation by running the generated script file, (5) Adjusting the script to create a different model according to the optimization process. The results of this process yields a FEM with individual elements updated with reduced constitutive properties representing the damaged regions.

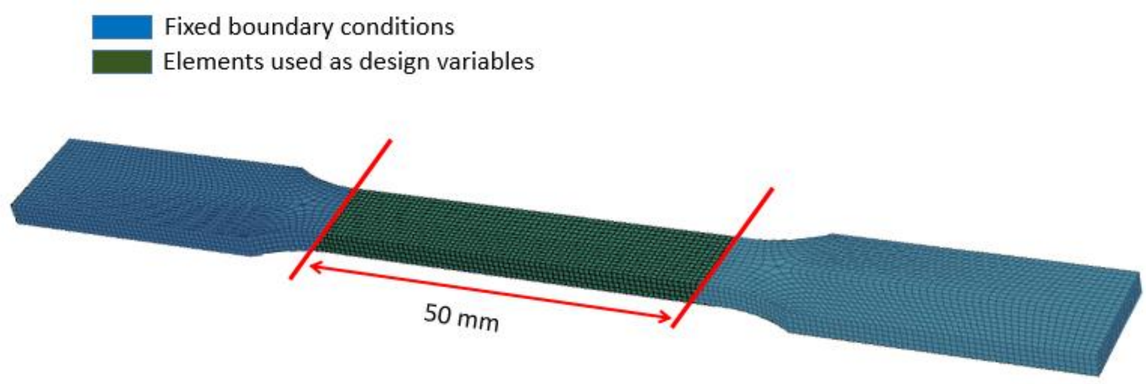

Figure 4.9. FEM of the coupons

4.10 Performance Evaluation

To examine and quantify the damage detection performance of the proposed approach, a number of performance metrics were used as defined and described in this section. Accuracy (ACC) is the ratio of all correct predictions over all predictions, and recall (REC) and precision (PRE) are the ratios of correct defect predictions to total defective elements, and to all defect predictions, respectively. F1 score is the harmonic mean of precision and recall and is used to provide an aggregate metric of classification performance. Equations 18 to 21 summarize the definitions for these performance metrics. In defining these criteria, defective and intact elements were referred to as positive (+) and negative (−) instances, respectively, and TP, TN, FP, and FN refer to true positives, true negatives, false positives, and false negatives, respectively, and shown in Figure 4.10.

$$ACC = \frac{TP+TN}{TP+FN+TN+FP} \tag{4-18}$$

$$REC = \frac{TP}{TP+FN} \tag{4-19}$$

$$PRE = \frac{TP}{TP+FP} \tag{4-20}$$

$$F_1 = \frac{2\times PRE\times REC}{(PRE+REC)} \tag{4-21}$$

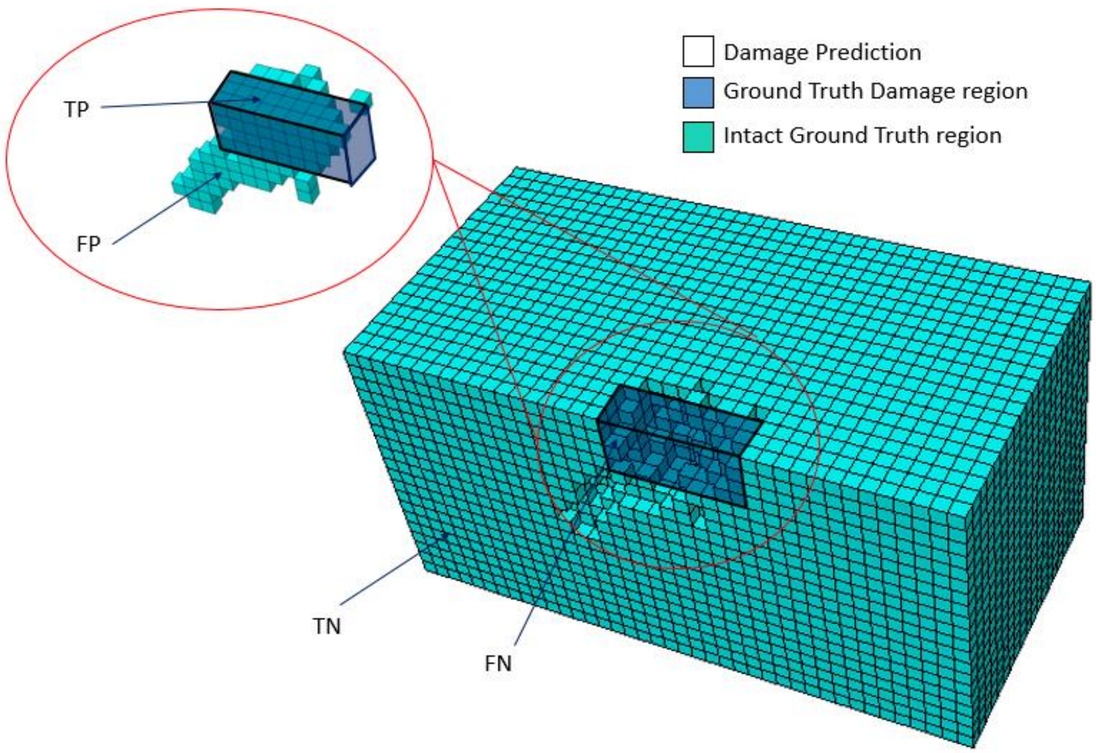

Figure 4.10. Performance metrics

To further demonstrate the performance of the proposed structural optimization, receiver operating characteristic (ROC) curves were also plotted for the optimized design variables. ROC curves plot true positive rate (TPR), which is equal to REC, against false positive rate (FPR), which is the ratio of elements incorrectly classified as defective over all intact elements as shown in Eq. 22. ROC curve examines the performance of the system throughout the full range of TPR-FPR trade-offs, where a curve with a higher area denotes a better classifier.

$$FPR = \frac{FP}{TN+FP} \tag{4-22}$$

4.11 Formulation Evaluation and Sensitivity Analysis

To evaluate the feasibility of the proposed approach using simulated measurements, a FEM of a coupon specimen with simulated defects was created and used as a preliminary substitute for laboratory experiments. The objective was twofold; first to evaluate the feasibility and performance of the proposed approach on a fully-controlled specimen using idealized surface measurements analogous to those to be derived from a DIC measurements, and second to conduct a sensitivity analysis on the main parameters affecting the performance (including the number of sensing points, mesh density, etc.). An intact coupon model, without any simulated damage was developed to initialize the optimization process. Configurations 2-4 (Figure 4.6) were used for this numerical study and the identification process using surface strain and displacement fields were used to reconstruct the elastic modulus distribution. The baseline model used for these experiments was discretized into 70×12×4 finite elements (an element size approximately equal to 1mm), with an initial element stiffness of one and 70×12 sensing points on the surface. Convergence of the objective function and accuracy of the specimens is presented in Figure 4.11, which demonstrates that the updated elastic modulus is well adjusted using surface strain and displacement fields and that both the objective function and accuracy reach a stable plateau with sufficient iterations.

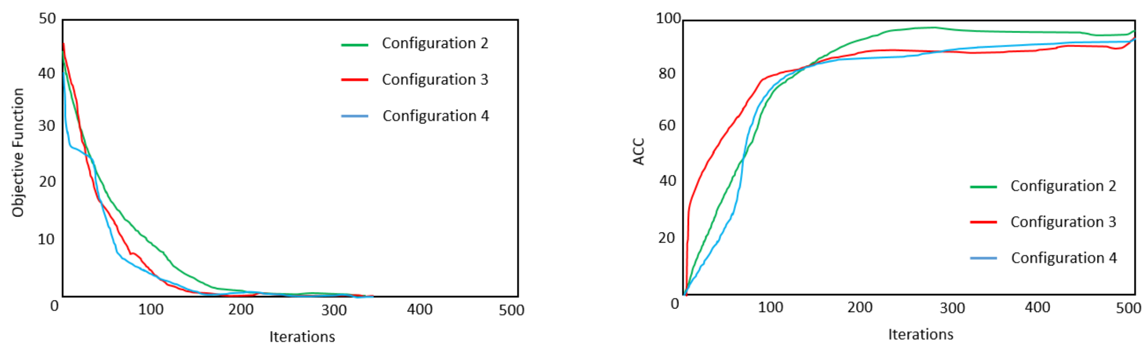

(a) (b)

Figure 4.11. Convergence of the defect detection process: (a) objective function, (b) accuracy

The initial and target configurations of the models are shown in Figure 4.12, and the updated configurations after 500 iterations are shown in Figure 4.13, to Figure 4.15. In Figure 4.13 to Figure 4.15, the color levels of the finite elements correspond to the x_i values, therefore, lower values indicate reduced stiffness denoting the existence of damage. As can be seen in each one of the results in Figure 4.13 to Figure 4.15, the general location of the damage is successfully identified in each case together with minor spurious detection noise.

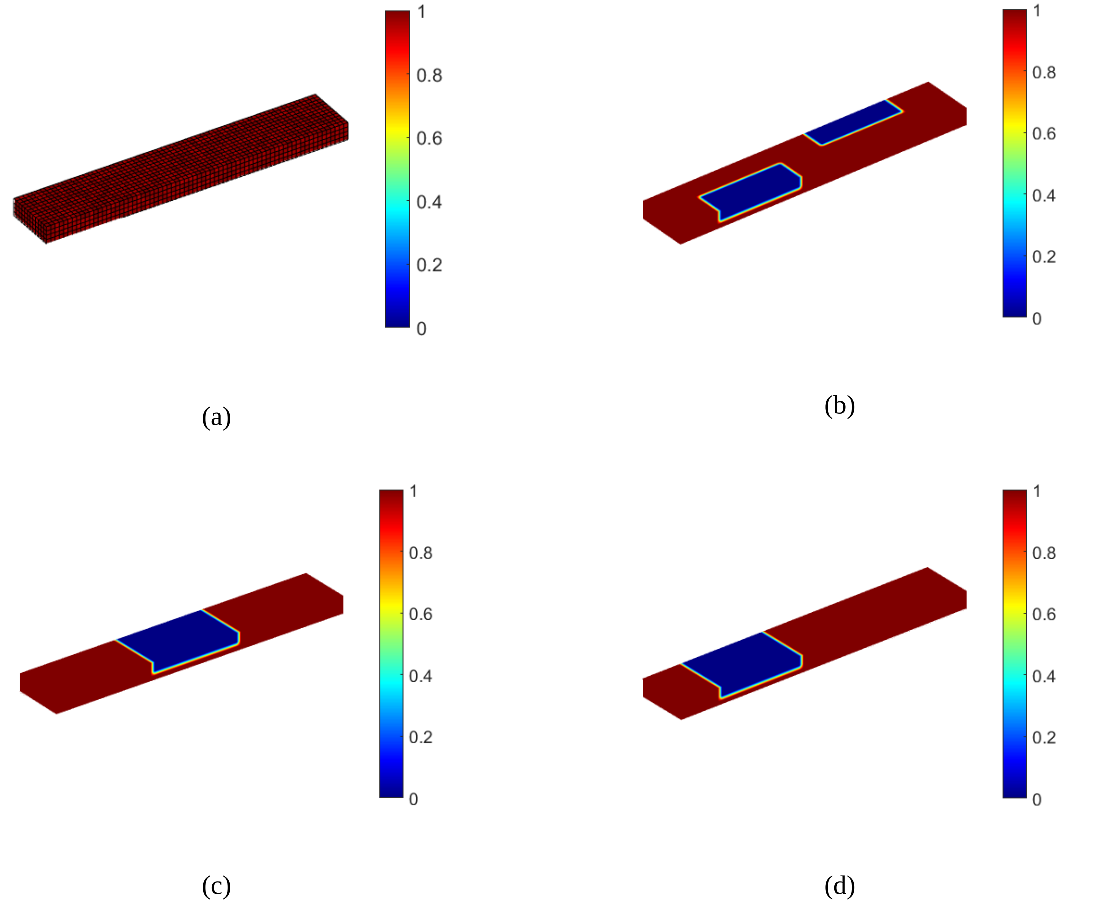

Figure 4.12. (a) Initial values at the beginning of topology optimization, and target values for (b) configuration 2, (c) configuration 3, (d) configuration 4.

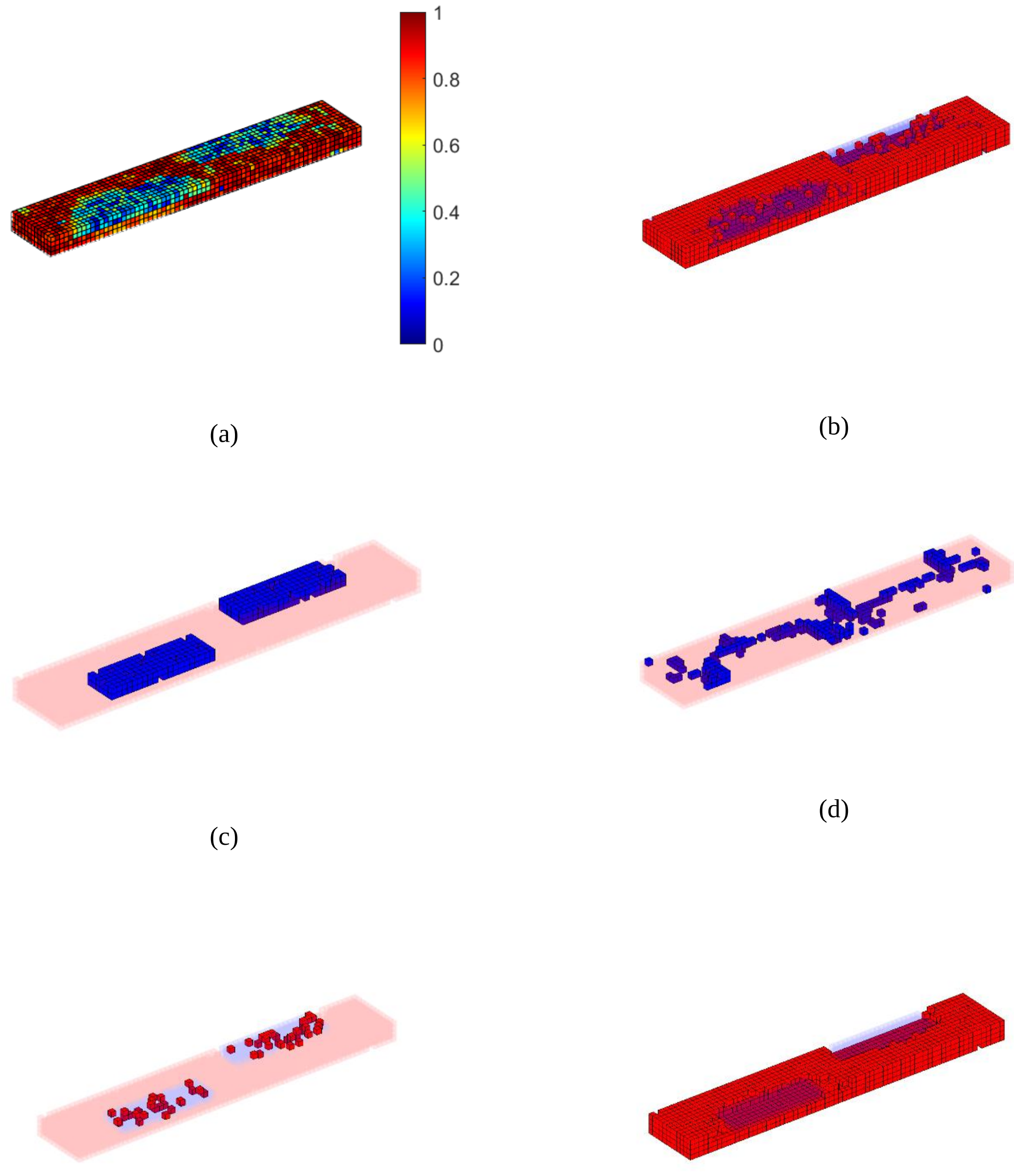

(a) (b)

(c) (d)

(e) (f)

Figure 4.13. Topology Optimization results for configuration 2 in the simulated experiments, (a) element stiffness parameter (x_i), (b) binary detections after thresholding, (c) true positives, (d), false positives, (e) false negatives, and (f) true negatives

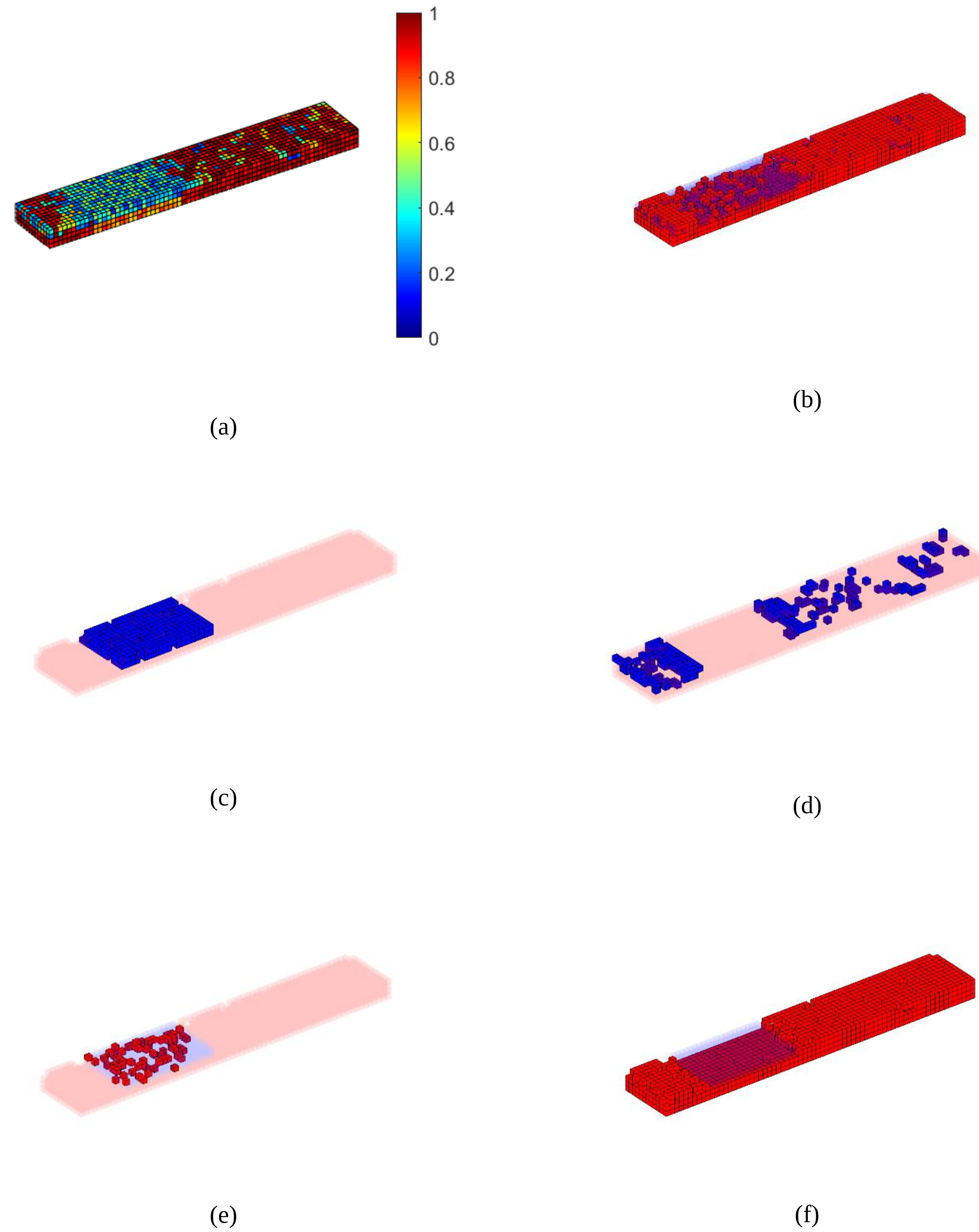

(a) (b) (c) (d) (e) (f)

Figure 4.14. Topology Optimization results for configuration 3 in the simulated experiments, (a) element stiffness parameter (x_i), (b) binary detections after thresholding, (c) true positives, (d), false positives, (e) false negatives, and (f) true negative

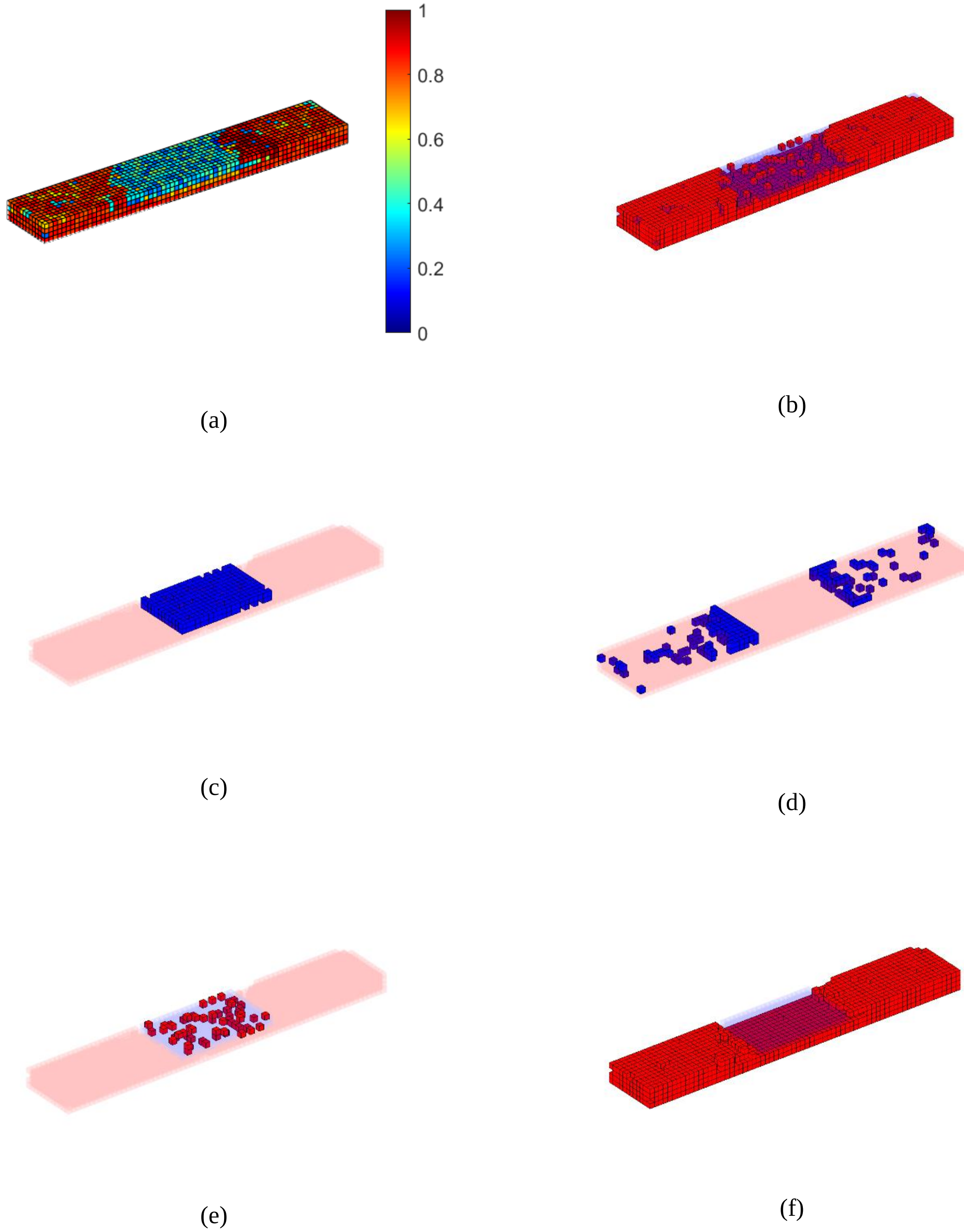

Figure 4.15. Topology Optimization results for configuration 4 in the simulated experiments, (a) element stiffness parameter (x_i), (b) binary detections after thresholding, (c) true positives, (d), false positives, (e) false negatives, and (f) true negatives

To better understand the performance of the proposed approach, Figure 4.16 quantifies and summarizes the detection results of the optimization for configurations 2-4 in Figure 4.16 in the form of confusion matrices, and generally shows the higher concentration of the detections around the true-prediction diagonal. Figure 4.16d also shows the ROC curves for the three configurations, which illustrates the trade-off between the ability of the model to detect truly defective elements, while avoiding false alarms, with varying values of threshold. As shown in this figure, the three configurations show a relatively similar detection behavior.

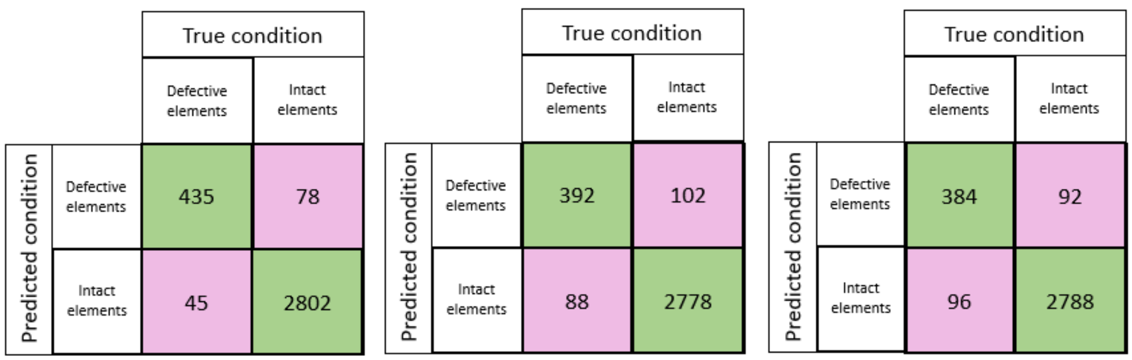

(a) (b) (c)

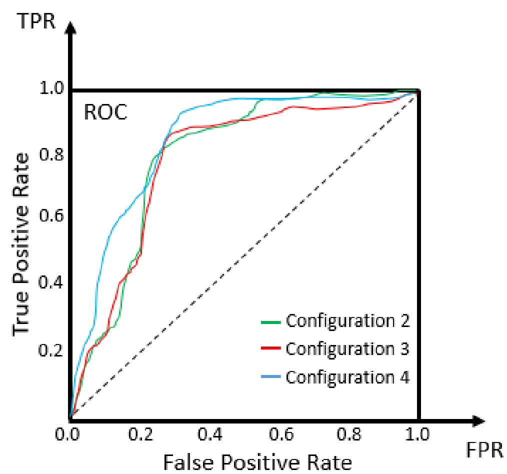

(d)

Figure 4.16. Performance of the damage detection method on simulated experiments, confusion matrix with threshold of 0.5 for (a) Configuration 2, (b) Configuration 3, (c) Configuration 4, (d) ROC curves for the three configurations with varying thresholds.

Table 4.2 summarizes the corresponding accuracy metrics computed based on the confusion matrices shown in Figure 4.16. It can be seen that the proposed approach provides an overall accuracy above 94% with precision and recall values above 80%, which demonstrates the ability of the optimization process in detecting the damage in the simulated experiments. A number of factors can affect the performance of the proposed approach and a series of sensitivity analyses will be carried out in the next section to describe their effect.

Table 4.2. Performance of the damage detection method on simulated experiment (threshold=0.5)

Configuration	ACC	PRE	REC	F1
2	96.3	84.8	90.6	87.6
3	94.3	79.4	81.7	80.5
4	94.4	80.7	80.0	80.3

4.11.1 *Effect of Sensing Density*

It was argued in the previous sections that the increased sensing density in the form of full-field response measurements achieved by DIC provides the improved ability to reconstruct internal damage. In this section a sensitivity analysis is conducted to compare the detection performance with varying numbers of sensing points. Using the simulated experiment for configuration 2, the number of sensing points (*n*) used in the objective function (Eq. 1) was gradually varied from 6 to 6,720. Figure 4.17 shows the sensing grid used in each case and the resulting sensing density, where the lower bound (e.g. the 2x3 grid) and the upper bound represent the traditional use of discrete sensors, and the use of full-field sensing with DIC, respectively. Figure 4.18 shows that increasing the sensing density significantly improves the detection performance and that high accuracy (e.g. higher than 90%) is not achievable without the use of full-field DIC data. This highlights the fundamental contribution of this paper which is the introduction of the method for internal damage reconstruction through the use of full-field sensing using DIC.

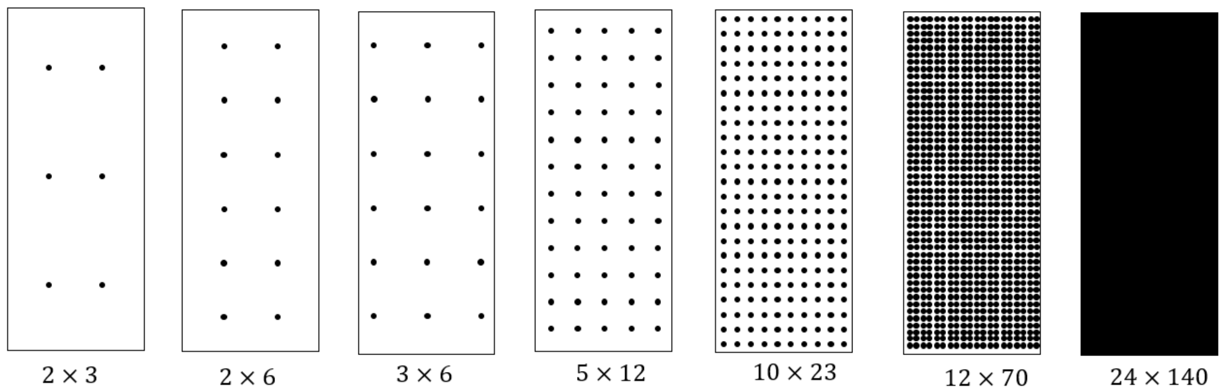

Figure 4.17. The grid used for the sensitivity analysis on sensing density

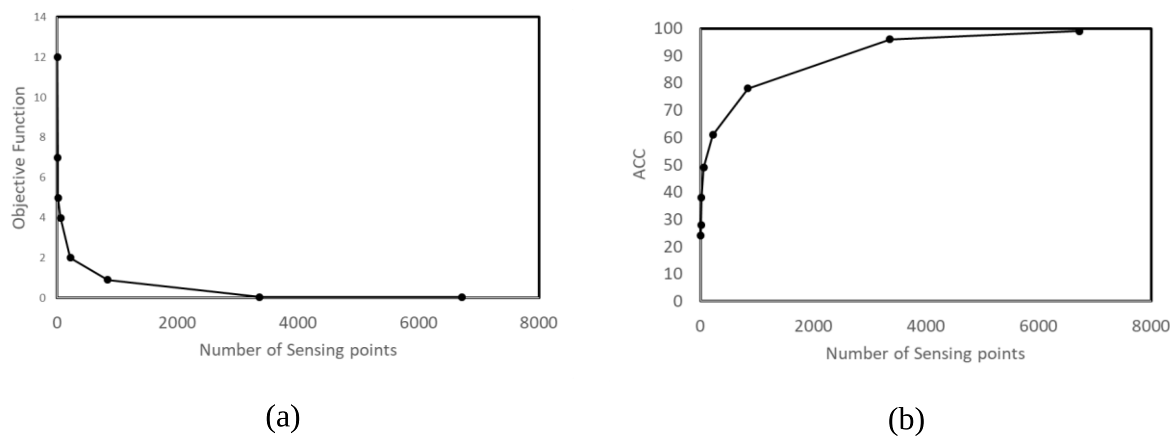

Figure 4.18. Analysis of the effect of sensing density on (a) objective function, and (b) accuracy

4.11.2 Effect of Defect Severity

The proposed technique relies on the detectability of the internal defects by matching the effect they have on the external surface strain and deflection patterns. As a result, it is expected that a shallow defect that is far from the surface of the specimen may not produce a noticeable effect on the strain patterns, thus limiting the capability of the proposed approach to detect the underlying defect. To investigate this effect, using the FEM simulated experiment, the performance of the proposed technique was evaluated for varying thicknesses of the simulated defect. Three defect thicknesses ($^{3t}/_{4}$, $^{2t}/_{4}$, $^{t}/_{4}$, where *t* denotes the overall specimen thickness) were simulated on configuration 2 and Table 4.3 shows the resulting defect detection performance. Moreover, to better realize the performance of the introduced approach, Figure 4.19 quantifies and summarizes the detection results of the optimization for configurations 2 with different thickness for the defects within the specimen in Figure 4.19 in the form of confusion matrices, and generally shows the higher concentration of the detections around the true-prediction diagonal. Based on Table 3, all performance metrics consistently improve with higher defect depth, which can be attributed to the corresponding increased effect on strain and displacement patterns. It is however noted that even in the case of the thinnest defect ($^t/_4$), the proposed approach maintains a reasonable detection performance. Convergence of the objective function and accuracy of the specimens is illustrated in Figure 4.20, which demonstrates that the optimized elastic modulus is well tuned by surface strain and displacement fields and that both the objective function and accuracy reach a stable plateau with sufficient iterations.

		True condition	
		Defective elements	Intact elements
Predicted condition	Defective elements	191	111
	Intact elements	49	3009

1/4t

		True condition	
		Defective elements	Intact elements
Predicted condition	Defective elements	435	78
	Intact elements	45	2802

2/4t

		True condition	
		Defective elements	Intact elements
Predicted condition	Defective elements	698	84
	Intact elements	22	2556

3/4t

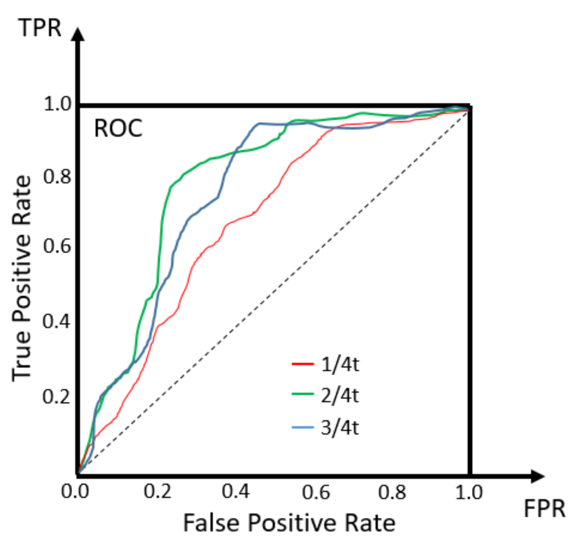

Figure 4.19. Performance of the damage detection method on simulated experimental results with different thickness defined for the defects on the back side of the specimen for configuration 2, (threshold=0.5), (a) 1/4t 2, (b) 2/4t, (3) 3/4t

Table 4.3. Performance of the damage detection method on DIC experimental results (threshold=0.5)

Damage Thickness	ACC	PRE	REC	F1
t/4	95.2	63.2	79.6	70.4
2t/4	96.3	84.8	90.6	87.6
3t/4	96.8	89.2	96.9	92.9

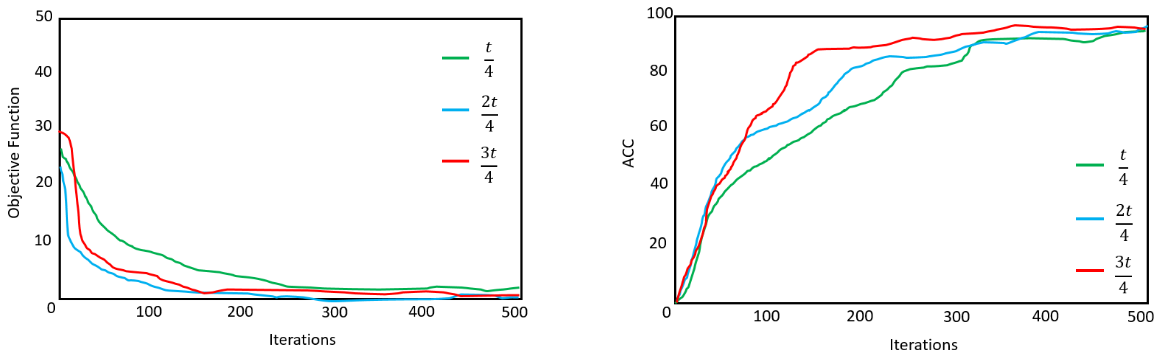

(a) (b)

Figure 4.20. Performance of the damage detection method on DIC experimental results

4.11.3 *Effect of Mesh Density*

The density of the finite element mesh used in the discretization of the model affects the degree to which potential damage can be localized in detail. A finer mesh provides a higher level of flexibility in reconstructing damaged areas. At the same time, the number of elements used in the discretization determines the number of unknown variables to be optimized during the proposed process. In order to investigate the effect of mesh size and density on the performance, the optimization was repeated for the simulated experiment with configuration 2 with varying mesh sizes and the resulting accuracy is plotted against the number of elements as shown in Figure 4.21a. Based on this figure, increasing the mesh size results in improved detection accuracy. It should also be mentioned that the finer discretization with a finer mesh comes with an increase in the computational demand. To observe this effect, Figure

4.21b plots the computation time spent on the optimization with each mesh density against the number of elements, which shows a constant increase in time as the number of elements increase.

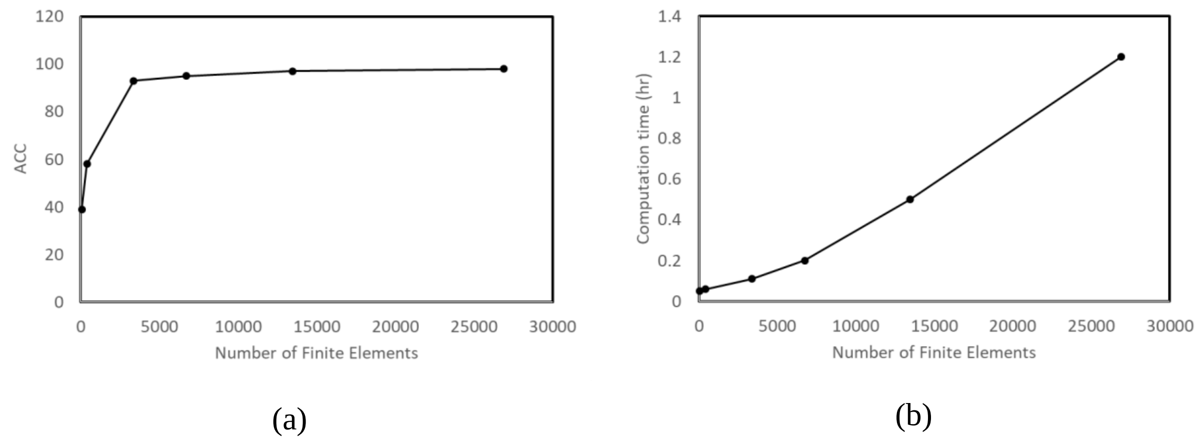

Figure 4.21. Finite element mesh sensitivity analysis on configuration 2

Therefore, it is necessary to investigate the effect of different partitioning configurations of the initial FEM on the size and location of the discovered damaged region.

4.11.4 Effect of Initial Optimization Starting Points

A different choice of initial stiffness parameter can affect the ability of the process to hone in on the damage patterns. To investigate the robustness of the proposed method and ensure that the results are not sensitive to and dependent on the initial values, a series of experiments with different random initial values were performed. Six sets of randomly-selected initial values were used in configuration 2 to evaluate the optimization performance with their convergence trends plotted in Figure 4.22. As can be noted from Figure 4.22, the proposed algorithm consistently converges to the optimal values, thus maximizing the accuracy and minimizing the objective function to approximately the same values. This demonstrates the robustness of the proposed approach to initial values used in the optimization.

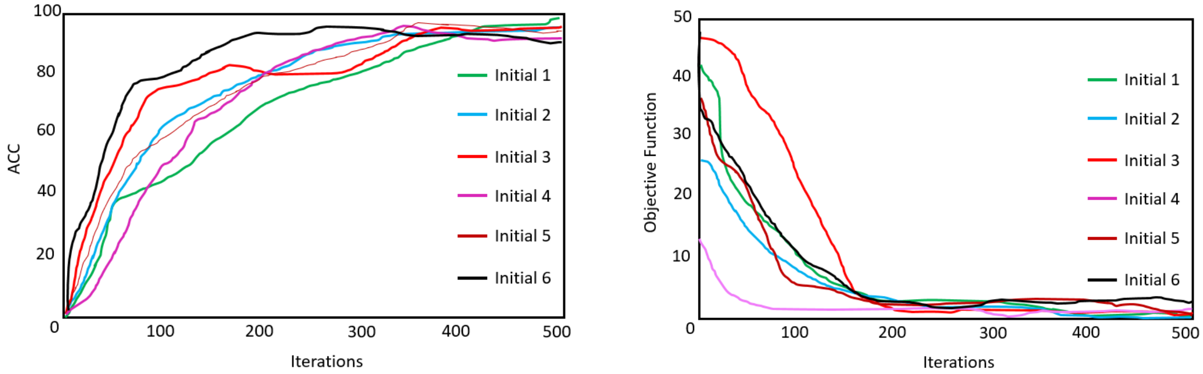

(a) (b)

Figure 4.22. Comparison of performance with different starting points; (a)convergence of accuracy (b) convergence of objective function

4.12 Results and Discussion

Defect Detection Using Experimental 3D-DIC Measurements

To evaluate the performance of the proposed approach on real-world sensing data, an experimental study was conducted where rectangular zones of damage were machined into the back side of the coupons to simulate damage unseen from the measurement surface (i.e. configurations 2-4 in Figure 4.6). For the defined configurations, the FEMs of the coupons were discretized using a mesh with an approximate element size equal to 1mm, and initially intact stiffness to initiate the optimization process. The optimization algorithm was then applied to the model of each steel coupon specimen. The response data used in the objective function was experimental static response obtained using DIC. Using the proposed hybridized algorithm, the minimization of the objective function was performed for 500 epochs. A summary of the results for the elastic modulus of the selected domain before and after optimization process for all configurations are illustrated in Figure 4.23, Figure 4.24 and Figure 4.25. As expected, it can be observed that the elastic modulus belonging to the defective regions converged to significantly smaller values when compared to the regions without any defect features. These results confirmed that the proposed approach is capable of inferring the existence and location of internal defective regions from real-world full-field sensing data, albeit the experimental data is expected to be noisier than the idealized simulation results described in the previous sections.

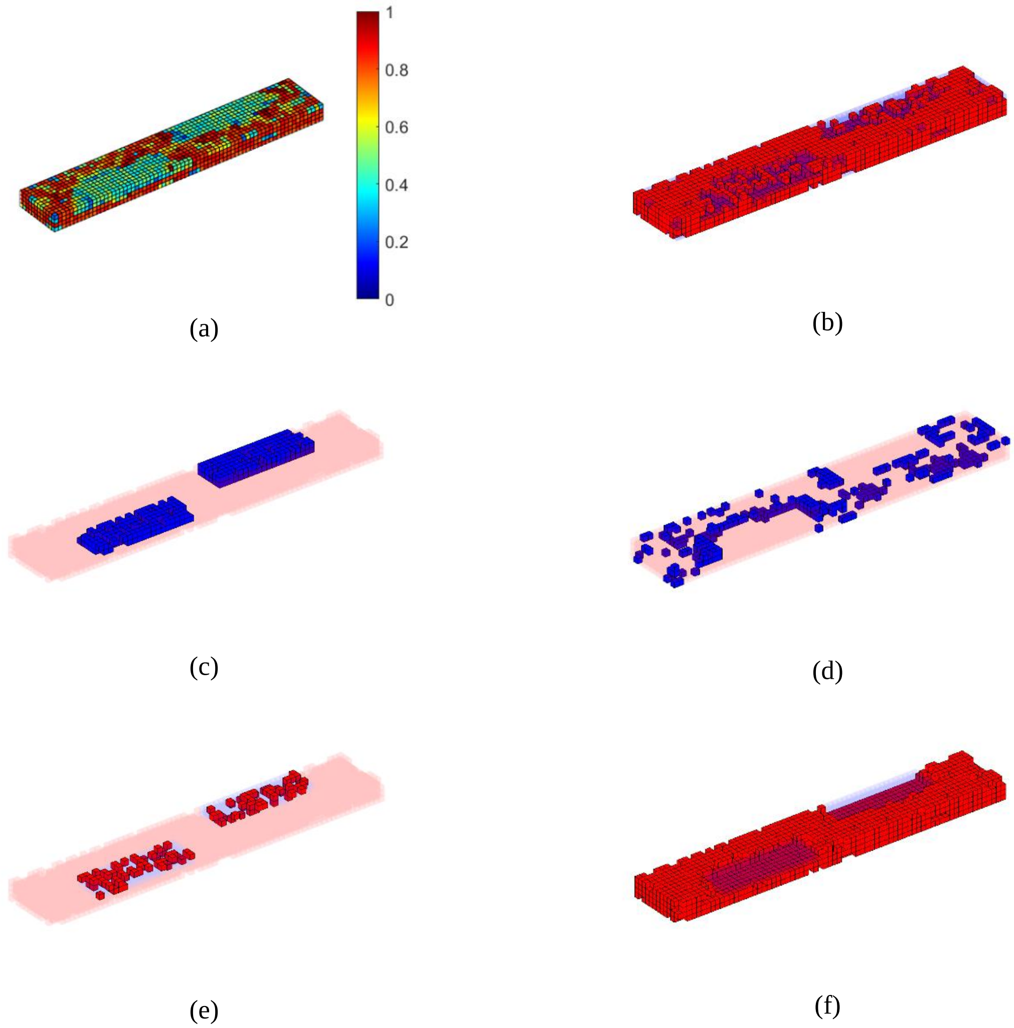

Figure 4.23. Topology Optimization results for configuration 2 in laboratory DIC experiments, (a) element stiffness parameter (x_i), (b) binary detections after thresholding, (c) true positives, (d), false positives, (e) false negatives, and (f) true negati

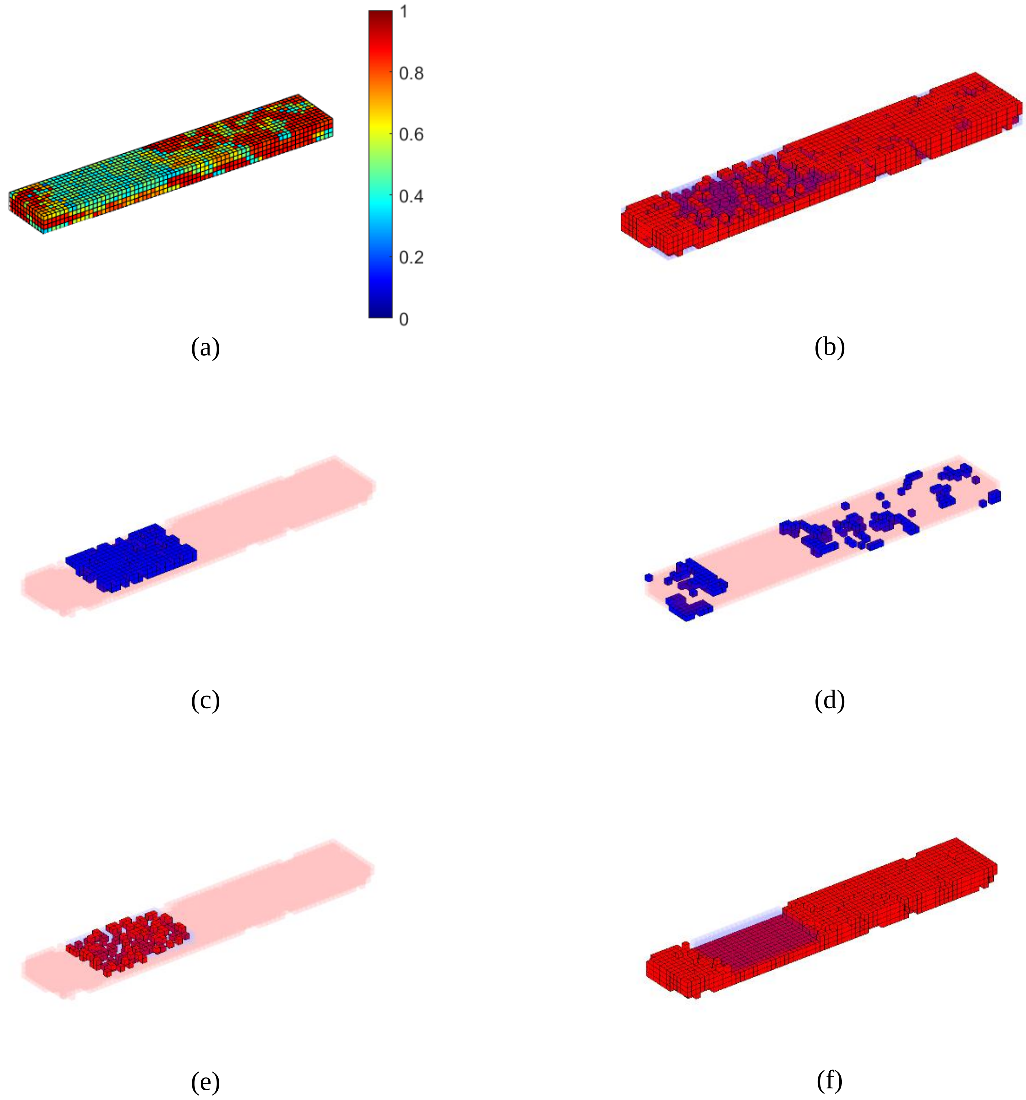

Figure 4.24. Topology Optimization results for configuration 3 in laboratory DIC experiments, (a) element stiffness parameter (x_i), (b) binary detections after thresholding, (c) true positives, (d), false positives, (e) false negatives, and (f) true negati

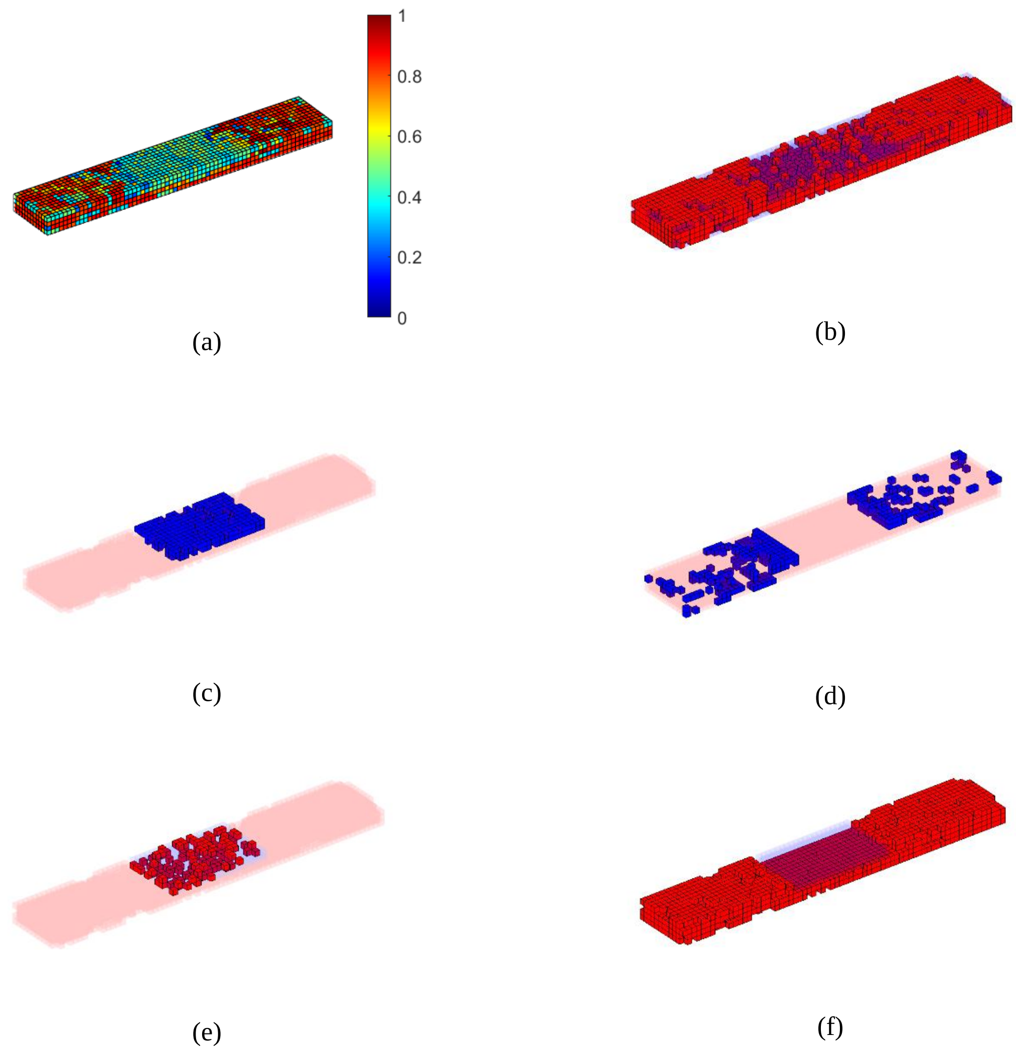

Figure 4.25. Topology Optimization results for configuration 4 in laboratory DIC experiments, (a) element stiffness parameter (x_i), (b) binary detections after thresholding, (c) true positives, (d), false positives, (e) false negatives, and (f) true negati

To quantify the performance with experimental data, confusion matrices and ROC curves are plotted for the defined configurations (Figure 4.26) and performance metrics are summarized in Table 4.4. It can be noted from these results and those in Table 4.4 that while the proposed method can successfully detect and locate damage, the performance slightly deteriorated compared with simulated experiments. This performance reduction can be attributed to potential internal non-homogeneity and the noise and uncertainties involved in the experimental setup. Some of the sources of these uncertainties include lightning fluctuations, glare, irregularities, poor quality of speckle pattern, as well as noise resulting from image acquisition (e.g. sensor noise) and quantization [49]. Moreover, the interpolation of DIC and FEM can also be a possible source of uncertainties. Briefly, in Figure 4.27, all the results of defect detections in the defined configurations are illustrated after conducting interpolation post-processing on the optimized design variables to better recognize the shape and location of the damaged region on the specimens.

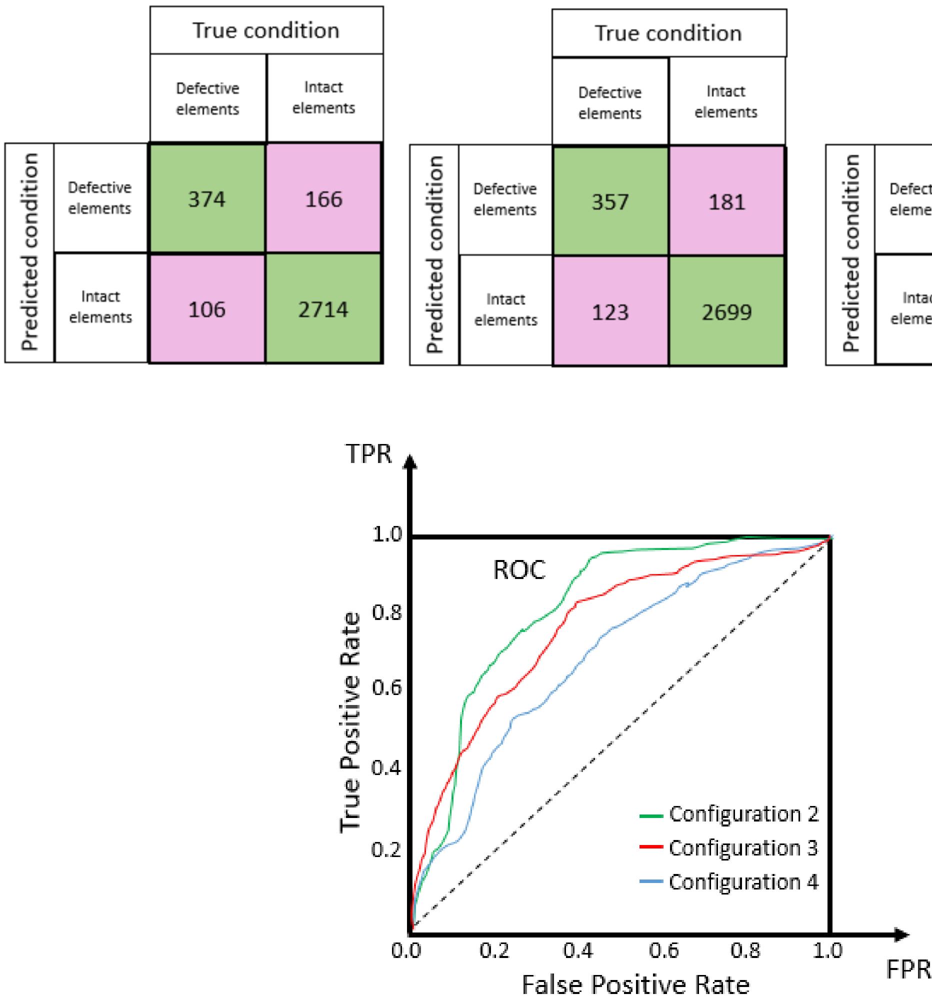

Figure 4.26. Performance of the damage detection method on simulated experiments, confusion matrix with threshold of 0.5 for (a) Configuration 2, (b) Configuration 3, (c) Configuration 4, (d) ROC curves for the three configurations with varying thresholds.

Table 4.4. Performance of the damage detection method on DIC experimental results (threshold=0.5)

Item	ACC	PRE	REC	F1
Configuration 2	91.9	69.2	77.9	73.3
Configuration 3	91.0	66.3	74.4	70.1
Configuration 4	88.3	56.6	77.3	65.3

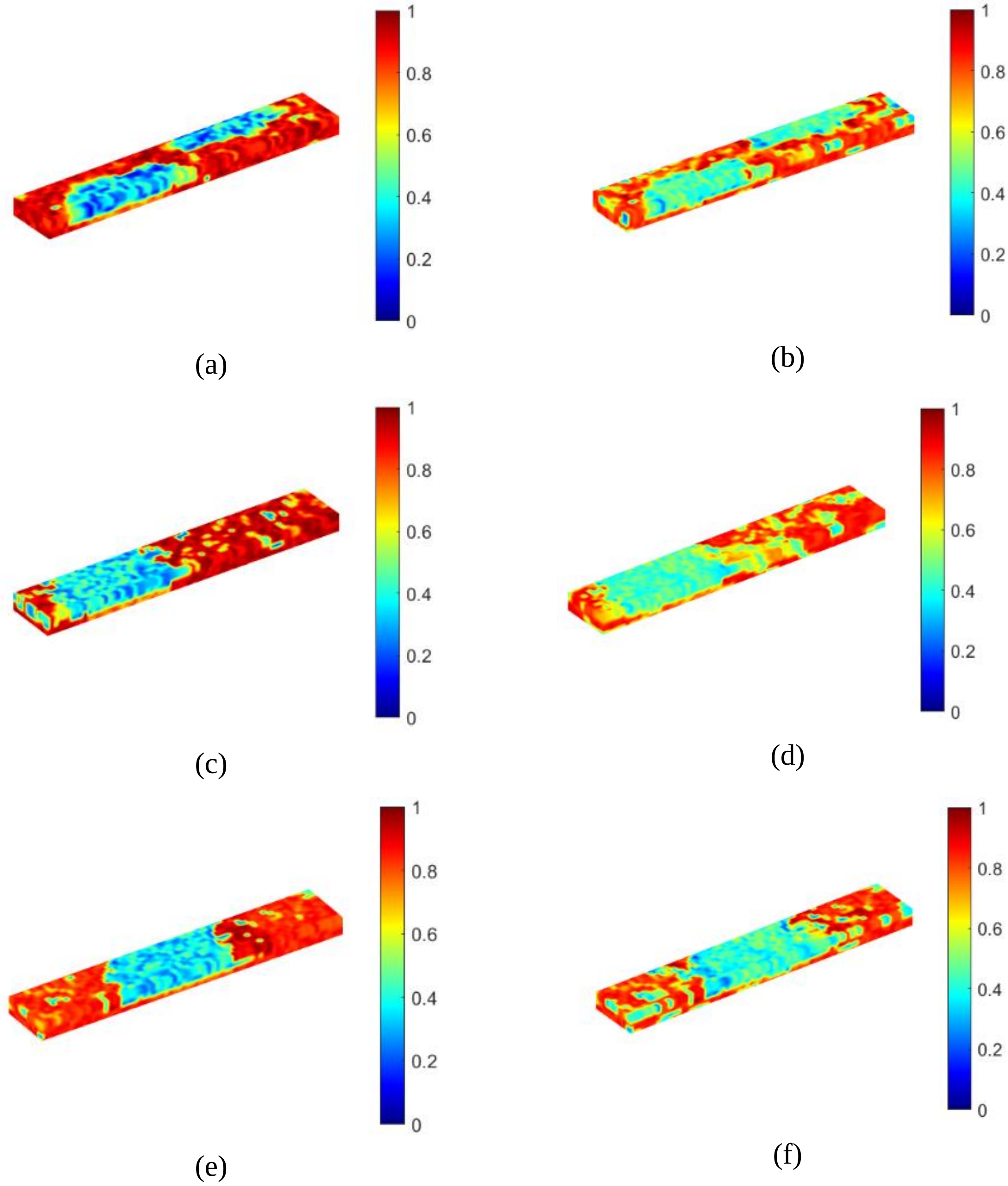

Figure 4.27. Interpolation of results for DIC and simulated data for all the configurations (a) configuration 2, simulated data, (b) configuration 2, DIC data, (c) configuration 3, simulated data, (d) configuration 3, DIC data, € configuration 4, simulated data, (f) configuration 4, DIC data

4.13 Alignment of Response from Experiment with the Optimized Model

To illustrate the success of the proposed method in adjusting the model to replicate the sensed surface response of components, Figure 4.28 show a comparison of ground truth surface strains and deflection measured using DIC with those obtained from the model after optimization together with the residual between the two. In these figures, ε_{xx} , ε_{yy}, ε_{xy} and W denote longitudinal, transverse, and shear strain, and longitudinal deformation, respectively. As can be clearly seen from Figure 4.28, the optimized model is able to replicate experimental full-field strain distributions including the complex disruptions incurred due to internal damage. It should be noted that in all of the cases, the initial model before optimization is a fully-intact specimen with a uniform stress and deflection map, and the proposed approach is shown to be able to adjust the model such that the estimated surface response closely matches that of defective specimens, thus helping to reconstruct the underlying structural deficiencies.

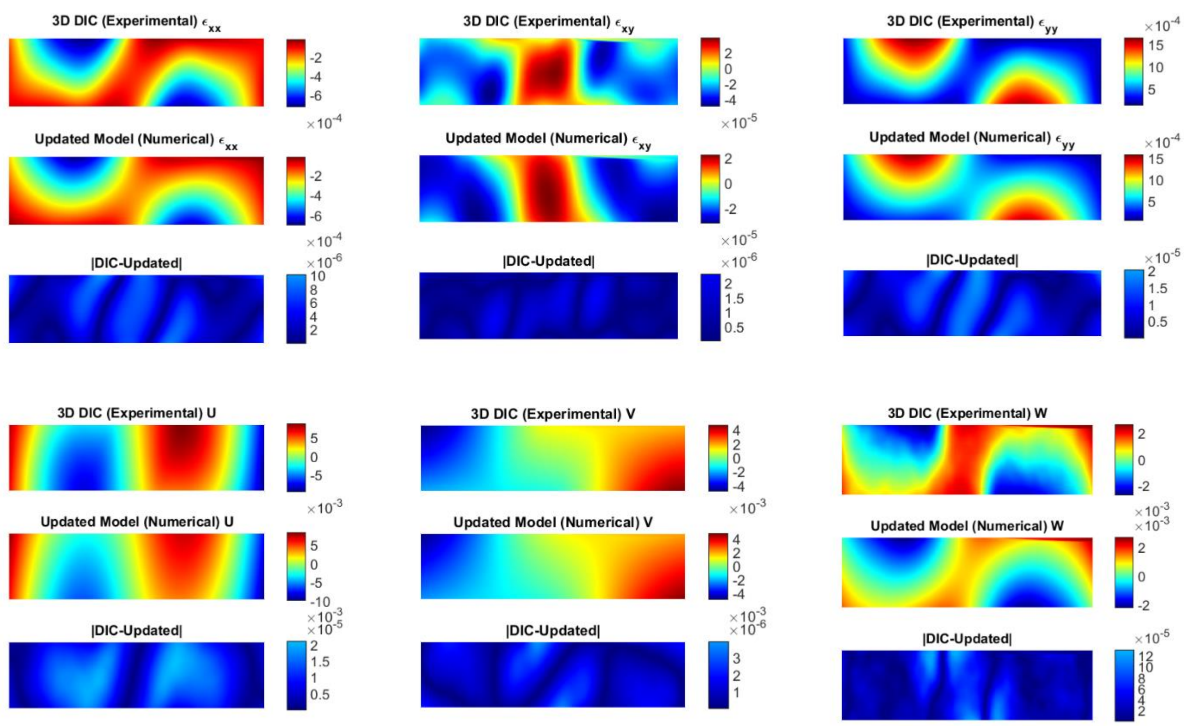

Figure 4.28. Contour plots of the experimental strain fields, the numerical strain fields and their absolute difference for the coupon with 2 defects on the back for the components ε_{xx}, ε_{yy}, ε_{xy}, U, V, W at the peak of the loading

4.14 Conclusion

This paper studied the employment of full-field structural response data obtained by DIC coupled with topology optimization for damage identification in structural components. A Solid Isotropic Material with Penalization (SIMP) based material model was defined to parametrize the optimization problem, and the discrepancy of response between real structure and the model was minimized to find the material distribution in the design domain. The proposed method was evaluated on a series of simulated and real-world experiments on tensile steel coupon specimens with artificially manufactured defects, and the following conclusions were drawn:

- The proposed approach has capability of reconstructing the damage with average accuracy-score of 96.30% and 91.90% on simulated and real experiments for configuration 2, respectively, which is indication of predicting very small number of false positive and false negative elements at the end of topology optimization. Therefore, the proposed idea was able to detect most of the elements as true positive and true negative elements. So, the proposed idea was able to find a unique solution for damage detection problem.
- Also, the ability of the proposed idea was demonstrated using average precision and recall-scores. For simulated experiments these values are 84.08% and 90.60% respectively. Also, the values for DIC experiments are 69.20% and 77.90% respectively. Interpretation of recall is that the most of the true defective elements are detected correctly. Also, interpretation of precision is that most of the defective elements are located in the true locations. Therefore, these measurements scores prove that the proposed approach was able to find a unique solution for the topology optimization problem.
- The proposed method was capable of reconstructing the damage with average F1-scores of 87.60% and 73.30% on simulated and real experiments, respectively. Three-dimensional visualization of the damage confirmed the overall success of the method in reconstructing the 3D shape of the damage, with a limited amount of spurious noisy detections that are mainly attributed to measurement noise.
- A detailed sensitivity analysis studied the effect of various factors on the performance of the proposed approach, including different optimization starting points, defect severity, sensing density, and discretization density. The method was shown to converge to similar detection results with a series of different random initiation points.

- According to the sensitivity analysis on the number of sensing points analysis, increasing the sensing density increased the detection capability of the method. This confirms the value of using full-field DIC sensing data compared with a limited set of discrete point mechanical sensor in reconstructing the detailed shape of internal damage.
- The conducted sensitivity analysis on various thicknesses for the defined defects shown that while more severe defects (higher volume) are easier to detect with the F1-score increasing by about 20% between defects of ¼ to ¾ thickness of the specimen, the proposed approach was still able to reasonably detect lower thickness defects.

In summary, the proposed approach demonstrated that the proposed method is able to successfully extract fine-grained subsurface damage information which is otherwise costly and difficult to achieve with state-of-the-art NDE/T or SHM methods and can therefore be used as a promising subsurface damage detection method.

5 CHAPTER 5 – Detecting and Reconstructing the 3D Geometry of Subsurface Structural Damage Using Full-Field Image-Based Sensing and Topology Optimization

Mehrdad S. Dizaji, Mohamad Alipour, Devin K. Harris

"Dizaji, M. Shafiei, M. Alipour, and D. K. Harris. " Detecting and Reconstructing the 3D Geometry of Subsurface Structural Damage Using Full-Field Image-Based Sensing and Topology Optimization", to be submitted."

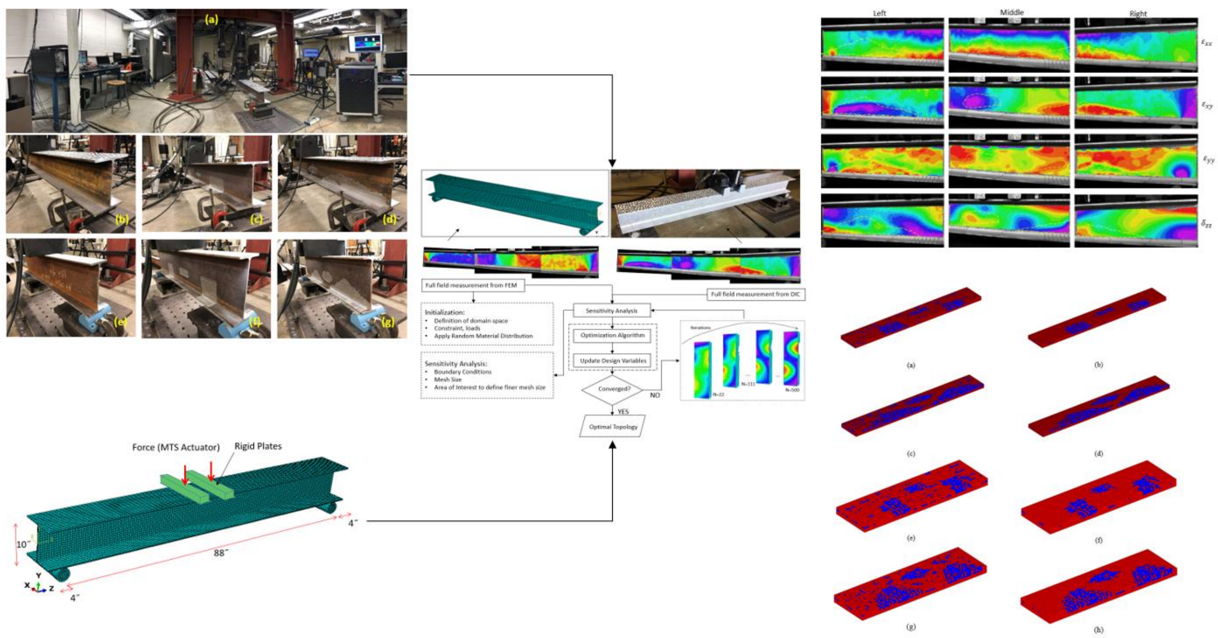

5.1 Abstract

Most of the critical defects in structural components can be invisible on the surface, mainly throughout early stages of deterioration, causing their timely detection to be a challenge. Assessing the actual and accurate 3D form and extent of interior defects is a complicated and also cumbersome task, unexpectedly with the developments in NDE techniques. Unlike the majority of traditional methods based on specialized forms of surface-penetrating waves or radiation imaging, this research uses optical cameras for full-field sensing of surface strains and deformations using the 3D-DIC technique as the basis for damage identification. This data-rich representation of behavior of the structural

component is then leveraged in an inverse mechanical problem to reconstruct the underlying subsurface abnormalities. The inverse problem is solved through a topology optimization formulation that iteratively adjusts a fine-tuned FEM of the structure to infer abnormalities within the structure.

Recently illustrated the feasibility of detecting and reconstructing the existence of 3D defects within small scale structural components such as coupons using the proposed idea. Owing to previous research, this work focuses on expanding on the work by the authors to reveal that the proposed idea can be employed on large scale structural components using the rich data from full-field image-based measurements to enable the identification of a more detailed picture of the internal defects. Thus, the goal of this research is to demonstrate the practicability and investigate the performance of the previously proposed method through an experimental program in which a sets of large scale structural components such as steel beams with and without buried defects are tested with full-field DIC sensing. A corresponding set of research steps with an increasing level of sophistication are designed to assess the capability of the approach to estimate steel material properties then to extent to infer the 3D shape of embedded defects. Upon completion, this research is expected to demonstrate the feasibility and practicality of the proposed subsurface structural components condition assessment technique and pave the way for its future implementation in existing structures.

Keywords: Internal damage, SHM, St-Id, 3D-DIC, FEM, Topology Optimization, Steel Beams

5.2 Introduction

Deterioration and damage within large scale structural components comes in a variety of forms some of which are the result of poor construction practices, while others are often the result of environmental exposure or operational conditions. Detecting structural damage is an important part of condition assessment and quality assurance of the physical infrastructure and the built environment. At the same time, it is widely known that structural damage and defects, especially those originating from adverse environmental exposure, tend to have stochastic and irregular shapes that are at least partially internal to the structural components or on hard-to-reach surfaces, and their detection and quantification is often not a trivial task. In the case of surface corrosion and distributed section loss of steel members, even when the defect is not completely invisible or internal, it can be hard to quantify on the surface, especially during earlier stages of deterioration before the defect has grown into extensive section loss, making their timely assessment and quantification challenging.

One of the approaches that can be used for assessing structural damage is NDE/T. Broadly speaking, NDE/T approaches detect internal damage based on observing differences in a physical phenomenon between an intact structure and its damaged condition. Several such methods employed on structural components to detect interior unseen defects include impact echo (IE), electrical resistivity (ER), ground-penetrating radar (GPR), half-cell potential (HCP), ultrasonic surface waves (USW), ultrasonic testing (UT), impulse response (IR), and infrared thermography (IRT). While these techniques have shown promise in detecting damage that will otherwise go undetected in manual visual inspections, they have their own disadvantages. Foremost, these techniques rely on the availability and usage of highly sophisticated testing equipment, usually including radars, scanners, or specialized signal recorders. This in turn, limits their usage to highly trained professionals and will involve high equipment and training costs. Secondly, the review of the NDE/T literature shows a widespread challenge highlighted by many researchers related to the reliability and interpretability of the results [1-5, 33-40, 48-57]. In other words, the signals obtained by these techniques can be affected in complex ways not only by the potential damage, but also by the existence of embedded reinforcing rebars, environmental effects (ambient temperature, humidity, sunlight, etc.), and surface coatings. These effects sometimes result in uncertainties and noise that can make the reliability and interpretability of the methods challenging.

A different approach to detecting damage in structures that employs mechanical response (vibrations, deformations, strains, etc.) is SHM. The mechanical response can be considered to have arguably simpler physics-based relations to underlying damage and has thus provided robust and relatively reliable damage detection performance [144-150]. SHM is a system performance evaluation strategy that describes the current state or health of an aging infrastructure through the examination of structural response recorded by means of a variety of sensing techniques. In this framework, detecting damage is usually achieved by monitoring the response of the structure and pinpointing deviations from a healthy baseline or detecting anomalies in the continuous trends of the response. Many SHM techniques have been successful in detecting damage at a global and coarse-grained level. For instance, SHM techniques based on vibration frequencies and mode shapes can inform the existence and location of damage along the length of a beam [147]. However, unlike NDE/T techniques, they can rarely provide detailed information about the shape and depth of damage and have proven most successful for large scale global damage mechanisms.

This paper introduces a new damage detection technique that has commonalities with both NDE/T and SHM approaches, but proposes new improvements that enhance its detection capability while addressing some of the limitations of these approaches. The proposed technique uses optical cameras for full-field sensing of surface strains and deformations using the 3D-DIC technique. This fine-grained and data-rich representation of behavior of the structural components is then leveraged in an inverse structural mechanics problem to reconstruct the underlying subsurface abnormalities. The resulting inverse problem is solved through a topology optimization formulation that iteratively adjusts a fine-tuned FEM of the structure. The feasibility of the proposed approach has been previously shown in a proof of concept by the authors on small-scale structural components (i.e., steel coupon specimens) [86]. Results from this proof of concept demonstrated that the disruptions to strain and deformation patterns on the surface of structural specimens can point to underlying damage (Figure 5.1). The current research therefore aims to expand on the work by Dizaji et al. [86] and to demonstrate that the rich data from full-field image-based measurements of larger-scale structural members (steel beams) can enable the identification of a more detailed picture of the internal defects at the component-level, which includes more complex damage characteristics and loading characteristics.

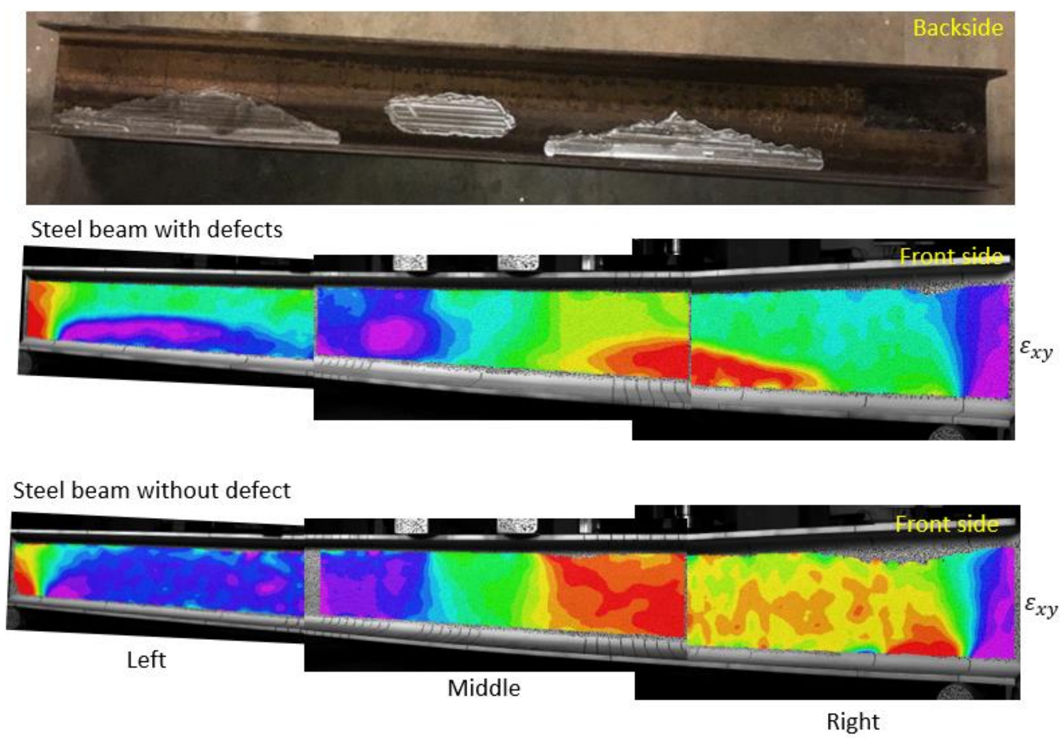

Figure 5.1. Qualitative strain and deformation patterns generated using DIC for steel beam specimens with random defects under flexural loads: (a) without any defect, (b) with two defects on the back side

5.3 Literature of the Related Work

5.3.1 3D-DIC and its applications in Civil Engineering

3D-DIC is a non-contact, full-field, optical measuring method capable of extracting surface displacement from images through a synchronized stereo camera configuration. 3D-DIC is a photogrammetric technique that leverages a correlation algorithm to map and track pattern movement and deformation from a series of sequential digital images; the sequence of images is typically captured during various stages of a specimen subjected to loading [16-21]. Images can be derived from a variety of sources (e.g. CCD, DSLR, etc.) with the choice of camera and lens configuration influenced by factors such as camera noise, lighting, acquisition speed, and geometric relationship between area of interest and field of view. A comprehensive treatment of DIC is not presented in this paper, but is available in the literature [16, 20, 22, 41, 70, 72, 77, 102, 159, 160].

Photogrammetry techniques have been investigated for assessing the structural integrity and the condition of engineering systems. They have proven to be practical approaches that can be used to evaluate the state of structural health and identify damage before in-service failures occur. In this section, a description of the principal SHM applications of DIC presented. Bridges are among the most monitored civil structures due to their strategic importance and safety issues. Nonis et al. [172] used 3D-DIC for periodic inspection of concrete bridges to locate non-visible cracks in concrete, quantify spalling, and measure bridge deformation. In a laboratory test, they demonstrated that optical based measurement correlated well with those performed using fiber optic strain gauges during three and four-point bending tests conducted on a concrete beam. Then, they used photogrammetric targets as extensometers to track the opening of joints and cracks over a 4.5-month period and a stochastic pattern to monitor the strain fields over two bridges in service. In the same study, they also used a projected pattern to quantify spalling phenomena. The same bridges were monitored for almost one year using 3D-DIC by [31, 173]. The researchers proposed a novel approach that combines the use of an unmanned aerial vehicle (UAV) and 3D-DIC to perform non-contact, optically based measurements to monitor the health of bridges. By installing a stereovision camera system on a drone payload, extensive laboratory tests, and long-term monitoring campaigns, they demonstrated the accuracy of this system in detecting structural changes and monitoring the dynamic behavior of hairline cracks and expansion joints over time. Results show that the combined 3D-DIC UAV system was able to perform structural investigations and detect changes to the bridge geometry with an uncertainty on the order of 10-5 m. These results outperformed the resolution that can be obtained when visual inspection techniques are employed, while also improving accessibility [31, 32, 173].

3D-DIC has also been employed for several other applications in the field of civil engineering. For instance, in 2017, Kohut et al. [174] proposed a vision-based method based on DIC to measure deformations of civil engineering structures under loading condition. The DIC technique and its suitability to achieve the SHM and NDE goals of identifying strain amplification or excessive deformation in regions of damage have been explored in several studies. Between 2011 and 2013, LeBlanc et al. [28-30] used 3D-DIC for the full field inspection of a 9 m long wind turbine blade manufactured for Sandia National Laboratories. The goal of the study was to extract full-field displacement and strain measurements from a composite turbine blade subjected to increasing static loading. The use of 3D-DIC allowed for observation of significant strain amplification in damaged areas, as well as discontinuities in the curvature of the blade at locations of damages. The optically-based technique was used to quantify the progression of damage as the load was applied during laboratory tests, providing more structural information than discrete point-strain measurements. Other studies performed on the same 9 m blade with embeded defects (i.e. wave defects of well-known geometry inserted at specified locations along the blade length) aimed to compare the pros and cons of different sensing techniques (e.g., DIC, shearography, acoustic emission, fiber-optic strain sensing, thermal imaging, and piezoelectric sensing) as SHM tools for detecting the defects and track the resultant damage due to fatigue testing. DIC measurements were able to reveal the areas characterized by higher levels of the strain compared to the surrounding footprint, revealing the location of the defects [166].

In addition, DIC has the potential to provide the linkage between experimental testing and computational simulations, by generating a rich full-field data-set that can be used for validation of the proposed numerical models and corresponding failure theories. It is also beneficial to use DIC to evaluate the performance of existing theoretical models in predicting the behavior of traditional civil engineering materials (e.g. concrete) across different scale levels. The discrepancies that may arise from comparing the numerical and image-based experimental data can help improve the existing models to better accommodate the size effect across scales. In 2018, Gheitasi et al. [83] developed an experimental-computational correlated study for describing the failure characteristics of concrete across two scale levels. Their work explored the extension of DIC to fully characterize the behavior of concrete across different structural scales. The investigation leveraged results from an experimental testing program at both mixture and structural member scale levels to evaluate the performance of two representative plasticity-based numerical models commonly used to describe the failure characteristics of concrete subjected to various states of stresses.

5.3.2 *3D-DIC for Material Identification Using Inverse Problem*

Moreover, DIC has potential use in the inverse problems and the identification of mechanical material behaviors by generating a rich full-field data-set that can be used for validation. In 2008, Cooreman et al. [127] developed an identification strategy using DIC measurements to identify mechanical material behavior of steel materials through an inverse problem. The basic principle of the inverse method is the comparison between experimentally measured strain fields and those computed by the FEM. The unknown material parameters in the FEM are iteratively tuned so as to match the experimentally measured and the numerically computed strain fields as closely as possible. In 2011, Robert et al. [130] used DIC to identify the hardening parameters of aluminum through developing a FEMU process which was based on different specimen geometries which induced heterogeneous strain fields. In 2015, another interesting application of DIC was studied on shape memory alloy to analyze the deformation paths and thermomechanical parameter identification. In this study the strain fields computed numerically were compared with experimental values obtained by DIC to find model parameters [126]. In 2018, Coppieters et al. applied FEMU technique and DIC to inversely identify the Hill48 yield function via a perforated cruciform specimen under biaxial tension. The FEMU technique was evaluated by comparing the results with experimental data gained from biaxial tensile testing using cruciform specimens [128].

5.3.3 *NDE/T, SHM and Damage Identification*

Structure damage and deterioration comes in a variety of forms some of which are the result of poor construction practices, while others are often the result of environmental exposure or operational conditions. Regardless of the cause, a primary challenge is that many of these mechanisms are internal to the structures and difficult to identify using traditional assessment strategies (i.e. visual inspection). These defects are usually internally localized and thus invisible during a portion of the service life of the structural member before the defect develops into a larger problem that affects the integrity of the member. Within the current state of practice, a number of NDE techniques have been proposed that primarily leverage principles of wave propagation or radiation imaging in elastic solids [143]. Some of such methods include acoustic sounding, impact echo, ultrasonic waves, ground penetrating radar, or infrared thermography. As an alternative strategy, SHM approaches rely on structural sensing to monitor and infer the state of structural health. These approaches typically employ model-based [144-146] or data-based [148-150] techniques to identify anomalies in mechanical response that point to damage. While the use of global dynamic response [147] or a set of isolated local strain and deformation response [148] has been relatively successful in providing information about basic constitutive properties and coarse-grained damage indication, the degree to which material or damage properties can be extracted has been limited. For example, using modal response for damage detection requires a minimum severity of damage to affect the measured response, and using a discrete set of sensing points (e.g. strain gages) requires prior knowledge of the behavior to decide and optimize the sensor locations and may not provide sufficient sensing resolution to reconstruct damage. While both NDE and SHM strategies have proven successful for many scenarios, there are still many shortcomings that cannot be readily addressed without highly sophisticated equipment or costly monitoring systems.

5.3.4 *Topology Optimization and Damage Detection*

Topology optimization is a mathematical framework that seeks to find the optimum structural layout and material distribution under a set of loading scenarios, boundary conditions and constraints. This approach is effective for finding the optimum design of a structure, which can be defined as one with the minimum weight or alternatively minimum compliance with a fixed material weight. A topology optimization problem usually starts with a preliminary FE model whose performance is evaluated and is iteratively fine-tuned to optimize the desired performance. In the case of structural design, once the component is discretized into a mesh of finite elements, the material constitutive properties of each element can be treated as the unknown variables of the problem. The optimization can be solved using a number of different techniques including gradient-based methods such as the optimality criteria algorithm and the Method of Moving Asymptotes, or non-gradient-based algorithms such as Particle Swarm Algorithms or GAs.

While the two problems of structural design and condition assessment and damage detection are usually regarded as different problems with construction objectives (creating a new structure versus evaluating an existing one), they are fundamentally similar in their use of structural mechanics to correlate structural properties to the observed response. This paper argues that the condition assessment and damage detection problem can be reformulated as a topology optimization problem by considering the sensing data as an additional constraint [161, 167-171, 175]. It follows that damage and defects in the existing structure being evaluated will be reproduced as cavities or soft regions within the optimized structure. A closer look at the relevant literature shows that a few papers have used the topology optimization framework for structural damage detection [162, 163, 165]. Using element-based topology optimization methods, Lee et al. utilized the Methods of Moving Asymptotes (MMA) to minimize discrepancy between some points of frequency response functions of the model and the real structure [162]. Nishizu et al. also exploited topology optimization to identify defects based on natural frequencies and by using MMA [163]. Recently, a level set based approach was proposed by Zhang et al. to find the location of damages again by considering natural frequencies [164].

Niemann et al. work focused on the development of a damage detection and localization tool using topology optimization approach [165]. The approach was based on the correlation of a local stiffness loss and the change in modal parameters due to damages in structures. The loss in stiffness is accounted by the topology optimization approach for updating undamaged numerical models towards similar models with embedded damages. In the process of experimental validation, their method could localize separate damage zones, but the results become less clear and the optimization might get stuck in wrong local optima. But it can be assumed, that the poor results for some of their cases follow from the lack of constraint data and not taking into account stain and displacement data in their optimization process [165]. These few works highlight to potential for using topology optimization within a damage identification framework, but also point to opportunities for refinement.

5.4 Proposed Study

This research aims to demonstrate the feasibility and investigate the performance of the proposed method through an experimental program in which several structural steel beam specimens with artificially embedded defects are tested with full-field DIC sensing. The proposed approach leverages full-field surface deformation measurements of structural elements derived using DIC coupled within an optimization process to search for and identify the presence of unseen damage. Figure 5.1 obviously indicates that interior damage patterns influence the surface strain and deformation fields, reflected in DIC measurements. While this prior work is promising, the concept needs further research to extend the framework towards a more robust approach that can be used for in-situ assessment of in-service structural systems. The research proposes herein centers on a laboratory scale investigation of large scale steel structural components, which exhibits variability in its constitutive properties that are typically uncertain within existing structures and is also vulnerable to internal damage that is unseen from the surface.

The proposed approach focuses on modifications to the corresponding constitutive relationships in the affected regions while maintaining original geometry. Modifications include adjustments to stiffness or overall scaling of material constitutive relationships. This approach aligns with topology optimization modification based on an iterative optimization algorithm, in which the effective stiffness (i.e. stiffness tensor components) is reduced based on the load configurations and defined objective functions. This concept is described in Figure 5.2 schematically. As it can be noted, all the elements belonging to the damaged areas such as section losses caused by corrosion are modified and optimized iteratively in order to mimic existence damage such as corrosion. Preliminary small scale steel specimen results were encouraging and opened up new opportunities to characterize the mechanical property distribution properties of structural components and damage in more complex systems such as large scale steel beams.

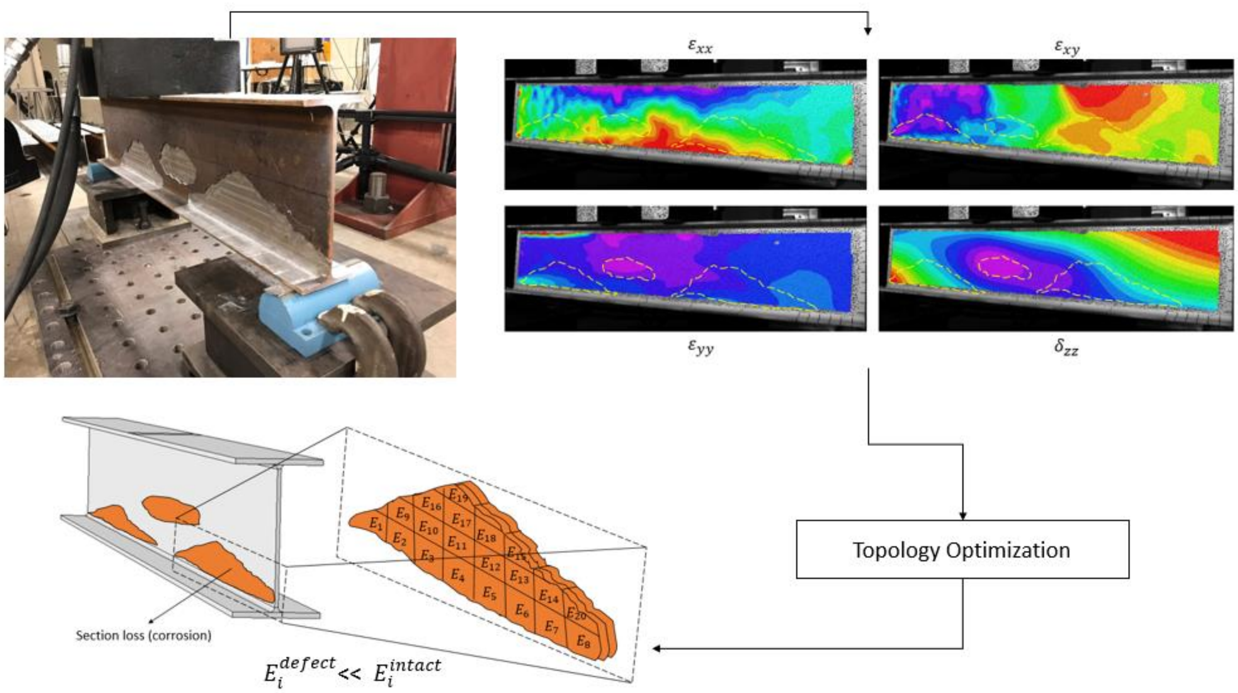

Figure 5.2. Representation of proposed modeling strategies

5.5 Research Challenges, Significance and Contributions

While both NDE and SHM strategies have proven successful for many scenarios, there are still many shortcomings that cannot be readily addressed without highly sophisticated equipment or costly monitoring systems. As such, there is a need for techniques that enable the detection of such subsurface modes of deterioration in a cost-effective and non-invasive manner. In response to these needs, the central hypothesis of this proposed research is to examine whether subsurface conditions (e.g. material properties and internal defects) can be reconstructed within a topology optimization framework through full-field surface measurements of structural response coupled with a model-based simulation. As a result, the significance of this proposed research stems primarily from its new approach to connecting SHM with NDE to create a condition assessment method based on basic structural response (strains and deformations) that does not rely on specialized NDE equipment. This is achieved by interfacing a FEM with full-field and fine-grained measurements from DIC through a topology optimization framework. The proposed concept introduces two major improvements over existing techniques:

- Unlike NDE/T techniques which depend upon specialized sensing equipment (e.g. radars or radiation-based scanners, etc.), the proposed approach applied digital cameras integrated with structural mechanics to imply subsurface conditions.
- The idea leverages the rich full-filed response data from DIC to enable the reconstruction of the 3D shape of damage, representing an advancement over current practice which has been limited primarily to identification and basic localization.

The idea of reconstructing the 3D geometry of subsurface defects via rich full-field surface sensing data can lead to major improvements in our understanding of internal properties and conditions of structures. More importantly, the proposed approach is flexible, allowing for multiple parameter identification (e.g. constitutive properties, damage and boundary conditions), which is another important improvement over the state-of-the-art NDE and SHM techniques.

5.6 Method of Study

In previous work, we proposed a new approach using full-field surface measurements together with topology optimization, on small scale structural components, to localize and reconstruct the 3D shape of unseen subsurface defects. This research aimed to expand on the previous work by the authors [86] on large scale structural components such as steel beams and to demonstrate that unlike a limited set of discrete sensing data points or global dynamic properties, the rich data from full-field image-based measurements can enable the identification of a more detailed picture of the internal defects.

The proposed idea aims to show that full-field experimental surface deformation measurements of structural members under loads can be used to optimize a FEM such that it reflects unknown internal material and damage properties. The proposed approach starts with a basic FE model of the member and compares its numerical response with DIC full-field experimental measurements.

The unknown parameters (e.g. material properties, boundary conditions, and internal damage) are then identified by iteratively minimizing the residual between the simulation and the experimental responses. The proposed process is depicted in Figure 5.3.

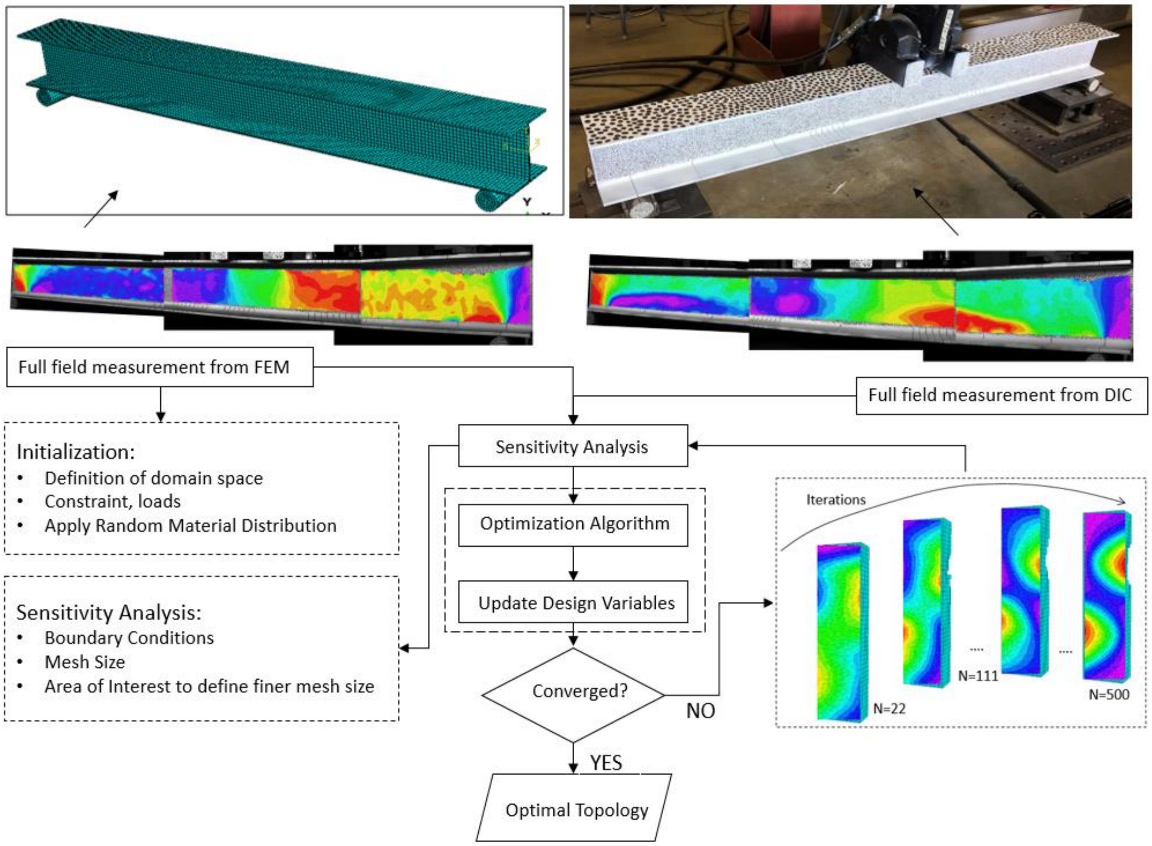

Figure 5.3. The optimization process of matching numerical (FEM) and experimental response (DIC)

The overall process used to formulate the damage detection problem in terms of a structural optimization problem can be summarized as the following step-by-step procedures:

1. At the beginning of the topology optimization process, the design region is initially discretized using the FEM introduced as an intact domain without any defects within the structure. The defected finite elements will later be recognized as voids at the end of optimization process.
2. Following interpolating both DIC and FEM responses to a common reference plane, full-field strains and displacement measurements using the DIC technique are compared with the corresponding response from the FE model and their residual is used in the objective function.
3. In each optimization iteration, element properties are treated as damage variables and are varied such that the objective function is minimized. If the damage variables are not fully converged to either the value of a void (completely damaged) or the value of a solid (completely intact) after an optimization iteration, all elements

having damage variables below a prescribed threshold are reused as damaged elements at the next optimization iteration and the remaining elements are considered intact. This process is repeated until convergence.

4. Based on the prescribed threshold, the damaged elements are distinguished from the intact elements. Then the 3D shape and location of the damaged regions are recovered successfully.

5.7 Damage Detection as a Structural Topology Optimization Problem

The optimization problem iteratively updates the material and geometrical properties such that the response (e.g. strains, deformations) obtained from the model approaches those experimentally observed via DIC. While the feasibility of the optimization procedure to identify a limited set of parameters in structural steel has been previously demonstrated by the authors [86], this work proposes to extend the feasibility study to fine-grained detection of material properties and damage at the element level in large scale steel beam members. To achieve this goal, the problem is formulated as a topology optimization problem, which is a mathematical method used to find the optimum design of a structure given a set of loads and constraints. The fundamental contribution proposed in this work is therefore to reformulate damage detection in steel members as a topology optimization problem where defects are seen as areas with significantly lower modulus of elasticity and/or mass. In other words, damage detection is achieved through optimizing the constitutive matrices (stiffness and mass) by matching fine-grained full-field measurements between the model and the experiment.

5.7.1 Optimization Problem for Damage Detection

The defect detection problem can be represented as an optimization problem where a simulated model is refined such that the residual discrepancy between the numerical response and the experimental measurements is minimized. Fine-tuning of the numerical model is executed by adjusting the stiffness distribution all over the structure through the damage variable (x). To carry out the minimization, the residuals are encapsulated in the manifestation of an objective (or penalty) function, that generally has the common form of a summation of different components of the residuals between the two responses over the region of interest. Quasi-static response data consisting of strains and deformations were utilized in the following objective function:

$$F(\boldsymbol{E}) = \sum_{k=1}^{p}\sum_{i=1}^{m}\sum_{j=1}^{n_i}\left[\left(\frac{\varepsilon_{xx,ij}^{exp}-\varepsilon_{xx,ij}^{num}(x)}{\varepsilon_{xx,ij}^{exp}}\right)^2+\left(\frac{\varepsilon_{yy,ij}^{exp}-\varepsilon_{yy,ij}^{num}(x)}{\varepsilon_{yy,ij}^{exp}}\right)^2+\left(\frac{\varepsilon_{xy,ij}^{exp}-\varepsilon_{xy,ij}^{num}(x)}{\varepsilon_{xy,ij}^{exp}}\right)^2+\left(\frac{\delta_{yy,ij}^{exp}-\delta_{yy,ij}^{num}(x)}{\delta_{yy,ij}^{exp}}\right)^2\right] \quad (5\text{-}1)$$

Where **x** is the vector of unknown design variables which are the constitutive properties of the finite elements, ***p*** is the number of experimental tests (***p*** = 1 in this work), ***m*** is the number of load steps (***m*** = 1 in this work) and ***q*** the number of data points in the DIC measurement at load step ***i***. The subscripts ***exp*** and ***num*** indicate the experimental and numerical responses, respectively. Three components of the strain tensor and the corresponding component of displacement are represented by $\varepsilon_{xx,ij}^{exp}, \varepsilon_{yy,ij}^{exp}, \varepsilon_{xy,ij}^{exp}$, , and $\delta_{yy,ij}^{exp}$ respectively, that are extracted at point j at the time *i*. Similarly, $\varepsilon_{xx,ij}^{num}, \varepsilon_{yy,ij}^{num}, \varepsilon_{xy,ij}^{num}$ and $\delta_{yy,ij}^{num}$ represent the corresponding values computed from the FEM considering an assumed stiffness distribution denoted by damage variables *x*. The proposed objective function and its components are shown in Figure 5.4 schematically.

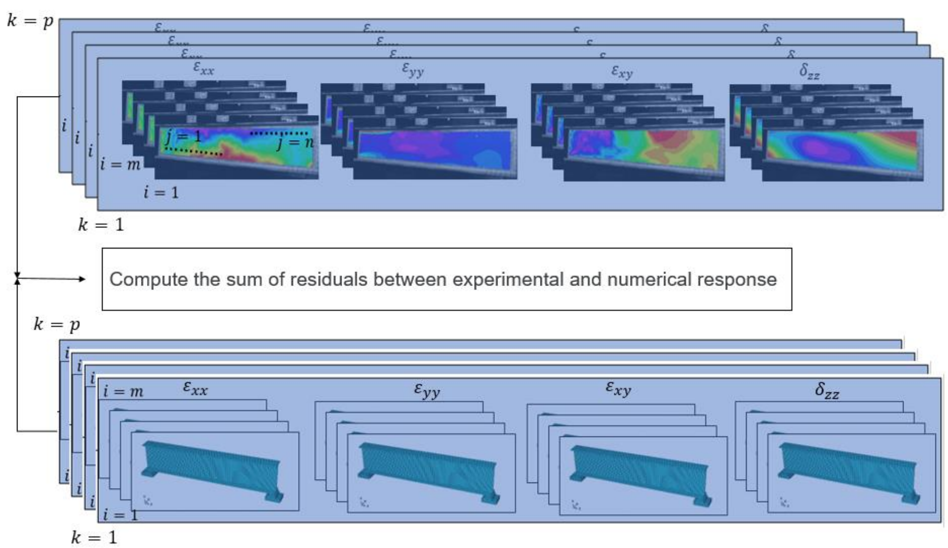

Figure 5.4. Systematic updating process between numerical and experimental results to identify unseen damage

To that end, it is required to interpolate both results on a newly-defined mesh grid. The concept of interpolation process is schematically illustrated in Figure 5.5. As it can be seen from Figure 5.5, FEA and DIC responses have different mesh grid spacing in the x-y plane. With both results mapped into a common grid, the residuals between FEA and DIC results can be calculated within the optimization process.

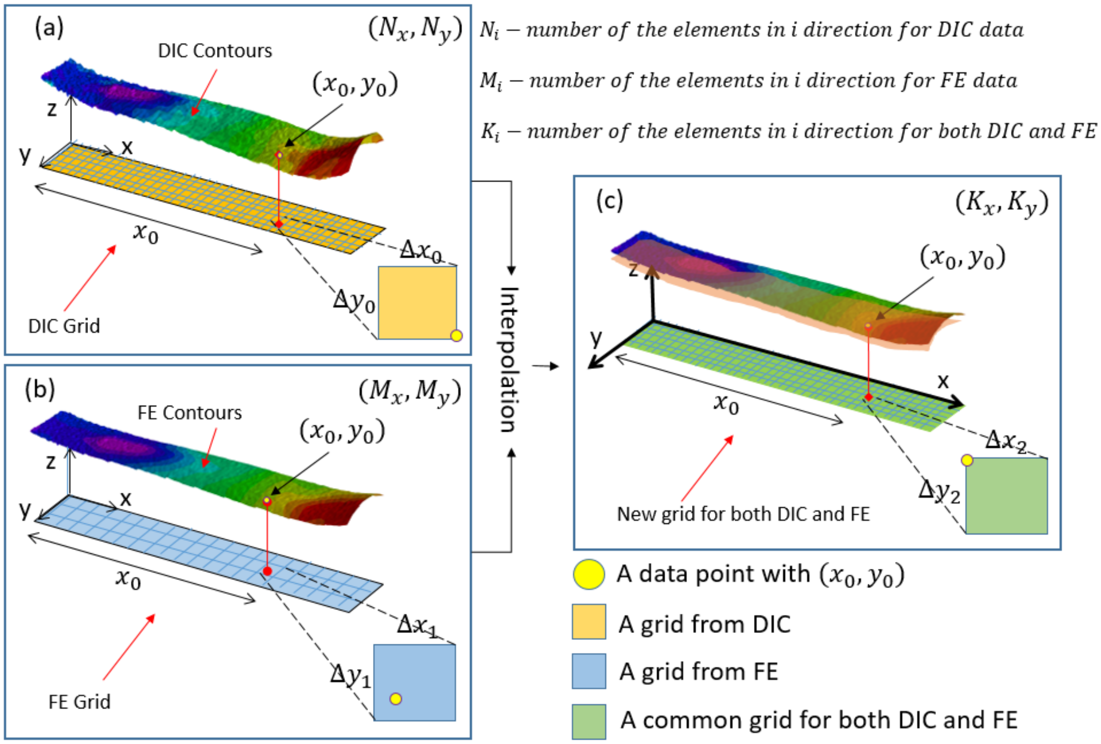

Figure 5.5. Interpolation of the experimental and numerical measurements into a common grid

5.7.1.1 *Method of Moving Asymptotes*

A fundamental component of the proposed approach is to use optimization to push the objective function to a minimum. For this objective function, the goal centers on minimizing the difference in responses between the finite element results and experimental DIC results, along with the elimination of elements describing unseen damaged regions. For this study the Method of Moving Asymptotes (MMA) optimization algorithm will be used within the optimization solution to minimize objective function. This algorithm has proven to be versatile and well-suited for large-scale topology optimization problems. MMA is a mathematical algorithm for solving smooth nonlinear optimization problems through an iterative process where a new strictly convex sub-problem is generated and solved for each iteration [171]. Each generated convex sub-problem is an approximation of the original problem with a set of parameters that set the curvature of the approximation and act as asymptotes for the associated sub-problem. The convergence of the overall process is stabilized by moving these asymptotes between each iteration. Additional details on the MMA optimization algorithm are available in the literature, but it should be noted that this algorithm was successfully utilized in the author's previous proof of concept study. The following section describes a proposed laboratory experimental program used to evaluate the hypothesis of the study.

5.8 Experimental Study

To investigate the hypothesis, an experimental study was performed. The focus of the experimental study was centered around a series of six steel beam specimens tested using the full-field 3D-DIC measurement capabilities of the structures laboratory at the University of Virginia. These include three 8 feet-long and three 4 feet-long flexural specimens to investigate the effects of member dimensions as well as damage type, size and location on the ability of the proposed approach to reconstruct material properties and damage. The selection of the specimens was based on the structural laboratory limitations such as the capacity of the actuators, boundary condition setups in the structural laboratory and the position of the actuator frames. Artificial volumetric defects representing corrosion-induced deterioration were created by a milling machine. Table 5.1 summarizes the specimens used and Figure 5.6 illustrates the geometrical properties of the beams with the embedded defects.

Table 5.1. Array of experimental specimens for the study

Configurations	Section	Length (ft.)	Web thickness (in.)	Defect thickness (in.)	Defect type
Intact	*W10×33*	8	0.29	0.15	None
1	*W10×33*	8	0.29	0.15	Controlled damage
2	*W10×33*	8	0.29	0.15	Random damage
Intact	*W10×17*	4	0.24	0.12	None
3	*W10×17*	4	0.24	0.12	Controlled damage
4	*W10×17*	4	0.24	0.12	Random damage

The specimens were subjected to concentrated loads at midspan. The loading frame consisted of a 110-kips MTS servo-hydraulic actuator to produce a concentrated load at the mid-span of the beam. In this study, a displacement-controlled loading setup was adopted, with a pre-determined maximum midspan deflection set as the limit. This limit was evaluated based on a preliminary numerical analysis to establish the minimum range of deformations that would cause the designed beam to experience flexural stresses in the linear elastic range.

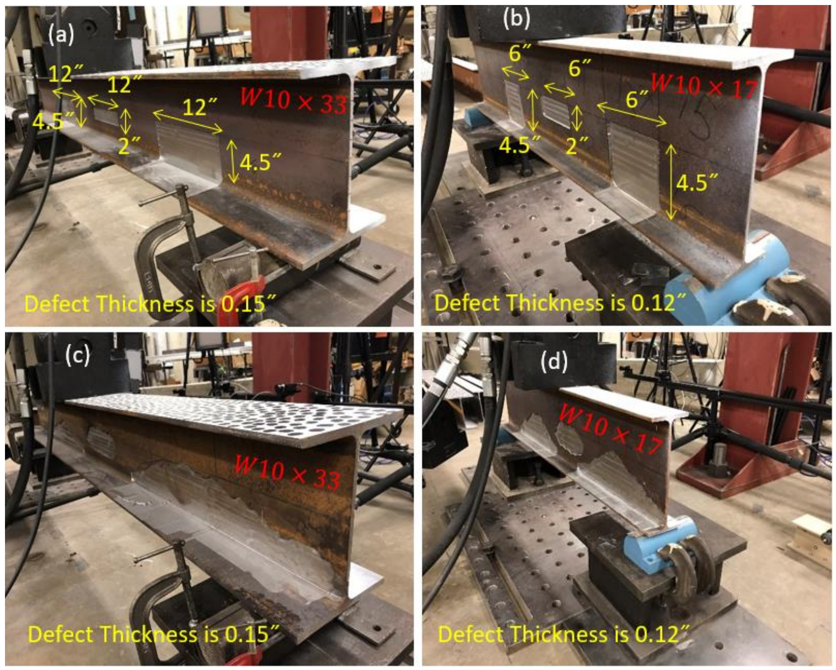

Figure 5.6. The dimension of the corresponding defects

Intact beams provided an essential ground truth reference for the overall modeling strategy, but also provide a mechanism to guide the experimental design, such that loading configurations can be tailored to yield a response pertinent to the specific state under evaluation. Also, it can provide sufficient information regarding boundary conditions. An investigation regarding the boundary conditions provides confidence that the updating process of structures for constitutive properties will not compensate with the effects of the existing boundary conditions. For these works with multiple unknowns, sensitivity of the boundary conditions versus constitutive properties of structures should be studied carefully so that the inverse problem will be executed accordingly. Therefore, the boundary conditions of the structures need to be modelled appropriately. For this purpose, two intact steel beams (configuration 00 and configuration 01) were tested to evaluate the boundary condition effects. The intact models were used in conjunction with the corresponding intact experimental specimens to update boundary conditions throughout the loading. This updating process is critical as uncertainty in the boundary conditions can have a significant effect on the overall structural behavior. Building from the intact modeling approach, models of the damaged members were developed.

After evaluating the full field displacement results from 3D-DIC on the support locations, the sufficient constraints are applied to secure miner movements of the supports. Thus, these sensitivity analysis of the boundary conditions provided confidence regarding the proper numerical simulation of boundary conditions. As it can be seen from Figure 5.7, after finishing the test and extracting the full field sensing measurements using 3D-DIC technique on intact beams, the results reveal some vertical displacements under the support which can be attributed to some flexibility of cylinders, steel pedestal and even the ground by itself. A similar observation was made in previous works by the authors [42, 104, 131, 132]. The initial goal of the updating boundary conditions was to spatially align the geometries, primarily the boundaries of the deterioration mechanisms and the numerical model.

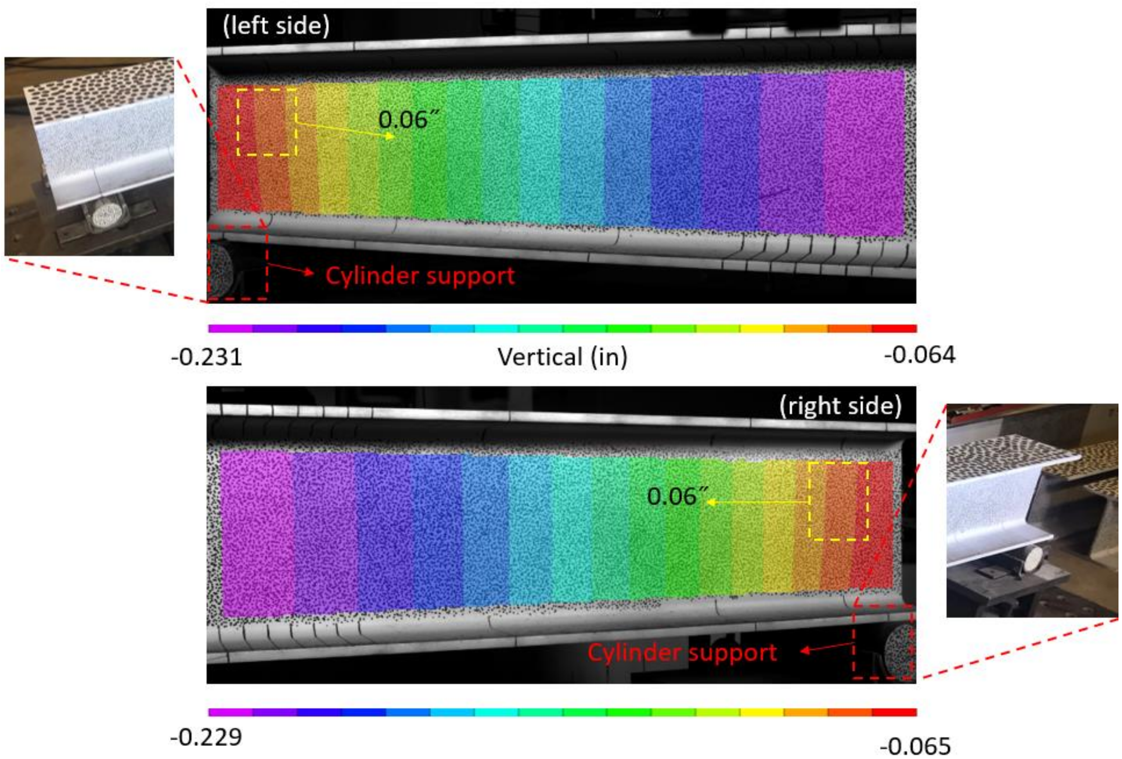

(a)

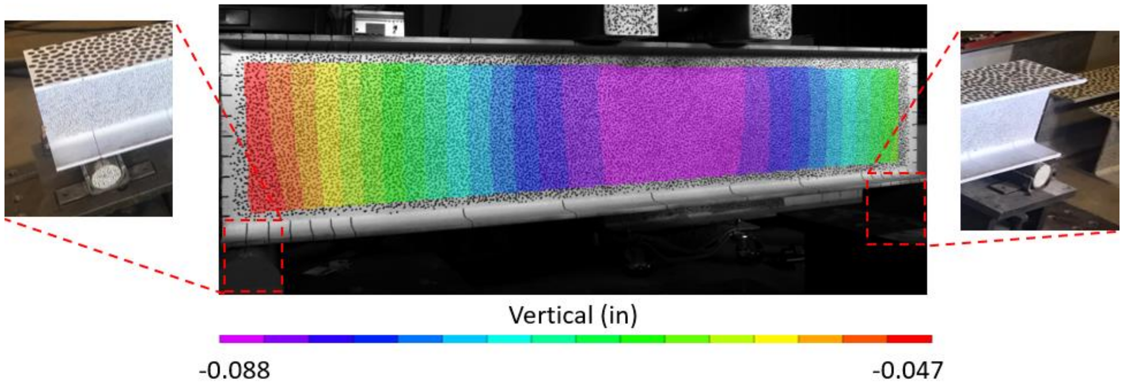

(b)

Figure 5.7. 3D-DIC experiment on support conditions (a) steel beam 8 feet long, (b) steel beam 4 feet long

5.9 Experimental setup

Illustrative experimental laboratory tests for the steel beams are shown in Figure 5.8. The tests consisted of a series of flexural loading cycles within the elastic range (ASTM A992 W10x33 and W10x17, σ_{yield}= 50 ksi) of a wide-flange hot-rolled structural steel beams. The beams were tested in the Structures Laboratory at the University of Virginia and configured for strong-axis bending. Three paired DIC camera (Point Grey Grasshopper 2.0 CCD with 5.0MP resolution) systems were used to evaluate the midspan (Schneider 8 mm lens) and two end span (Schneider 12 mm lenses) locations. The midspan camera system will utilize a different lens configuration due to the physical constraints of the load frame location relative to the test specimen.

The whole beam surface was patterned over the full depth of the beam web by applying a flat white paint base coat, followed by random speckle pattern with a permanent marker. The DIC data acquisition (DAQ) integrated output signals (load and displacement) from MTS actuators and controller to allow for simultaneous acquisition of load, displacement, and images. Figure 5.9 provides a basic illustration of the experimental setup and instrumentation configuration during testing. For each of the configurations, the beam was loaded monotonically under displacement-control, with the beam response kept within the elastic range.

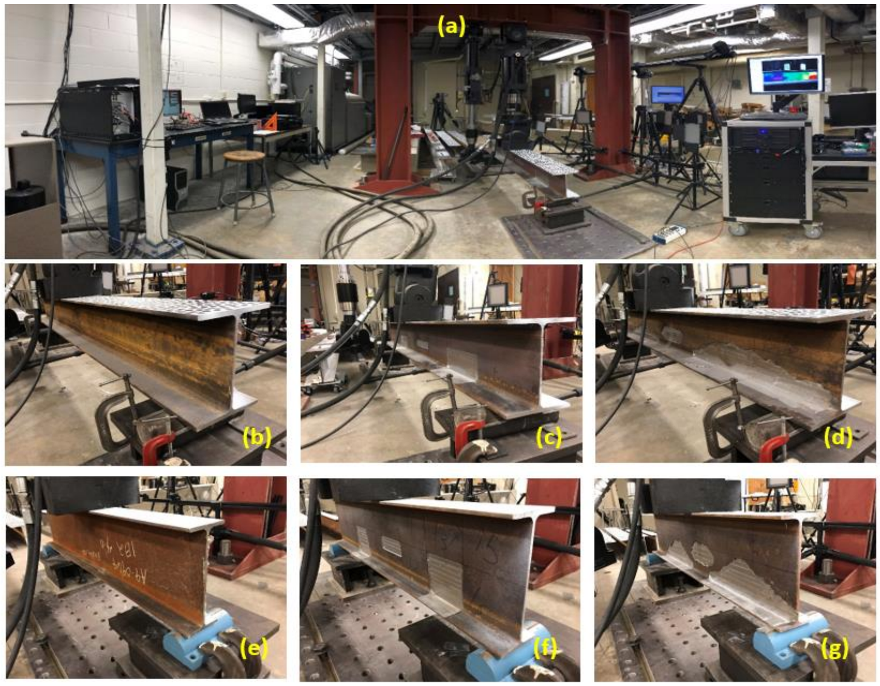

Figure 5.8. Experiment setups for steel beams, (a) Overview of experimental setups, (b) configuration, intact, (c) configuration1, (d) configuration 2, (e) configuration, intact, (f) configuration 3, (g) configuration 4

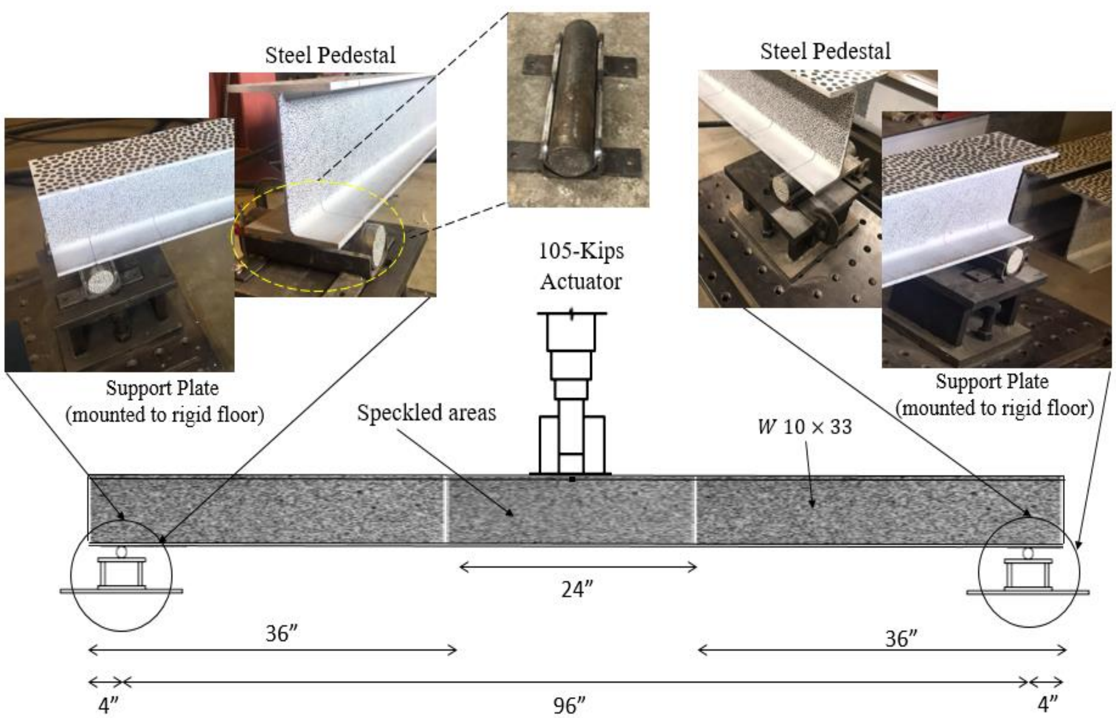

(a)

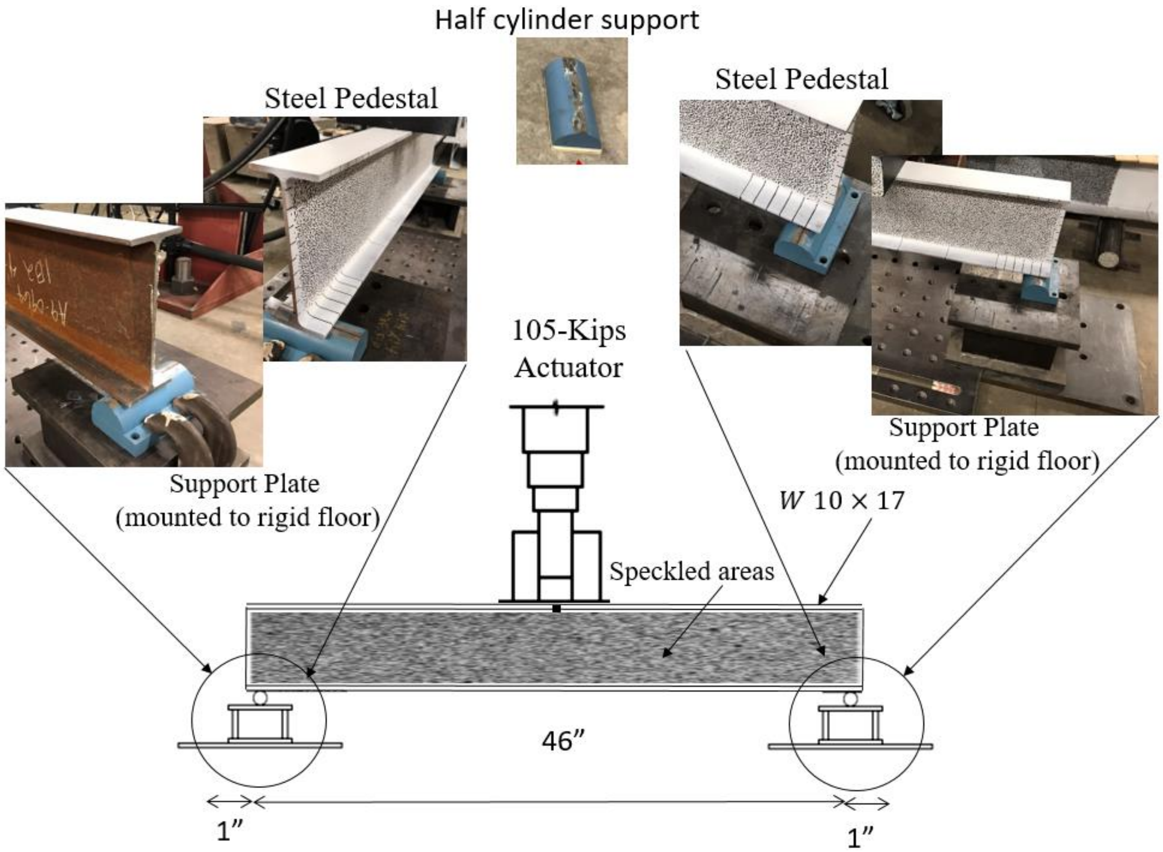

(b)

Figure 5.9. (a) Boundary and loading fixtures for configuration 1 – 2 (b) Boundary and loading fixtures for configuration 3 – 4 configurations

5.9.1 *Loading regime*

For each of the configurations, the beam was loaded monotonically under displacement-control, with the beam response maintained within the elastic range. The loading sequence consisted of loading the beam to a displacement of 0.05 in. at a rate of 0.002 in. per second, followed by a two-cycle sinusoidal loading from 0.05 in. up to a peak displacement of 0.4 in., for the large beam and a peak displacement of 0.15 in. for the small beams and concluding with an unloading through the reverse of the initial loading sequence. The initial loading and final unloading occurred over a period of 50 s (25 s each), while the sinusoidal sequence occurred over a period of 500 s (250 s for each cycle) (Table 5.2).

Table 5.2. The loading regime for the defined configurations

Configurations	Maximum Force (*lbs*)	Maximum Displacement (*in.*)	Rate of loading (in. per second)	Duration (Sec)
1	57000	0.40	0.002	550
2	57000	0.40	0.002	550
3	33000	0.15	0.002	550
4	33000	0.15	0.002	550

5.9.2 *Design of the 3D-DIC Setup (partly from our previous papers)*

The instrumentation consisted of a series of paired camera systems for acquisition of 3D–DIC images. As it is depicted in Figure xx, whole areas of the beam were painted with a random speckle pattern. For each area, a pair of CCD cameras (a total of 6 cameras in 3 systems for large beams and a total of 2 cameras in only one system for small beams) was used for data acquisition. The focal lengths of the deployed lenses as well as the distance of the cameras were adjusted to the new scale level. Accordingly, for large beams 8 mm lenses were used for the systems collecting data at the middle span, while 12 mm lenses used for the system aligned with the left/right-span of the beam (Figure 5.10). Also, for small beams 8 mm lenses were used for the system collecting data at the whole span (Figure 5.11). The corresponding details on the DIC system setup including focusing, lighting, calibration, and data acquisition followed the approach used at the mixture level, with adjustments made as needed to accommodate the conditions (e.g. field of view, lighting, etc.) associated with destructive testing at the structural component scale level.

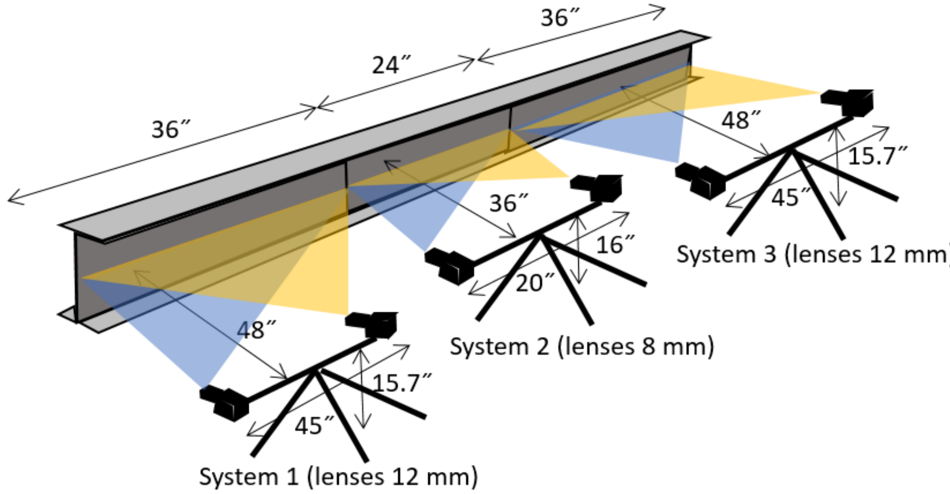

(a)

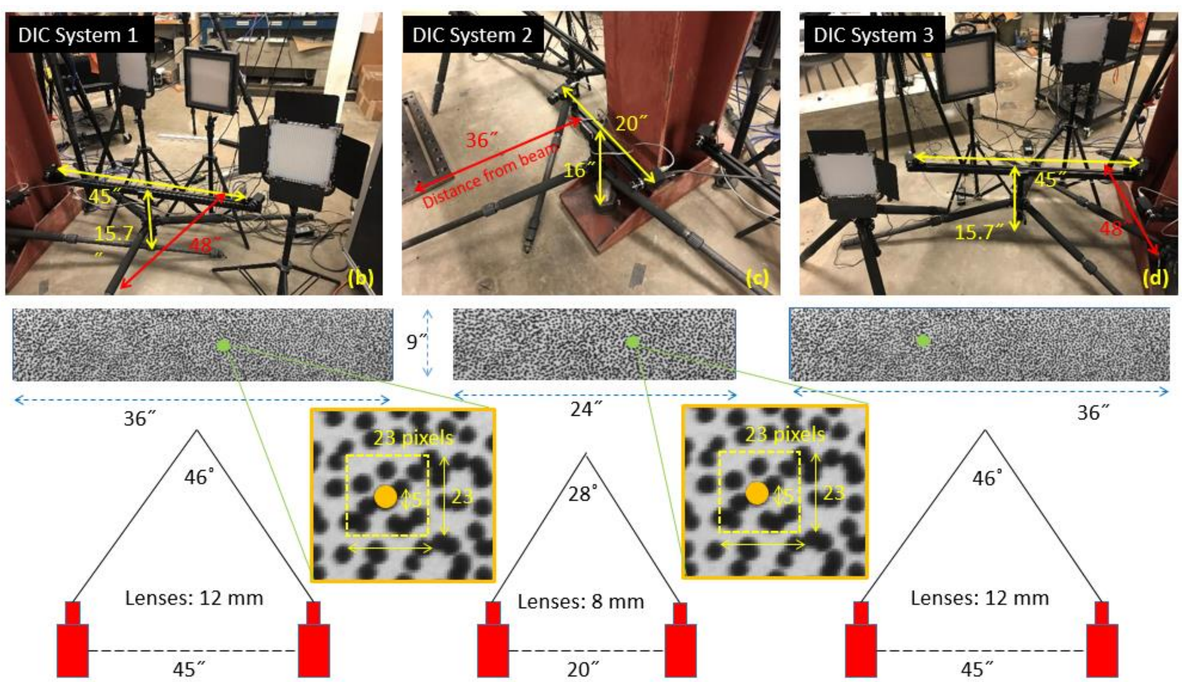

(b)

Figure 5.10. (a) Schematic of the DIC setup for configuration 1 – 2, (b) DIC setup for configuration 1 – 2

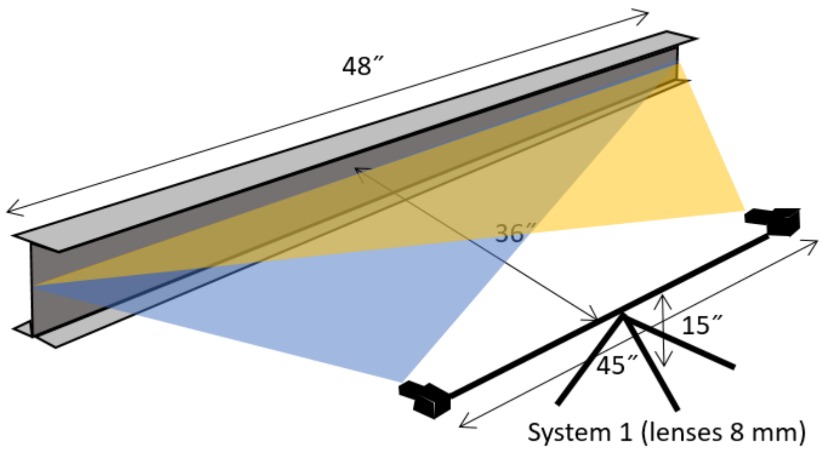

(a)

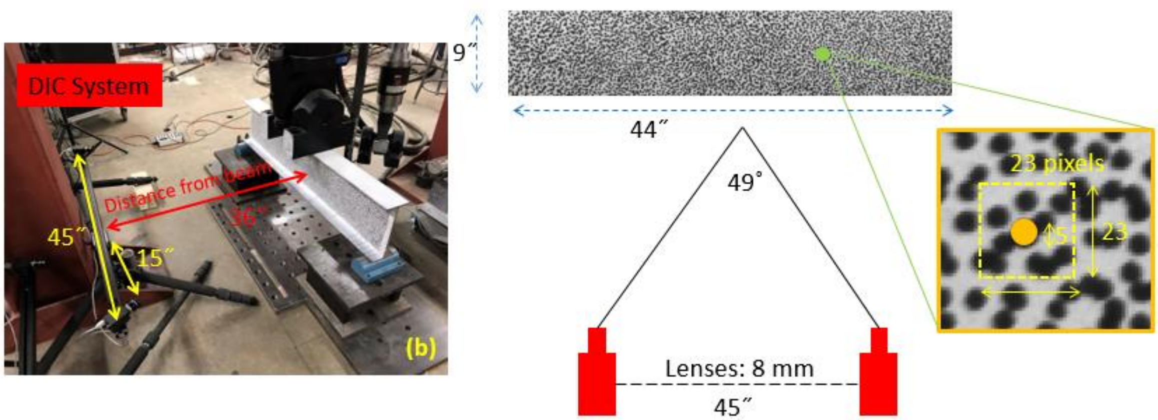

(b)

Figure 5.11. (a) Schematic of the DIC setup, (b) DIC setup for configurations 3 – 4

In terms of hardware for the image acquisition, a digital camera with an appropriate lens to provide the magnification required to see the target is needed. To determine the required specifications, the relationship between internal imaging system parameters (e.g., focal length, sensor size, pixel resolution) and the field of view (FOV) can be leveraged, using the pinhole camera relationship integrated with known camera parameters (Figure 5.12), the FOV can be written in terms of sensor size ($w \times h$), focal length (f), and imaging distance (d) (Eq. (5-2)). As it can be noted for FOV = 36 in. The size of the lens was designed to be 12 mm for system 1 and 3. Also, due to some laboratory limitation for the middle area of the beam, the imaging distance was required to be less than 3ft. Therefore, based on the calculations, the lens focal length for system 2 was selected as 8 mm. Using the proportions between the image size of objects in pixels and the physical size in millimeters, Eq. (5-3) provides a means to calculate the required dimensions. Eq. (5-4) calculates the size of objects (e.g., speckle dots) in millimeters (Sm) in terms of the pictured size in pixels (S_p), FOV, and the image width (or height) in pixels (W_p). For example, for an FOV of 914.4×228.6 mm (36×9.0 in.) and a 5-megapixel photo of size of 2448×2048 pixels, if a speckle pattern of 5 pixels is desired, the size of the dots to be painted on the target will be 2 mm (Figure 5.12b).

$$\frac{w}{W} = \frac{h}{H} = \frac{f}{d} \tag{5-2}$$

$$\frac{image\ size\ (pixels)}{FOV\ (mm)} = \frac{object\ size\ (pixel)}{object\ size\ (mm)} \tag{5-3}$$

$$S_m = \frac{FOV}{W_p} S_p \tag{5-4}$$

In preparation for testing, the surface of the test specimen was covered with a fine, dense and random speckle pattern for the correlation process. To achieve a high spatial resolution of calculated results while at the same time being large enough to be resolved in the images, the pattern had an average speckle size of 0.0787 inch (2 mm), which corresponds to approximately 5 pixels in the captured images. For the pixel tracking process in DIC, the area of interest on the speckle pattern is split into rectangular windows or "subsets" and unique patterns of speckles need to be available within each subset to allow for tracking in subsequent frames. The patterns in the subsets are tracked on a grid of a specific "step" size, which dictates the spatial resolution of the calculated points. To achieve a fine grid of unique patterns in subsets, the selection of the subset size was achieved through direct experimentation and a square subset of 23 pixels at a step of 5 pixels was selected (Figure 5.12b). Also the detailed characteristics of 3D-DIC for all the beams are described in

Table 5.3.

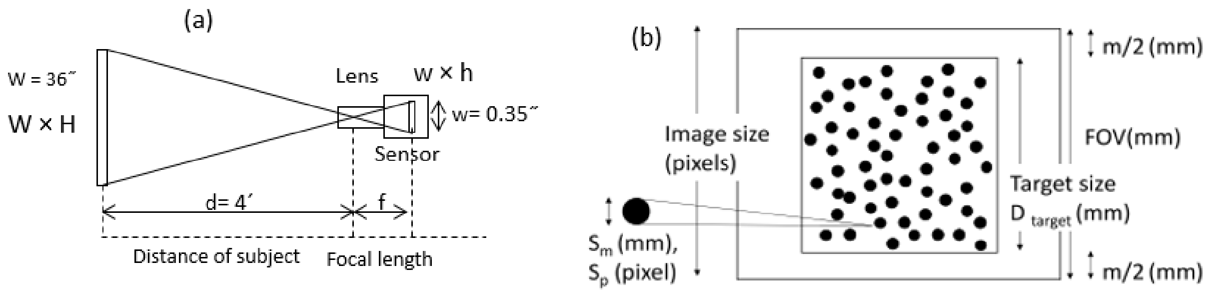

Figure 5.12. The design of DIC experiment and parameters, (a) The pinhole camera relationship integrated with known camera parameters, (b) Selection of subset size

Table 5.3. Characteristic of 3D-DIC for 8 feet long steel beam

DIC setup characteristics and Experimental setup	DIC stereo systems, 8 feet long beam			DIC stereo systems, 4 feet long beam
	Left Region	Middle Region	Right Region	Whole region
Focal Length (mm)	12	8	12	8
speckle size (Pixel)	5	5	5	5
Noise Floor (microstrain)	20	25	22	20
Distance from specimen (in.)	48	36	48	36
Distance of cameras (in.)	45	20	45	45
Cameras angles (°)	46	28	46	49
Height from ground (in)	15.7	16.0	15.7	15
AOI (in. × in.)	36×9	24×9	36×9	48×9
Pixel resolution (Pixels/in.)	64	64	64	64
Subset Size (Pixel)	23	23	23	23
Step Size (Pixel)	7	7	7	7
Calibration Grid (mm)	28	28	28	28
Software	VIC-3D-8	VIC-3D-8	VIC-3D-8	VIC-3D-8
Loading Frame	100 – kip servo-hydraulic load frame			
Type of DIC cameras	Point Grey Grasshopper 2.0 CCD with 5.0MP resolution			
Image Acquisition	Images acquired every 0.5 seconds, set of images acquired at tare load for noise estimates ~ 50 images, Load line recorded by DIC to synchronize with data acquisition system, VIC-3D Real-time module used during testing: each of the three systems was monitored. DIC results compared to predictions in real-time to identify anomalies that could influence loading decisions			

5.9.3 *Measurement noise*

Prior to employing the DIC results in the St-Id framework, it was essential to determine the acceptable noise-floor for each test. Therefore, an analysis of the measurement noise was performed. The noise-floor can be assessed during the design of the measurement to aid in the selection of different DIC hardware (i.e. camera and lens, patterning technique, lightning, etc.) and processing parameters (i.e. subset size, step size, etc.).

To assess the noise in the measurements, a series of images were captured from the zero-load state of the specimen and processed using the same settings utilized for the rest of the data. While in theory the displacements and strains should be equal to zero in the zero-load state, in practice, noise from different sources influence the measurements. Some of these sources include lighting fluctuations and glare, irregularities and poor quality of speckle pattern, as well as noise resulting from image acquisition (e.g. sensor noise) and quantization.

Table 5.4 to Table 5.6, summarizes the average and standard deviation of the displacement (U, V, W) and strain (ε_{xx}, ε_{yy}, ε_{xy}) measurements in 50 frames with zero loads. The standard deviation of the measurements quantifies the variation of the noise and can be employed as an estimate of the resolution of the measurements. To better comprehend the distribution of noise in zero-load frames, Figure 5.13, Figure 5.14 and Figure 5.15, exemplifies histograms of the non-zero displacements and strains in a sample zero-load frame. It is important that all of the no-load frames have a similar shape with a mean close to zero and a bell-shaped distribution/frequency which is in accord with the expected random Gaussian noise.

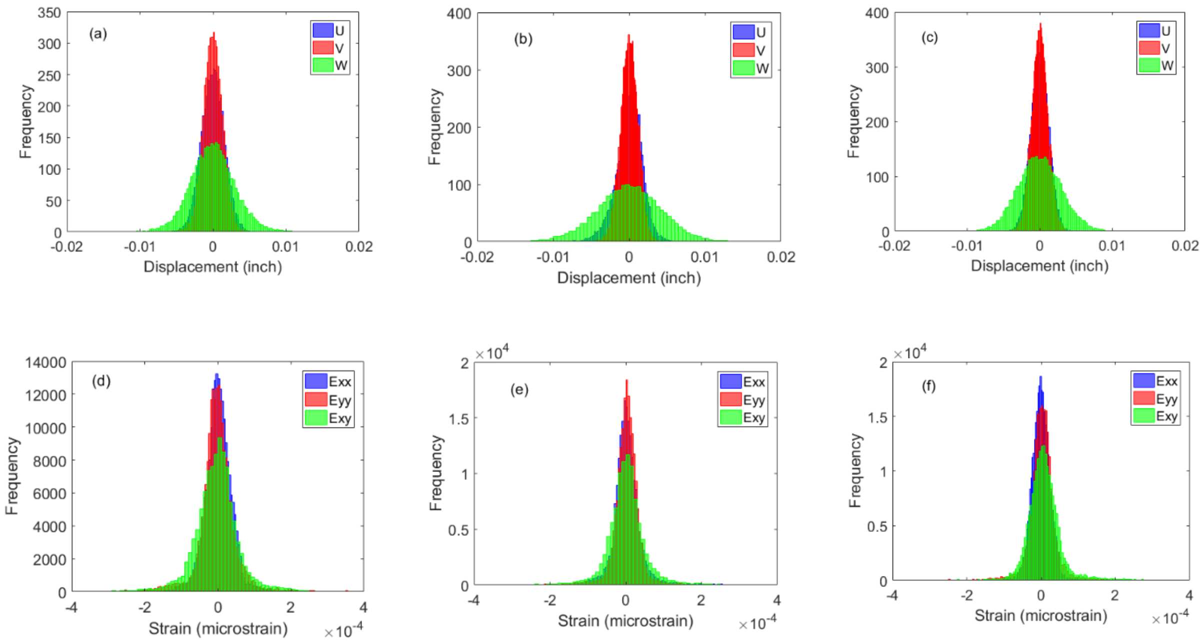

Figure 5.13. Histogram of non-zero measurements in a sample zero-load frame for configuration 1, the left column is for left region of the beam, the middle column is for the middle region of the beam and the right column is for the right region of the beam.

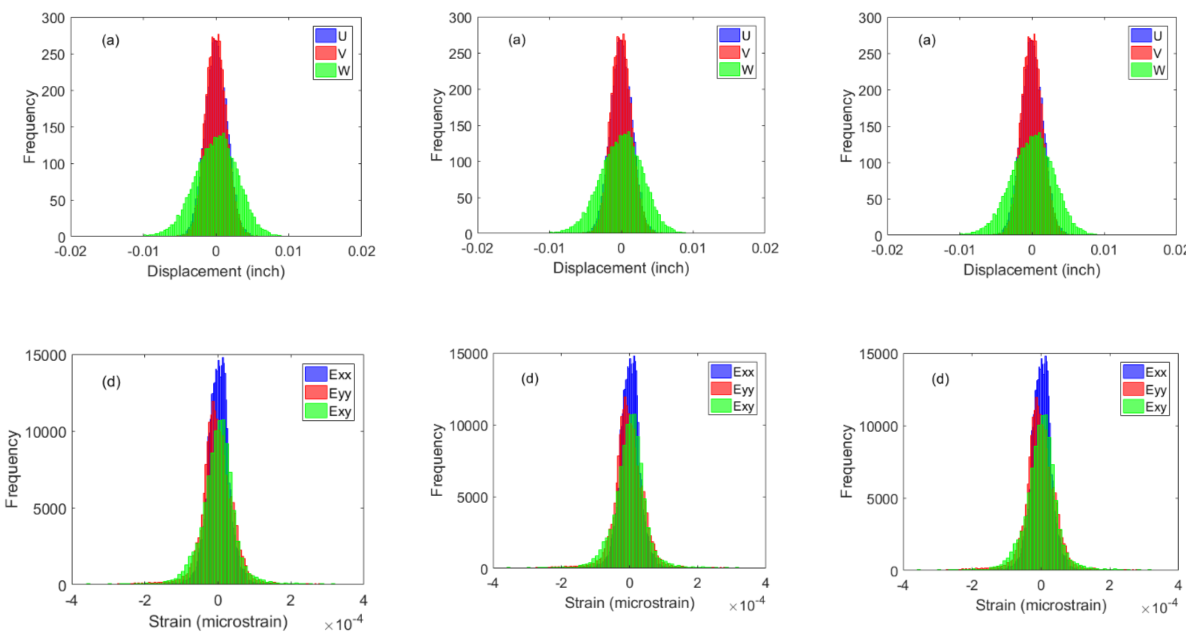

Figure 5.14. Histogram of non-zero measurements in a sample zero-load frame for configuration 2, the left column is for left region of the beam, the middle column is for the middle region of the beam and the right column is for the right region of the beam.

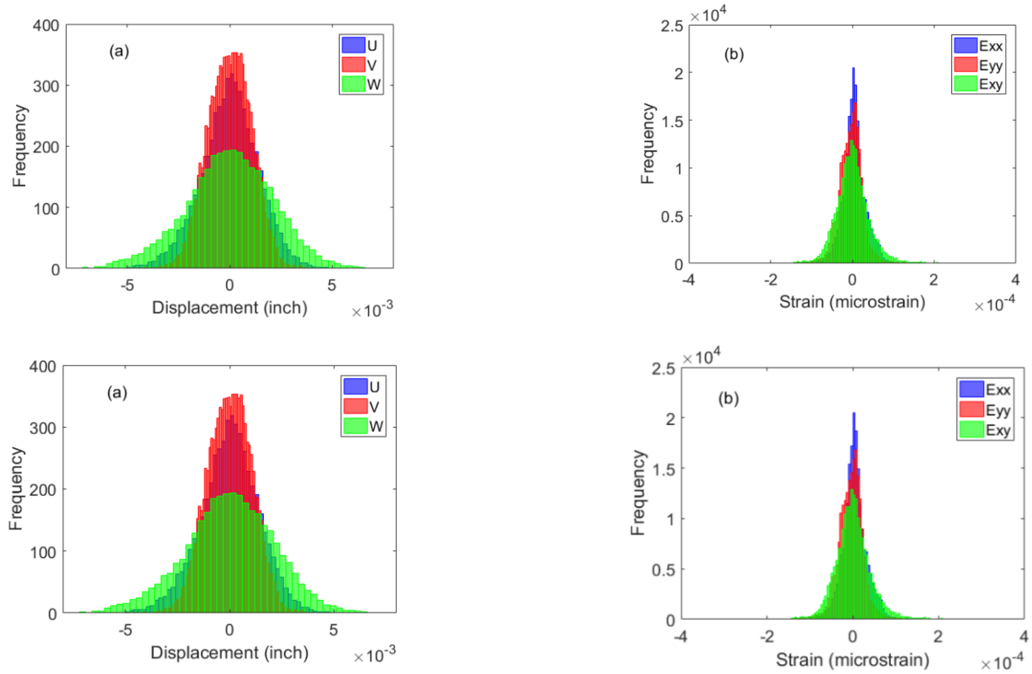

Figure 5.15. Histogram of non-zero measurements in a sample zero-load frame for configuration 3 (Top), configuration 4 (bottom)

Table 5.4. Noise statistics from measurements in 10 frames with zero load for configuration 1

Variable		Left region		Middle region		Right region	
		Mean	StD	Mean	StD	Mean	StD
U	$(\frac{1}{1000}\ in.)$	-0.10	0.63	0.09	0.41	-0.14	0.31
V		-0.12	0.67	-0.11	0.84	-0.12	0.77
W		-0.13	0.55	0.14	0.45	-0.18	0.48
ε_{xx}	(με)	-0.13	32.01	-0.74	32.44	-0.54	32.33
ε_{yy}		-0.86	55.12	0.66	55.23	-0.46	32.11
ε_{xy}		0.52	23.12	-0.32	33.12	-0.52	28.18

Table 5.5. Noise statistics from measurements in 10 frames with zero load for configuration 2

Variable		Left region		Middle region		Right region	
		Mean	StD	Mean	StD	Mean	StD
U	$(\frac{1}{1000}\ in.)$	0.15	0.51	0.17	0.61	0.23	0.71
V		0.11	0.57	0.45	0.47	0.15	0.37
W		0.14	0.63	0.25	0.43	0.38	0.55
ε_{xx}	(με)	0.69	28.02	0.61	38.20	0.45	43.24
ε_{yy}		-0.85	42.02	-0.75	43.25	0.55	28.29
ε_{xy}		0.43	23.02	0.63	54.12	0.57	17.02

Table 5.6. Noise statistics from measurements in 10 frames with zero load for configuration 3 and 4

Variable		Left region		Middle region	
		Mean	StD	Mean	StD
U	$(\frac{1}{1000}\ in.)$	-0.35	0.51	0.65	0.45
V		-0.25	0.47	-0.29	0.67
W		-0.41	0.44	-0.71	0.77
ε_{xx}	(με)	0.61	41.45	0.55	55.44
ε_{yy}		-0.71	32.64	0.74	23.88
ε_{xy}		-0.62	25.09	-0.60	17.08

5.10 Numerical Simulation

St-Id requires the development of an initial numerical model that can be updated based on experimentally derived results. In this investigation, FEMs of each loading/boundary condition scenario were developed in ABAQUS [10], a robust commercially available finite element software package. For configuration 1 - 2 scenarios, the steel beam was modeled using a total of 5442 Continuum 3D hexahedral solid elements (C3D8) with full integration and for configuration 3 - 4 scenarios, the steel beam was modeled using a total of 2214 finite elements. The size of the biggest element for the configuration 1-2 and 3-4 were 0.5 and 0.2 mm respectively. According to the view of the cross section (I) with its mesh that shows 8 and 4 element layers are used along the thickness of the web for configurations 1-2 and 3-4 respectively, with 4 elements used along the thickness of the web. The geometry was developed from standard section properties available within the AISC Manual of Steel Construction [101]. A global view of the model of the steel beam has been shown in Figure 5.16. With the model representing a relatively non-complex structural component, a dense mesh was not required; however, the mesh density was initially developed and later refined to allow for alignment with the coordinate system of the DIC results. It should be noted that ABAQUS allowed for the development of a direct interface with Python packages, a multi-paradigm numerical computing environment, which facilitated the iterative parameter optimization algorithm.

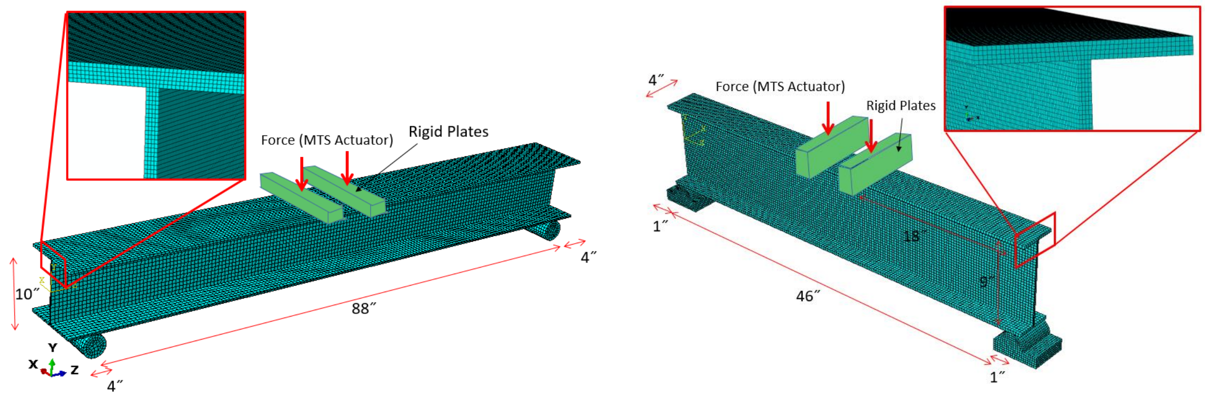

Figure 5.16. Experimental setups and FEM of the steel beams (a) Steel beam 8 feet long, (b) Steel beam 4 feet long

5.11 Performance Evaluation

To examine and quantify the damage detection performance of the proposed approach, a number of performance metrics were used as defined and described in this section. Accuracy (ACC) is the ratio of all correct predictions over all predictions, and recall (REC) and precision (PRE) are the ratios of correct defect predictions to total defective elements, and to all defect predictions, respectively. F1 score is the harmonic mean of precision and recall and is used to provide an aggregate metric of classification performance. Equations 5 to 8 summarize the definitions for these performance metrics. In defining these criteria, defective and intact elements were referred to as positive (+) and negative (−) instances, respectively, and TP, TN, FP, and FN refer to true positives, true negatives, false positives, and false negatives, respectively, and shown in Figure 5.17.

$$ACC = \frac{TP+TN}{TP+FN+TN+FP} \tag{5-5}$$

$$REC = \frac{TP}{TP+FN} \tag{5-6}$$

$$PRE = \frac{TP}{TP+FP} \tag{5-7}$$

$$F_1 = \frac{2\times PRE\times REC}{(PRE+REC)} \tag{5-8}$$

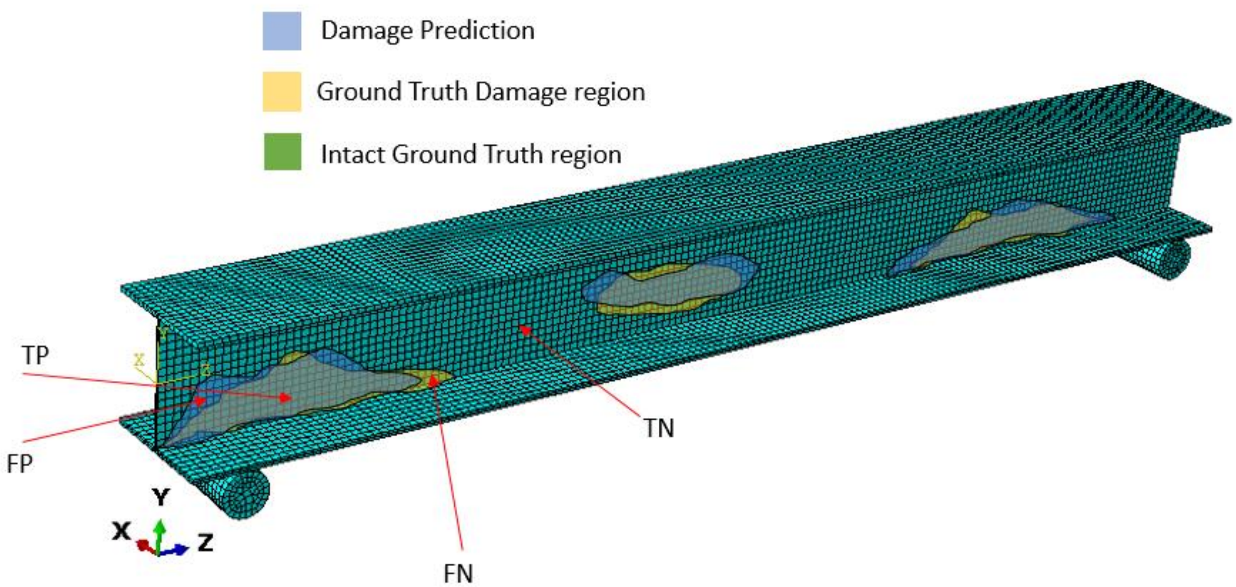

Figure 5.17. Performance metrics

5.12 Discussion and Results

To evaluate the performance of the proposed approach, controlled rectangular/random distributed zones of artificial damage to mimic the effect of real corrosion, were fabricated into the back side of the steel beams (i.e. configurations 1-4) to mimic invisible damage on a component. For the defined configurations, to detect the unseen damage by the proposed technique, the initial FEM of the beams was created and all the finite elements were considered within the updating process, as inputs into an objective function aimed at simultaneous local and global system parameter identification. According to the proposed method, after the optimization process the value of the elasticity modulus for all the elements which belong to defects would be expected to decrease dramatically to infer of existence defects in the regions.

To compare the results from DIC and FEM, it was necessary to interpolate the data from DIC and FEM onto a new defined mesh grid. With both results mapped onto a common grid, the discrepancy between FEA and DIC results could be used within optimization process. For configuration 1-2, the number of the discretized grid points from FEM and DIC before the interpolation process and also the number of sensing points after interpolation on the common grid were 600×80, 350×70 and 160×24 respectively. Also, for configuration 3-4, the number of the discretized grid points from FEM and DIC before the interpolation process and also the number of sensing points after interpolation on the common grid were 300×50, 250×40 and 80×24 respectively. Within the interpolation process both results from DIC and FEM were mapped within a common introduced grid to acquire residual of both results to utilize in the defined objective function during optimization procedure.

Using the proposed topology optimization algorithm, the minimization of the objective function was performed for 500 epochs. In Figure 5.18, the region of interest of the steel beams which are selected as design variables to be modified during topology optimization process are shown. As illustrated in Figure 5.18, in the FEM of the beams, the stiffness of the corresponding elements belongs to the selected regions which are chosen as design variables are adjusted during topology optimization process.

The summary of results for the elastic modulus of the elements after the optimization process for the configurations 1 and 2 are illustrated in Figure 5.18. As previously mentioned, configuration 1 is 8 feet long steel beam with fabricated controlled rectangular defects within the back region. Moreover, configuration 2 is 8 feet long steel beam with machined random defects within the back region to mimic the effects of real corrosion. For the introduced configuration, after the topology optimization process, it was observed that most of the elastic modulus of the elements belonging to the defect regions exhibit values less than those in the region without any defects. Thus, the proposed topology optimization based approach manifested the capability of implying the existence of defect regions from constitutive property of material appropriately. In Figure 5.18, the color levels of the finite elements correlate to the x_i values (x_i is defined as design) consequently, lower values stipulate decreased stiffness indicating the existence of damage. According to each one of the results in Figure 5.18, the general shape and location of the damage is successfully recognized in each case together with some fictitious noise detections.

Furthermore, to study the performance of the proposed method on different structural elements, configurations 3 and 4 are selected. The summary of results for the constitutive properties of the design variables after the optimization process for the configurations 3 and 4 are displayed in Figure 5.19. Configuration 3 and 4, the four feet long steel beam with manufactured defects on the back region. Similar to previous configurations, following the topology optimization process, the observation indicates that the majority of the constitutive properties (elastic modulus) of the elements affiliated with the defect regions exhibit lower values when compared to the regions with no defects. Therefore, again the approach illustrated the capability of implying the existence of defect regions from constitutive property of material appropriately. According to the results in Figure 5.19, the general shape and location of the damage is properly replicated in each case together with minor factitious detection noise which are removed after utilizing post processing step accordingly. Convergence of the objective function and accuracy of the specimens is denoted in Figure 5.20, revealing that the optimized constitutive properties belonging to each of the finite elements is well tuned using merely surface strain and displacement fields and that both the objective function and accuracy come to a steady plateau with adequate iterations.

To enhance accuracy of the detected damage regions a post-processing approach has been applied: an algorithm that looks at the positive detections (elements detected as defect, those with $k<0.5$). A general assumption regarding the continuity of the defects, and their manifestation within a structural component allows for a smoothing of FP/FN predictions that are in isolation. The assumption builds from the premise that defects in the systems are seldomly a set of isolated and disconnected points which means if a defective element is alone by itself or by less than a number of elements (e.g. the number is less than 10 elements), it probably belongs to the incorrect prediction rather than a defect. In another way, also, we can set a threshold for the size (volume) of individual connected components and remove those below a specific threshold volume. The rationale for selecting 10 as the number of isolated elements is that the defect size of interest can be determined by the expert based on the application; for example, a corrosion detection smaller than 25 mm by 48 mm is not large scale structural application. The results after applying the post processing step are shown in Figure 5.21. As seen in Figure 5.21, the minor spurious detection noises (False Positive elements) are eliminated using post processing step accordingly. The results for configurations emphasize high performance of the proposed method in detecting and correlating the shape and location of the defect properly.

To quantify the performance of the topology optimization based approach on identifying damage region within the defined configurations, confusion matrices and ROC curve are depicted for the configurations (Figure 5.22) and performance metrics are outlined in Table 5.7. The appearance of confusion matrix generally displays the higher concentration of the detections around the true-prediction diagonal. Figure 5.22b also exhibits the ROC curve for the configurations, which demonstrates the trade-off between the ability of the model to recognize truly defective elements, while avoiding false alarms, with varying values of threshold. As it can be realized from the figures, all the four configurations show a relatively similar detection behavior.

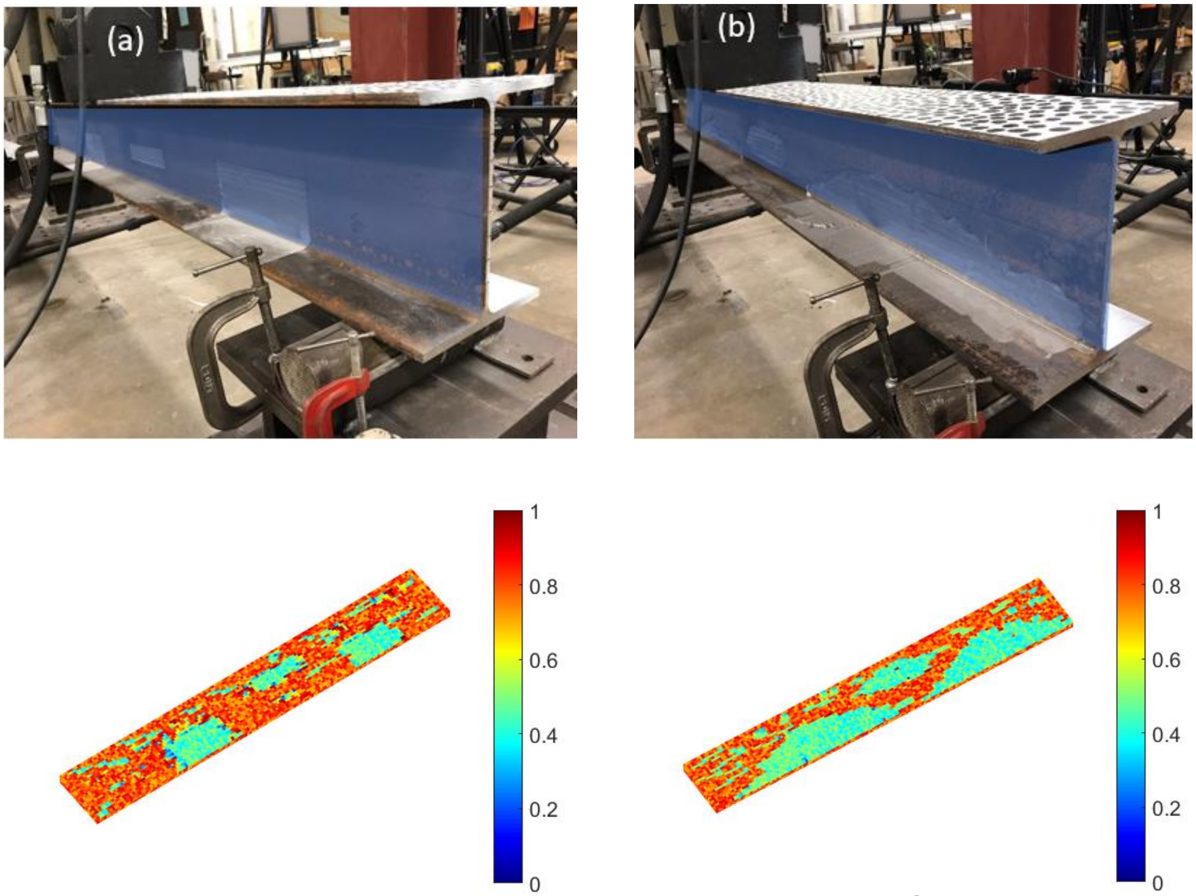

(c) (d)

Figure 5.18. Topology Optimization results for configuration 1 – 2, non-binary architecture containing varying mixtures of solid and void at all locations, (a) The web region for configuration 1, (b) The web region for configuration 2, (c) non-binary results for configuration 1, (d) non-binary results for configuration 2

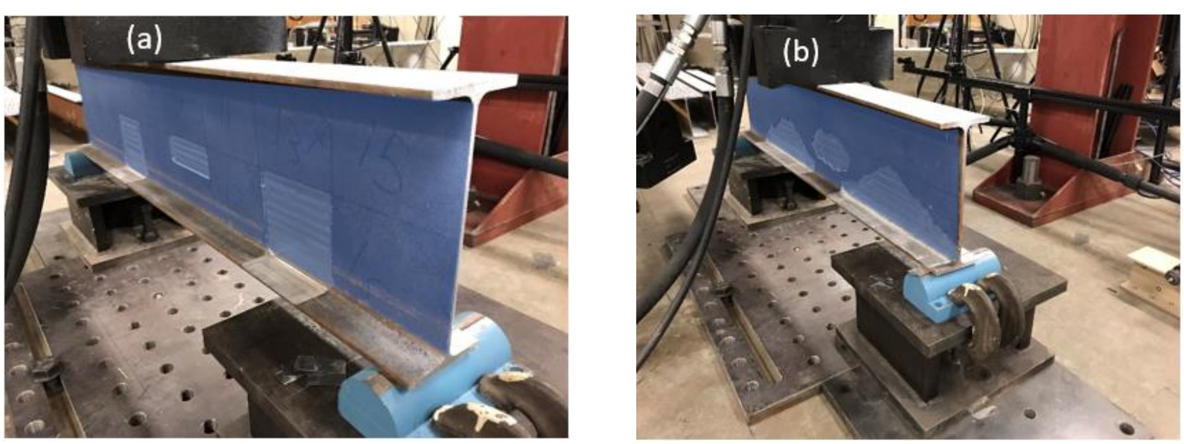

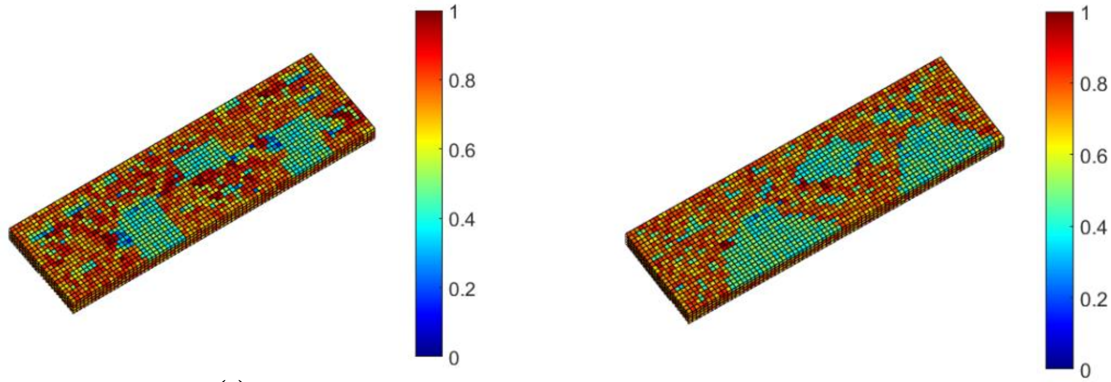

(c) (d)

Figure 5.19. Topology Optimization results for configurations 3 – 4, non-binary architecture containing varying mixtures of solid and void at all locations, (a) The web region for configuration 3, (b) The web region for configuration 4, (c) non-binary results for configuration 3, (d) non-binary results for configuration 4

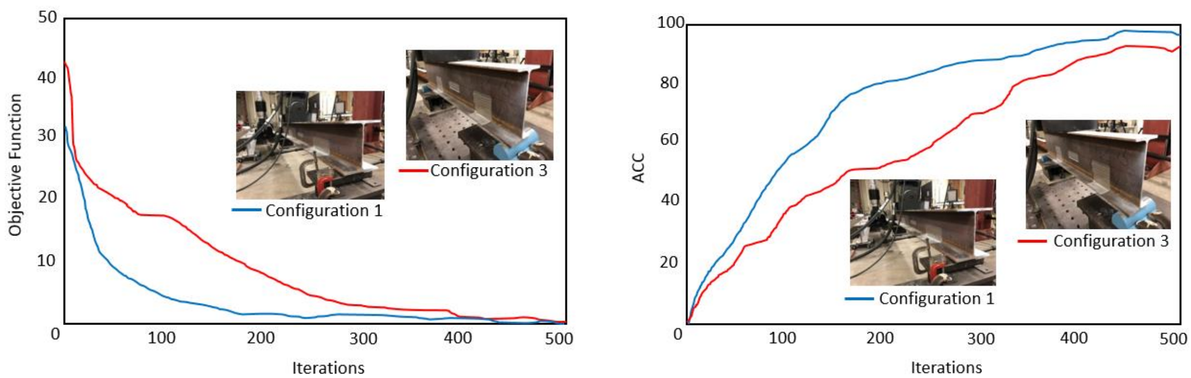

(a) (b)

Figure 5.20. Convergence of the defect detection process: (a) objective function, (b) accuracy

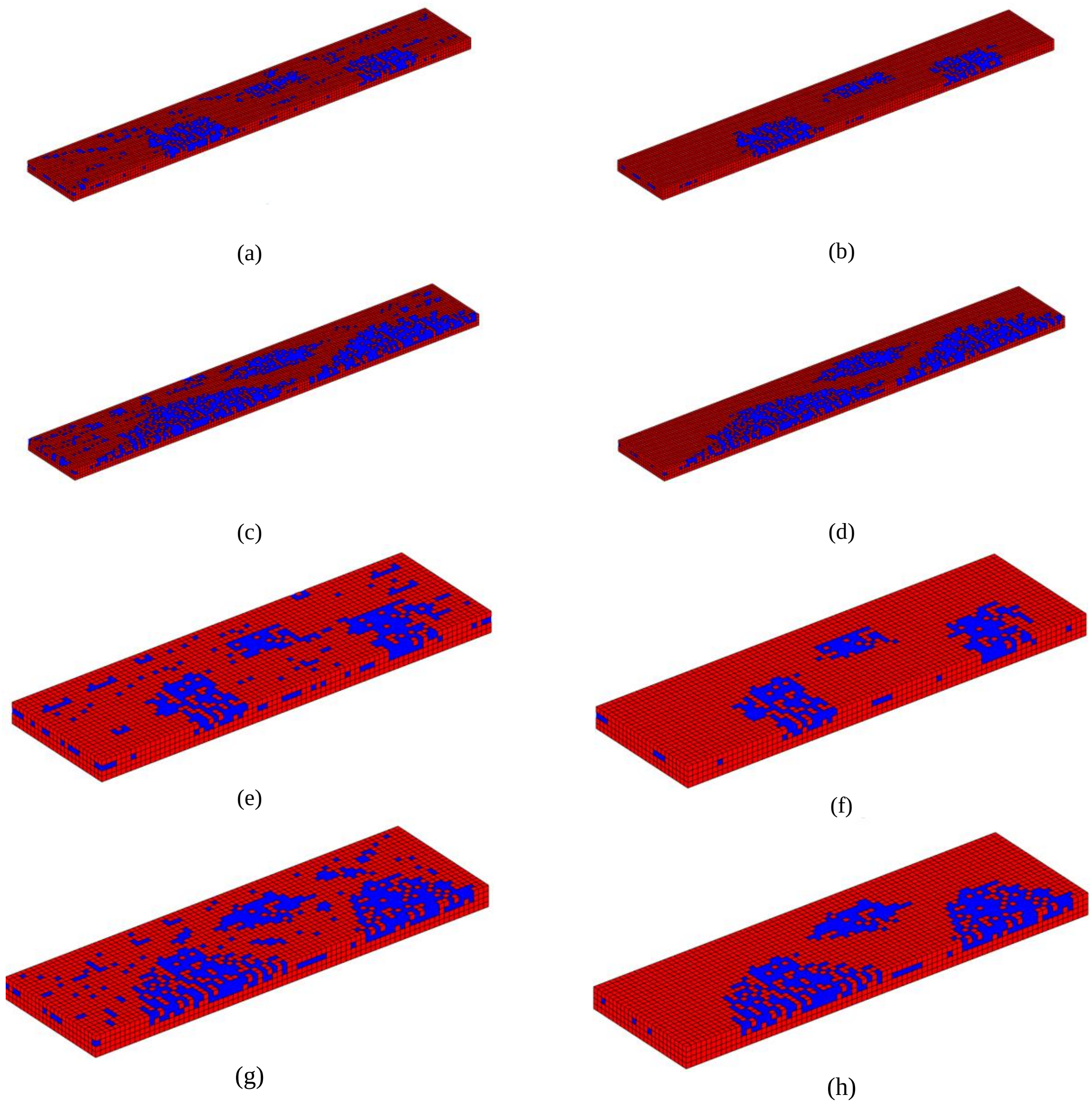

Figure 5.21. Topology Optimization results, binary architecture containing solid and void at all locations, (a) configuration 1 before post processing, (b) configuration 1 after post processing, (c) configuration 2 before post processing, (d) configuration 2 before post processing, (e) configuration 3 before post processing, (f) configuration 3 after post processing, (g) configuration 4 before post processing, (h) configuration 4 before post processing

Moreover, to well perceive the performance of the introduced approach, Figure 5.22 quantifies and outlines the discovered results of the optimization for configurations 3 in Figure 5.22 in the form of confusion matrices, and usually stipulates the higher concentration of the detections around the true-prediction diagonal. Figure 5.22b also specify the

ROC curves for the configuration, which illustrates the trade-off between the ability of the model to detect truly defective elements, while avoiding false alarms, with varying values of threshold.

Table 5.7 sums up the corresponding accuracy metrics computed according to the confusion matrices shown in Figure 5.22. It can be realized that for configuration 1, the proposed approach performed an accuracy 94.85% which signifies the capability of the topology optimization based technique in detecting the damage in large scale structural component experiment. Moreover, it can be denoted that for the configuration, the proposed approach performed the precision and recall 64.74 and 74.83 which shows that the existence of spurious detection noise (i.e., False Positive) are relatively higher. It can be realized from the results in Table 5.7 that although the proposed method can properly detect the shape and position of the existence damage, the performance moderately decayed. This performance deterioration can be attributed to potential internal non-homogeneity and the noise and uncertainties involved in the experimental setup. Some of the sources of these uncertainties include lightning fluctuations, glare, irregularities, poor quality of speckle pattern, as well as noise resulting from image acquisition (e.g. sensor noise) and quantization. Furthermore, the interpolation of DIC and FEM can also be a possible source of uncertainties.

Also, for configuration 3, to improve accuracy of the detected damage regions the proposed post-processing approach was applied with results shown in Table 5.7 alongside pre-presented results. Results highlighted that many of the minor erroneous predictions were eliminated using post processing step accordingly and the performance of the precision and recall were enhanced to 77.05 and 84.25 respectively. Additionally, the accuracy was improved to 96.80 which indicates the overall success of the proposed approach in reconstructing the 3D shape of the damage.

Also, in Table 5.7 the correlating accuracy metrics computed stems from the confusion matrices are described for configuration 3. It shows that for configuration 3, the proposed approach performed an accuracy 90.93% which successfully highlights the capability of the optimization in detecting the damage within another different large specimen. However, it also shows that the accuracy is slightly decreased compared to configuration 1, which also, can be attributed to the existence of noise measurements. The precision and recall values are obtained 48.87 and 79.50 which after post processing step ameliorated to 69.81 and 85.16.

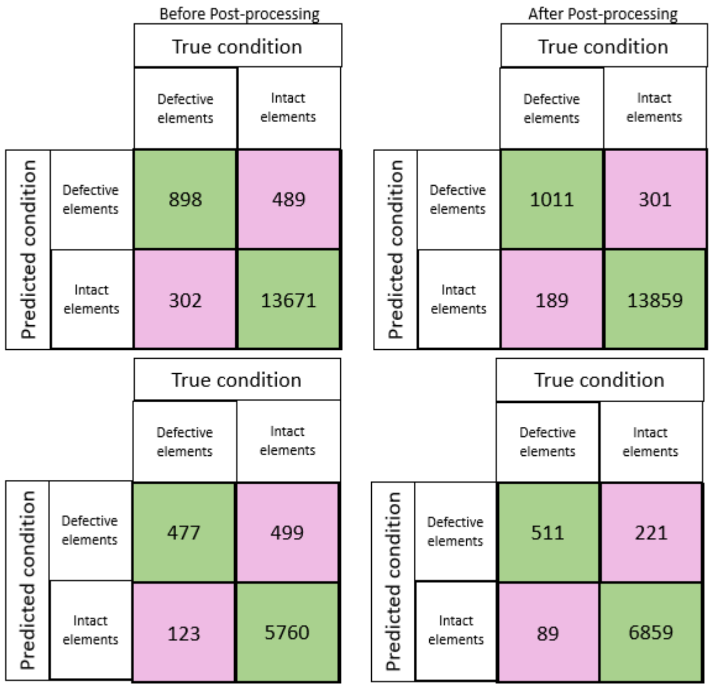

(a)

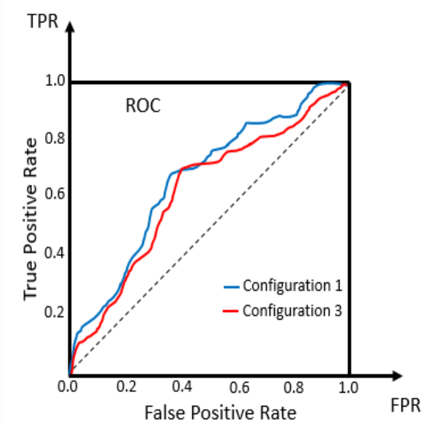

(b)

Figure 5.22. (a) Confusion matrix, Top is for configuration 1 and bottom is for configuration 3, (b) ROC

Table 5.7. Performance of the damage detection method on DIC experimental results (threshold=0.5)

Item	ACC		PRE		REC		F1	
	Before post processing	After post processing	Before post processing	After post processing	Before post processing	After post processing	Before post processing	After post processing
Configuration 1	94.85	96.80	64.74	77.05	74.83	84.25	69.20	80.64
Configuration 3	90.93	95.91	48.87	69.81	79.50	85.16	60.70	76.17

5.13 Comparison of Response from DIC, initial model and the Optimized Model

To demonstrate the capability of the proposed topology optimization based technique in modifying the model for replicating the surface response of components, Figure 5.23 to Figure 5.30 display a comparison of ground truth surface strains and deflection measured by 3D-DIC, with those acquired from the model before (Initial model) and after optimization (Updated or optimized model) together with the residual between the two of the results. In the figures, ε_{xx}, ε_{yy}, ε_{xy} and W indicate longitudinal, transverse, and shear strain, and out of plane deformation, respectively. Figure 5.23 to Figure 5.30, illustrate that the optimized model\are able to reproduce experimental full-field strain distributions including the complicated disruptions incurred due to backside damage machined into the beams.

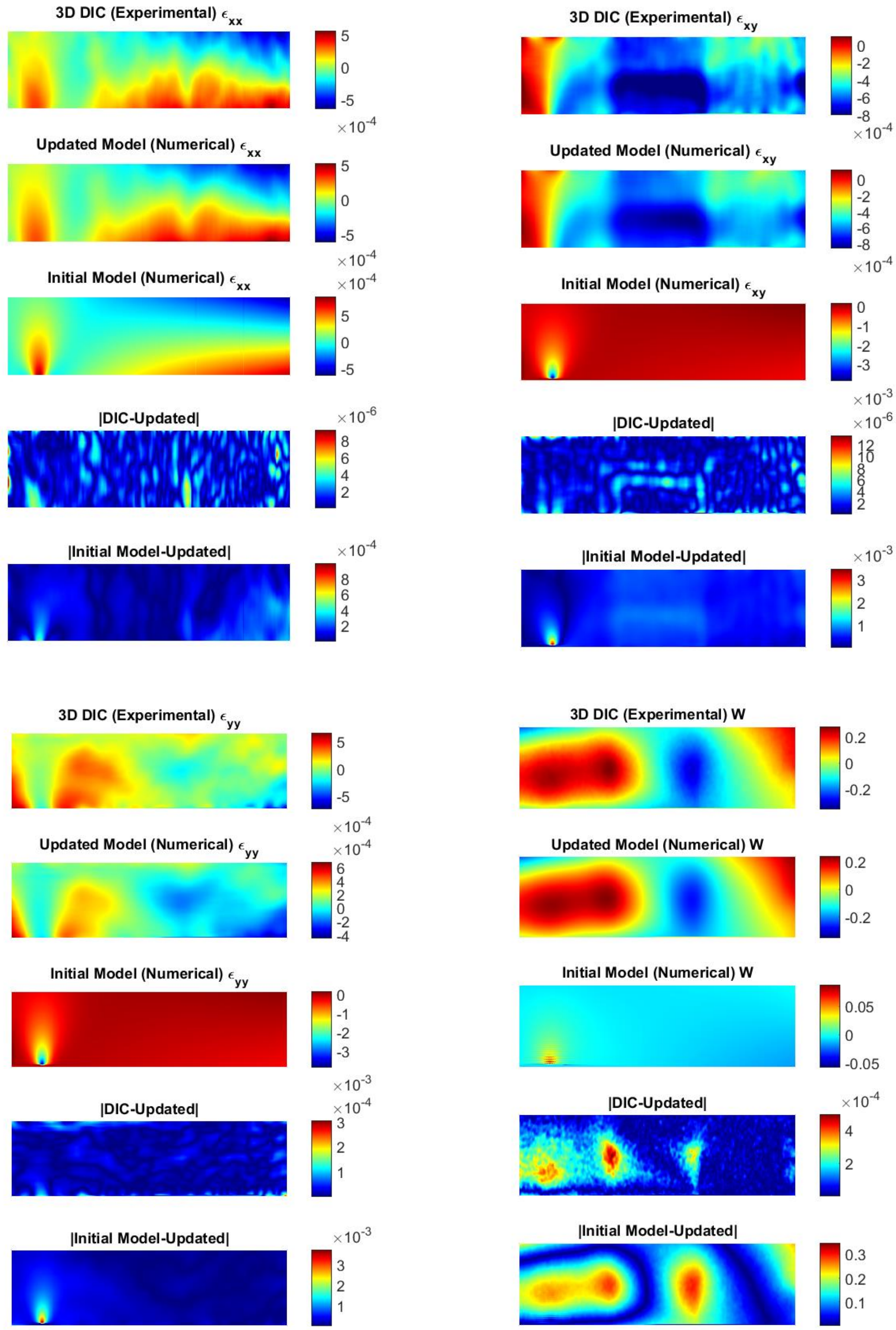

Figure 5.23. Full field measurements from DIC for configuration 1, left region.

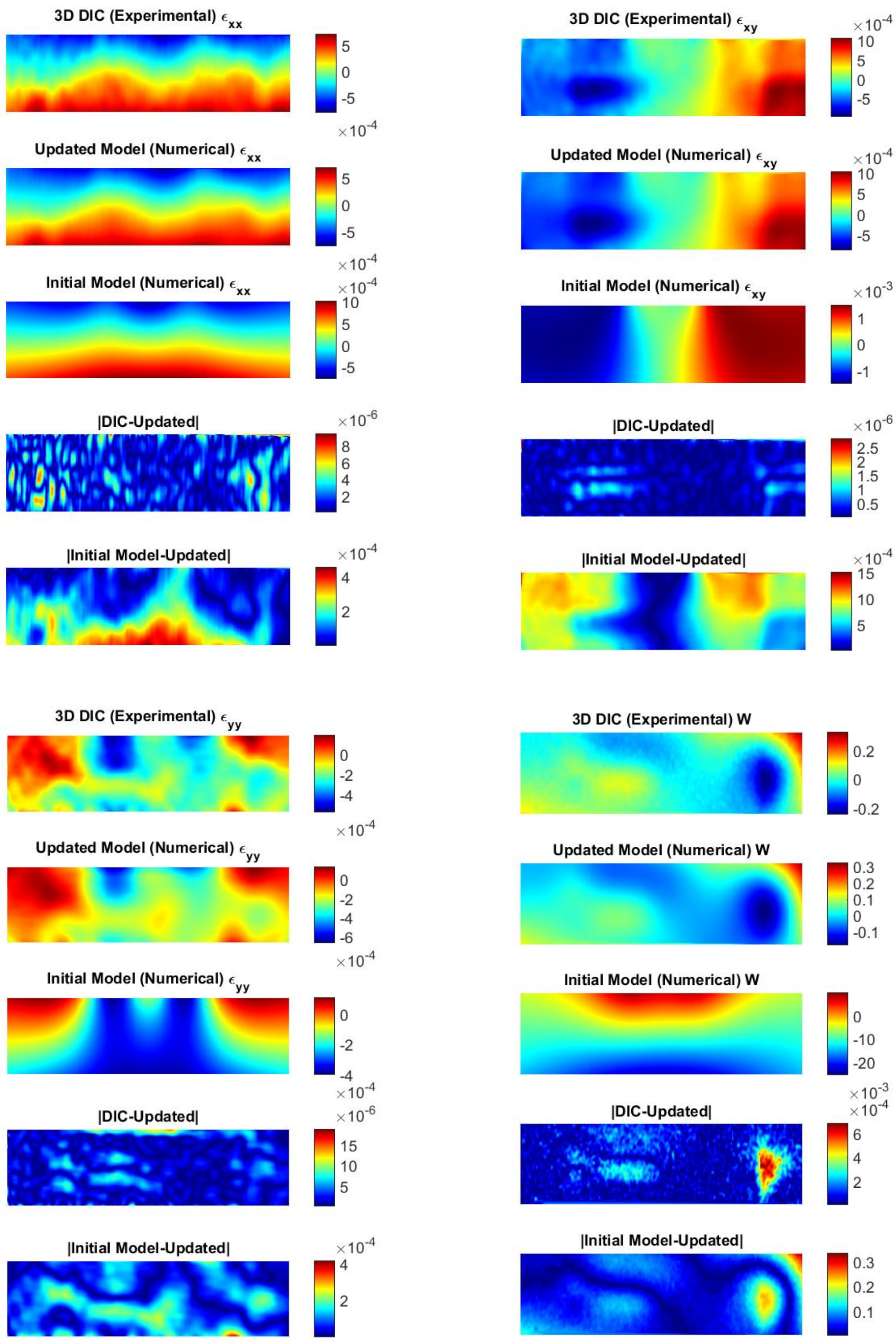

Figure 5.24. Full field measurements from DIC for configuration 1, the middle region.

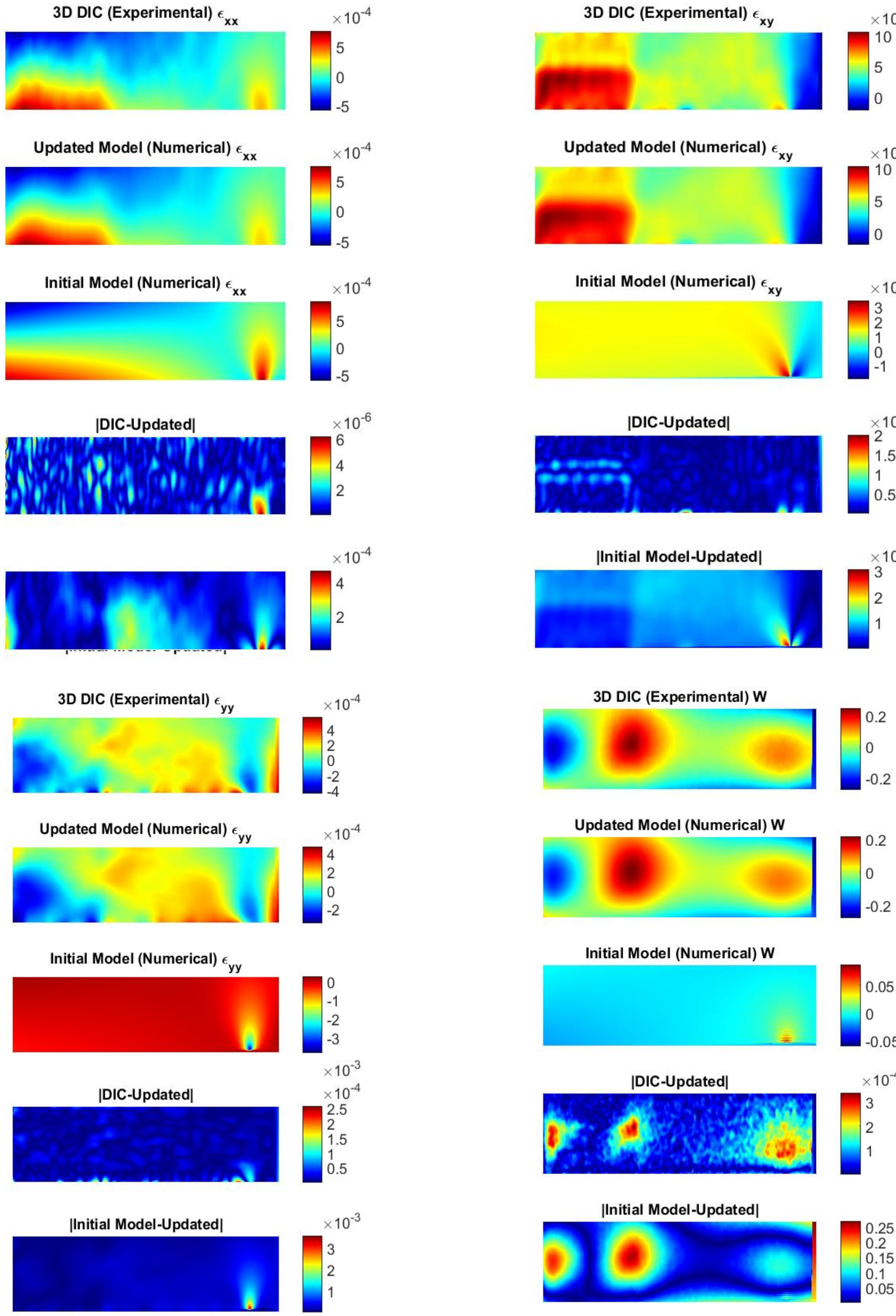

Figure 5.25. Full field measurements from DIC for configuration 1, right region.

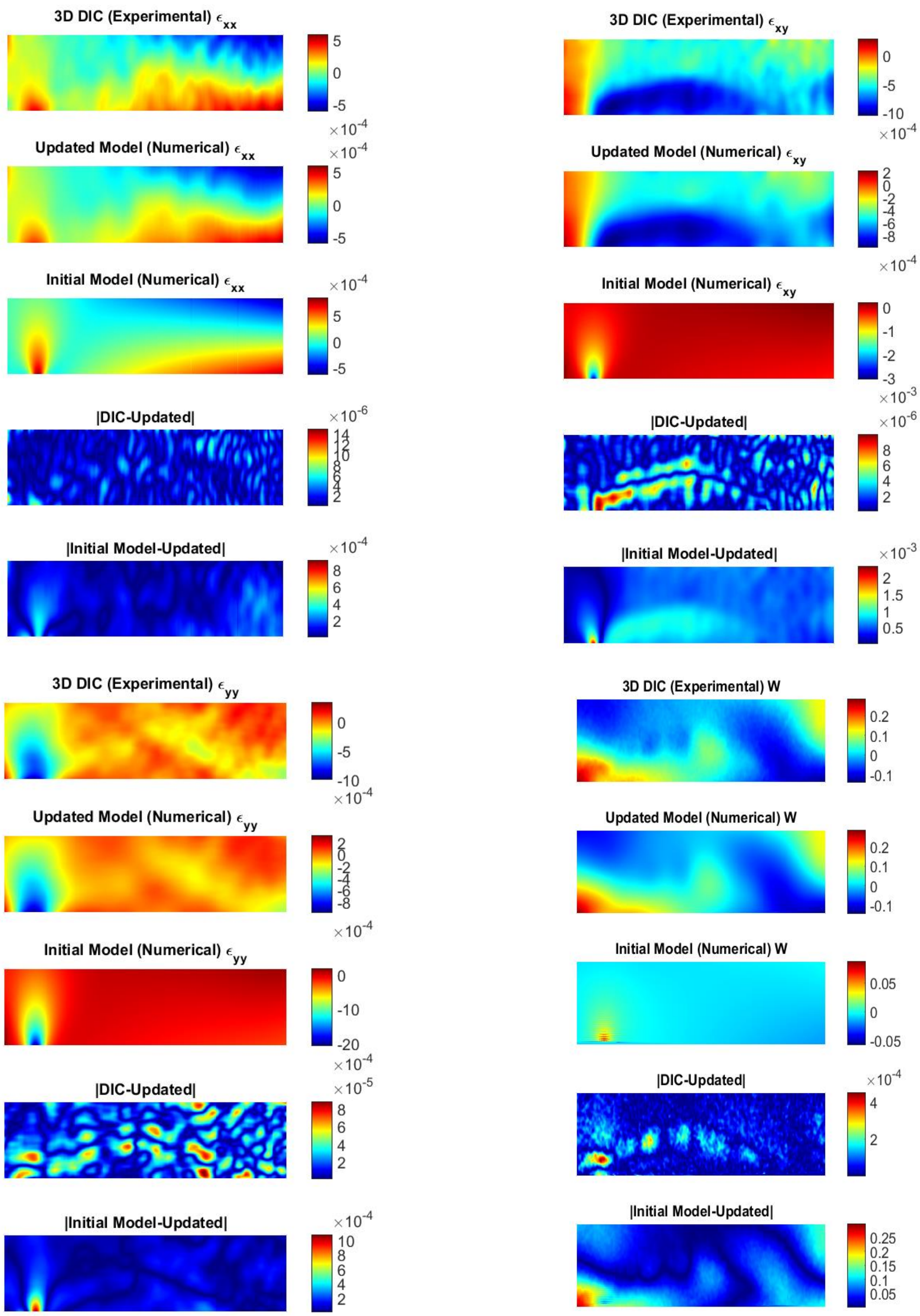

Figure 5.26. Full field measurements from DIC for configuration 2, left region.

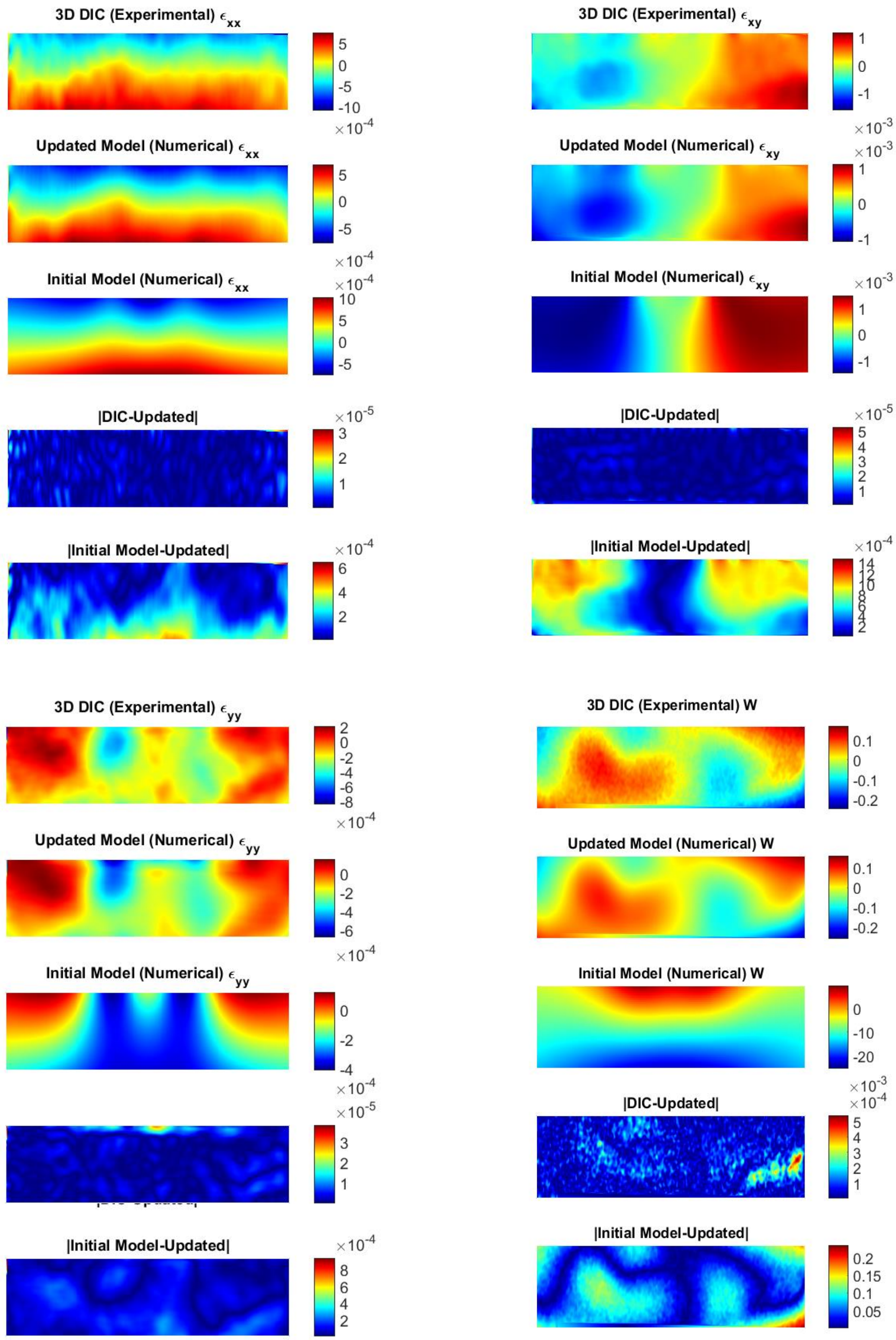

Figure 5.27. Full field measurements from DIC for configuration 2 middle region.

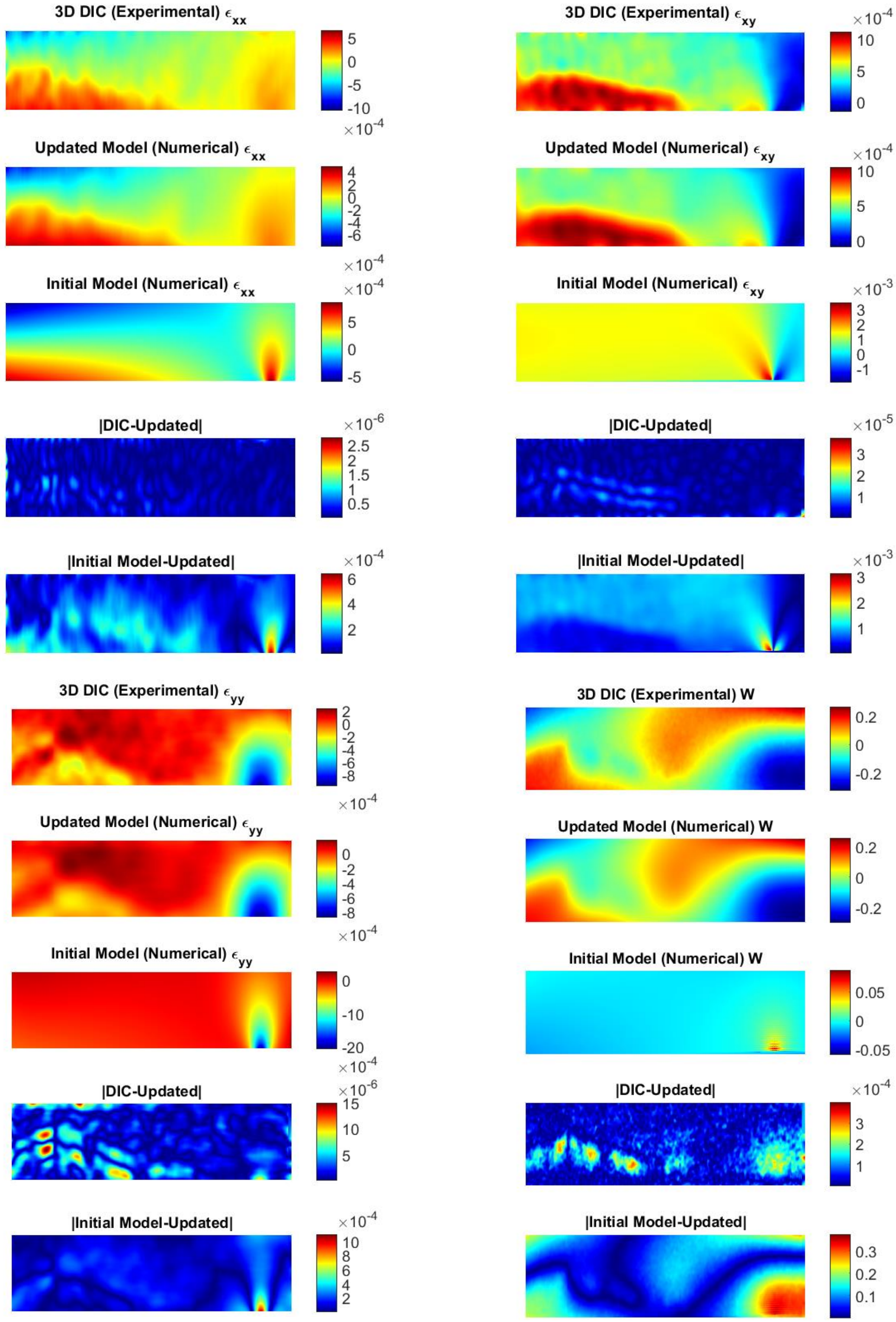

Figure 5.28. Full field measurements from DIC for configuration 2, right region.

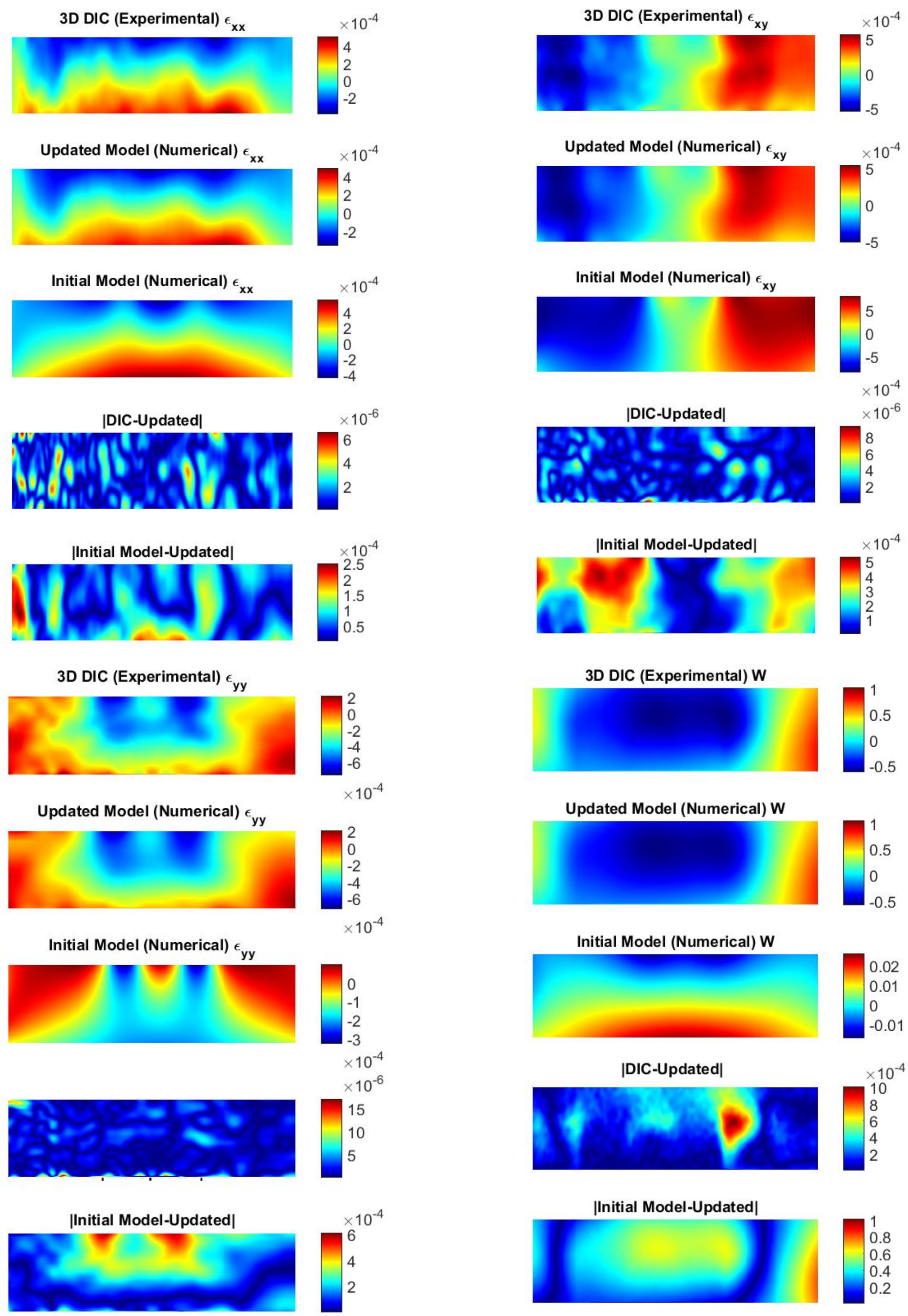

Figure 5.29. Full field measurements from DIC for configuration 3.

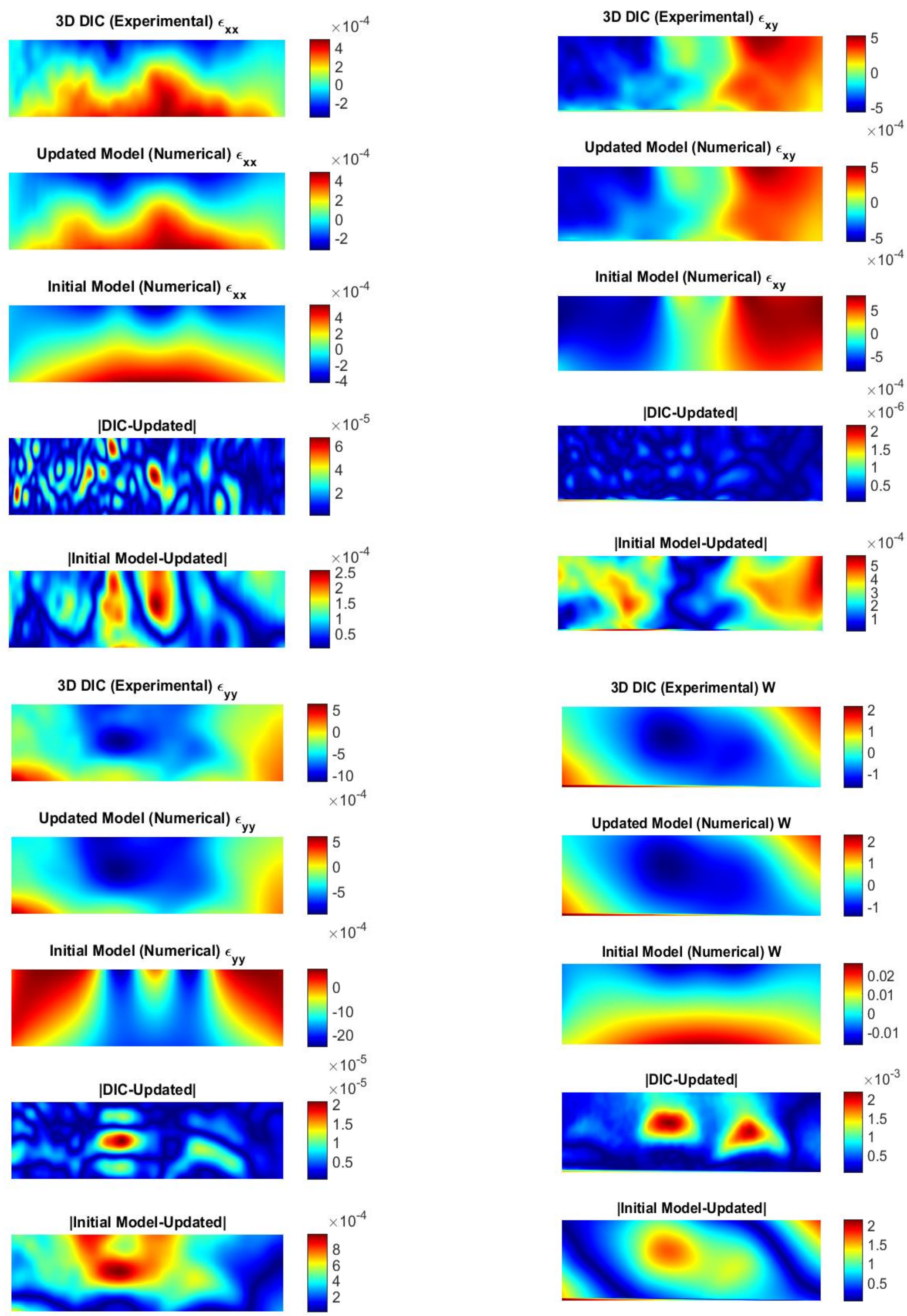

Figure 5.30. Full field measurements from DIC for configuration 4.

5.14 Conclusion

The scope of this study was to assess the practicality of a non-invasive image-based measurement approach to characterize unknown/uncertain properties and damage mechanisms inherent to large scale structural components. The presented approach leverages the full-field measurement capabilities of DIC within a hybrid SHM/NDE framework to converge on material properties and damage mechanisms unique to steel such as corrosions. The approach offers a strategy that links global response-based SHM with the localized capabilities of NDE without discrete sensors or specialized measurement equipment. Building from the previous investigations using a full-field St-Id approach for structural components, unseen or internal damage was successfully identified. A more recent proof of concept of this strategy successfully leveraged a topology optimization approach, allowing the identification to move beyond limitations associated with a priori information on the candidate damaged area.

With large scale structural components such as steel beams, the identification challenge is further complicated due to boundary condition complexity, and variety of damage mechanisms; hence, further study was necessary to explore the robustness of the proposed approach. The method was evaluated on a series of steel beam structural components with artificially fabricated defects, representing section loss and the following conclusions were drawn:

- Average three-dimensional visualization of the damage confirmed the overall success of the method in reconstructing the 3D shape of the damage, with a limited amount of spurious noisy detections that are mainly attributed to noise or incorrect estimates.
- The proposed approach was capable of reconstructing the damage with average accuracy-score of 96.80% and 95.91% on configuration 1 and configuration 3, respectively. This outcome indicates that approach is able to predict a very small number of false positive and false negative elements at the end of topology optimization, with most of the predictions being designated as true positive and true negative elements.
- These accuracy outcomes were reinforced with strong average precision and recall and precision scores, which are the ratios of correct defect predictions to total defective elements, and to all defect predictions, respectively. For configuration 1 these values are 84.025% and 77.05% respectively. Also, the values for configuration 3 are 85.15% and 69.81% respectively. The concept is shown in Figure 5.17 schematically.

- To improve the reliability of the proposed approach for detecting damage region a post-processing enhancement was employed, which relies on the premise of damage continuity to eliminate spurious predictions. After applying the post-processing step for configuration 1 the accuracy, precision and recall scores improved from 94.85%, 64.74% and 74.83% to 96.80%, 77.05% and 84.25% respectively. Similarly, for configuration 3, the post-processing step enhanced those score values from 90.93%, 48.87% and 79.50% to 95.91%, 69.81% and 85.16%.

This paper proved that the proposed method has capability of successfully extracting fine-grained subsurface damage information from large scale structural components which is otherwise costly and difficult to achieve with state-of-the-art NDE/T or SHM methods and can therefore be used as a promising subsurface damage detection method. While the capability and promise of the proposed technique is shown in this paper, it should be noted that in order to detect damage in a large structural component, large areas may need to be subject to the surface preparation required for DIC, and multiple sets of cameras may be required to cover the area of interest. However, the DIC technique has been shown to continue to be effective in relatively large components. Furthermore, for very large components, a multi-step procedure can be followed which starts by locating the vicinity of the damage using traditional global-response methods, and then using the proposed technique to obtain a fine-grained and detailed view of the internal damage.

6 CHAPTER 6 – Summary and Future Work

As structures age, routine inspection and repair become more frequent. In the United States of America, most infrastructures must to be subjected to routine inspections during their life-cycle. Civil infrastructure systems must undergo periodic or condition-driven inspections to assess their integrity. These assessments are designed to capture a range of changes such as systemic corrosion, damage from a natural disaster and, more generally, changes that affect performance under operating conditions. Beyond immediate and fundamental safety assessments, the desired goal of these evaluations is to provide maintenance engineers and managers with projections of the expected remaining service life, as well as to provide a foundation for decision support strategies applicable to a portfolio of similar assets. However, it is difficult to quantify inspection observations in a manner that illustrates the capacity of infrastructure, consequently making it extremely challenging to create numerical predictions suitable to prognose remaining service life from these observations. Improvements in simulation would ultimately lead to improved decision making for both system and network level asset management, with direct economic and safety benefits across a broad range of infrastructure sectors as a result. And, given the aging state of infrastructure in the United States, improving such assessment capabilities is both an economic and public safety priority.

The focus of this dissertation was on the quantification and modeling of non-visually observable geometric manifestations of damage. Such defects have a direct impact on the mechanical performance of infrastructure systems, and the advancement of new analytical techniques for the modeling of such defects would improve decision-support capabilities across a variety of infrastructure sectors. However, the arbitrary geometric complexities and stochastic evolution of such defects inhibits both high-fidelity numerical simulations of the impacts of defects. The primary objective of the proposed research was to develop an image - based SHM mechanism for integrating damage into a measure of system performance. Additionally, the goals aim to correlate the influence of damage on the capacity of the structural elements so as to predict updated numerical simulation of structural systems. This introduced concept represents a fundamental shift in current industry practice, which has no apparent linkage between decisions and practices in design, maintenance, and repair over the life of a structure. In order to accurately evaluate the system-level behavior, an ideal approach would be the implementation of full scale field tests on a series of representative structures; however, this approach is neither feasible nor cost-effective. Laboratory testing can also be considered as an alternative approach, but challenges with dimensional scaling and simulation of exact boundary conditions are considered as limitations of this method, in addition to associated costs. With today's computational resources and capabilities, the development of an analytical model to study the performance of intact or damaged structural systems could be best handled numerically, using a tool such as the FEM. While FEM provides an efficient mechanism to simulate the structure system behavior, there are certain challenges that must be properly treated to yield representative results. Of most important challenges to use finite element modeling, is how to simulate the constitutive properties, boundary conditions and geometric descriptions as precise as possible to real model; especially if the structures are complicated enough to define those constitutive properties, boundary conditions and geometric description.

6.1 Summary

This dissertation presents the results of a study on St-Id to recognize the constitutive properties and boundary conditions using image based full field sensing measurements attained from 3D-DIC by inferring internal abnormalities from constitutive property distribution. The outcomes demonstrate that full-field measurement techniques are sufficiently robust for use within a St-Id framework for SHM. This dissertation describes the core components of the proposed full-field St-Id process including the experimental setup, numerical model development, creation of common reference plan, and model updating methods as optimization techniques. Based on the findings of these laboratory studies, the following outcomes were realized:

6.1.1 Global Boundary and Constitutive Property Identification Using DIC

In the first step of the research a full-field measurement from 3D-DIC technique for St-Id of a large scale steel beam is leveraged. The research investigated the use of full-field sensing of structural response coupled with St-Id as a promising tool for SHM applications. Specifically, 3D-DIC was used to measure mechanical response of a laboratory-scale simply supported steel I-beam specimen. The measured responses were then used for St-Id of the unknown parameters of the system through FEMU. To this end, the problem was formulated as an optimization problem where objective functions signifying the differences between the actual experimental response and that predicted by the model was pushed to a minimum. For the identification, a novel hybrid algorithm, incorporating a combination of a GA and a gradient-based scheme was utilized for updating the FEA model and obtaining the optimal values of the selected parameters. Overall, the St-Id results obtained in this work suggested that image-based measurements sensing using 3D-DIC can be successfully used as an alternative to physical in-place sensors for characterizing the response of large scale structural systems. Based on the findings of this laboratory study, the following conclusions were drawn:

- The St-Id results obtained in this work suggest that image-based full-field measurements sensing using 3D-DIC can be successfully employed as an alternative to physical in-place sensors for characterizing the response of large scale structural systems. Overall, the excellent agreement of the strain and displacement responses achieved after the completion of the updating process confirmed the efficacy of the proposed identification method. The observed advantage in the developed full-field approach is expected to enable to usage of a reduced sensor suite for St-Id as the rich data derive across the surface is more informative than a local sensing approach.
- Features observed using 3D-DIC are available in post-processing, allowing for the identification of unforeseen behavior. In this work, in terms of boundary condition modeling, support deflections were identified from the 3D-DIC measurements and would have gone unmeasured using a traditional sensing if this response was not expected a priori.
- The spatial correspondence between the DIC measurements and finite element simulation results provided a basis for further identification of highly localized features that may not present in local sensor measurements. An example of this phenomena was present when evaluating the local strain concentrations that manifested at the location of the load application.

6.1.2 Image-based Tomography of Structures Using DIC

In the next step, the research went one step further and the purpose was to evaluate the feasibility of leveraging full-field measurements for St-Id, with a goal of recovering the volumetric interior defect distribution in structural components. Within this image-based tomography framework, steel coupon specimens with simulated defects were used to evaluate the performance of the St-Id approach to identify unknown and uncertain constitutive properties of the material based on full-field deformation measurements correlated with finite element predictions. DIC was utilized to extract full-field deformation measurements of the test specimen, subjected to standard ASTM E8 tension testing, with the measurements collected of only the intact surface. The results of this investigation and the ability of the proposed method to detect internal abnormalities hint at the possibility of determining not only the material distribution of a specimen, but also determining the location, dimensions, and shape of the defect. The results of this research were encouraging and may open up new opportunities to characterize heterogeneous materials for their mechanical property distribution. Based on the findings of this laboratory study, the following are all of these conclusions were drawn:

- The technique was proposed to recover volumetric interior defect distribution inferred from discrepancy in constitutive property distribution analysis implicitly. Analysis using the proposed technique could be employed to detect both natural and induced defects such as voids, inclusions, impurities, contaminants, and other defects that may occur within a structure and may therefore not be visible (i.e., visible with a naked eye because the defect is contained within the structure) on the surface.
- The research aligned with St-Id work using 3D-DIC measurements, constitutive properties of small-scale element level validation were studied by conducting laboratory test on a small scale structural elements such as several steel coupons. The goal of this investigation was to evaluate the capability of utilizing full-field measurements on St-Id to find constitutive properties of materials with the assumption that the coupon specimens has sections with different material properties.
- This approach can not only determine material distribution of a sample that is homogenous or (intentionally) non-homogenous in its properties, but also determine the location size, dimensions, and shape and to determine quantitative values for the material properties of defects that imply defects such as internal abnormalities, including those that may develop inside structural elements, or manufacturing defects that may also include voids or contaminants.
- The results of this work demonstrates the potential to identify invisible internal defect by the proposed computer vision technique and established the potential for new opportunities to characterize internal heterogeneous materials for their mechanical property distribution and condition state.

6.1.3 *Subsurface Condition Assessment and SHM of Structures:*

In earlier investigations using FEMs, either few partitions or only a part of a structure was considered as the damaged region, but neither the total number of elements nor an entire structure. The small-region damage assumption is valid only when the information on the candidate damaged area is available. This limitation may be overcome by applying topology design method for damage identification because this approach has been used to design an entire structure. The topology design method was originally developed to find an optimal material distribution of a structure having the minimum compliance and subject to a given mass usage. In this investigation, a topology design formulation suitable for full field measurement data-based damage detection was developed applied to non-complex specimens. Based on the findings of this laboratory study, the following conclusions were drawn:

- This study introduces to take advantages of image-based full-field sensing measurement acquired from DIC in a topology optimization framework to recover the interior damage in structural components which in turn means, to illustrate how perturbations in the observable full-field surface measurements can be used as a proxy to detect the unobservable internal abnormalities.
- The proposed Topology optimization based approach uses the Solid Isotropic Material with Penalization (SIMP) based material model to parametrize the optimization problem, and the discrepancy of response between real structure and the model was minimized to find the material distribution in the design domain to eventually infer internal defects from material distributions.
- Finally, this paper denoted that the proposed method has the capability of properly extracting fine-grained subsurface damage information which is otherwise costly and difficult to attain with state-of-the-art NDE/T or SHM methods and can hence be employed as a promising subsurface damage detection method.

6.1.4 *Detecting and Reconstructing the 3D Geometry of Subsurface Structural Damage*

The final phase of this investigation focused on extending the topology optimization St-Id approach to more complex structural components with internal damage to demonstrate the feasibility and investigate the performance of the previously proposed method through an experimental program in which a few steel beams with and without buried defects are tested with full-field DIC sensing. A corresponding set of research tasks with an increasing level of sophistication were designed to evaluate the capability of the approach to estimate steel material properties and extent and 3D shape of embedded defects. Upon completion, this investigation demonstrated the feasibility and practicality of the proposed subsurface steel condition assessment technique Based on the findings of this laboratory study, the following conclusions were drawn:

- Average three-dimensional visualization of the damage confirmed the overall success of the method in reconstructing the 3D shape of the damage, with a limited amount of spurious noisy detections that are mainly attributed to noise or incorrect estimates.
- The proposed approach leverages full-field surface deformation measurements of structural elements derived using DIC coupled within a topology optimization based technique to search for and identify the presence of unseen damage components.
- The work described herein centers on a laboratory scale investigation of large scale steel structural components, which exhibits variability in its constitutive properties that are typically uncertain within existing structures and is also vulnerable to internal damage that is unseen from the surface.
- The investigation proved that the proposed method has capability of successfully extracting fine-grained subsurface damage information from large scale structural components which is otherwise costly and difficult to achieve with state-of-the-art NDE/T or SHM methods and can therefore be used as a promising subsurface damage detection method. While the capability and promise of the proposed technique is shown in this investigation, it should be noted that in order to detect damage in a large structural component, large areas may need to be subject to the surface preparation required for DIC, and multiple sets of cameras may be required to cover the area of interest. However, the DIC technique has been shown to continue to be effective in relatively large components. Furthermore, for very large components, a multi-step procedure can be followed which starts by locating the vicinity of the damage using traditional global-response methods, and then using the proposed technique to obtain a fine-grained and detailed view of the internal damage

6.2 Future work

Based on the analyses performed and reported in this dissertation, the following road map for future work is recommended to further improve the state of St-Id:

6.2.1 *Subsurface Condition Assessment and SHM of Concrete Structures Using the Proposed Approach*

Based on the outcomes of this dissertation, it is evident that there is great potential for leveraging 3D-DIC as a tool for efficient St-Id. The study evaluated the feasibility of the technique using a large experimental program. Future work in this area should evaluate the robustness of the proposed framework on more complex structural systems. This complexity should include large scale structural systems with more complex load sharing characteristic, variations in materials used and additional uncertainty in the condition state and boundary conditions. As an example, subsurface condition assessment and SHM of concrete structures using the proposed approach can shed light on the potentials for performance improvement on realizing structure behavior. Because many internal defects in concrete structures are invisible on the surface, especially during early stages of deterioration, making their timely detection challenging. In addition, evaluating the accurate 3D shape and extent of internal defects is a daunting task, even with the advances in NDE techniques. This fine-grained and data-rich representation of behavior of the concrete member can be then leveraged in an inverse mechanical problem to reconstruct the underlying subsurface abnormalities.

6.2.2 *Integrating the Proposed Approach with Photogrammetry Methods*

Another future goal can be merging photogrammetry methods with the proposed approach to characterizing structure condition on a local level while also describing the impact on structural component and system behavior. In the photogrammetry methods, a combination of high-resolution 3D laser scanning and computer vision can be used to detect and measure observable defects in structural components. The localized measurements are then mapped into numerical simulations capable of describing the in-situ behavior of the structural component. Complementary to this direct scan-to-modeling approach, a second strategy is based on the proposed approach, a refined St-Id approach using full-field deformation measurements derived from 3D-DIC coupled with a topology optimization strategy to detect internal abnormalities. In this indirect approach, measurements derived from the measured structural components will be used to characterize and refine uncertain parameters (i.e. boundary and constitutive properties). The research provides a pathway for future work in the area of identification of unseen damage using the same basic St-Id approach.

While the proposed research effort studied this problem in the context of structural engineering, the findings will potentially benefit a range of communities, including geotechnical, construction, biomedical, and mechanical engineering, all of whom face similar challenges with respect to damage characterization.

6.3 List of References

[1] S.W. Doebling, C.R. Farrar, M.B. Prime, D.W. Shevitz, Damage identification and health monitoring of structural and mechanical systems from changes in their vibration characteristics: a literature review, Los Alamos National Lab., NM (United States), 1996.
[2] C.R. Farrar, K. Worden, An introduction to structural health monitoring, Philosophical Transactions of the Royal Society A: Mathematical, Physical and Engineering Sciences 365(1851) (2007) 303-315.
[3] J. Seo, J.W. Hu, J. Lee, Summary review of structural health monitoring applications for highway bridges, Journal of Performance of Constructed Facilities 30(4) (2016) 04015072.
[4] H. Sohn, C.R. Farrar, F.M. Hemez, J.J. Czarnecki, A review of structural health review of structural health monitoring literature 1996-2001, Los Alamos National Laboratory, 2002.
[5] H. Zhou, H. Dou, L. Qin, Y. Chen, Y. Ni, J. Ko, A review of full-scale structural testing of wind turbine blades, Renewable and Sustainable Energy Reviews 33 (2014) 177-187.
[6] T. Ahlborn, R. Shuchman, L. Sutter, C. Brooks, D. Harris, J. Burns, K. Endsley, D. Evans, K. Vaghefi, R. Oats, The State-of-the-Practice of Modern Structural Health Monitoring for Bridges: A Comprehensive Review, (2010).
[7] American Society of Civil Engineers (ASCE), Report card for America's infrastructure, 2017. http://www.infrastructurereportcard.org. (Accessed June 1 2017).
[8] K. Vaghefi, R.C. Oats, D.K. Harris, T.M. Ahlborn, C.N. Brooks, K.A. Endsley, C. Roussi, R. Shuchman, J.W. Burns, R. Dobson, Evaluation of commercially available remote sensors for highway bridge condition assessment, Journal of Bridge Engineering 17(6) (2012) 886-895.
[9] G. Webb, P.J. Vardanega, C.R. Middleton, Categories of SHM deployments: technologies and capabilities, Journal of Bridge Engineering 20(11) (2015) 04014118.
[10] ABAQUS Software, Dassault Systèmes (2016), "ABAQUS analysis user's manual." Abaqus, 2016.
[11] M.S. Dizaji, M. Alipour, D. Harris, "Leveraging Vision for Structural Identification: A Digital Image Correlation Based Approach.",, *International Digital Imaging Correlation Society*, Springer, 2016, pp. 121-124.
[12] M.S. Dizaji, D. Harris, M. Alipour, O. Ozbulut, En"vision"ing a Novel Approach for Structural Health Monitoring – A Model for Full-Field Structural Identification using 3D Digital Image Correlation,, The 8th International Conference on Structural Health Monitoring of Intelligent Infrastructure,, Bridbane, Australia,, 2017.
[13] C. Rainieri, G. Fabbrocino, Operational modal analysis of civil engineering structures, Springer, New York 142 (2014) 143.
[14] D. Ribeiro, R. Calçada, R. Delgado, M. Brehm, V. Zabel, Finite element model updating of a bowstring-arch railway bridge based on experimental modal parameters, , Engineering Structures, 40, (2012) 413-435.
[15] M.A. Sutton, J.J. Orteu, H. Schreier, Image correlation for shape, motion and deformation measurements: basic concepts, theory and applications, Springer Science & Business Media2009.
[16] J. Blaber, B. Adair, A. Antoniou, Ncorr: open-source 2D digital image correlation matlab software, Experimental Mechanics 55(6) (2015) 1105-1122.
[17] M. Bornert, P. Doumalin, J.-C. Dupré, C. Poilâne, L. Robert, E. Toussaint, B. Wattrisse, Assessment of digital image correlation measurement accuracy in the ultimate error regime: improved models of systematic and random errors, Experimental Mechanics 58(1) (2018) 33-48.
[18] P. Cheng, M.A. Sutton, H.W. Schreier, S.R. McNeill, Full-field speckle pattern image correlation with B-spline deformation function, Experimental mechanics 42(3) (2002) 344-352.
[19] G. Crammond, S. Boyd, J. Dulieu-Barton, Speckle pattern quality assessment for digital image correlation, Optics and Lasers in Engineering 51(12) (2013) 1368-1378.
[20] F. Hild, S. Roux, Comparison of local and global approaches to digital image correlation, Experimental Mechanics 52(9) (2012) 1503-1519.
[21] B. Pan, K. Li, W. Tong, Fast, robust and accurate digital image correlation calculation without redundant computations, Experimental Mechanics 53(7) (2013) 1277-1289.
[22] F. Chen, X. Chen, X. Xie, X. Feng, L. Yang, Full-field 3D measurement using multi-camera digital image correlation system, Optics and Lasers in Engineering 51(9) (2013) 1044-1052.
[23] F. Hild, S. Roux, Digital image correlation: from displacement measurement to identification of elastic properties–a review, Strain 42(2) (2006) 69-80.
[24] Z. Kahn-Jetter, T. Chu, Three-dimensional displacement measurements using digital image correlation and photogrammic analysis, Experimental Mechanics 30(1) (1990) 10-16.
[25] X.-D. Ke, H. Schreier, M. Sutton, Y. Wang, Error assessment in stereo-based deformation measurements, Experimental mechanics 51(4) (2011) 423-441.

[26] G. Lionello, L. Cristofolini, A practical approach to optimizing the preparation of speckle patterns for digital-image correlation, Measurement Science and Technology 25(10) (2014) 107001.
[27] B. Pan, K. Qian, H. Xie, A. Asundi, Two-dimensional digital image correlation for in-plane displacement and strain measurement: a review, Measurement science and technology 20(6) (2009) 062001.
[28] B. LeBlanc, C. Niezrecki, P. Avitabile, J. Chen, J. Sherwood, Damage detection and full surface characterization of a wind turbine blade using three-dimensional digital image correlation, Structural Health Monitoring 12(5-6) (2013) 430-439.
[29] B. LeBlanc, C. Niezrecki, P. Avitabile, J. Chen, J. Sherwood, S. Hughes, Full-field inspection of a wind turbine blade using three-dimensional digital image correlation, Industrial and Commercial Applications of Smart Structures Technologies 2011, International Society for Optics and Photonics, 2011, p. 79790L.
[30] B. LeBlanc, C. Niezrecki, P. Avitabile, J. Sherwood, J. Chen, Surface stitching of a wind turbine blade using digital image correlation, Topics in Modal Analysis II, Volume 6, Springer2012, pp. 277-284.
[31] D. Reagan, A. Sabato, C. Niezrecki, Feasibility of using digital image correlation for unmanned aerial vehicle structural health monitoring of bridges, Structural Health Monitoring 17(5) (2018) 1056-1072.
[32] D. Reagan, A. Sabato, C. Niezrecki, T. Yu, R. Wilson, An autonomous unmanned aerial vehicle sensing system for structural health monitoring of bridges, Nondestructive Characterization and Monitoring of Advanced Materials, Aerospace, and Civil Infrastructure 2016, International Society for Optics and Photonics, 2016, p. 980414.
[33] M.A. Drewry, G. Georgiou, A review of NDT techniques for wind turbines, Insight-Non-Destructive Testing and Condition Monitoring 49(3) (2007) 137-141.
[34] B.W. Drinkwater, P.D. Wilcox, Ultrasonic arrays for non-destructive evaluation: A review, NDT & e International 39(7) (2006) 525-541.
[35] S. Gholizadeh, A review of non-destructive testing methods of composite materials, Procedia Structural Integrity 1 (2016) 50-57.
[36] S. Gholizadeh, Z. Leman, B. Baharudin, A review of the application of acoustic emission technique in engineering, Structural Engineering and Mechanics 54(6) (2015) 1075-1095.
[37] J.P. Lynch, An overview of wireless structural health monitoring for civil structures, Philosophical Transactions of the Royal Society A: Mathematical, Physical and Engineering Sciences 365(1851) (2007) 345-372.
[38] S.K.U. Rehman, Z. Ibrahim, S.A. Memon, M. Jameel, Nondestructive test methods for concrete bridges: A review, Construction and building materials 107 (2016) 58-86.
[39] A. Sabato, C. Niezrecki, G. Fortino, Wireless MEMS-based accelerometer sensor boards for structural vibration monitoring: a review, IEEE Sensors Journal 17(2) (2016) 226-235.
[40] P.J. Shull, Nondestructive evaluation: theory, techniques, and applications, CRC press2002.
[41] M. Alipour, S.J. Washlesky, D.K. Harris, Field Deployment and Laboratory Evaluation of 2D Digital Image Correlation for Deflection Sensing in Complex Environments, Journal of Bridge Engineering 24(4) (2019) 04019010.
[42] M.S. Dizaji, M. Alipour, D. Harris, Leveraging full-field measurement from 3D digital image correlation for structural identification, Experimental Mechanics 58(7) (2018) 1049-1066.
[43] D. Ribeiro, R. Calçada, R. Delgado, M. Brehm, V. Zabel, Finite element model updating of a bowstring-arch railway bridge based on experimental modal parameters, Engineering Structures 40 (2012) 413-435.
[44] M. Friswell, J.E. Mottershead, Finite element model updating in structural dynamics, Springer Science & Business Media2013.
[45] M. Sanayei, J.E. Phelps, J.D. Sipple, E.S. Bell, B.R. Brenner, Instrumentation, nondestructive testing, and finite-element model updating for bridge evaluation using strain measurements, Journal of bridge engineering 17(1) (2012) 130-138.
[46] H. Schlune, M. Plos, K. Gylltoft, Improved bridge evaluation through finite element model updating using static and dynamic measurements, Engineering structures 31(7) (2009) 1477-1485.
[47] J. Zapico, M. Gonzalez, M. Friswell, C. Taylor, A. Crewe, Finite element model updating of a small scale bridge, Journal of Sound and Vibration 268(5) (2003) 993-1012.
[48] M. Pieraccini, Monitoring of civil infrastructures by interferometric radar: A review, The Scientific World Journal 2013 (2013).
[49] V. Giurgiutiu, A. Cuc, Embedded non-destructive evaluation for structural health monitoring, damage detection, and failure prevention, Shock and Vibration Digest 37(2) (2005) 83.
[50] B. Glisic, D. Inaudi, Fibre optic methods for structural health monitoring, John Wiley & Sons2008.
[51] X. Ye, Y. Su, J. Han, Structural health monitoring of civil infrastructure using optical fiber sensing technology: A comprehensive review, The Scientific World Journal 2014 (2014).
[52] M. Çelebi, Seismic instrumentation of buildings, US Department of the Interior, US Geological Survey2000.

[53] V. Udod, Y. Van, S. Osipov, S. Chakhlov, E.Y. Usachev, M. Lebedev, A. Temnik, State-of-the art and development prospects of digital radiography systems for nondestructive testing, evaluation, and inspection of objects: a review, Russian Journal of Nondestructive Testing 52(9) (2016) 492-503.
[54] R. Hanke, T. Fuchs, N. Uhlmann, X-ray based methods for non-destructive testing and material characterization, Nuclear Instruments and Methods in Physics Research Section A: Accelerators, Spectrometers, Detectors and Associated Equipment 591(1) (2008) 14-18.
[55] R. Usamentiaga, P. Venegas, J. Guerediaga, L. Vega, J. Molleda, F.G. Bulnes, Infrared thermography for temperature measurement and non-destructive testing, Sensors 14(7) (2014) 12305-12348.
[56] P. Rizzo, Sensing solutions for assessing and monitoring railroad tracks, Sensor Technologies for Civil Infrastructures, Elsevier2014, pp. 497-524.
[57] P. Tchakoua, R. Wamkeue, M. Ouhrouche, F. Slaoui-Hasnaoui, T.A. Tameghe, G. Ekemb, Wind turbine condition monitoring: State-of-the-art review, new trends, and future challenges, Energies 7(4) (2014) 2595-2630.
[58] P.H. Bischoff, S. Perry, Compressive behaviour of concrete at high strain rates, Materials and structures 24(6) (1991) 425-450.
[59] T. Cuccovillo, M. Coop, The measurement of local axial strains in triaxial tests using LVDTs, Géotechnique 47(1) (1997) 167-171.
[60] S. Neild, M. Williams, P. McFadden, Development of a vibrating wire strain gauge for measuring small strains in concrete beams, Strain 41(1) (2005) 3-9.
[61] B. Erzar, P. Forquin, An experimental method to determine the tensile strength of concrete at high rates of strain, Experimental Mechanics 50(7) (2010) 941-955.
[62] X. Gu, Z. Chen, F. Ansari, Embedded fiber optic crack sensor for reinforced concrete structures, Structural Journal 97(3) (2000) 468-476.
[63] C. Merzbacher, A.D. Kersey, E. Friebele, Fiber optic sensors in concrete structures: a review, Smart materials and structures 5(2) (1996) 196.
[64] K.T. Wan, C.K. Leung, Applications of a distributed fiber optic crack sensor for concrete structures, Sensors and Actuators A: Physical 135(2) (2007) 458-464.
[65] Z. Zhang, F. Ansari, Fiber-optic laser speckle-intensity crack sensor for embedment in concrete, Sensors and Actuators A: Physical 126(1) (2006) 107-111.
[66] U. Hampel, H.-G. Maas, Application of digital photogrammetry for measuring deformation and cracks during load tests in civil engineering material testing, Optical 3-D Measurement Techniques VI 2 (2003) 80-88.
[67] H.-G. Maas, U. Hampel, Photogrammetric techniques in civil engineering material testing and structure monitoring, Photogrammetric Engineering & Remote Sensing 72(1) (2006) 39-45.
[68] T. Whiteman, D. Lichti, I. Chandler, Measurement of deflections in concrete beams by close-range digital photogrammetry, Proceedings of the Symposium on Geospatial Theory, Processing and Applications, 2002, pp. 9-12.
[69] C. Citto, S.I. Wo, K.J. Willam, M.P. Schuller, In-Place Evaluation of Masonry Shear Behavior Using Digital Image Analysis, ACI materials journal 108(4) (2011).
[70] F. Ghrib, A. El Ragaby, B. Boufama, L. Li, S. Memar, A Novel Technique for Displacement Measurements in RC Beams using Digital Image Correlation, Special Publication 298 (2014) 1-16.
[71] J.S. Lawler, D.T. Keane, S.P. Shah, Measuring three-dimensional damage in concrete under compression, Materials Journal 98(6) (2001) 465-475.
[72] C. Murray, A. Hoag, N.A. Hoult, W.A. Take, Field monitoring of a bridge using digital image correlation, Proceedings of the Institution of Civil Engineers-Bridge Engineering, Thomas Telford Ltd, 2015, pp. 3-12.
[73] J. Peddle, A. Goudreau, E. Carlson, E. Santini-Bell, Bridge displacement measurement through digital image correlation, Bridge Structures 7(4) (2011) 165-173.
[74] J. Xiao, W. Li, Z. Sun, S.P. Shah, Crack Propagation in Recycled Aggregate Concrete under Uniaxial Compressive Loading, ACI Materials Journal 109(4) (2012).
[75] S. Yoneyama, H. Ueda, Bridge deflection measurement using digital image correlation with camera movement correction, Materials transactions 53(2) (2012) 285-290.
[76] D. Lattanzi, G.R. Miller, Robust automated concrete damage detection algorithms for field applications, Journal of Computing in Civil Engineering 28(2) (2014) 253-262.
[77] K. Vaghefi, T.M. Ahlborn, D.K. Harris, C.N. Brooks, Combined imaging technologies for concrete bridge deck condition assessment, Journal of Performance of Constructed Facilities 29(4) (2015) 04014102.
[78] R. Butterfield, R. Harkness, K. Andrews, A stero-photogrammetric method for measuring displacement fields, Geotechnique 20(3) (1970) 308-314.
[79] W. Peters, W. Ranson, Digital imaging techniques in experimental stress analysis, Optical engineering 21(3) (1982) 213427.

[80] M. Sutton, W. Wolters, W. Peters, W. Ranson, S. McNeill, Determination of displacements using an improved digital correlation method, Image and vision computing 1(3) (1983) 133-139.
[81] B. Pan, H. Xie, Z. Wang, Equivalence of digital image correlation criteria for pattern matching, Applied optics 49(28) (2010) 5501-5509.
[82] W. Tong, An evaluation of digital image correlation criteria for strain mapping applications, Strain 41(4) (2005) 167-175.
[83] A. Gheitasi, D. Harris, M. Hansen, An experimental-computational correlated study for describing the failure characteristics of concrete across two scale levels: mixture and structural component, Experimental Mechanics 58(1) (2018) 11-32.
[84] N.A. Hoult, W.A. Take, C. Lee, M. Dutton, Experimental accuracy of two dimensional strain measurements using digital image correlation, Engineering Structures 46 (2013) 718-726.
[85] J. Torrenti, J. Desrues, E. Benaija, C. Boulay, Stereophotogrammetry and localization in concrete under compression, Journal of engineering mechanics 117(7) (1991) 1455-1465.
[86] M.S. Dizaji, Alipour M, Harris D. , Image-based Tomography of Structures to Detect Internal Abnormalities using Inverse Approach. , under review (2020).
[87] B.A. Graybeal, B.M. Phares, D.D. Rolander, M. Moore, G. Washer, Visual inspection of highway bridges, Journal of nondestructive evaluation 21(3) (2002) 67-83.
[88] K. Wardhana, F.C. Hadipriono, Analysis of recent bridge failures in the United States, Journal of performance of constructed facilities 17(3) (2003) 144-150.
[89] H. Sohn, C.R. Farrar, F.M. Hemez, D.D. Shunk, D.W. Stinemates, B.R. Nadler, J.J. Czarnecki, A review of structural health monitoring literature: 1996-2001, Los Alamos National Laboratory, Los Alamos, NM, 2004.
[90] A.E. Aktan, F.N. Catbas, K.A. Grimmelsman, C.J. Tsikos, Issues in infrastructure health monitoring for management, Journal of Engineering Mechanics 126(7) (2000) 711-724.
[91] G. Webb, P. Vardanega, C. Middleton, Categories of SHM Deployments: Technologies and Capabilities, Journal of Bridge Engineering 10.1061/(ASCE)BE.1943-5592.0000735 (2014) 04014118.
[92] M.V. Gangone, M.J. Whelan, K.D. Janoyan, R. Jha, Field deployment of a dense wireless sensor network for condition assessment of a bridge superstructure, SPIE 6933: Smart Sensor Phenomena, Technology, Networks, and Systems, International Society for Optical Engineering - SPIE, Bellingham WA, 2008, p. 69330.
[93] K.J. Loh, J.P. Lynch, N.A. Kotov, Mechanical-electrical characterization of carbon-nanotube thin films for structural monitoring applications, Proceedings of the SPIE - The International Society for Optical Engineering (2006) 61741Z-1-12.
[94] N.P. Shamim, L.F. Gregory, K. Sukun, E.C. David, Design and Implementation of Scalable Wireless Sensor Network for Structural Monitoring, Journal of Infrastructure Systems 14(1) (2008) 89-101.
[95] G. Bartoli, L. Facchini, M. Pieraccini, M. Fratini, C. Atzeni, Experimental utilization of interferometric radar techniques for structural monitoring, Structural Control and Health Monitoring 15(3) (2008) 283-298.
[96] S.W. Doebling, C.R. Farrar, M.B. Prime, Summary review of vibration-based damage identification methods, Shock and Vibration Digest 30(2) (1998) 91-105.
[97] K. Vaghefi, R. Oats, D. Harris, T. Ahlborn, C. Brooks, K. Endsley, C. Roussi, R. Shuchman, J. Burns, R. Dobson, Evaluation of Commercially Available Remote Sensors for Highway Bridge Condition Assessment, Journal of Bridge Engineering 17(6) (2011) 886-895.
[98] American Society of Civil Engineers, Report card for America's infrastructure, 2013. http://www.infrastructurereportcard.org. (Accessed August 14 2015).
[99] D.-S. Jung, C.-Y. Kim, Finite element model updating of a simply supported skewed PSC I-girder bridge using hybrid genetic algorithm, KSCE Journal of Civil Engineering 17(3) (2013) 518-529.
[100] N.M. Okasha, D.M. Frangopol, A.D. Orcesi, Automated finite element updating using strain data for the lifetime reliability assessment of bridges, Reliability Engineering & System Safety 99 (2012) 139-150.
[101] A.I.o.S. Construction, Manual of Steel Construction: Load and Resistance Factor Design Manual of Steel Construction, AISC, 1986.
[102] C. Solutions, Vic-3D User Manual. Correlated Solutions, Inc., Columbia, SC (2005).
[103] Z. Wang, H. Li, J. Tong, J. Ruan, Statistical analysis of the effect of intensity pattern noise on the displacement measurement precision of digital image correlation using self-correlated images, Experimental Mechanics 47(5) (2007) 701-707.
[104] M.S. Dizaji, M. Alipour, D.K. Harris, Leveraging vision for structural identification: a digital image correlation based approach, International Digital Imaging Correlation Society, Springer2017, pp. 121-124.
[105] G. Zames, N. Ajlouni, N. Ajlouni, N. Ajlouni, J. Holland, W. Hills, D. Goldberg, Genetic algorithms in search, optimization and machine learning, Information Technology Journal 3(1) (1981) 301-302.

[106] D.C. Drucker, INTRODUCTIONS TO MECHANICS OF DEFORMABLE SOLIDS, 1967.
[107] I. ASTM, ASTM E8/E8M-16a: Standard Test Methods for Tension Testing of Metallic Materials, West Conshohocken, PA, USA: ASTM International (2016).
[108] H. Li, W.A. Weiss, M. Medved, H. Abe, G.M. Newstead, G.S. Karczmar, M.L. Giger, Breast density estimation from high spectral and spatial resolution MRI, Journal of Medical Imaging 3(4) (2016) 044507.
[109] M.A. Aguilo, W. Aquino, J.C. Brigham, M. Fatemi, An inverse problem approach for elasticity imaging through vibroacoustics, IEEE transactions on medical imaging 29(4) (2010) 1012-1021.
[110] M. Bayat, S. Ghosh, A. Alizad, W. Aquino, M. Fatemi, A generalized reconstruction framework for transient elastography, The Journal of the Acoustical Society of America 139(4) (2016) 2028-2028.
[111] S. Goenezen, J.-F. Dord, Z. Sink, P.E. Barbone, J. Jiang, T.J. Hall, A.A. Oberai, Linear and nonlinear elastic modulus imaging: an application to breast cancer diagnosis, IEEE transactions on medical imaging 31(8) (2012) 1628-1637.
[112] S. Goenezen, A.A. Oberai, J.-F. Dord, Z. Sink, P. Barbone, Nonlinear elasticity imaging, 2011 IEEE 37th Annual Northeast Bioengineering Conference (NEBEC), IEEE, 2011, pp. 1-2.
[113] N.H. Gokhale, P.E. Barbone, A.A. Oberai, Solution of the nonlinear elasticity imaging inverse problem: the compressible case, Inverse Problems 24(4) (2008) 045010.
[114] Y. Mei, S. Goenezen, Spatially weighted objective function to solve the inverse elasticity problem for the elastic modulus, Computational Biomechanics for Medicine, Springer2015, pp. 47-58.
[115] Y. Mei, S. Kuznetsov, S. Goenezen, Reduced boundary sensitivity and improved contrast of the regularized inverse problem solution in elasticity, Journal of Applied Mechanics 83(3) (2016).
[116] M. Wang, D. Dutta, K. Kim, J.C. Brigham, A computationally efficient approach for inverse material characterization combining Gappy POD with direct inversion, Computer Methods in Applied Mechanics and Engineering 286 (2015) 373-393.
[117] B.K. Bay, T.S. Smith, D.P. Fyhrie, M. Saad, Digital volume correlation: three-dimensional strain mapping using X-ray tomography, Experimental mechanics 39(3) (1999) 217-226.
[118] M. Gates, J. Lambros, M. Heath, Towards high performance digital volume correlation, Experimental Mechanics 51(4) (2011) 491-507.
[119] T.S. Smith, B.K. Bay, M.M. Rashid, Digital volume correlation including rotational degrees of freedom during minimization, Experimental Mechanics 42(3) (2002) 272-278.
[120] C. Franck, S. Hong, S. Maskarinec, D. Tirrell, G. Ravichandran, Three-dimensional full-field measurements of large deformations in soft materials using confocal microscopy and digital volume correlation, Experimental Mechanics 47(3) (2007) 427-438.
[121] A. Germaneau, P. Doumalin, J.-C. Dupré, 3D strain field measurement by correlation of volume images using scattered light: recording of images and choice of marks, Strain 43(3) (2007) 207-218.
[122] Z. Yang, W. Ren, R. Sharma, S. McDonald, M. Mostafavi, Y. Vertyagina, T. Marrow, In-situ X-ray computed tomography characterisation of 3D fracture evolution and image-based numerical homogenisation of concrete, Cement and Concrete Composites 75 (2017) 74-83.
[123] P. Luo, Y. Mei, M. Kotecha, A. Abbasszadehrad, S. Rabke, G. Garner, S. Goenezen, Characterization of the stiffness distribution in two and three dimensions using boundary deformations: a preliminary study, MRS Communications 8(3) (2018) 893-902.
[124] Y. Mei, R. Fulmer, V. Raja, S. Wang, S. Goenezen, Estimating the non-homogeneous elastic modulus distribution from surface deformations, International Journal of Solids and Structures 83 (2016) 73-80.
[125] Y. Mei, S. Goenezen, Non-Destructive characterization of heterogeneous solids from limited surface measurements, Proceedings of the 24th International Congress of Theoretical and Applied Mechanics, Montreal, QC, Canada, 2016, pp. 21-26.
[126] Y. Chemisky, F. Meraghni, N. Bourgeois, S. Cornell, R. Echchorfi, E. Patoor, Analysis of the deformation paths and thermomechanical parameter identification of a shape memory alloy using digital image correlation over heterogeneous tests, International Journal of Mechanical Sciences 96 (2015) 13-24.
[127] S. Cooreman, D. Lecompte, H. Sol, J. Vantomme, D. Debruyne, Identification of mechanical material behavior through inverse modeling and DIC, Experimental Mechanics 48(4) (2008) 421-433.
[128] S. Coppieters, T. Hakoyama, D. Debruyne, S. Takahashi, T. Kuwabara, Inverse Yield Locus Identification of Sheet Metal Using a Complex Cruciform in Biaxial Tension and Digital Image Correlation, Multidisciplinary Digital Publishing Institute Proceedings, 2018, p. 382.
[129] J. Olofsson, I.L. Svensson, P. Lava, D. Debruyne, Characterisation and investigation of local variations in mechanical behaviour in cast aluminium using gradient solidification, Digital Image Correlation and finite element simulation, Materials & Design (1980-2015) 56 (2014) 755-762.

[130] L. Robert, V. Velay, N. Decultot, S. Ramde, Identification of hardening parameters using finite element models and full-field measurements: some case studies, The Journal of Strain Analysis for Engineering Design 47(1) (2012) 3-17.
[131] M.S. Dizaji, D.K. Harris, M. Alipour, O.E. Ozbulut, Reframing measurement for structural health monitoring: a full-field strategy for structural identification, Nondestructive Characterization and Monitoring of Advanced Materials, Aerospace, Civil Infrastructure, and Transportation XII, International Society for Optics and Photonics, 2018, p. 1059910.
[132] M. Shafiei Dizaji, D. Harris, M. Alipour, O. Ozbulut, En "vision" ing a novel approach for structural health monitoring–a model for full-field structural identification using 3D-digital image correlation, The 8th International Conference on Structural Health Monitoring of Intelligent Infrastructure, Bridbane, Australia, 2017, pp. 5-8.
[133] M. Farrokh, M.S. Dizaji, A. Joghataie, Modeling hysteretic deteriorating behavior using generalized Prandtl neural network, Journal of Engineering Mechanics 141(8) (2015) 04015024.
[134] A. Joghataie, M. Farrokh, Dynamic analysis of nonlinear frames by Prandtl neural networks, Journal of engineering mechanics 134(11) (2008) 961-969.
[135] O. Ghouati, J. Gelin, An inverse approach for the identification of complex material behaviours, Material identification using mixed numerical experimental methods, Springer1997, pp. 93-102.
[136] M. Meuwissen, C. Oomens, F. Baaijens, R. Petterson, J. Janssen, Determination of parameters in elasto-plastic models of aluminium, Material Identification Using Mixed Numerical Experimental Methods, Springer1997, pp. 71-80.
[137] M. Alipour, D.K. Harris, Increasing the robustness of material-specific deep learning models for crack detection across different materials, Engineering Structures 206 (2020) 110157.
[138] M. Alipour, D.K. Harris, G.R. Miller, Robust pixel-level crack detection using deep fully convolutional neural networks, Journal of Computing in Civil Engineering 33(6) (2019) 04019040.
[139] D.J. Atha, M.R. Jahanshahi, Evaluation of deep learning approaches based on convolutional neural networks for corrosion detection, Structural Health Monitoring 17(5) (2018) 1110-1128.
[140] Y.J. Cha, W. Choi, O. Büyüköztürk, Deep learning-based crack damage detection using convolutional neural networks, Computer-Aided Civil and Infrastructure Engineering 32(5) (2017) 361-378.
[141] C.M. Yeum, S.J. Dyke, Vision-based automated crack detection for bridge inspection, Computer-Aided Civil and Infrastructure Engineering 30(10) (2015) 759-770.
[142] F.N. Çatbaş, T. Kijewski-Correa, A.E. Aktan, Structural identification of constructed systems: approaches, methods, and technologies for effective practice of St-Id, American Society of Civil Engineers, 2013.
[143] A. Davis, F. Ansari, R. Gaynor, K. Lozen, T. Rowe, H. Caratin, F. Heidbrink, V. Malhotra, B. Simons, N. Carino, Nondestructive test methods for evaluation of concrete in structures, American Concrete Institute, ACI 228 (1998).
[144] A. Bagchi, J. Humar, H. Xu, A.S. Noman, Model-based damage identification in a continuous bridge using vibration data, Journal of Performance of Constructed Facilities 24(2) (2010) 148-158.
[145] R.J. Barthorpe, On model-and data-based approaches to structural health monitoring, University of Sheffield, 2010.
[146] S. Jang, J. Li, B.F. Spencer Jr, Corrosion estimation of a historic truss bridge using model updating, Journal of Bridge engineering 18(7) (2013) 678-689.
[147] H.S. Atamturktur, C.R. Gilligan, K.A. Salyards, Detection of internal defects in concrete members using global vibration characteristics, ACI Materials Journal 110(5) (2013) 529-538.
[148] C. Sbarufatti, A. Manes, M. Giglio, Performance optimization of a diagnostic system based upon a simulated strain field for fatigue damage characterization, Mechanical Systems and Signal Processing 40(2) (2013) 667-690.
[149] K. Worden, G. Manson, The application of machine learning to structural health monitoring, Philosophical Transactions of the Royal Society A: Mathematical, Physical and Engineering Sciences 365(1851) (2007) 515-537.
[150] R. Yao, S.N. Pakzad, Autoregressive statistical pattern recognition algorithms for damage detection in civil structures, Mechanical Systems and Signal Processing 31 (2012) 355-368.
[151] M. Bruggi, S. Mariani, Optimization of sensor placement to detect damage in flexible plates, Engineering Optimization 45(6) (2013) 659-676.
[152] Z. Shi, S. Law, L. Zhang, Optimum sensor placement for structuraldamage detection, Journal of Engineering Mechanics 126(11) (2000) 1173-1179.
[153] W.J. Staszewski, K. Worden, Overview of optimal sensor location methods for damage detection, Smart Structures and Materials 2001: Modeling, Signal Processing, and Control in Smart Structures, International Society for Optics and Photonics, 2001, pp. 179-187.

[154] C. Swann, A. Chattopadhyay, Optimization of piezoelectric sensor location for delamination detection in composite laminates, Engineering Optimization 38(5) (2006) 511-528.
[155] A. Bagheri, M. Alipour, S. Usmani, O.E. Ozbulut, D.K. Harris, Structural stiffness identification of skewed slab bridges with limited information for load rating purpose, Dynamics of Civil Structures, Volume 2, Springer2017, pp. 243-249.
[156] D.K. Harris, M.S. Dizaji, Preserving Coastal Infrastructure through the Design and Implementation of Image-Based Structural Health Monitoring (iSHM), iSHM, 2019, p. 13.
[157] A. Al-Radaideh, A. Al-Ali, S. Bheiry, S. Alawnah, A wireless sensor network monitoring system for highway bridges, 2015 International Conference on Electrical and Information Technologies (ICEIT), IEEE, 2015, pp. 119-124.
[158] A.B. Noel, A. Abdaoui, T. Elfouly, M.H. Ahmed, A. Badawy, M.S. Shehata, Structural health monitoring using wireless sensor networks: A comprehensive survey, IEEE Communications Surveys & Tutorials 19(3) (2017) 1403-1423.
[159] M. Bornert, F. Brémand, P. Doumalin, J.-C. Dupré, M. Fazzini, M. Grédiac, F. Hild, S. Mistou, J. Molimard, J.-J. Orteu, Assessment of digital image correlation measurement errors: methodology and results, Experimental mechanics 49(3) (2009) 353-370.
[160] B. Pan, Recent progress in digital image correlation, Experimental mechanics 51(7) (2011) 1223-1235.
[161] M.P. Bendsoe, O. Sigmund, Topology optimization: theory, methods, and applications, Springer Science & Business Media2013.
[162] J.S. Lee, J.E. Kim, Y.Y. Kim, Damage detection by the topology design formulation using modal parameters, International journal for numerical methods in engineering 69(7) (2007) 1480-1498.
[163] T. Nishizu, A. Takezawa, M. Kitamura, Damage detection method by topology optimization based on eigenvalue analysis, The Twenty-fourth International Ocean and Polar Engineering Conference, International Society of Offshore and Polar Engineers, 2014.
[164] Z. Zhang, X. Dai, W. Chen, A piecewise constant level set method for damage identification of continuum structures based on natural frequencies, Structural and Multidisciplinary Optimization 60(6) (2019) 2477-2491.
[165] H. Niemann, J. Morlier, A. Shahdin, Y. Gourinat, Damage localization using experimental modal parameters and topology optimization, Mechanical systems and signal processing 24(3) (2010) 636-652.
[166] C. Niezrecki, P. Avitabile, J. Chen, J. Sherwood, T. Lundstrom, B. LeBlanc, S. Hughes, M. Desmond, A. Beattie, M. Rumsey, Inspection and monitoring of wind turbine blade-embedded wave defects during fatigue testing, Structural Health Monitoring 13(6) (2014) 629-643.
[167] M.P. Bendsøe, Optimal shape design as a material distribution problem, Structural optimization 1(4) (1989) 193-202.
[168] M. Zhou, G. Rozvany, The COC algorithm, Part II: Topological, geometrical and generalized shape optimization, Computer methods in applied mechanics and engineering 89(1-3) (1991) 309-336.
[169] O. Sigmund, J. Petersson, Numerical instabilities in topology optimization: a survey on procedures dealing with checkerboards, mesh-dependencies and local minima, Structural optimization 16(1) (1998) 68-75.
[170] T.E. Bruns, D.A. Tortorelli, Topology optimization of non-linear elastic structures and compliant mechanisms, Computer methods in applied mechanics and engineering 190(26-27) (2001) 3443-3459.
[171] K. Svanberg, The method of moving asymptotes—a new method for structural optimization, International journal for numerical methods in engineering 24(2) (1987) 359-373.
[172] C. Nonis, C. Niezrecki, T.-Y. Yu, S. Ahmed, C.-F. Su, T. Schmidt, Structural health monitoring of bridges using digital image correlation, Health Monitoring of Structural and Biological Systems 2013, International Society for Optics and Photonics, 2013, p. 869507.
[173] D. Reagan, A. Sabato, C. Niezrecki, Unmanned aerial vehicle acquisition of three-dimensional digital image correlation measurements for structural health monitoring of bridges, Nondestructive Characterization and Monitoring of Advanced Materials, Aerospace, and Civil Infrastructure 2017, International Society for Optics and Photonics, 2017, p. 1016909.
[174] P. Kohut, K. Holak, A. Martowicz, T. Uhl, Experimental assessment of rectification algorithm in vision-based deflection measurement system, Nondestructive Testing and Evaluation 32(2) (2017) 200-226.
[175] M.S. Dizaji, M. Alipour, and D. K. Harris, Subsurface Condition Assessment and Structural Health Monitoring of Structures Using Digital Image Correlation and Topology Optimization, Ready to submit.